Azadipyrromethenes as near-infrared absorber materials for organic solar cells

Synthesis and characterization of structure-property relationships

DISSERTATION

Zur Erlangung des akademischen Grades
Doktor rerum naturalium
(Dr. rer. nat.)

Vorgelegt
der Fakultät Mathematik und Naturwissenschaften
der Technischen Universität Dresden

von

Dipl. Chem. Roland Gresser

geboren am 14.06.1981 in München

Die Dissertation wurde in der Zeit von Oktober 2007 bis
Dezember 2010 am Institut für Angewandte Photophysik angefertigt.

Eingereicht am 27.09.2011

1. Gutachter: Prof. Dr. K. Leo
2. Gutachter: Prof. Dr. T. Wolf

Verteidigt am 23.11.2011

Contents

Contents i

1 Introduction 1

2 General aspects of azadipyrromethene dyes 3

- 2.1 Introduction 3
- 2.2 Synthesis of azadipyrromethenes 6

3 Basics of organic semiconductors and solar cells 13

- 3.1 Organic Solids 13
  - 3.1.1 π-conjugated systems 13
  - 3.1.2 Excitation in organic solids 17
  - 3.1.3 Charge carriers and transport 17
- 3.2 Organic solar cells 21
  - 3.2.1 Basic solar cell theory 21
  - 3.2.2 Working principle of an organic solar cell 24
  - 3.2.3 Organic solar cell materials and architecture 26
  - 3.2.4 Requirements to the absorber materials 29

4 Quantum chemical methods 33

- 4.1 Hartree Fock 33
- 4.2 DFT 36
- 4.3 Basis sets 37
- 4.4 Geometry optimization and transition state search 39

5 Azadipyrromethenes 41

- 5.1 Borondifluoride aryl-azadipyrromethenes 41
  - 5.1.1 Synthesis 41
  - 5.1.2 Physical properties 46
- 5.2 Borondifluoride thienyl-azadipyrromethenes 58
  - 5.2.1 Synthesis 58
  - 5.2.2 Physical properties 60

6 Azadiisoindomethenes 71

6.1 Borondifluoride azadiisoindomethenes 71

6.1.1 Synthesis 72

6.1.2 Physical properties 79

6.2 Azadiisoindomethene metal-(II)-complexes 88

6.2.1 Synthesis 89

6.2.2 Physical properties 92

7 Thin film characterization 101

7.1 Evaluation of the charge carrier mobility 101

7.2 Application in organic solar cells 106

8 Conclusions and Outlook 113

8.1 Conclusions 113

8.2 Outlook 116

9 Experimental section 121

9.1 General remarks 121

9.2 Synthesis of azadipyrromethene precursors 123

9.2.1 Synthesis of chalcones 123

9.2.2 Synthesis of 4-nitro-1,3-diarylbutan-1-ones 126

9.2.3 Synthesis of 4-Keto-2,4-diphenylbutanenitrile 127

9.3 Synthesis of azadipyrromethenes 127

9.3.1 Synthesis of borondifluoride-azadipyrromethenes 129

9.3.2 Synthesis of thienyl-substituted azadipyrromethenes 131

9.3.3 Synthesis of borondifluoride-thienyl-azadipyrromethenes 132

9.4 Synthesis of azadiisoindomethene dyes 136

9.4.1 Synthesis of bis-(aryl)-azadiisoindolmethene dyes 136

9.4.2 Synthesis of borondifluoride bis-(aryl)-azadiisoindomethenes 138

9.4.3 Synthesis of boron catecholat bis-(aryl)-azadiisoindomethenes 140

9.4.4 Synthesis of bis-(phenyl)-azadiisoindomethene metal complexes 142

10 Appendix 145

Bibliography 153

Acknowledgements 163

Abstract

Organic solar cells have the potential to become a low-cost photovoltaic technology. One approach to further increase the device efficiency aims to cover the near-infrared region of the sun spectrum. However, suitable absorber materials are rare. This thesis focuses on the material class of aza-bodipy and dibenzo-aza-bodipy as near-infrared absorber materials for organic solar cells.

Besides the synthesis of novel thiophene-substituted aza-bodipys, azadiisoindomethenes were prepared by the addition of Grignard reagents to phthalodinitrile an subsequent reduction with formamide. Starting from these azadiisoindomethenes as precursors, complexes with borondifluoride, boroncatechole and transition metals were synthesized. The optical and electrochemical properties of all compounds prepared were investigated by experimental and theoretical methods. The (dibenzo-)aza-bodipys are characterized by their electronic structure, comprising a central electron acceptor core and peripheral electron donor units. The substituents at the donor units offer a stronger impact on the HOMO energy than on the LUMO energy. Electron donating substituents at the donor units result in an overall decreased HOMO-LUMO gap. This allows to redshift the absorption maximum up to 800 nm. The corresponding dibenzo-analogues already demonstrate a bathochromic shift of the absorption compared to the (non-annulated) aza-bodipys. Yet, the central acceptor is weakened and a further redshift by substituents is less distinct.

The compounds can be thermally evaporated in high vacuum. The required thermal stability is increased in some cases by boroncatechol compared to borondifluoride complexes, without significant influence on the optical and electrochemical properties. Besides the characterization of the molecular properties, promising materials were evaluated in thin films and solar cell devices.

The charge carrier mobility in the measured compounds were found to be between 10^{-6} and 10^{-4} cm^{2}V^{-1}s^{-1}. The charge transport parameters were calculated on the basis of obtained single crystal structures. It was found that a high charge carrier mobility may be attributed to a better molecular overlap and a short intermolecular distance in the corresponding solid state structure. Selected materials were characterized in organic solar cells. In solution processed devices, the dibenzo-aza-bodipys reached efficiencies of 1.6 % and 2.1 %, as donor materials in combination with $PC_{61}BM$ and $PC_{71}BM$ as acceptor. The main limiting factor in these devices turned out to be the low fill factor of 30 %. From a series of vacuum processed devices with aza-bodipys and dibenzo-aza-bodipys, increased voltages were obtained with decreasing HOMO energy of the bodipy derivatives. A suitable near-infrared absorbing dibenzo-aza-bodipy exhibited a contribution to the photocurrent from 750 - 950 nm.

Kurzfassung

Die organische Photovoltaik hat das Potential eine kostengünstige Solarzellentechnologie zu werden. Ein Ansatz die Effizienz weiter zu steigern besteht darin den aktiven Spektralbereich in den nahen Infrarotbereich zu erweitern. Bisher gibt es jedoch nur wenige geeignete Materialien. In dieser Arbeit werden Verbindungen aus der Materialklasse der Aza-Bodipy und Dibenzo-Aza-Bodipy als Absorbermaterialien für den nahen Infrarotbereich zur Verwendung in organischen Solarzellen untersucht.

Neben der Synthese von neuen Thiophen-substituierten Aza-Bodipys wurden Azadiisoindomethine durch die Addition von Grignardverbindungen an Phthalodinitril und anschließender Reduktion mit Formamid dargestellt. Ausgehend von den Azadiisoindomethinen sind neue Bordifluorid, Borbrenzcatechin und Übergangsmetallkomplexe synthetisiert worden. Alle Substanzen sind mit experimentellen und theoretischen Methoden auf ihre optischen und elektrochemischen Eigenschaften hin untersucht worden.

Die elektronische Struktur der (Dibenzo-)Aza-Bodipys ist charakterisiert durch periphere Elektronendonoreinheiten um einen zentralen Elektronenakzeptor. Die langwelligste Absorptionsbande kann in beiden Systemen durch Elektronen schiebende Gruppen an den Donoreinheiten bathochrom, auf über 800 nm verschoben werden. Die Ursache liegt in einem stärkeren Einfluss der Substituenten auf das HOMO als auf das LUMO und einem damit einhergehenden stärkeren Anstieg der HOMO-Energie woraus eine verkleinerte HOMO-LUMO Lücke resultiert.

Die Dibenzo-Aza-Bodipys zeichnen sich durch eine rotverschobene Absorption gegenüber den (nicht benzannulierten) Aza-Bodipys aus. Jedoch ist der Akzeptor in den Dibenzo-Aza-Bodipys abgeschwächt, so dass die Rotverschiebung durch die selben Substituenten weniger stark ausgeprägt ist und die Energieniveaus tendenziell höher liegen.

Die Verbindungen lassen sich thermisch im Vakuum verdampfen. Die für das Verdampfen wichtige thermische Stabilität, kann durch Austausch von Bordifluorid mit Borbrenzcatechol erhöht werden, ohne die optischen und elektronischen Eigenschaften wesentlich zu beeinflussen. Neben der Charakterisierung der molekularen Eigenschaften, sind einige Verbindungen im Dünnfilm auf ihre elektrischen Eigenschaften und in Solarzellen untersucht worden.

Die Ladungsträgerbeweglichkeit liegt bei den gemessenen Verbindungen zwischen 10^{-6} und 10^{-4} $\mathrm{cm^2V^{-1}s^{-1}}$. Durch Berechnung der Ladungstransportparameter auf Basis erhaltener Kristallstrukturen ist eine höhere Beweglichkeit auf eine günstigere Packung und einen geringeren intermolekularen Abstand zurückgeführt worden.

Ausgewählte Verbindungen sind als Donormaterialien in organischen Solarzellen charakterisiert worden. Aus Lösungsmittel prozessierte Solarzellen mit Dibenzo-Aza-Bodipys erreichen eine Effizienz von 1.6 % mit $PC_{61}BM$, und 2.1 % mit $PC_{71}BM$ als Akzeptor. Der Effizienz limitierende Faktor ist hierbei der niedrige Füllfaktor von ca. 30 %. In vakuumprozessierten Solarzellen mit planarem Dono-Akzeptor-Übergang von Aza-Bodipys und Dibenzo-Aza-Bodipys hat sich gezeigt, dass die erhaltene Spannung mit abnehmender HOMO Energie der Materialien gesteigert wird. Ein geeignetes Dibenzo-Aza-Bodipy Material ist mit einen Beitrag zum Photostrom im nahen Infrarotbereich, von 750 - 950 nm, gezeigt worden.

Publications

- R. Gresser, H. Hartmann, M. Riede, and K. Leo. *Synthesis and characterization of new NIR absorbing benzannulated aza-BODIPY dyes*, Chemistry - A European Journal **17**, 2939-2947 (2011) .
- R. Gresser, A. Hoyer, M. Hummert, H. Hartmann, M. Riede, and K. Leo. *Homoleptic Co(II), Ni(II), Cu(II), Zn(II) and Hg(II) complexes of bis-(phenyl)-diisoindole-aza-methene*, Dalton Transactions **40**, 3476-3483 (2011).
- R. Gresser, M. Riede, H. Hartmann, and K. Leo. *Synthesis of thiophene-substituted aza-BODIPYs and their optical and electrochemical properties*, Tetrahedron **67**, 7148-7155 (2011).
- T. Mueller, R. Gresser, M. Riede, and K. Leo. *Organic solar cells based on novel infrared absorbing aza-BODIPY dyes*, Solar Energy Materials and Solar Cells, accepted.
- J. Meiss, F. Holzmueller, R. Gresser, K. Leo, and M. Riede. *Near-infrared absorbing semi-transparent organic solar cells*, Appl. Phys. Lett. **99**, 193307-193310 (2011).
- H. Ziehlke, R. Fitzner, C. Koerner, R. Gresser, E. Reinold, P. Bäuerle, K. Leo, and M. Riede. *Side Chain Variations on a Series of Dicyanovinyl-Terthiophenes: A Photoinduced Absorption Study*, J. Phys. Chem. A **115**, 8437–8446 (2011).
- J. Meyer, A. Wadewitz, Lokamani, C. Toher, R. Gresser, K. Leo, M. Riede, F. Moresco, and G. Cuniberti. *Molecules for organic electronics studied one by one*, Phys. Chem. Chem. Phys. **13**, 14421-14426 (2011).
- R. Gresser, Toni Mueller, M. Hummert, M. Riede, H. Hartmann, and K. Leo. *Organisches halbleitendes Bauelement*, DE 102009021881 A1.
- R. Gresser, Toni Mueller, M. Hummert, M. Riede, H. Hartmann, and K. Leo. *Organisches halbleitendes Bauelement*, DE 102009021882 A1.

1 Introduction

We are facing a long range and comprehensive change, originating from the growing world population, increased urbanization and mobility, as well as rising energy consumption, just to name a few. Energy is required for any human activity but the supply with energy is often taken for granted. In fact, 80% of the world total primary energy supply is shared by the fossil fuels gas, oil or coal. Considering electricity as most important and versatile form of energy, the total shares of fossil fuels for the world generation is still 66%.[1] The burning of coal or other fossil fuels for energy supply releases carbon dioxide into the earth's atmosphere which contributes to the greenhouse effect. The large release of anthropogenic greenhouse gases since the industrialization will lead in the long term to a global warming and a destabilization of the balanced climate. As a further aspect, all fossil fuels are limited due to the fact that their generation required millions of years. Accordingly, the supply of energy via fossil fuels is not sustainable.[2]

In contrast, renewable energies like solar power, wind power, hydro power, geothermal or biomass energy do not deplete their source. The emission of greenhouse gases is nearly restricted to the fabrication of the plants, with the exception of biomass conversion. An elegant form of solar power is the photovoltaic technology. Besides the established silicon technologies, current research is also conducted on organic photovoltaics, which is based on conjugated polymers or small molecular dyes as semiconductors.[3] The basic concept used today goes back to the work of Tang in 1986, where the organic donor-acceptor heterojunction was invented and an efficiency of 1% was reached.[4] The involved organic materials are characterized by their intense extinction coefficient and high absorbance. This property makes it possible to fabricate very thin films, in the range of a few hundred nanometers, and still absorb most of the sunlight. The thin films might be fabricated by low-cost printing or vacuum deposition techniques, with a low energy and material consumption. This allows for the production of solar cells on plastic and even flexible substrates, opening new and broad, especially mobile applications.[5] Organic photovoltaics has the potential to contribute to the energy supply mix in future. A prerequisite for the widespread application is an improvement of the efficiency and the longterm stability of devices. Currently, the most efficient organic solar cells reach an efficiency of over 8% and a further enhancement will be driven by the development of new functional organic materials.[6] Since todays absorber materials only cover a small part of the (visible) sun spectrum, one approach increasing the device efficiency is the design of new absorber materials for the near infrared (NIR) region, in order to make an enlarged part of the solar spectrum accessible. Numerous dyes absorbing in the NIR region are known, however, the material requirements for the applications in organic solar cells are divers and promising materials are rare.[7] The present thesis is aimed at the development of novel suitable NIR absorber materials, to partially overcome the lack of NIR dyes meeting all requirements of vacuum-processed organic solar cells.

The material class of aza-bodipys is known for their high thermal stability essential for vacuum processing, and some derivatives already showed an absorption in the NIR region.[8] This appears as promising starting point, although the application in organic solar cells was not yet investigated. The purpose of this thesis is the identification, the synthesis and the characterization of appropriate compounds. The pursued strategy to find the right structures is the evaluation of optical and electrochemical properties followed by the clarification of the underlying structure-property relationship of the aza-bodipys with both experimental and theoretical methods.

In the beginning, an introduction of the materials class of aza-bodipys is given together with the known synthesis strategies. The basics of organic molecular semiconductors and the working principle of organic solar cells is detailed together with the applied theoretical methods in chapters 3 and 4. In chapter 5 the investigation of the basic properties is discussed and the synthesis of new thiophene-substituted aza-bodipys is presented. The synthetic efforts and characterization of novel dibenzo-aza-bodipy derivatives is demonstrated in chapter 6. In chapter 7, the charge carrier transport properties of the most promising candidates are finally evaluated including the characterization in organic solar cell devices.

2 General aspects of azadipyrromethene dyes

(Aza)dipyrromethenes are promising materials for various applications and are intensively investigated. This chapter aims to give a brief introduction to the materials class of azadipyrromethenes. Besides a short historical review, the syntheses of azadipyrromethenes are explained in more detail.

2.1 Introduction

The heterocyclic compound pyrrole is one of the most important π-electronic building blocks of a variety of organic molecules or polymers, in particular of the more complex macrocycles such as porphyrines **1** and phthalocyanine **4**. Porphyrines **1** and its metal derivatives **5** have a remarkable biological importance. For instance as prosthetic group in the iron containing and oxygen transporting hemoglobin in the red blood cells, or as photosynthetic actuator in the magnesium containing chlorophyll, which allows plants to obtain energy from light.[9, 10, 11] Phthalocyanines **4** and the metalized derivatives **8** are of technical interest due to their high chemical and thermal stability. They found application as deeply colored dyes in optical recording media (CD-ROM) or as pigments in lacquers.[12]

Besides that, several acyclic derivatives with two pyrrole derivatives such as the dipyrromethenes **9** and their aza analogues **10**, the benzo-condensed derivatives **11** and **12** as well as their metal derivatives found increasing interest.[13] [1]

---

[1] For the sake of completeness, the expanded sapphyrin and superphthalocyanine as well as the contracted subporphyrins and subphthalocyanines shall be mentioned.[14, 15]

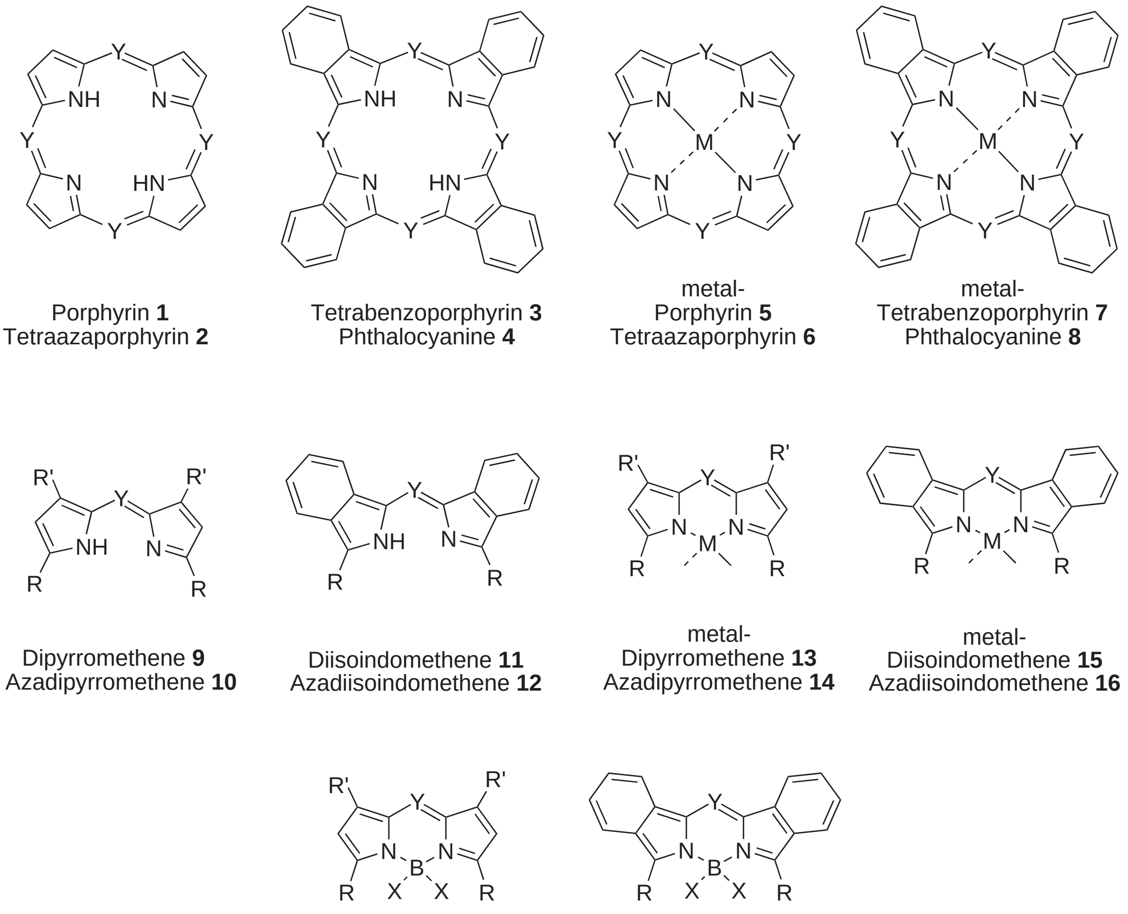

Y = CH: Porphyrin **1**
Y = N: Tetraazaporphyrin **2**

Tetrabenzoporphyrin **3**
Phthalocyanine **4**

metal-
Porphyrin **5**
Tetraazaporphyrin **6**

metal-
Tetrabenzoporphyrin **7**
Phthalocyanine **8**

Y = CH: Dipyrromethene **9**
Y = N: Azadipyrromethene **10**

Diisoindomethene **11**
Azadiisoindomethene **12**

metal-
Dipyrromethene **13**
Azadipyrromethene **14**

metal-
Diisoindomethene **15**
Azadiisoindomethene **16**

Y = CH: Bodipy **17**
Y = N: Aza-Bodipy **18**

Dibenzo-Bodipy **19**
Dibenzo-aza-Bodipy **20**

Figure 2.1: Overview of pyrrol containing π-aromatic molecules: Relationship of porphyrin and tetrabenzoporphyrin macrocycles **1-4** and the corresponding metal derivatives **5-8**. Hemicyclic dipyrromethenes **9-10**, the benzo-fused diisoindomethenes **11-12** and their metal complexes **13-16**. Boron containing complexes of dipyrro- **17-18** and diisoindomethenes **19-20** called bodipys (4,4-difluoro-4-bora-3a,4a-diaza-s-indacene).

Within these acyclic derivatives, the boron(difluoride) compounds **17-20**, called bodipys (4,4-difluoro-4-bora-3a,4a-diaza-s-indacene) are most important.[8] Especially, their long wavelength absorption and intense emission stimulated various experimental and theoretical studies in the last years.[16, 17] The basic research on dipyrromethenes has been done in the early 1930s by Fischer et al. for the purpose of porphyrin synthesis.[18] He investigated their synthesis as well as reactions like bromination or complex salt formation of dipyrromethenes. Later, improved synthesis of dipyrromethenes lead to their investigation as coloring matters and early research was conducted on magnetic and semiconducting properties of dipyrromethene metal complexes.[19, 20] The borondifluoride complex of a dipyrromethene structure was first reported 1968 by Treibs and Kreuzer, shortly after Daltrozzo et al. described the first phenylboron complexes of diquinolylmethane.[21, 22] The reaction of a dipyrromethene with borontrifluoride etherate results in a neutral complex which can be regarded as a rigidified or bridged cyanine dye **22**, derived from a nonamethine streptocyanine **21** as it is illustrated in Figure 2.2. Instead of the N,N'-dimethyl-dipyrromethene **23**, the borondifluoride complexation lead to the electronically neutral bodipy core **24**.[23, 24]

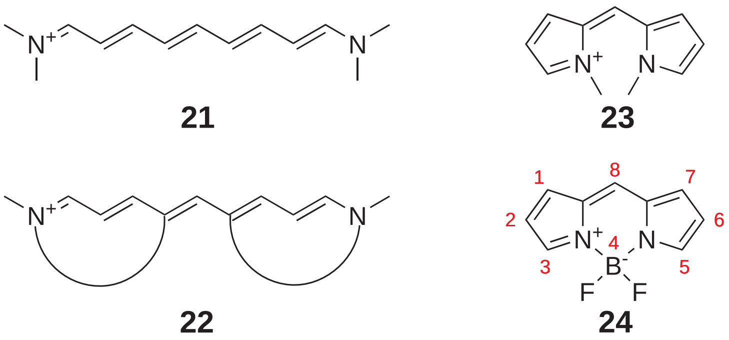

Figure 2.2: Illustration of a streptocyanine dye **21**, a bridged cyanine dye **22** and the resulting dimethylated dipyrromethene dye **23**, and the borondifluoride dipyrromethene core **24**.

The boron chelate complex **17** and **18** offers a high stability of the dipyrromethene core **9** and **10**, since torsion of the pyrrole rings is prevented. The stiff structure of the difluorboron dipyrromethenes causes intense fluorescence with high quantum yields, which has been immediately recognized as their most important property.[21] The dipyrromethene framework provides a complete conjugation of the 12 π-electrons along the backbone except the boron atom due to its tetrahedral configuration. As a consequence, by the attachment of suitable substitutents or conjugated groups to the dipyrromethene framework, the π-system and hence the absorption and fluorescence properties can be tuned. Additionally, the simple synthesis based on pyrrole and aldehydes or acid clorides and the variety of subsequent tolerant functionalization led to a great popularity of the borondifluoride dipyrromethene complexes. Hence, over 3000 scientific publications have been reported on the preparation and diverse use e.g. in biological staining, as laser dyes and in organic solar cells. They are further commercially distributed from MOLECULAR PROBES. The related structures of azadipyrromethenes **10** are obtained by the substitution of the meso-bridge carbon atom in the position 8 by a nitrogen atom, as it can be seen in Figure 2.1 and Figure 2.2. These azadipyrromethenes and their transition metal complexes **14** were first discovered by Rogers in the 1940s and investigated as coloring matters.[25, 26] The first borondifluoride azadipyrromethene **18** was then synthesized by Boyer et al. 50 years later in 1993.[27] However, the azamethenes **10,12,14,15,18,20** have been investigated to a much lower extent compared to their non-aza analogues **9,11,13,15,17,19**. This might be due to the harsh reaction conditions and the resulting limitation of the synthesis. Only about 60 journal articles and 25 patents can be found in the literature.

This thesis, deals on the one hand with the synthesis and characterization of the azadipyrromethenes **10** and their dibenzo-condensed derivatives **12**, on the other hand with the corresponding aza-bodipy **18**, dibenzo-aza-bodipy **20**, and metal azadiisoindomethene compounds **16** and their evaluation as organic solar cell absorber materials. The principal synthesis to these compounds will be discussed in more detail in the next section. The synthetic approaches and modifications of the non aza-analogues will not be discussed in further detail. The reader is referred to the variety of review articles [13, 8, 16, 17].

2.2 Synthesis of azadipyrromethenes

The tetraaryl-azadipyrromethene **26** was the first azadipyrromethene structure published.[25] Rogers reacted γ-nitro-β-phenyl-butyrophenone **25** either with formamide under reflux or with ammonium formate in a melt process under the conditions of the Leuckart reaction (see Scheme 2.1, conditions i).[25, 26] The main synthetic effort towards an optimization of the reaction conditions has been done by the group of O'Shea. They introduced ammonium acetate as an alternative ammonium source for the synthesis and discovered major improvements by the use of alcoholic solvents instead of solvent-less conditions (see Scheme 2.1, conditions ii).[28] Still, the mechanism is not fully understood, since no intermediate products were yet isolated. However, a postulated mechanism for this reaction (according to [8]) is shown in Scheme 2.2.

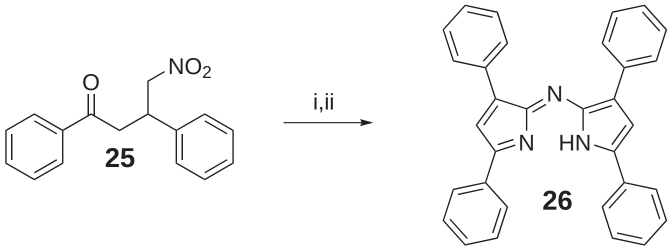

Scheme 2.1:
Reagents and conditions: (i) NH_4CO_2H/neat, 30 min, 30 %. (ii) NH_4OAc/neat, 1.5 h, 47 %; NH_4OAc/EtOH, 24 h, 33 %; NH_4OAc/BuOH, 24 h, 39 %.

The key step is the ring closure of the ketimine moitey **29** to the nitronate moity which was activated by deprotonation **28**. According to the Nef reaction, the species **30** formed can now eliminate hyponitrous acid (forming finally nitrous oxide) and water yielding **32**. With the rearrangement of **32** the pyrrole **33** is formed.[8, 29, 30] This pyrrole is supposed to be nitrosated *in situ* to give the nitroso-pyrrole **35**, that condenses with another pyrrole to the azadipyrromethene **37**, as shown in Scheme 2.3.[8] The azadipyrromethene chromophore may also be obtained by a nitrosation and condensation reaction of 2,4-diarylpyrroles, which is shown in Scheme 2.3. This method has the advantage compared to others, that also asymmetric azadipyrromethenes are available with this procedure. The diarylpyrroles **34** can be nitrosated readily in the 5-position with sodium nitrite, although nitrosation of pyrroles usually occur in the 3-position. This 5-nitroso-2,4-diarylpyrrole **35** condenses efficiently with a second equivalent 2,4-diarylpyrrole **36** to yield the tetraaryl-azadipyrromethene **37**. The synthesis strategy, first described by Rogers, was later applied by the groups of O'Shea and Carreira for the preparation of asymmetric and rigidized azadipyrromethene dyes.[25, 31, 32] A third synthesis method shown in Scheme 2.4 uses as educt β-benzoyl-α-phenylpropionitrile **38** which is heated with formamide or another nitrogen source like ammonium formate as described by Rogers and Knott to yield **26**.[25, 26, 33] This reaction leads also to the same symmetric azadipyrromethene as it is the case for the reaction in Scheme 2.1.

During the reaction according to Scheme 2.4, ammonia is released either from thermal decomposition of formamide or from the dissociation of the ammonium salt and adds subsequently to the ketone **39** to form **40**, as it is shown in Scheme 2.5. Cyclization and dehydration of **40** leads

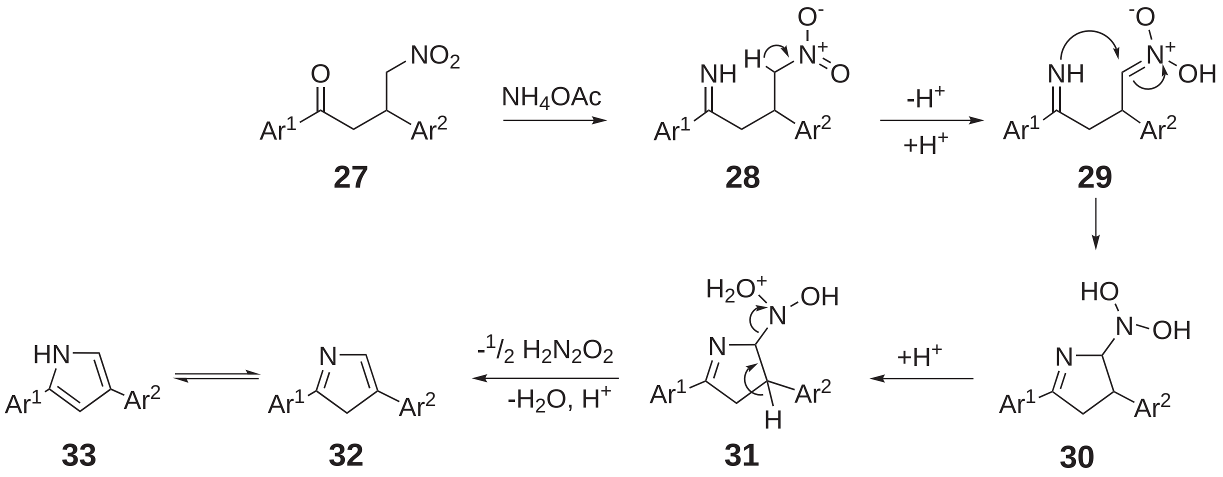

Scheme 2.2: Proposed mechanism for the transformation of the γ-nitro-β-phenyl-butyrophenone **27** into pyrrole **33**.

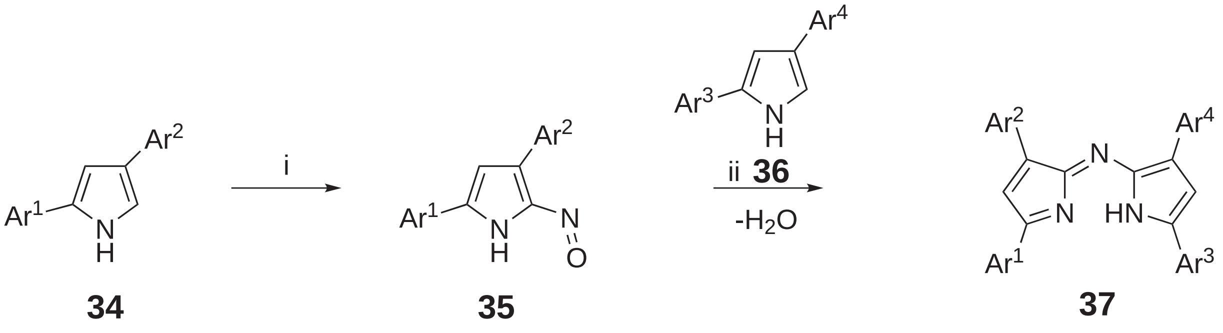

Scheme 2.3: Nitrosation of 2,4-diarylpyrrole and subsequent condensation to the tetraaryl-azadipyrromethene **37**. Reagents and conditions: (i) $NaNO_2$, EtOH, HCl (aq), rt, 30 min. (ii) Ac_2O, HOAc, 100°C, 1 h.

finally to the 5-amino-pyrrole **41** which is readily converted into the azadipyrromethene **42**. The last step of the mechanism in which oxidation and elimination of ammonia occur is not clear yet. However, the final product of the reaction of propionitrile with ammonia is not the aminopyrrole **41**, but the azadipyrromethene **42**.[25, 26, 33]

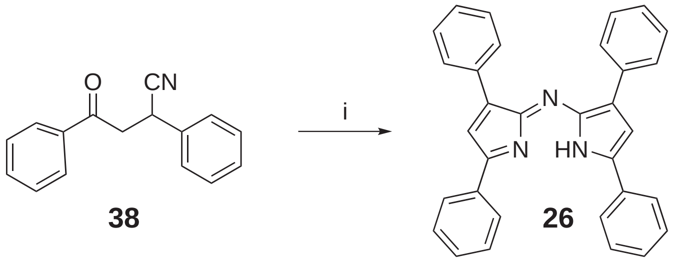

Scheme 2.4: Reagents and conditions: (i) NH_4CO_2H, EtOH, reflux, 20 min, 21 %.

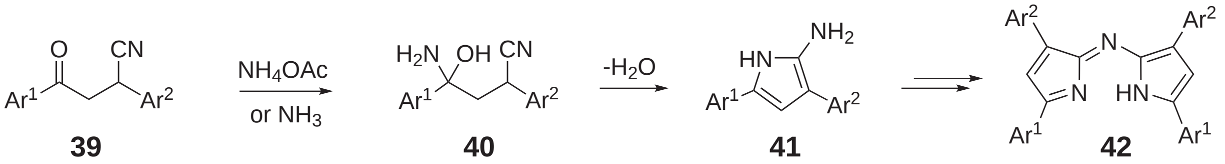

Scheme 2.5: Proposed mechanism (according to [26]) for the transformation of the β-benzoyl-α-phenylpropionitrile **39** to aminopyrrole **41**, and subsequent azadipyrromethene formation.

Another method to obtain azamethenes was described by Bredereck (for indole analogues) and Bird et al. and is shown in Scheme 2.6.[34, 35] Both pursued the same strategy and investigated the addition of Grignard reagents **44** to dinitriles like succinonitrile **45** or phthalodinittril **46**. In both cases the intermediate addition product underwent a ring closure to either a pyrrole or an isoindole species which then were converted to the corresponding azamethene **47** and **48**. In both cases, the reaction mixture was quenched with an ammoniumchloride solution and the 5,5'-diaryl-aza-dipyrromethene **47** was then formed after oxidation in acidic aqueous solution. The diisoindoazamethene **48** was isolated after a steam distillation and recrystallization from pyridine.

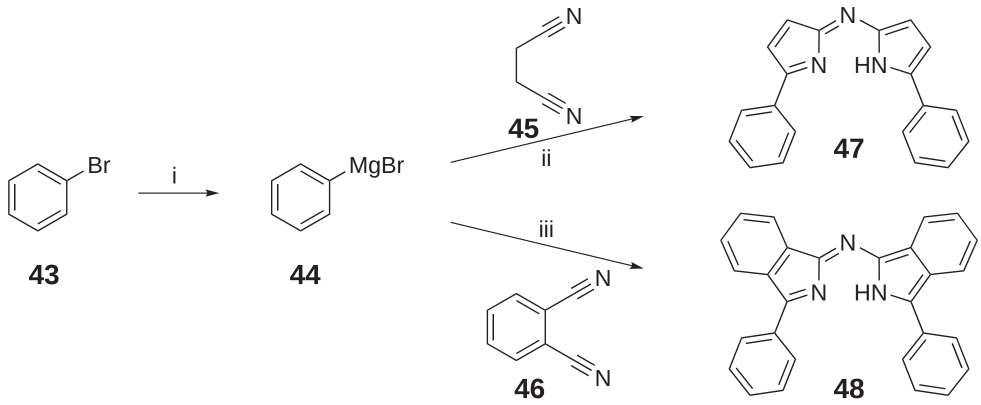

Scheme 2.6: Reagents and conditions: (i) Mg, Et_2O (abs.); (ii)benzene, reflux, 2 h, NH_4Cl (aq) solution, HCl; (iii) benzene, 2 h, NH_4Cl (aq) solution, steam distillation.

Dipyrrromethenes and their aza-methene analogue ligands are able to form extremely stable complexes with a variety of metal or pseudo-metal ions, which is shown in Scheme 2.7. In this context, the boric acid derivatives, especially the borondifluoride complexes **49** have an outstanding importance. The metal complexes of azadipyrromethenes **50** were described with metal-(II) ions like Co or Zn and their structural and spectroscopic properties were investigated.[36, 37]

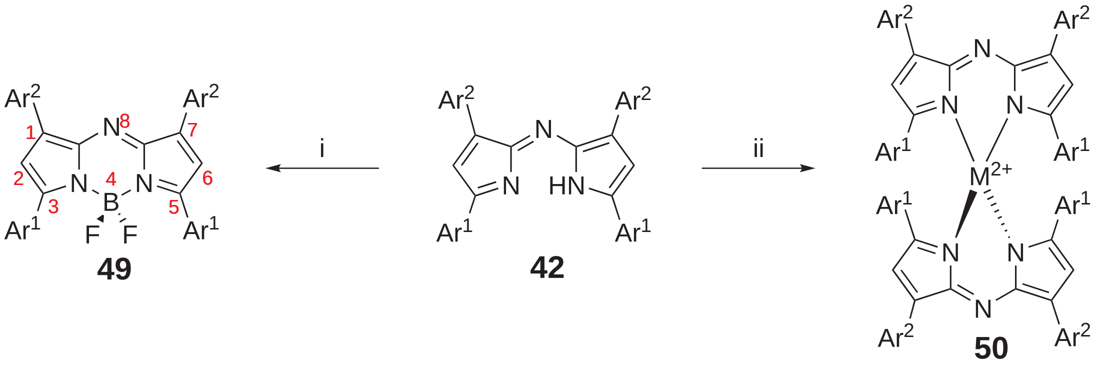

Scheme 2.7: Reagents and conditions: (i) $BF_3{\cdot}OEt_2$, *i*-$PrNEt_2$, $CH_2Cl_2Et_2$, reflux; (ii) metal-(II)-acetate, *i*-$PrNEt_2$, BuOH, reflux.

The most important property of azadipyrromethenes is their intense long wavelength absorption (between 650 nm and 800 nm) and fluorescence (up to 840 nm). These spectroscopic characteristics are bathochromically shifted compared to the ones of the corresponding non-aza dipyrromethene analogues. The red and near infrared spectroscopic range reached, is important for various applications, e.g. for chemosensors and borondifluoride azadipyrromethenes are investigated for that purpose, among other applications.[28]

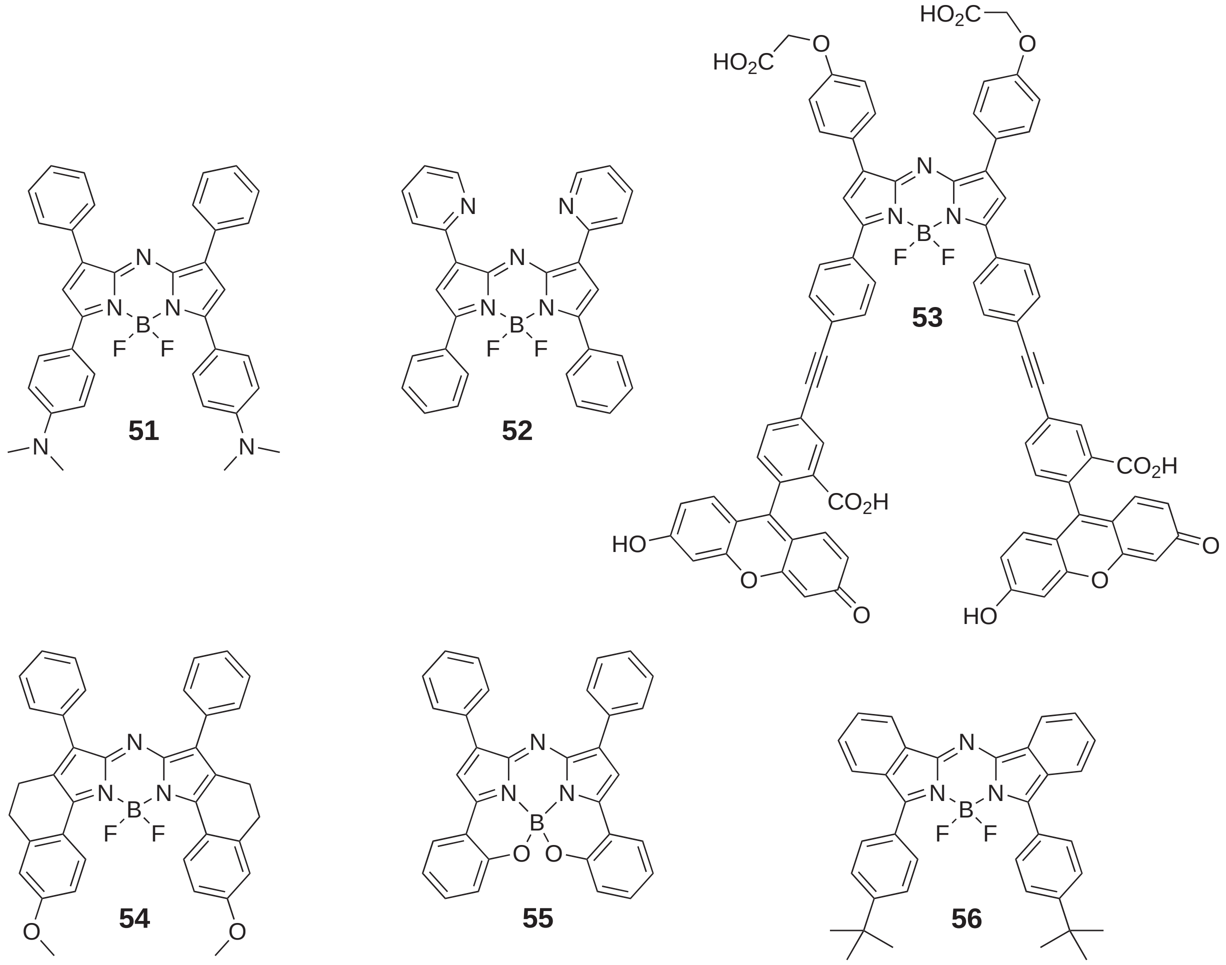
51 **52** **53** **54** **55** **56**

Figure 2.3: Diverse azadipyrromethenes for applications as chemosensors (**51**, **52**), as energy transfer cassette (**53**), for bio-imaging (**54**, **55**) and photodynamic therapy (**56**).

It was found that electron donating substituents in the 3,5-position of tetraaryl-azadipyrromethenes (see Scheme 2.7) tend to redshift the absorption. The substitution with dimethylamino groups in the *para*-positions of the 3,5-diphenylrings lead to compound **51** which gives rise to NIR fluorescence. It was investigated in sensor application with a pH-responsive absorption and fluorescence change across a broad acidity range.[38] An example of a chemosensor for metal-(II)-ions is the azadipyrromethene **52**. In this compound, mercury-(II)-ions are preferentially chelated between the pyridyl groups allows to distinguish between other ions.[39]

The azadipyromethenes can also be functionalized by cross-coupling reactions. This method was applied for compound **53** to realize a through-bond energy transfer cassette with fluorescine as donor in combination with an alkyne spacer and the azadipyrromethene core as acceptor.[40] In order to manipulate the absorption and fluorescence, conformational restrictions of the aryl groups in the 3,5-position of tetraaryl-azadipyrromethenes has been investigated.[41, 32] In one example, shown in compound **54**, the restriction of the aryl groups was realized by a short alkane bridge. Another method uses ortho-hydroxy groups to fully chelate the central boron atom, as in compound **55**. Here the rotation of the aryl groups is inhibited by coordination. The optical properties can further be modified by benzannulation of the 1,7-phenyl rings, as it is the case in the bisphenyl-azadiisoindomethene **56**.[42] In all examples these modifications led to a significant bathochromic shift with increased absorbance and redshifted fluorescence compared to the parent tetraphenyl-azadipyrromethene. For that reason, these compounds are interesting candidates for intracellular bio-imaging or as photosensitizers in photodynamic therapy, where emission wavelengths from 700-900 nm are desired. Despite of the known optical properties, which are promising for future applications, little is known about their electrochemical properties of the aza-bodipy compounds and investigations on this topic have not been conducted so far. This issue is of particular importance for the usage and application of such materials in organic electronic devices. The goal of this thesis is to elucidate the basic correlation between molecular structure and optical and electrochemical properties in the aza-bodipys and to obtain suitable materials from this class for organic solar cell applications.

3 Basics of organic semiconductors and solar cells

In this chapter an introduction into the field of organic solids and semiconductors is given and the basics of organic photovoltaics will be discussed.

3.1 Organic Solids

The major characteristics of molecules in organic solids, which are used for application in organic electronic devices, is the extended π-system. The basics of π-orbitals, the excitation of electrons from π-bonding to anti-bonding orbitals as well as the charge carrier transport will be shortly reviewed in the following sections.

3.1.1 π-conjugated systems

Molecular orbital theory

In molecular orbital (MO) theory, each molecule is described by a set of molecular orbitals. It is assumed that the molecular orbital wave function ψ_{MO} may be written as a simple weighted linear combination of the n constituent atomic orbitals ψ_{AO},[43]

$$\psi_{\mathrm{MO}} = \sum_{i}^{n} c_i \psi_{\mathrm{AO}}. \tag{3.1}$$

For example, in the case of ${H_2}^+$, the molecular wavefunction can be written either as the sum or the difference of the corresponding 1s atom orbitals of the hydrogen atom A and B

$$\psi = N\psi_{1s}(\mathrm{A}) + \psi_{\mathrm{1s}}(\mathrm{B}), \text{ and} \tag{3.2}$$

$$\psi = N\psi_{1s}(\mathrm{A}) - \psi_{\mathrm{1s}}(\mathrm{B}). \tag{3.3}$$

The distribution of the electron over the molecule is described by the square absolute value $|\psi|^2$ of the molecular orbital and in this example has the form

$$\psi^2 \quad = \quad N^2\psi_{1s}(A)^2 + \psi_{1s}(B)^2 \pm 2\psi_{1s}(A)\psi_{1s}(B). \text{ [43]} \tag{3.4}$$

Here, the first and the second term is the probability density of the electron at the atom A or B. The third term, also called overlap density, is related to the chemical bond present in the molecule. If this term has a positive sign, the probability to find the electron between the two nuclei is increased, due to the constructive superposition of the respective atomic orbitals. This leads to an attractive force between the nuclei and results in an energetically stabilized bonding orbital (see Figure 3.1). If this term has a negative sign, the probability density to find the electron between the two nuclei is decreased due to the destructive superposition of the atomic orbitals and leads to a nodal plane between the two nuclei. The anti-bonding orbital (marked by an asterisk in Figure 3.1) is energetically destabilized with respect to the atomic orbital and its occupation leads to a weakened chemical bond.[43]

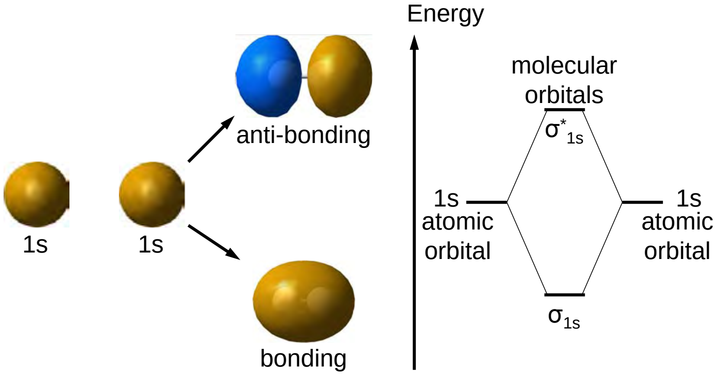

Figure 3.1: Interaction of two 1s hydrogen orbitals leads to constructive and destructive interference, resulting in an increase of electron density (bonding) or a decrease of electron density (anti-bonding) between the two nuclei. The bonding case stabilizes the molecular orbitals, whereas the anti-bonding case destabilizes the molecular orbitals, with respect to the atomic orbitals.

π-Orbitals and aromatic conjugation

Organic semiconductors consist of organic, π-electron conjugated molecules. In contrast to these materials, in molecules without π-bonds, the σ-electrons are tightly bound between the nuclei and cannot interact with adjacent molecules. Instead, laterally overlapping π-bonds are required for semiconducting properties or electrical conductivity. Here, the example of ethylene is quoted to describe the prototype of a π-bond. In MO-theory, the orbitals of ethylene consist of the 1s-orbitals of four hydrogen atoms and the 2s-, $2p_x$-, $2p_y$-, and $2p_z$-orbitals of two carbon atoms. All orbitals except of the $2p_z$-orbital contribute to the formation of MOs which have a σ-bonding character for carbon-carbon and carbon-hydrogen interactions. The σ-bond is formed coplanar, between the two respective nuclei. The $2p_z$-orbitals are perpendicular to the carbon-carbon σ-bond and characterized by a laterally overlap, above and underneath the plane of the nuclei. As for the σ-bond, this leads to bonding and anti-bonding π-orbitals.

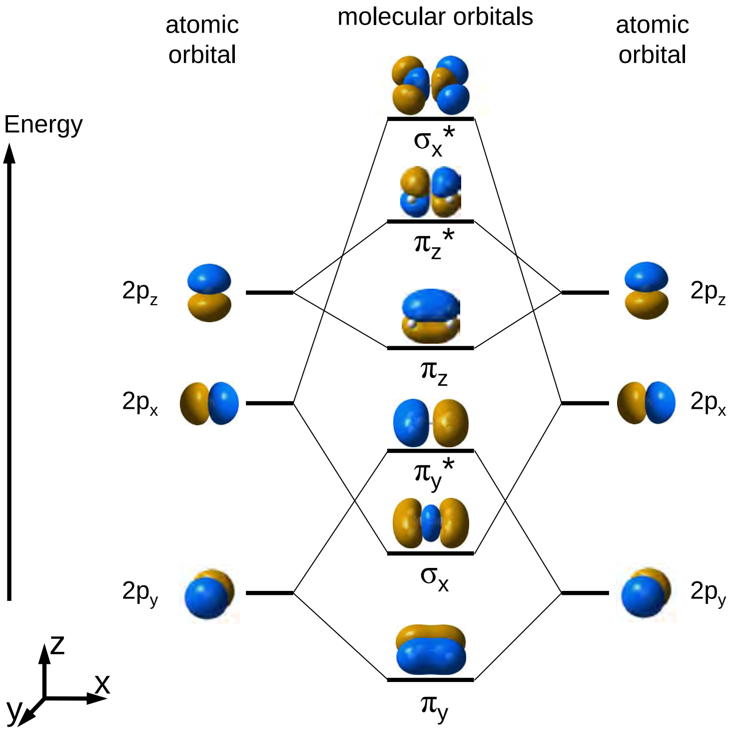

Figure 3.2: Molecular orbitals of ethylene resulting of the overlap of the carbon p-orbitals (schematic representation on the left and right). The p_x-orbitals lead to an overlap coplanar to the nuclei and therefore to a σ-(anti-)bond. The p_y- and p_z-orbitals lead to a laterally overlap and to π-(anti-)bonds.

Overall, this binding situation results in double-bonded carbon atoms, with one σ- and one π-bond, strengthening the carbon-carbon bond. In a larger molecule like benzene, the overlap of adjacent $2p_z$ atomic orbitals lead to MOs, which are delocalized over the whole molecule. As a result, the electron density is equally distributed over the benzene ring (since every carbon atom is equal). Additionally, this delocalization leads to a stabilization of the molecule which is characteristic for conjugated systems, and sums up to 152 kJmol^{-1} in case of benzene.[43] In π-orbitals the degree of lateral overlap is lower compared to the direct overlap of σ-orbitals. As a result, the energetical stabilization in the bonding π-orbital as well as the destabilization in the corresponding anti-bonding orbitals π^* is smaller compared to respective σ-orbitals. This leads to the fact, that usually the MOs with π-character are the highest occupied molecular orbital (HOMO) and the lowest unoccupied molecular orbital (LUMO). The set of HOMO and LUMO is called frontier orbitals.

Figure 3.3: Six p_z-orbitals of every carbon atom form π-orbitals extended over the whole benzene ring. One of them is depicted here, with solely constructive interference of the $2p_z$-orbitals. The corresponding π-electrons are delocalized in this orbital over every carbon atom in the benzene ring.

This π-π^*-frontier orbitals have a strong impact on the optical and electrical properties of optoelectronic materials. In π-systems, lowest energetic optical excitation leads to a $\pi \rightarrow \pi^*$ transition. The excitation energy for an isolated double-bond is about 7 eV, corresponding to 180 nm (in the UV-regime).[43] If the double bond is part of a larger conjugated system, the π-π^* orbital energy difference is smaller and the wavelength for the $\pi \rightarrow \pi^*$ transition is larger and can reach the visible or even the infrared region of the spectrum. Since the frontier orbitals have discrete energies, the absorption occurs in a specific wavelength range and is more or less narrow. This is in contrast to inorganic semiconductors where the band formation leads to a continuous light absorption. Silicon absorbs from in the infrared region into the visible region of the spectrum, according to the band gap of >1.1 eV corresponding to 1130 nm. The transition dipole moment of organic conjugated π-systems is usually large and leads to a very high absorption coefficient in the order of 10^5 cm^{-1}, without any symmetry restrictions. A thickness of only some hundred nanometers of an organic dye is already sufficient to absorb nearly the complete incident light in its absorption range.[44, 45]

3.1.2 Excitation in organic solids

In the solid state, aromatic organic molecules interact by van-der-Waals forces, which are a result of induced dipoles of the nonpolar species due to the polarizability of the electron shell. They have a short range, decaying with $1/\mathrm{r}^6$, and are in general very weak.[43] For that reason organic solids are usually soft, have relatively low melting points and may be evaporated at low temperature. The electrical and optical properties are mainly defined by the identity of the single molecules. This can be seen from the comparison of the absorption spectra of an organic dye in solution and in solid state. The absorption characteristics in the neat material stay predominantly the same, although the absorption bands are broadened compared to the solution spectra.[46] As mentioned above, the first excited state is reached by a transition of an electron from an occupied π-orbital to an unoccupied π^*-orbital, with a hole remaining in the former occupied orbital. In solid state theory, this excitation results in an electrically neutral quasi-particle consisting of a bound electron-hole pair, known as Frenkel exciton, with a certain lifetime. Since the excitons are located on one molecular site, the exciton binding energy caused from the Coulomb interaction is high with typical values of 0.2-0.5 eV.[47, 48] Instead, in inorganic semiconductors, optical excitation leads to weakly bound Mott-Wannier excitons, due to the higher dielectric constant of the inorganic semiconductor, which shield the Coulomb attraction. Accordingly, the smaller exciton binding energy can be overcome by the thermal energy, in the inorganic case and easily leads to free charge carriers.[49, 50] The optically excited state in the neat organic semiconductor can only be separated by high electrical fields (of 10^6 Vcm^{-1}) or at interfaces.[51, 52] The electron-hole pair has a certain lifetime and can also travel through the organic bulk layer until it recombines. Since the exciton is a neutral quasi-particle, its transport occurs by diffusion.[47, 53]

3.1.3 Charge carriers and transport

In contrast to solid silicon, where neighboring Si-atoms are covalently bond, the distance between organic molecules in solid state is much larger due to the weaker van-der-Waals forces. The charge carrier transport process in such a layer is considered to occur by a hopping mechanism for several reasons. First, the large distance of two neighboring molecules in organic solids leads to a weak overlap of the corresponding orbitals. Consequently, the molecular LUMOs and HOMOs do not interact strongly enough in order to form a conduction or valence band along the 3D crystal lattice. Besides that the orientation between two neighboring molecules is often disadvantageous since the molecules are usually disordered. As a consequence, the bandwidth of the organic solid is low (<1 eV) since it is proportional to the overlap. The mean free path of charge carriers is typically lower than the crystal lattice distance. Accordingly, the charge can be considered as localized in energetically disordered transport states on a few or even one molecule.[54, 55, 56, 57] A localized charge in these states polarizes the environment. Since the transfer time for the charge is about 100 times larger than the relaxation time of the polarization, the polarization follows the charge immediately and a polaron is formed. Several models describing charge transport by a hopping process can be found in literature. [56, 58] The main difference is how the hopping rate is evaluated.[56, 59, 60] In the following section, the Marcus theory for the calculation of hopping rates is described and the main parameters influencing it are explained.

Charge transport parameters

In general, the charge hopping process can be regarded as a self-exchange electron-transfer reaction between neighboring molecules. This step can be described as a redox reaction between transport sites with physically different but chemically identical entities[56]

$$\mathrm{M_i^-} + \mathrm{M_j} \rightarrow \mathrm{M_i} + \mathrm{M_j^-}. \tag{3.5}$$

Within the framework of Marcus theory and extensions thereof, the rate constant for electron transfer k_{ij} (i.e., polaron hopping) is then defined as

$$k_{ij} = \frac{t_{ij}^2}{\hbar}\sqrt{\frac{\pi}{k_B T \lambda}} \exp\left(-\frac{(\lambda + \epsilon_\mathrm{j} - \epsilon_\mathrm{i})^2}{4\lambda \mathrm{k_B T}}\right), \tag{3.6}$$

where t_{ij} is the electronic coupling element (transfer integral) between neighboring molecules, λ is the reorganization energy for the intermolecular electron transfer, $\hbar$ is the reduced Planck constant, k_B is the Boltzmann constant, T is the temperature, and ϵ is the site energy for the molecule i and j, respectively.[56, 60, 61] At high temperatures, the mobility can be approximated by

$$\mu = \frac{ed^2}{k_\mathrm{B} T} k_{ij}, \tag{3.7}$$

where e is the carrier charge and d is the intermolecular distance between adjacent molecules (which defines the length of the carrier hops). From the calculation of the charge transport parameters λ and t, rough estimates of the transfer rates k and the carrier mobilities can be made.

Reorganization energy In organic molecular solids, the charge carriers localize on a given site and are stabilized by the polaron binding energy which results from the deformations in molecular and lattice geometries. This quantity can be related to the reorganization energy in

electron-transfer theory.[55, 56]
The reorganization energy λ can be separated into the sum of two primary components

$$\lambda = \lambda_i + \lambda_o. \tag{3.8}$$

The outer-sphere reorganization energy λ_o which includes electronic polarization and electron-phonon coupling of the surrounding molecules in molecular crystals is small compared to the inner-sphere reorganization energy λ_i and, hence, will be neglected in this thesis. The inner-sphere or intra-molecular reorganization energy has contributions from the individual relaxation process energies for the electron-donor (oxidation process) and electron-acceptor (reduction process) species

$$\lambda_i = \lambda_i^1 + \lambda_i^2. \tag{3.9}$$

The total relaxation energy can be calculated directly from the adiabatic potential energy surfaces (see Figure 3.4).

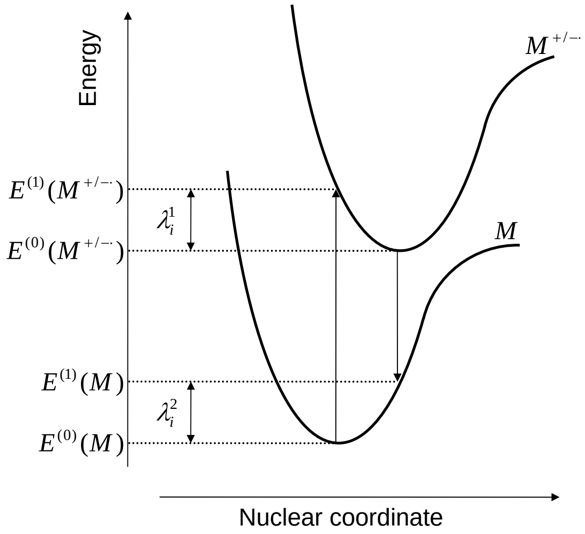

Figure 3.4: Sketch of the potential energy surfaces for the neutral M and charged molecular state $M^{+/-\cdot}$, showing the vertical transitions (single arrows) and the reorganization energies λ_i^1 and λ_i^2.

The surfaces are shown for both negatively charged and neutral electronic states as a function of the reaction coordinate. Both the electron transfer and subsequent thermal relaxation are shown; electron transfer occurs vertically, in accordance to the Franck-Condon principle. The reorganization energies are calculated from

$$\lambda_i^1 = E^{(1)}(\mathrm{M}) - \mathrm{E}^{(0)}(\mathrm{M}), \tag{3.10}$$

$$\lambda_i^2 = E^{(1)}(\mathrm{M}^{+/-\cdot}) - \mathrm{E}^{(0)}(\mathrm{M}^{+/-\cdot}). \tag{3.11}$$

Here, $E^{(0)}(\mathrm{M})$ and $E^{(0)}(\mathrm{M}^{+/-\cdot})$ are the ground-state energy of the neutral molecule and the energy of the charged species, respectively. $E^{(1)}(\mathrm{M})$ is the energy of the neutral molecule at the equilibrium ion geometry, and $E^{(1)}(\mathrm{M}^{+/-\cdot})$ is the energy of the ionic species at the equilibrium geometry of the neutral molecule.

Transfer integrals The electronic coupling between two adjacent molecules dominate the charge-transport properties in organic molecular solids. The Hamiltonian of a simple two-site dimer pair can be written as

$$\hat{H} = \begin{pmatrix} \epsilon_i & t_{ij} \\ t_{ji} & \epsilon_j \end{pmatrix}. \tag{3.12}$$

The electronic coupling is defined by the matrix element $t_{ij} = t_{ji} = \left\langle \Psi_i \middle| \hat{H} \middle| \Psi_j \right\rangle$ where Ψ_i and Ψ_j are the wave functions for two charge-localized (diabatic) states and $\hat{H}$ is the electronic Hamiltonian of the dimeric system. In the one-electron approximation, the diabatic states are associated with localized monomer orbitals φ_i. The transfer integrals can then be computed directly from

$$t_{ij} = \left\langle \varphi_i \middle| \hat{H} \middle| \varphi_j \right\rangle, \tag{3.13}$$

assuming that the dimer HOMO (LUMO) and HOMO-1 (LUMO+1) results only from the interaction of the monomer HOMO (LUMO), see Figure 3.5. The diagonal elements of the matrix in equation 3.12 are the site energies

$$\epsilon_{i,j} = \left\langle \varphi_{i,j} \middle| \hat{H} \middle| \varphi_{i,j} \right\rangle. \tag{3.14}$$

Different site energies ϵ originate from differences in polarization of the single molecules or different molecular geometries due to thermal fluctuations. Solving the determinant of the matrix in equation 3.12, the dimer energy splitting ΔE_{ij} can be derived in terms of the site energies ϵ_i, ϵ_j and the transfer integral t_{ij} as

$$\Delta E_{ij} = \sqrt{(\epsilon_i - \epsilon_j)^2 + 4t_{ij}^2}. \tag{3.15}$$

In the simplest case represented by a symmetric dimer configuration, the excess charge is delocalized over both sites equally. Thereby, the site energies ϵ_i and ϵ_j become equal and the

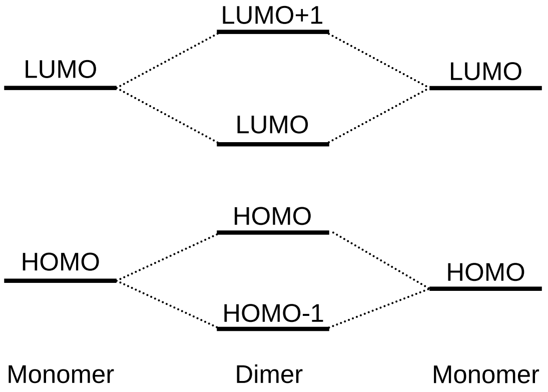

Figure 3.5: From a simple approximation, the transfer integrals for hole (or electron) transfer can be calculated as half the difference of the HOMO and HOMO-1 (LUMO and LUMO+1) energy level of a symmetric molecular dimer, according to equation 3.16.

transfer integral can be written as $t = \frac{\Delta E}{2}$. Applying Koopman's theorem and the one-electron approximation, the absolute value of the transfer integral can be calculated as

$$t = \frac{\epsilon_{\mathrm{H[L+1]}} - \epsilon_{\mathrm{H-1[L]}}}{2}, \tag{3.16}$$

where $\epsilon_{\mathrm{H[L+1]}}$ and $\epsilon_{\mathrm{H-1[L]}}$ are the energies of the HOMO or LUMO+1 and LUMO or HOMO-1, taken from a closed shell, neutral and symmetrical dimer of two organic molecules as it is illustrated in Figure 3.5.

3.2 Organic solar cells

In this section the basics of solar cells, the working principle of organic solar cells as well as typical architectures and materials are described.

3.2.1 Basic solar cell theory

Solar cells convert light directly into electrical energy and the basic requirement is a semiconductor exhibiting the photo effect.[50] Practically, all silicon solar cells contain a photoactive p-n-junction. A p-n-junction is achieved with one p-doped part and one n-doped part of the neat silicon. The doping is fulfilled by incorporating elements with one additional valence electron e.g. arsene (n) or with elements with less valence electrons e.g. aluminum or boron (p) in the silicon crystal structure. Upon illumination, weakly bound electron-hole pairs are created and become already thermally dissociated. The large built-in electric field of the p-n-junction causes the transport of the separated electrons and holes to the electrodes, and finally a current results.[50] A solar cell with an ideal diode behavior under illumination is described by the Shockley equation for diodes with an additional term I_{Ph} originating from the charge generation by the illumination

$$I = I_0(e^{\frac{eV}{k_{\mathrm{B}}T}} - 1) - I_{\mathrm{Ph}}. \tag{3.17}$$

In equation 3.17 I_0 is the dark current, e the elementary charge, k_{B} is the Boltzmann constant, V is the applied voltage, and I_{Ph} is the photocurrent.[50, 53, 62] In Figure 3.6, the IV-characteristics of such a photodiode is schematically shown in the dark and under illumination. Under illumination and $V = 0$, the device generates the current I_{SC} according to I_{Ph} in equation 3.17. The current is extracted for voltages $0 < V < V_{\mathrm{OC}}$. Above V_{OC} charge carriers are injected into the solar cell and the current increases exponentially as shown in Figure 3.6.

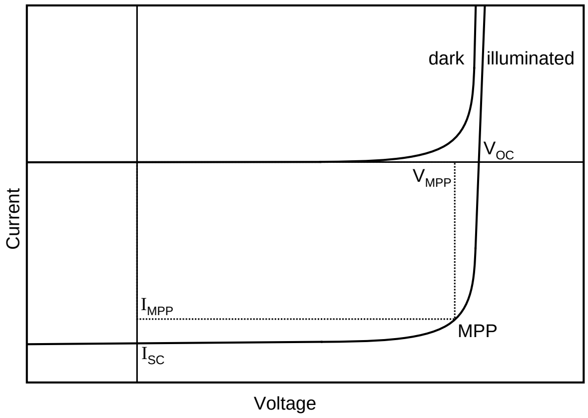

Figure 3.6: Current-voltage characteristics of a solar cell according to eq. 3.17 in dark and under illumination, with the short circuit current I_{SC} which is equivalent to I_{Ph}, here, and the open circuit voltage V_{OC}. The maximum generated power is obtained at the maximum power point MPP with the corresponding voltage V_{MPP} and current I_{MPP}.

The point of the IV-characteristic where the generated power of a solar cell, as the product of current and voltage is largest, denotes the maximum power point MPP. The corresponding voltage is V_{MPP} and the current is I_{MPP}. The fill factor FF is given as the fraction

$$\mathrm{FF} = \frac{\mathrm{V_{MPP} \cdot I_{MPP}}}{\mathrm{V_{OC} \cdot I_{SC}}}. \tag{3.18}$$

The power conversion efficiency η_{PCE} is the relation of the electrical power P_{out} produced by the device per incident photon power P_{in}. It is calculated from the maximum power at the MPP over the incident light power P_{light} [62]

$$\eta_{\text{PCE}} = \frac{P_{\text{out}}}{P_{\text{in}}} = \frac{I_{\text{MPP}} \cdot V_{\text{MPP}}}{P_{\text{light}}} = \frac{\text{FF} \cdot \text{I}_{\text{SC}} \cdot \text{V}_{\text{OC}}}{P_{\text{light}}}. \tag{3.19}$$

The electrical characteristics of a non-ideal solar cell can be described by equation 3.20 which is extended by a parallel and a series resistance that it accounts for several loss mechanisms in a real device [53, 62]

$$I = I_0(e^{\frac{e(V-R_{\text{S}}I)}{k_B T}} - 1) - I_{\text{Ph}} + \frac{V - R_{\text{S}}I}{R_{\text{P}}}. \tag{3.20}$$

In this equation R_{S} denotes the series and R_{P} the shunt resistance. The corresponding equivalent circuit diagram is shown in Figure 3.7. The series resistance R_{S} describes among others the contributions from the nonideal charge transport in the organic layer. The parallel resistance R_{P} accounts for leakage currents and recombination losses at the donor-acceptor interface.

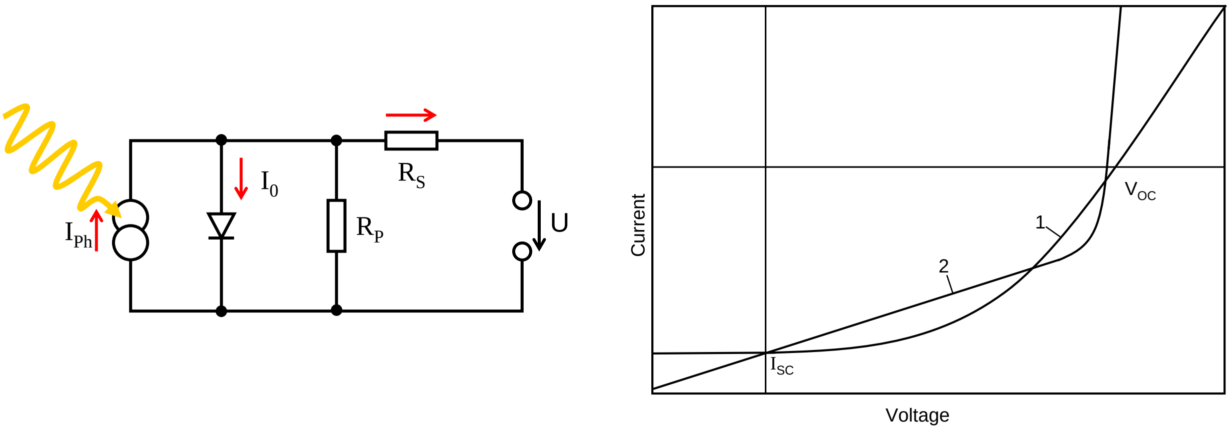

Figure 3.7: Equivalent circuit (left) of a solar cell and IV-characteristics of non-ideal solar cells (right). 1: The series resistance $R_{\text{S}} > 0$ accounts for imperfect charge transport or low conductivity. 2: The parallel resistance $R_{\text{P}} < \infty$ describes leakage currents or recombination.

To achieve a high fill factor and a high efficiency, the parallel resistance should be as large as possible, ideally infinite, whereas the series resistance should be as small as possible, ideally zero.[44] The I_{SC} of the photovoltaic device is ideally proportional to the absorbed photons and dependent on the dissociated excitons and created charges that are flowing to the electrodes. The number of absorbed photons depends on the absorption coefficient of the material and the layer thickness, as well as on the device architecture, e.g. reflecting back electrodes.[62] The V_{OC} is equivalent to the splitting of the quasi-Fermi levels of the separated positive and negative charges at the contacts (at V_{OC}).[44] The V_{OC} is not governed by the HOMO of the donor ($\mathrm{HOMO_D}$) and the LUMO of the acceptor of both materials, as it is always significantly smaller. The major losses resulting in a decreased V_{OC} are related to the exciton binding energy and charge separation. Furthermore, charge transport and extraction barriers decrease the V_{OC}.[62, 44, 63] In order to guarantee that different solar cells can be compared, the devices are measured under standard conditions at 25°C with a light intensity of 100 $\mathrm{mWcm^{-2}}$ and a simulated AM1.5 spectrum. AM1.5 (air mass) denotes the sun spectrum which is similar to the mid European latitude. Compared to the equatorial spectrum (AM1.0) with a perpendicular sun irradiation, the AM1.5 spectrum corresponds to a tilted incident of 48.2° and accounts for the (1.5 times) increased length of path of the light through the atmosphere.

3.2.2 Working principle of an organic solar cell

A comprehensive overview of organic solar cells can be found in several review articles and will be discussed here briefly.[53, 57, 62, 64] The fundamental difference between inorganic and organic photovoltaics arises from the fact that light absorption in organic semiconductors first leads to the formation of tightly bound Frenkel-excitons. In order to generate a photocurrent, the excited state has to be separated into free charge carries before recombination occurs. The first organic solar cells consisted of a single organic layer between two electrodes.[65] The efficiency was very low with 0.1%, since excitons were quenched at the metal contact and were not efficiently separated into free charge carriers.[65] In 1986, Tang at Kodak published for the first time that excitons can be separated efficiently at a donor-acceptor heterojunction.[4] The heterojunction was formed at the interface of a perylene derivative (acceptor) and a phthalocyanine (donor), two materials which differ in their electron affinity and their ionization potential. The donor material in such a system has a higher ionization potential and the acceptor a higher electron affinity as shown in Figure 3.8 a).

Upon illumination with the energy $\mathrm{E_{exc}}$, a photoinduced charge transfer from one molecule to the other molecules occurs. The corresponding charge transfer with the associated rate $\mathrm{k_{CT}}$ (schematically shown in Figure 3.8 b)) e.g. from the donor to the acceptor is orders of magnitudes larger than all other competing processes, but does not directly lead to free charge carriers (separated charges).[66] Instead, a charge transfer (CT) state is formed, with the hole on the donor and the electron on the acceptor molecule. This state can either relax to the triplet or the ground state of the donor molecule (if $\mathrm{T_1}$ is lower in energy), with a certain rate $\mathrm{k_{r1}}$ and $\mathrm{k_{r2}}$.

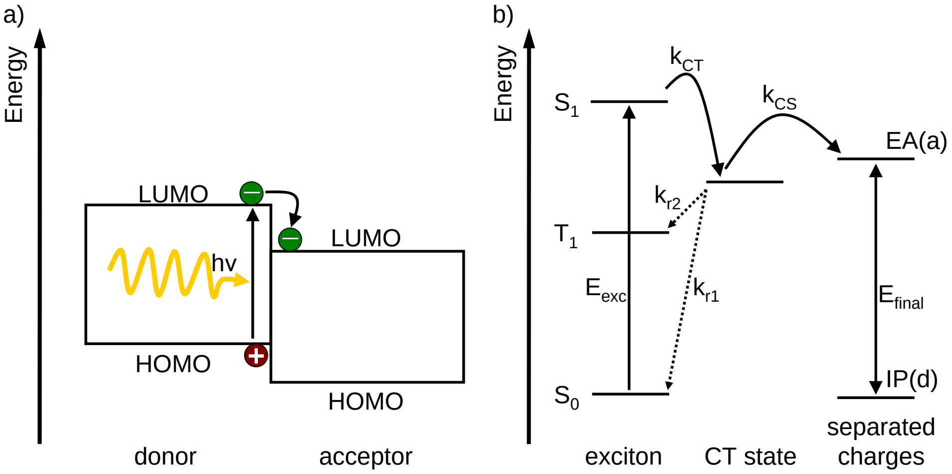

Figure 3.8: a) Energetic offset at a donor acceptor heterojunction and light induced electron transfer. b) Energy diagram describing the light induced charge generation. S_0 denotes the singlet ground state of the donor or the acceptor, S_1 denotes the first singlet, T_1 the triplet excited state. At the interface the intermolecular charge transfer leads to a CT-state. Dotted arrows indicate relaxation pathways.

The desired process in the solar cell is the charge separation with the rate k_{CS}, where the Coulomb attraction of the charges in the CT-state has to be overcome. The exciton separation efficiency depends on the electron-hole distance in the CT-state, the electrical field, and on the temperature. One attempt to describe it theoretically is the Onsager-Braun theory.[58, 67] A full separation finally leads to a relaxed positively charged donor and negatively charged acceptor molecule. In order to enhance the charge separation, the energetic $LUMO_D$-$LUMO_A$ (and $HOMO_D$-$HOMO_A$) offset in these materials has to be larger than the exciton binding energy.[68, 69] After exciton separation, the generated charge carriers have to be transported to the electrodes, which is regarded to occur by a hopping in most organic solid state systems.[70] Figure 3.9 summarizes schematically the fundamental processes in a working solar cell under short circuit conditions. The first step is the light absorption (1), the second step is the exciton diffusion to the interface (2), and the third step shows the exciton separation (3). The fourth and fifth step comprise the charge transport (4) through the organic layers and the charge extraction (5) to the electrodes.

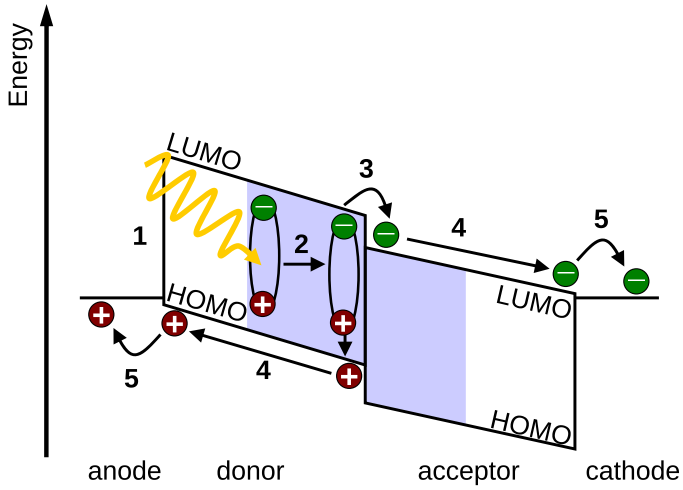

Figure 3.9: Scheme of fundamental processes in a working solar cell with (1) light absorption, (2) exciton diffusion, (3) exciton separation, (4) charge transport, (5) charge collection.

3.2.3 Organic solar cell materials and architecture

The most simple schematic architecture of an organic solar cell is shown in Figure 3.10 a) and b). A basic requirement for all solar cells is a transparent substrate and a transparent electrode, a light absorbing active layer and a counter-electrode. The transparent electrode is usually realized with transparent indium tin oxide (ITO) coated on glass as a substrate. As active layers, either small molecules which are usually processed by vacuum sublimation, or polymers which are processed from solution, can be applied. The commonly used acceptor is the fullerene C_{60} or its derivatives which is taken in evaporated solar cells or the [6,6]-phenyl-C_{61}-butyric-acid-methylester ($PC_{61}BM$) in solution processed devices. The most intensely investigated donor materials are metal-phthalocyanines like ZnPc for small molecule solar cells and poly-3-hexyl-thiophene (P3HT) for polymer solar cells.[62, 66, 71, 72, 73, 74, 75] Currently, donor materials combining intramolecular donor-acceptor groups, with electron rich donor and an electron poor withdrawing character are investigated. Examples are the DCV6T as a small molecule or the PCPDTBT polymer.[76, 77] As cathode materials mostly metals like Ag or Al are chosen due to their workfunction and high reflectivity, which are evaporated on top of the stack, often with an ultrathin interfacial layer, to guarantee an ohmic contact to the electrode.[53, 62] Common examples of solar cell materials are shown in Figure 3.1, together with hole transport materials used in this work.[5, 78]

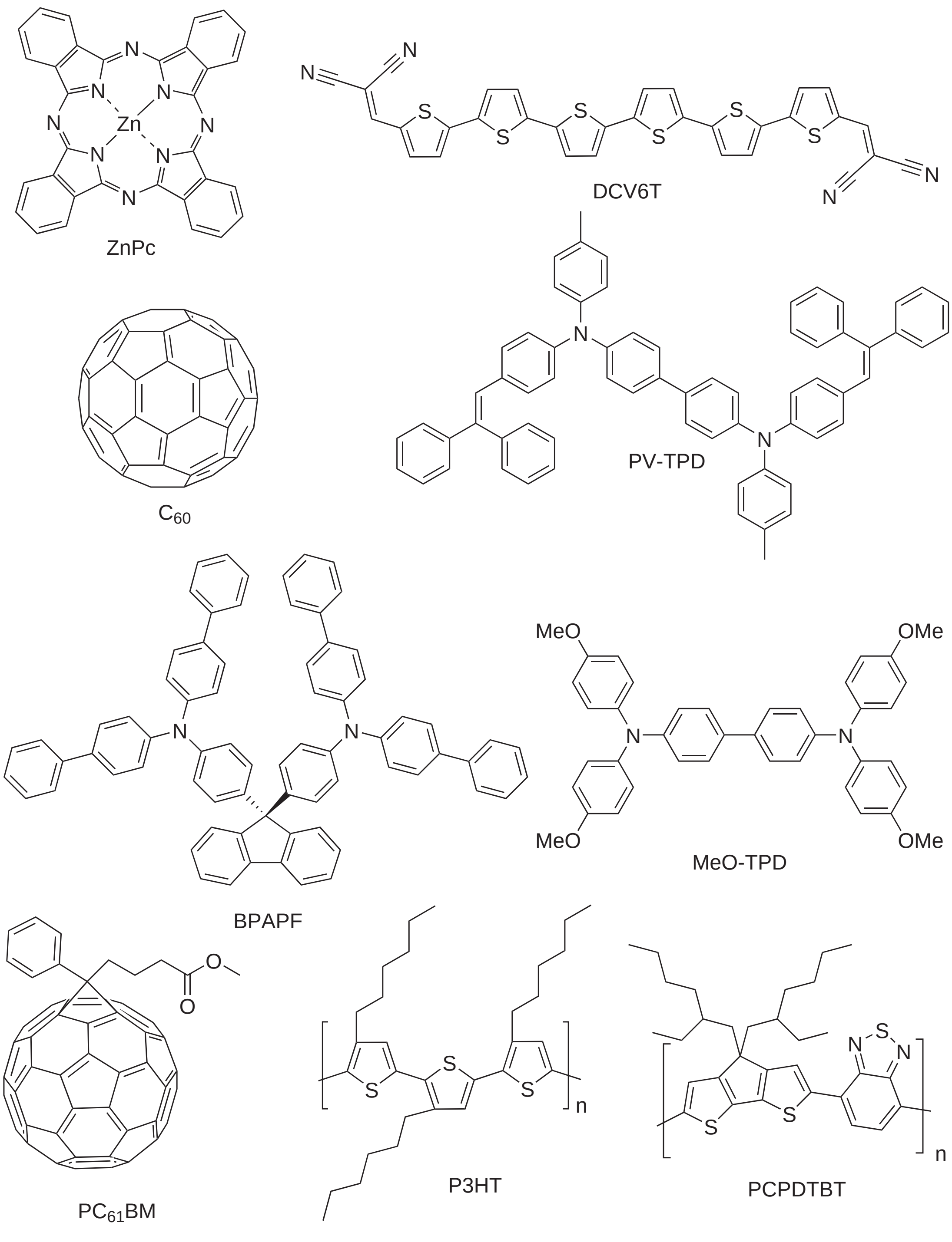

Scheme 3.1: Chemical structures of commonly used materials in small molecule (ZnPc, DCV6T, C_{60}) and polymer ($PC_{61}BM$, P3HT, PCPDTBT) organic solar cells. Hole transport materials (PV-TPD, BPAPF, MeO-TPD) used in this thesis. The full chemical name of the materials can be found in the list of abbreviations.

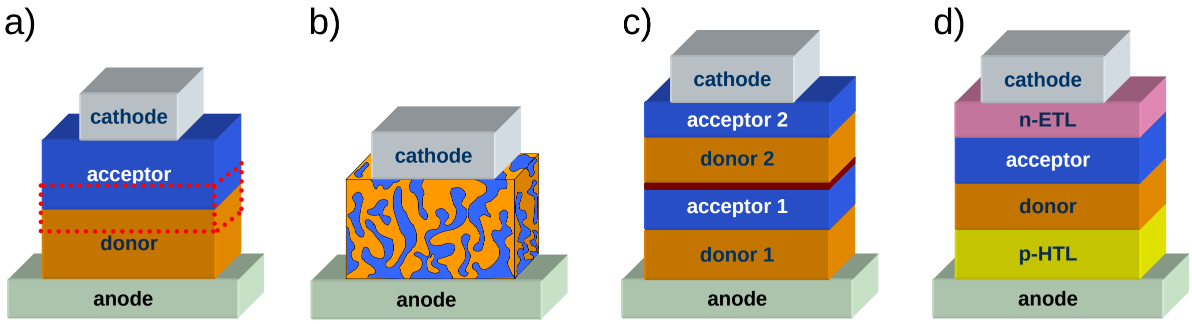

Figure 3.10: Different solar cell architectures: a) Flat bilayer heterojunction; b) bulk heterojunction; c) tandem device with two subcells and interstitial layer; d) p-i-n solar cell with the intrinsic donor-acceptor active layers between n-doped and p-doped charge transport layers.

The first efficient organic solar cell of Tang used a bilayer flat-heterojunction heterojunction, shown in Figure 3.10 a).[4] This architecture has an important limitation which relates to the exciton diffusion length in the organic materials. The exciton diffusion length is dependent on the exciton lifetime and is in the range of 10-40 nm. This is much lower than the penetration depth of the light.[53, 46] Accordingly, only excitons generated within the exciton diffusion length distance to the donor-acceptor interface (photoactive region) can be separated into free charge carriers and contribute to the photocurrent whereas the others will recombine. This photoactive region is schematically displayed by the red dots in Figure 3.10 a). Several solar cell concepts were developed to overcome the limitation of the small diffusion length and to increase the device efficiency. A certain expansion of the photoactive region is achieved by using an inter-penetrating network of donor and acceptor materials instead of a planar or flat interface.[79, 80, 81] Such a configuration, called bulk heterojunction, can be obtained in a mixed layer with an appropriate morphology, induced by a nanoscale phase separation of both materials shown in Figure 3.10 b).[82] In bulk heterojunction solar cells, the largest distance to the donor-acceptor interface is much lower compared to flat heterojunction solar cells. This accounts for the intrinsically low exciton diffusion lengths and allows for more generated excitons to be separated into free charge carriers. However, the charges have to be transported to the electrodes via closed and short percolation pathways. Otherwise transport losses by trapping or recombination may occur. Therefore, a material specific mixture ratio and often annealing is applied to find the optimal configuration. As a result, the photocurrent is usually higher in bulk heterojunction than in flat heterojunction solar cells.[53, 72, 83] Additionally, tandem solar cells can be built which were first presented by Hiramoto et al. in 1990.[84] Especially vacuum sublimation processing allows for an easy stacking of organic layers to form two heterojunctions. The two donor-acceptor layers were separated by a thin interstitial gold layer as recombination zone, shown in Figure 3.10 c).[85] In these devices the sum of the produced individual voltages of both donor-acceptor systems can be gained. Ideally, a broader coverage of the solar spectrum is achieved, by using different donor and acceptor absorber materials in the individual subcells.[86] Today, this approach is combined with bulk heterojunction architecture in the subcells.

A major improvement of the solar cell architecture is achieved with the p-i-n concept, where the (intrinsic: i) donor-acceptor active layers are sandwiched between molecular (p- and n-)doped electron and hole transport layers.[71] The transport layers should only show an absorption in the UV-part of the spectrum where the active layers do not display absorption, in order to avoid any parasitic absorption. This is achieved with charge transport layers exhibiting a large HOMO-LUMO gap. The concept was first introduced by Pfeiffer et al. and further developed by Maennig et al., with controlled doping of the transport layers by co-evaporation of molecular dopands.[71, 87] In these solar cells, the photocurrent is enhanced and the series resistance (see Figure 3.7) is significantly lowered due to the increased conductivity of the charge transport layers. Furthermore, it allowed for the optimization of the optical properties of the solar cells by placing the active region at the maximum of the optical field distribution. Both effects lead to an improved overall efficiency in the device. The p-i-n concept can be applied as well for bulk heterojunction and for tandem solar cells.[71, 87, 88] The most efficient organic solar cells today reach an efficiency of over 8 %, e.g. for small molecules by the company Heliatek in collaboration with IAPP and polymer solar cells from the companies Konarka and Solarmer.[89, 90, 91]

3.2.4 Requirements to the absorber materials

From the working principle of an organic solar cell, the properties of an ideal active donor material for small molecule organic solar cells can be derived. It is obvious that the extinction of the donor material should be as high as possible, to absorb as much incident light as possible. Usually small molecules show a narrow absorption and are often not covering the red region of the sun spectrum, although 50 % of the photons of the sun correspond to wavelengths between 600 nm and 1000 nm. Since one material with an optimized (near-infrared) absorption usually results in a lowered V_{OC} due to its high HOMO energy and small gap, the benefits to I_{SC} from the additional absorbance is negated.[53] Accordingly, the best strategy to overcome this issue is the construction of a tandem solar cell comprising several different complementary absorption layers to cover a larger part of the sun spectrum. For such an optimized (polymer) tandem device Brabec et al. estimated the optimal electrical gap of both donor materials in combination with $PC_{61}BM$ as acceptor. The maximum efficiency appears achievable with an electrical gap of 1.6 eV and 1.3 eV for each donor material.[92] This corresponds to wavelengths of ca. 770 nm and ca. 950 nm, respectively. Based on the $PC_{61}BM$ as acceptor with a LUMO of -4.3 eV the ideal LUMO value of the donor is assumed to be between 3.7 eV and 4.0 eV in order to guarantee a sufficient exciton separation. [69, 92, 93] In Figure 3.11 the absorption spectra of commonly used active small molecules (for tandem devices) are shown in comparison to the sun spectrum. It can clearly be seen that the large spectral overlap of ZnPc and DCV6T is not ideal. Furthermore, the sun spectrum is not covered at all in the near infrared region above 800 nm. Accordingly, an active absorber material is desirable which comprises both, the specified electrical and optical properties mentioned above.

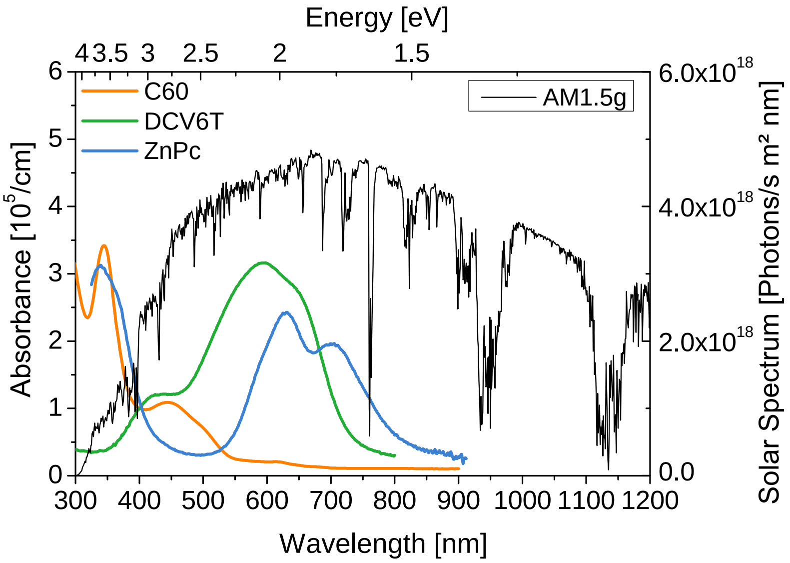

Figure 3.11: Thin film absorption spectra (20 nm on glass) of commonly used active materials (C_{60}, DCV6T, ZnPc) for small molecule organic tandem solar cells. The large overlap of both absorber material as well as the insufficient coverage of the sun spectrum (>800 nm) are not ideal.

In addition to these molecular properties, the material should feature some important bulk properties in its solid state. In the neat layer, an optimal overlap of adjacent molecules and a very tight packing in a 3D crystalline ordered way is desired, featuring high charge carrier mobilities. In the mixed layer, a cooperative effect is desired for a phase separation of both materials to enhance the charge separation, i.e. the phase separation should be about two times the exciton diffusion length.[94, 95, 96] Furthermore, the good charge carrier transport properties should be achieved in the mixed layer for efficient charge carrier extraction. Since the individual layers are processed by thermal vacuum sublimation, it is also decisive that all developed materials exhibit a high thermal stability and can be evaporated.

4 Quantum chemical methods

The design of materials for organic electronics is a challenging task, since the desired properties have to be translated into a molecular structure. The theoretical prediction of properties or trends within a given class of materials helps to understand structure-property relationships and to identify relevant target molecules and the synthetic effort can be minimized. In this thesis, several molecular parameters like frontier orbital energies, absorption energies or molecular structures were calculated with quantum chemical methods. This chapter gives an introduction into the theoretical methods applied within this work.

4.1 Hartree Fock

Several molecular characteristics can be calculated by means of quantum chemical methods.[97, 43, 98] The basis of these calculations is formed by the laws of quantum mechanics. The solution of the time independent Schrödinger equation

$$\hat{H}_{\mathrm{mol}}\Psi \quad = \quad E\Psi, \tag{4.1}$$

allows to determine certain molecular properties which are essential molecular characteristics when discussing the suitability of these molecules for the application in organic electronic devices. Here, $\hat{H}_{\mathrm{mol}}$ is the molecular Hamilton operator, containing all interactions between electrons and nucleus, and Ψ is the wavefunction of the system. Since in case of multi-electron systems the Schrödinger equation 4.1 is not solvable analytically, different quantum chemical approximations and procedures have been developed to solve it numerically. In general one distinguishes between semi-empirical and *ab initio*-methods (including density functional theory). In contrast to semi-empirical calculations, *ab initio* calculations are free from external parameters, e.g. experimental values. They are exclusively based on quantum mechanics and use mathematical approximations to solve the Schrödinger equation. Density functional theory (DFT) represents a special class of *ab initio* methods. Here, the ground state energy is computed as a function of the electron density. The molecular Schrödinger equation of any molecule with the electronic wavefunction Ψ and N_e electrons in the Coulomb field of N_N atomic nuclei can be written as

$$\hat{H}_\mathrm{mol}\Psi(\vec{r}_j, \vec{R}_\mathrm{N}) \quad = \quad E\Psi(\vec{r}_i, \vec{R}_\mathrm{N}), \tag{4.2}$$

with the electron coordinates r_j ($j = 1, ..., N_\mathrm{e}$) and the nuclei coordinates R_N ($N = 1, ..., N_\mathrm{N}$).[98, 99, 100]

In a first approximation, the motion of the electrons and the nuclei is separated according to the Born-Oppenheimer approximation. This is justified, as the mass of electrons is significantly lower compared to the mass of the nuclei. Thus, the molecular Hamilton operator $\hat{H}_\mathrm{mol}$ can be divided into a nuclear and an electronic part

$$\hat{H}_\mathrm{mol} \quad = \quad \hat{H}_\mathrm{N} + \hat{H}_\mathrm{e}. \tag{4.3}$$

The electronic term $\hat{H}_\mathrm{e}$ contains the potential and kinetic energy, $\hat{V}_\mathrm{ee}$ and $\hat{T}_\mathrm{e}$, as well as the interactions between nuclei and electrons $\hat{V}_\mathrm{eN}$

$$\hat{H}_\mathrm{e} \quad = \quad \hat{T}_\mathrm{e} + \hat{V}_\mathrm{ee} + \hat{V}_\mathrm{eN}, \tag{4.4}$$

with

$$\hat{T}_\mathrm{e} \quad = \quad \sum_{i=1}^{N_\mathrm{e}} \frac{\vec{p}_i^{\,2}}{2\,m_\mathrm{e}}, \tag{4.5}$$

$$\hat{V}_\mathrm{ee} \quad = \quad \sum_{i=1}^{N_\mathrm{e}} \sum_{j=1}^{N_\mathrm{e}} \frac{e^2}{4\,\pi\,\varepsilon_0\,|\vec{r}_i - \vec{r}_j|} \qquad \text{for j > i, and} \tag{4.6}$$

$$\hat{V}_\mathrm{eN} \quad = \quad -\sum_{N}^{N_\mathrm{N}} \sum_{i}^{N_\mathrm{e}} \frac{Z_\mathrm{N} e^2}{4\,\pi\,\varepsilon_0\,|\vec{r}_i - \vec{R}_\mathrm{N}|}. \tag{4.7}$$

Here, m_e is the electron mass and $\vec{p}_i$ represents the momentum of the electrons.[98] The molecular wave function Ψ can be written as a product of the electronic and nuclear wave function

$$\Psi(\vec{r}, \vec{R}) \quad = \quad \Psi_\mathrm{e}(\vec{r}; \vec{R}) \cdot \Psi_\mathrm{N}(\vec{R}), \tag{4.8}$$

and the electronic Schrödinger equation can be formulated according to

$$\hat{H}_\mathrm{e}\Psi_\mathrm{e}(\vec{r}, \vec{R}) \quad = \quad E_\mathrm{e}(\vec{R})\Psi_\mathrm{e}(\vec{r}; \vec{R}). \tag{4.9}$$

The electronic energy $E_\mathrm{e}(\vec{R})$ of a molecule can be calculated in parametric dependence of the nuclear coordinates according to equation 4.9. In general, the electronic Schrödinger equation 4.9

can be solved with different quantum chemical techniques, such as Hartree Fock (HF) theory, post HF methods or DFT.

In Hartree Fock theory, the electronic wave function is expressed by Slater determinants, consisting of products of one-electron functions

$$\Psi_{\mathrm{e}}(\vec{r}) = \frac{1}{\sqrt{N_{\mathrm{e}}!}} \begin{vmatrix} \chi_1(\vec{r}_1) & \chi_2(\vec{r}_1) & \cdots & \chi_{N_{\mathrm{e}}}(\vec{r}_1) \\ \chi_1(\vec{r}_2) & \chi_2(\vec{r}_2) & \cdots & \chi_{N_{\mathrm{e}}}(\vec{r}_2) \\ \vdots & \vdots & \ddots & \vdots \\ \chi_1(\vec{r}_{N_{\mathrm{e}}}) & \chi_2(\vec{r}_{N_{\mathrm{e}}}) & \cdots & \chi_{N_{\mathrm{e}}}(\vec{r}_{N_{\mathrm{e}}}) \end{vmatrix}. \tag{4.10}$$

The spin-orbital χ_i is a one-particle wavefunction and is a product of both, the spatial orbital ψ_i and a spin function, α or β (which can be either $+1/2$ or $-1/2$). The formulation obeys the Pauli principle where a permutation of two electrons in the wavefunction leads to its anti-symmetric form. In equation 4.10 χ_i denotes the spin orbitals which can be constructed from the spatial orbitals ψ_i

$$\chi_i(\vec{r}_j) = \psi_i(\vec{r}_j) \begin{cases} \alpha(j) \\ \beta(j) \end{cases} \quad (i, j = 1, \ldots, N_e). \tag{4.11}$$

The energy expectation value of the wave function $\Psi_{\mathrm{e}}(\vec{r})$ (eq. 4.10) is given by

$$E \quad = \quad \langle \Psi_{\mathrm{e}} | \hat{H}_{\mathrm{e}} | \Psi_{\mathrm{e}} \rangle. \tag{4.12}$$

In order to find the best description of the wavefunction which is equivalent to the minimum of the electronic energy of the regarded system from fixed nuclear coordinates, a calculus of variations is performed. In consideration of the orthonormality of the spatial orbitals ($\langle \phi_i | \phi_j \rangle = \delta_{ij}$) the HF equations for the spin orbitals i ($i = 1, \ldots, N_{\mathrm{e}}$) can be derived

$$\hat{F} \chi_i(\vec{r}_i) \quad = \quad \varepsilon_i \chi_(\vec{r}_i). \tag{4.13}$$

Initially, an appropriate set of spatial orbitals is used to set up the Fock operator $\hat{F}$. The operator accounts for the Coulomb and exchange interactions of the electrons, where these parts themselves depend on the orbitals. The eigenvalue problem (eq. 4.13) is solved for the initial set of the orbitals and the corresponding Fock operator. As a result, a new set of orbitals is obtained. From these orbitals a new Fock operator can be constructed and the procedure is continued until self-consistency of the orbitals is reached. According to the variational principle, the result will correspond to the ground state wave function of the applied geometry and a set of occupied and virtual orbitals will be obtainable, with the total number equal to the number of basis functions used.[98, 100, 101]

4.2 DFT

Kohn and Hohenberg proved that the energy of the ground state system can be computed from the electron density $\rho(\vec{r})$ [100, 102]

$$\begin{aligned} \rho(\vec{r}) &= \sum_{i=1}^{N_\mathrm{e}} \psi_l^*(\vec{r})\psi_l(\vec{r}), && (4.14)\\ E &= f(\rho(\vec{r})). && (4.15) \end{aligned}$$

According to equation 4.15, the energy can be separated into different terms and by means of the variational principle, the Kohn-Sham equation can be derived for the one-electron orbitals [100, 103]

$$E\rho(\vec{r}) \quad = \quad E^\mathrm{T}\rho(\vec{r}) + E^\mathrm{V}\rho(\vec{r}) + E^\mathrm{J}\rho(\vec{r}) + E^\mathrm{XC}\rho(\vec{r}). \qquad (4.16)$$

In equation 4.16, E^T corresponds to the kinetic energy of the electrons, the nuclear electron interaction and the nuclear-nuclear repulsion is included in E^V. E^J denotes the Coulomb interaction and E^XC represents the exchange correlation energy.[100] The exchange correlation energy E^XC depends on the total electron density of the whole molecule and is approximated by using the local density approximation (LDA) or the generalized gradient approximation (GGA). In the LDA one assumes a homogeneous distribution of the electron cloud over the molecule, like an electron gas. Since in molecules, the electron density is not uniformly distributed over the complete system, the validity of this approach is limited. In the exchange correlation functional of the GGA, the variation of electron density with position is taken into account. This is done by including the gradient of the electron density. Widely used exchange GGA functionals ($\mathrm{E_X}$) are: B88, P, PW, B86, PBE, and correlation functionals ($\mathrm{E_C}$) are: PW91, B95, P86, LYP.[100] In the quantum chemical specification, the exchange correlation functionals are usual denoted by a contraction of the exchange and correlation acronyms, e.g. BLYP : $\mathrm{E_X} = \mathrm{B}; \mathrm{E_C} = \mathrm{LYP}$.[98] To date, the exchange correlation functional B3LYP is the most commonly used

$$E_\mathrm{XC}^\mathrm{B3LYP} = (1-a)E_\mathrm{X}^\mathrm{LSDA} + aE_\mathrm{X}^\mathrm{HF} + bE_\mathrm{X}^\mathrm{B} + (1-c)E_\mathrm{C}^\mathrm{LSDA} + cE_\mathrm{C}^\mathrm{LYP} \qquad (4.17)$$

with a, b and c optimized to 0.20, 0.72, and 0.81, respectively.[100, 104, 105] A three parameter scheme is used in this hybrid functional consisting of the GGA exchange and correlation functionals $\mathrm{E^B}$ and $\mathrm{E^{LYP}}$ the expectation value of the exchange for a non interacting system from HF theory $\mathrm{E_X^{HF}}$, and the LSDA term $\mathrm{E_X^{LSDA}}$ (LDA for systems including spin polarization e.g. open shell systems). B3LYP has shown to be very good in the prediction of minimum-energy structures of first-row elements and transition state geometries.[98, 101, 106] In this thesis, it is the predominantly used exchange correlation functional for the quantum chemical calculations.

TDDFT Absorption of light by the ground-state of a molecule leads to excited states where at least one electron occupies a higher level than it does in the ground state. Such states cannot be described directly by DFT. An extension of DFT to excited states is the time-dependent DFT (TDDFT) method. In TDDFT the interaction of electromagnetic radiation with the electron density is calculated within time-dependent perturbation theory.[107, 108] The system's response to the time-dependent perturbation denoted as

$$E = r\cos(\omega \cdot t), \tag{4.18}$$

is the polarizability $\alpha(\omega)$:

$$\alpha(\omega) = \sum_{i}^{\text{states}} \frac{|\langle\Psi_0|r|\Psi_i\rangle|^2}{\omega - \omega_i}. \tag{4.19}$$

In case the disturbance frequency equals the electronic excitation energy ω_i,

$$E_i - E_0 = \hbar \cdot \omega_i, \tag{4.20}$$

the polarizability α has a pole and indicates the transition from the electronic ground state Ψ_0 to the excited state Ψ_i. The intensity of the electronic transition is denoted by the oscillator strength and proportional to the square of the transition dipole moment $f \propto \langle\Psi_0|r|\Psi_i\rangle^2$. The oscillator strength determines the transition probability to the final state Ψ_i and is an observable in spectroscopy.[109]

4.3 Basis sets

In the quantum chemical methods like HF, post-HF and DFT, the initial spatial orbitals are defined as a linear combination (LCAO) of basis function ϕ_k

$$\psi_i(\vec{r}_j) = \sum_{k=1}^{M} c_{ik} \cdot \phi_k. \tag{4.21}$$

Here, M denotes the total number of basis functions used and c_{ik} are the expansion coefficients. Different types of basis functions exist, e.g. Slater-type or Gaussian-type atomic orbitals.[101, 110] Slater-type orbitals (STO) consist of the product of an exponential and a power function, combined with the angular part of a hydrogen-like orbital and have the form

$$\psi^{\text{STO}} = N r^{n-1} e^{-\zeta r} Y_l^m(\theta, \phi), \tag{4.22}$$

with the normalization constant N, the principle quantum number n of the orbital, the electron-nucleus distance r and the angular part of the orbital $Y_m^m(\delta, \psi)$. The parameter ζ is called the orbital exponent and is defined as

$$\zeta = \frac{Z - s}{n}, \tag{4.23}$$

where Z is the atomic number and s is a screening constant.[100] Today, atomic orbitals for many-electron atoms are approximated by linear combinations of several STOs and the ζs are evaluated by means of the self-consistent field method. There a two Gaussian type functions, the Gaussian-Lobe-functions

$$\psi = Ne^{-\beta r^2}, \tag{4.24}$$

and the cartesian Gaussian-functions or primitive Gaussian functions (GTO) with the form

$$\psi = Nx^l y^m z^n e^{-\beta r^2}, \tag{4.25}$$

with the scaling factor N, the electron radius to the core $r = |r_\mathrm{e} - R_\mathrm{N}|$ and $r^2 = x^2 + y^2 + z^2$, the cartesian coordinates x, y and z, the integers l, m, n, and the orbital exponent β. The basis functions implemented in quantum chemical codes for HF and DFT calculations are linear combinations of primitive Gaussian functions (eq. 4.25), called contracted Gaussian-type functions with the form

$$\chi_y = \sum_{w=1}^{b} d_{wy} g_w, \tag{4.26}$$

where the constants d_{wy} are contraction coefficients, g_w are primitive Gaussians functions, and the values of b typically range from 1 to 7. When $l + m + n = 0$, then g is said to be a s-type Gaussian function; when $l + m + n = 1$, then g is a p-type Gaussian; and when $l + m + n = 2$, then g is a d-type Gaussian. For an efficient numerical implementation of the basis set expansion usually Gaussian type functions are employed. In order to reach a high accuracy of the results, the basis set needs to be as large and as flexible as possible within the limits of computational resources.

Throughout this thesis, the split-valence basis sets introduced by Pople were used, such as 6-31g(d) and 6-31+g(d,p).[98, 100, 101] In a split-valence basis set the inner-shell atomic orbitals are represented by one contracted basis function and the valence orbitals are represented by two or more contracted basis functions. Here, a contraction of six primitive Gaussian functions, that is a linear combination of six primitive Gaussian functions, is used to describe each inner-shell atomic orbital (e.g. 1s orbitals in case of carbon) and a contraction of three plus an additional primitive function is used to describe the valence orbitals (e.g. 2s and 2p orbitals of carbon).[101] Additional flexibility is introduced by polarized functions (denoted by (d,p)) which includes d-type orbitals for the second row elements and p-type functions for hydrogen, in order to correct spatial differences in electron density in case of a polar molecule. This is essential for the adequate description of transition states. The + sign introduces diffuse basis functions with small exponents, leading to a broad Gaussian distributions which allows to describe the electron density furthermost of the nuclei. Accordingly, this is crucial for the description of anionic systems.[101]

4.4 Geometry optimization and transition state search

The geometry of a nonlinear molecule with N nuclei is defined by $3N - 6$ independent coordinates, and its electronic energy U is a function of these coordinates and specifies what is called the potential-energy-surface (PES) of the molecule. If the first derivative, called the gradient of U, equals zero a stationary point is reached on the PES which may be a minimum, maximum, or a saddle point. For geometry optimization purposes the global minimum has to be found, and different approaches have been developed to obtain them.[100] Some procedures require only repeated calculation of U at various values of its variables. They are called zero-order or energy-only methods. More efficient procedures require repeated calculation of both, U and its first derivatives, which are known as first-order or steepest-descent methods. Some energy minimization methods also use the second derivatives of U, called the Hessian or the force constant matrix. They are known as second-order or Newton-Raphson methods. The Newton-Raphson method explicitly calculates the first and second partial derivatives of U. Since this is very costly in computer time, program packages like GAUSSIAN use a quasi-Newton-Raphson method e.g. the Berny-algorithm. Here, an approximate Hessian-matrix is constructed at the beginning of the optimization procedure through application of a simple valence force field, and then the energies and first derivatives calculated along the optimization pathway are used to update this approximate Hessian matrix.[101, 111]

After guessing the geometry, one searches for the minimum nearest the initially assumed geometry. The SCF method is used to find the electronic energy and its gradient at the guessed initial structure. Using the calculated energy value and the gradient, the geometry optimization program changes the atomic coordinates to obtain a new structure that is likely to be closer to a minimum. The process is repeated until changes of the electronic energy, in the gradient and the structure on two successive iterations are smaller than prefixed values in the convergence criteria.[101] Subsequent to the geometry optimization, a calculation of the vibrational frequencies is performed in order to classify the stationary point as a local minimum or a saddle-point. In these calculations the second derivatives of the electronic energy U with respect to the $3N$ nuclear coordinates are evaluated at the equilibrium geometry. The obtained matrix is diagonalized and the resulting eigenvalues correspond to the force constants of the vibrational normal modes. In case all vibrational frequencies are real (positive sign), a local minimum was reached, otherwise n imaginary frequencies (negative sign) characterize an nth-order saddle-point, being a transition state if $n = 1$.[100]

5 Azadipyrromethenes

In this chapter aryl- and thienyl-substituted azadipyrromethenes are described. Besides the synthesis, a detailed characterization of the optical, electrochemical and thermal properties will be given.

5.1 Borondifluoride aryl-azadipyrromethenes

As azadipyrromethenes have not been considered yet for applications in organic electronic devices, little is known about the influence of substituents on the electronic characteristics, such as electrochemical properties. For that reason this chapter focuses on the synthesis, the optical and electrochemical characterization and quantum chemical calculations, also for aza-bodipys already described in the literature.[28, 38, 112] The characterization offers new insights and a better understanding of the material class of aza-bodipys in general.

5.1.1 Synthesis

The most appropriate synthetic route to azadipyrromethenes is the conversion of nitrobutyrophenones with ammonium acetate as illustrated in Scheme 2.1. In the first step, a substituted acetophenone **57** was condensated with a benzaldehyde **58** at room temperature in ethanol according to standard conditions to the desired chalcone **59** in good yields (Scheme 5.1).[113] The chalcone **59** can undergo a Michael addition with either nitromethane (ii in Scheme 5.1) or cyanide (iii in Scheme 5.1) to yield the corresponding addition product **60** or **61**, respectively. Since the cyanide is very toxic, the addition is unsuitable as standard procedure, especially in larger scale reactions. Consequently, most of the described products (except the tetraphenyl-azadipyrromethene) were prepared via the pathway (ii) in Scheme 5.1. The Michael addition of nitromethane to the bis(dimethylaminophenyl)-chalcone **59e** did not work as well as the other reactions. As alternative, modified conditions were applied by the use of pyrrolidine as base instead of the usual K_2CO_3. However, the desired product was obtained only once. Although the reaction was repeated several times with increased reaction times of a few days up to a week, the thin layer chromatography (TLC) did not show any reaction progress, and it could not be reproduced.

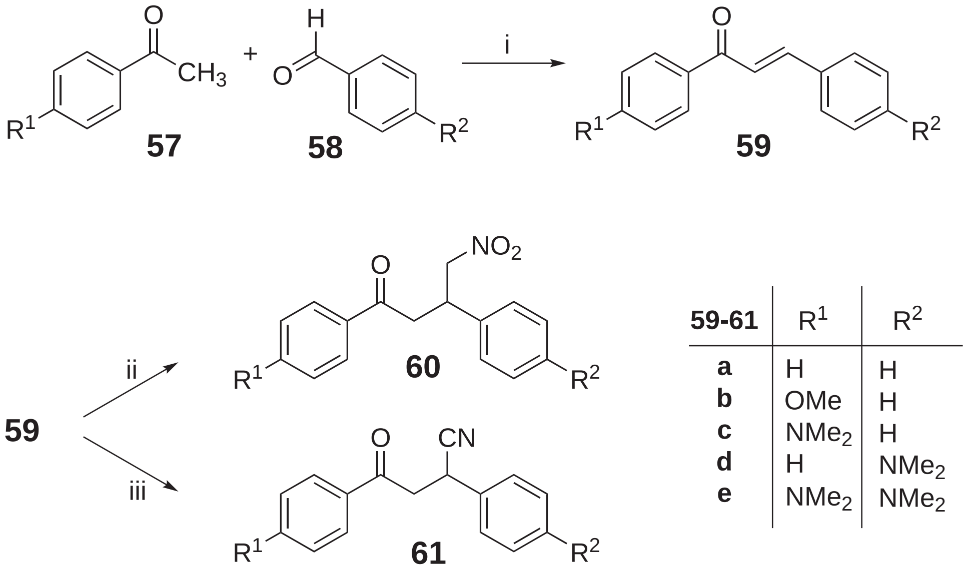

59-61	R^1	R^2
a	H	H
b	OMe	H
c	NMe_2	H
d	H	NMe_2
e	NMe_2	NMe_2

Scheme 5.1: Aldole condensation of substituted acetophenones **57** with aryl-aldehydes **58** to the corresponding chalcones **58** and following Michael addition to **60** and **61**. Reagents and conditions: (i) KOH, Ethanol, rt, 24 h; (ii) NO_2CH_3, EtOH, K_2CO_3, reflux, 3-120 h; (iii) NaCN, HOAc, EtOH.

The azadipyromethenes **62** were subsequently obtained by reaction of the γ-nitroketones **60** with ammonium acetate either in formamide or in butanol under reflux (Scheme 5.2). The solvent formamide has the advantage of a higher boiling point compared to butanol. This leads to a shorter reaction time and also to a precipitation of the product upon cooling. The rather low yields were between 10% for the *p*-methoxy substituted and 40% for the diemthylamino susbtituted azadipyrromethene but comparable with the ones reported in literature.[28, 38, 112] However, higher yields for this conversion were reached with the butanolic solution. The bis-(dimethylaminophenyl)aza-bodipy **63e** was synthesized from a crude precursor as a test reaction. Since the nitroketone **60e** could not be reproduced as mentioned above, the bis-(dimethylaminophenyl)azadipyrromethene **62e** could not be synthesized a second time and analyzed. Subsequent complexation of **62a-e** with borontrifluorid etherate in dichloroethane with diisopropylethylamine gave finally the desired aza-bodipy dyes **63a-e** after column chromatography in good yields in the range of 73-92%.

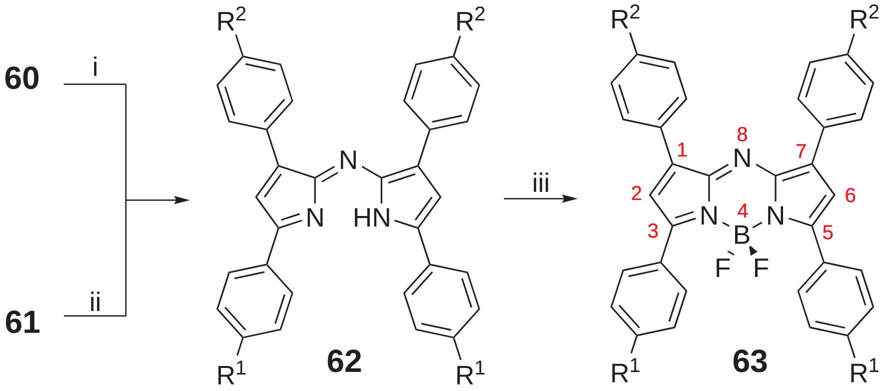

	R^1	R^2
a	H	H
b	OMe	H
c	NMe_2	H
d	H	NMe_2
e	NMe_2	NMe_2

Scheme 5.2: Azadipyrromethene formation and complexation. Reagents and conditions: (i) NH_4OAc, formamide or butanol, reflux, 5 min; (ii) NH_4OAc, BuOH, reflux, 6 h; (iii) $BF_3{\cdot}OEt_2$, $^i PrNEt_2$, $CH_2Cl_2Et_2$, reflux.

The NMR spectra of all aza-bodipys **63** were in accordance with the data reported in the literature.[28, 38, 112] The aromatic proton signals overlap more or less and were found throughout between 6.5 ppm and 8.2 ppm. The most pronounced peak is the singlet peak originating from the pyrrol-hydrogen in the 2,6-position of the aza-bodipy core. This peak does not shift significantly in the aza-bodipy series and is found to be at 7.03 ppm for the parent compound **63a** and the *p*-methoxy aza-bodipy derivative **63b**. The dimethylaminophenyl substituted aza-bodipys show the pyrrole hydrogen peak at 7.09 ppm for **63c** and at 6.82 ppm for **63d** and **63e**. The dimethylaminophenyl subsitutents can lead to a strong broadening in the NMR signals for the pyrrole hydrogen as well as for the methyl signal.

Single crystals suitable for X-ray structural analysis were obtained for the parent tetraphenyl aza-bodipy **63a** by slow evaporation of a chloroform solution. The molecular structure of the aza-bodipy **63a** is displayed in Figure 5.1, together with the packing of the four borondifluoride azadipyrromethenes in the unit cell. The crystal data and structure refinement details are summarized in the appendix and the data can be obtained from the *Cambridge Crystallographic Data Center* with the deposition number *CCDC 826779* as private communication. The tetraphenyl-aza-bodipy compound **63a** crystallizes in a mono-clinic space group P2*1/c*, with four molecules in the unit cell. The boron atom exhibits a distorted tetrahedral environment. The bond angles are 105.9(5) for N-B-N and 110.8(2) for F-B-F, respectively. The average B-N bond lengths are

1.56(0) Å, and comparable to the bond lengths observed in other aza-bodipys or benzannulated aza-bodipys.[42, 112, 114]

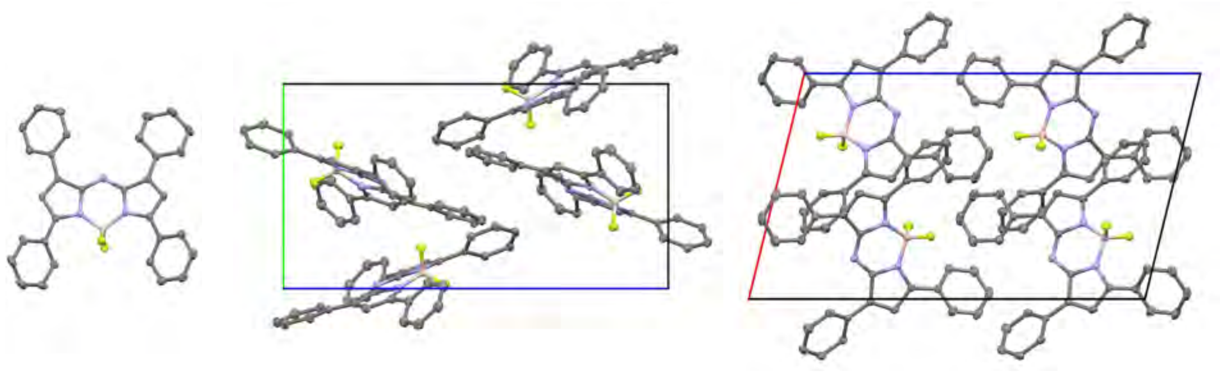

Figure 5.1: Molecular structure (left) and molecular packing (middle and right) of the 1,3,5,7-tetraphenyl-aza-bodipy **63a**. The view of the packing is along the crystallographic axis *a* (middle) and *c* (right) of the unit cell.

The two pyrrole fragments are not exactly coplanar to each other but bended at about 10.4°. This distortion is most likely induced by the sterical hindrance of the phenyl rings in the 3,5-position which is due to the non-propeller-like orientation. The dihedral angles between the phenyl rings and the aza-bodipy core are quite different, with 33.4° for the 1-phenyl, 35.2° for the 3-phenyl, 31.2° for the 5-phenyl and only 10.7° for the phenyl ring in the 7-position. However, these dihedral angles and the non-propeller-like orientation of the 3,5-phenyl rings are strongly influenced by solid packing effects and further structural isomers with a complete propeller-like orientation might be expected. During this work the crystal structure of the borondifluoride tetraphenyl-aza-bodipy has been published by another group, with almost the same structural data.[115] Our experimentally determined structure, however, was used for the calculations of the charge transport parameter.

Attempts to prepare bis-styryle-aza-dipyrromethene dyes

In the well known polymethine series, a bathochromic shift occurs by elongation of the methine chain from e.g. trimethine to pentamethine and further to a heptamethine dye.[116] This effect of a methine shift was also observed for bodipys and corresponding bis(styryle)-bodipys. In these dyes a bathochromic shift of 73 nm from 555 nm to 628 nm was observed.[8] In this context, no styryle system with an aza-bodipy dye was synthesized although one might expect a bathochromic shift as well. In literature, the styryle-bodipys were prepared by condensation of a 3,5-dimethyldipyrromethene derivative with benzaldehyde.[8, 13] Unfortunately, nitrosation of 3,5-dimethylpyrrole and condensation does not lead to the corresponding 1,3,5,7-tetramethyl-aza-dipyrromethene but to 3-amino or 3-acetamido (non aza) dipyrromethenes.[117] Since the 1,3,5,7-tetramethyl-aza-dipyrromethene were intended to undergo condensation reactions with benzaldehyde to form the bis-styryle-aza-bodipys, other synthetic pathways were studied.

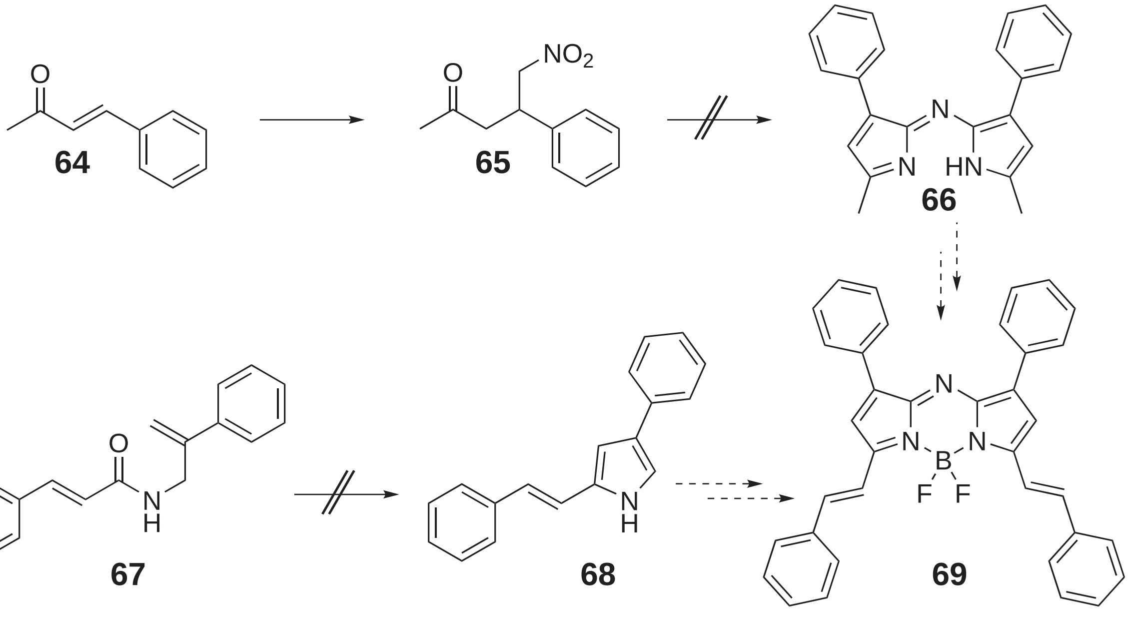

Scheme 5.3: Attempted synthesis strategies to the bis(syryle)-aza-bodipy **69**.

The first attempt for the synthesis of the 3,5-dimethyl-aza-dipyrromethene uses the Michael addition of nitromethane to benzylideneacetone **64** to the necessary nitroketone **65**. However, it was not possible to transform this intermediate **65** into the corresponding aza-dipyrromethene **66**, neither with ammoniumacetate in butanol nor in formamide. The obtained product was a yellowish mixture of various compounds. These compounds were not further analyzed since a colored spot on the TLC plate, as one would expect, could not be detected and mass spectrometry did not show masses corresponding to the product. The second synthesis strategy adopts the synthesis of the corresponding styryle-pyrroles **68** developed by Steglich and nitrosation of them to the aza-dipyrromethene.[118] In this reaction imidoylchlorides from allylcarboxamides were used to obtain the pyrrole in a 1,5 dipolar ring closing reaction. The allylcarboximides **67** were synthesized from the aminomethylstyrene and cinnamonacid chlorides.[118] Ther latter ones were obtained according to standard procedures.[113] The allylamine was synthesized via Gabriel synthesis of the brominated α-methyl-styrene. The carboxamides **67** were transformed with oxalylchloride into the corresponding imidoylchlorides which cyclizise to the styryle-pyrrole **68** under basic conditions. Unfortunately, the cinnamoyl-substituted allylcarboxamides **67** do not yield the desired pyrroles but give rise to the formation of a yellow product which did not show a positive respond to the Ehrlich's reagent with dimethylaminobenzaldehyd and hydrochloric acid. Another approach to styryle-pyrrole could use a Wittig reaction of a pyrrole-2-aldehyde, but this strategy was not further studied.

5.1.2 Physical Properties

As suitable absorber materials for organic solar cells have to fulfill certain requirements, the spectroscopic, electrochemical and thermal properties of the presented compounds are studied in this section.

Spectroscopic characteristics

In order to give a comprehensive explanation of the absorption behavior of the azadipyrromethene compounds **63a-63e**, the absorption spectra were measured although the absorption data were already described in the literature.[28, 38, 112] It is worth mentioning, that the absorption spectra were here recorded in dichloromethane which led to a bathochromic shift of the maxima recorded in chloroform, due to the higher dielectric constant and increased solvent polarity of DCM. The spectroscopic data of the compounds **62a** and **63a** demonstrate that the absorption maximum is shifted from the borondifluoride-free azadipyrromethene (ligand) **62a** to the borondifluoride aza-bodipy (complex) **63a** about 60 nm bathochromically. Simultaneously, the extinction increases strongly which is characteristic. Comparing the absorption behavior of the aza-bodipys **63a-63c** with electron donating substituents, an additional bathochromic shift is observed. Going from the unsubstituted **63a** over the methoxy- **63**, to the dimethylamino-substituted aza-bodipy **63c**, the absorption maximum is strongly shifted from 650 nm to 680 nm up to 805 nm. Obviously, the electron donating substituents in the 3,5-position of the aza-bodipy core lead to a significant bathochromic shift (see the spectrum in Figure 5.2). For the dipyrromethene ligand **62a** an extinction coefficient of 45500 $\mathrm{Lmol^{-1}cm^{-1}}$ was measured and for the corresponding aza-bodipy a much higher value of 79000 $\mathrm{Lmol^{-1}cm^{-1}}$ was determined.

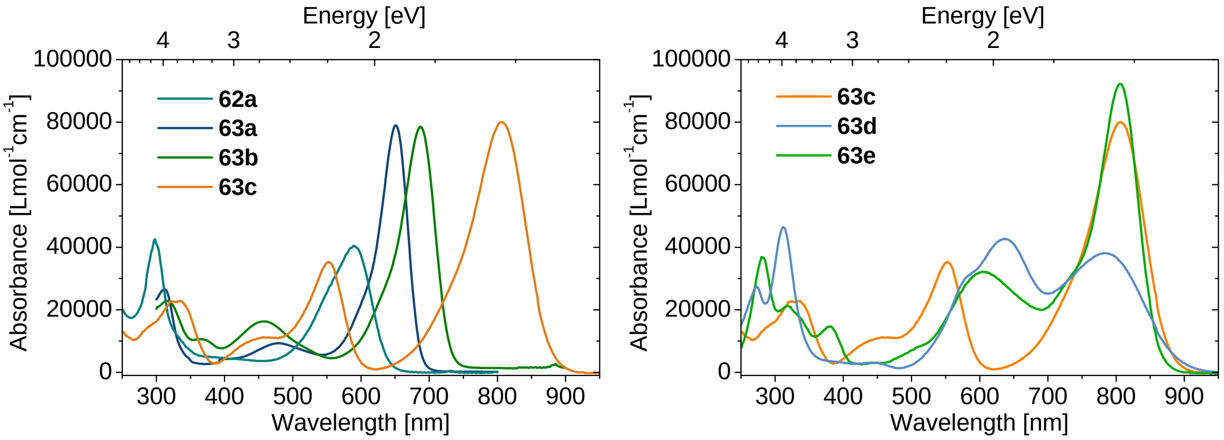

Figure 5.2: Absorption characterisitcs of the aza-bodipys. Left: Bathochromic shift upon complexation (**62a**,**63a**) and due to electron donating substitutents (**63a**,**63b**,**63c**). Right: Influence of the substituent position on the absorption characteristics.

Surprisingly, the absorption maximum of the ligand is not in the visible but in the UV around 300 nm, whereas the boron complexes show the highest extinctions for the absorption band in the visible range. In comparison, the borondifluoride aza-bodipys show extinction coefficients in the visible region from 40000 to 80000 $\mathrm{Lmol^{-1}cm^{-1}}$ with much lower extinction in the UV region. The full width at half maximum (FWHM) of the absorption peak in the visible decrease from 78 nm for the dipyrromethene **62a** to 49 nm for the aza-bodipy **63a**, leading to an intense and narrow absorption maximum by complex formation. In the substituted complexes, the fwhm increases from 49 nm to 58 nm for the methoxy complex, up to 92 nm for the dimethylamino substituted complex. To study the influence of the substitutents position on the absorption characteristics, aza-bodipys with dimethylamino groups in the *para*-position of the phenyl rings in the 3,5-position **63c**, the 1,7-position **63d** and 1,3,5,7-position **63e** were synthesized and examined. All compounds exhibit two absorption bands which is in contrast to the other aza-bodipys. The long wavelength band appears around 800 nm and the other one between 550 nm to 650 nm. In both 3,5-bis(dimethylaminophenyl)-substituted aza-bodipys **63c** and **63e**, the absorption maxima are measured at 800 nm in the NIR in dichloromethane solution. The tetra(dimethylaminophenyl) substitution in **63e** cannot shift the absorption peak further bathochromically. The most red-shifted absorption band of the 1,7-substituted **63d** is at 785 nm and therefore blue-shifted compared to the other compounds **63c** and **63e**. This behavior was observed for several borondifluoride azadipyrromethenes, e.g. methoxy-substituted compounds, where the absorption is slightly blue-shifted with the substitution at the 1,7-position.[8] The second absorption peak rises at 552 nm and at 605 nm for the 3,5-bis- and the 1,3,5,7-tetra-

Table 5.1: Spectroscopic characteristics of the dipyrromethene **62a** and the aza-bodipys **63a-63e,70** in dichloromethane.

	$\lambda_{uv}^{[a]}$ [nm]	$\epsilon^{[a]}$ [$Lmol^{-1}cm^{-1}$]	$\lambda_{max}^{[b]}$ [nm]	$\epsilon^{[b]}$ [$Lmol^{-1}cm^{-1}$]	$\lambda^{[c]}$ [nm]	$\epsilon^{[c]}$ [$Lmol^{-1}cm^{-1}$]
62a	298	42,500	590	40,000	-	-
63a	313	27,000	650	79,500	-	-
63b	317	23,000	687	79,000	-	-
63c	335	23,000	805	80,500	552	35,500
63d	311	46,500	636	42,500	785	38,000
63e	280	36,500	805	93,000	605	32,000
70	282	26,500	780	60,500	565	26,000

[a] Wavelength and extinction of the UV band; [b] Wavelength and extinction of the absorption maximum; [c] Wavelength and extinction of the second strongest long-wavelength absorption.

substituted aza-bodipy, respectively. In **63d**, the peak at 650 nm indicates two absorption bands since a pronounced shoulder can be observed in the spectrum. The extinctions depend highly on the substitution position. Consequently, the lowest extinction was observed for compound **63d** with 425000 $Lmol^{-1}cm^{-1}$. The extinction for the aza-bodipy **63c** is nearly twice with 80000 $Lmol^{-1}cm^{-1}$ compared to **63d**. The highest extinction was found for the tetra-substituted compound **63e** with 92000 $Lmol^{-1}cm^{-1}$.

Electrochemical Characterization

Electrochemical data are not known yet for any aza-bodipy dye. Since the electrochemical properties are important for application of these compounds in organic electronic devices, the aza-bodipys were analyzed with cyclic voltammetry (CV) to obtain the corresponding oxidation and reduction potentials. The measurements were done in dichloromethane, using an Ag/AgCl reference electrode with the ferrocene/ferrocinium couple (Fc/Fc^+) as internal redox standard.[119, 120] The corresponding measurements results are shown in Figure 5.3. The tetraphenyl-azadipyrromethene **62a** as example displays a reversible reduction and a irreversible oxidation. All examined aza-bodipys **63a-63e** exhibit at least one reversible oxidation and reduction wave. Reversible redox waves indicate the formation of stable radical cations or anions, respectively, in the corresponding solution. The irreversible oxidation wave for the azadipyrromethene **62a** points to a consecutive reaction of the corresponding radical cation, whereas the redox wave of the aza-bodipy **63a** appears to be reversible. The methoxy-substituted aza-bodipy **63b** shows four distinct redox steps. The two reversible oxidation and reduction waves implies that both the dicationic and dianionic states are sufficiently stable under these conditions. The dimethylamino-substituted aza-bodipys **63c-63e** exhibit two reversible reduction waves and one reversible oxidation. This is somehow surprising because one would expect a stabilization of the radical cationic state through the electron donating dimethylamino groups, as it is the case for triarylamine-containing hole transport materials. For the bis-dimethylamino substituted aza-bodipy **63e** only one reduction and oxidation wave could be measured due to a superposition of the reduction wave below -1 V. All measured redox potentials are listed in Table 5.2 and are specified against the Fc/Fc$^+$ redox couple. The redox potentials of the azadipyrromethene **62a** are shifted to higher potentials compared to the corresponding borondifluoride aza-bodipy **63a**. The electron withdrawing BF$_2$ moiety in the aza-bodipy lead to a facilitated reduction of the molecule, whereas the oxidation becomes less favored. The substitution with electron donating groups in the aza-bodipy series **63a-63c** clearly shifts the oxidation and reduction potentials to lower potentials. The oxidation is favored with increasing donor strength of the substituents. Thus, potentials (all vs. Fc/Fc$^+$) shift from 0.84 V for **63a**, over 0.58 V for **63b**, to 0.01 V for the dimethylamino-substituted **63c**. This trend of potential lowering is also observed for reduction but not as pronounced, since the potentials shift is only about 0.24 V compared to 0.83 V for the oxidation. Comparing the different dimethylamino-substituted aza-bodipys **63c-63e**, the redox potentials depend on the substituent position in the compounds.

Table 5.2: Electrochemical characteristics of the azadipyrromethene **62a**, and the aza-bodipys **63a-63e** and **70**.

	E^2_{ox} [a] [V]	E^1_{ox} [a] [V]	E^1_{red} [b] [V]	E^2_{red} [b] [V]	HOMO[c] [eV]	LUMO[c] [eV]	E_{gap} [d] [eV]
62a	-	0.55	-1.22	-	-5.33	-3.55	-1.78
63a	-	0.84	-0.84	-	-5.62	-3.94	-1.68
63b	0.96	0.58	-0.91	-1.69	-5.36	-3.87	-1.49
63c	-	0.01	-1.08	-1.77	-4.79	-3.70	-1.09
63d	-	0.21	-1.02	-1.80	-4.99	-3.76	-1.23
63e	-	-0.06	-1.20	-	-4.72	-3.58	-1.14
70	0.13	-0.07	-1.08	-	-4.71	-3.69	-1.02

[a,b] First E^1 and second E^2 oxidation and reduction potentials vs. Fc/Fc$^+$, in CH_2Cl_2, Bu_4PF_6 (0.1 M), scan rate 100 mVs^{-1}. [c] E_{HOMO}(Fc) = -4.78 eV, E_{HOMO}=-4.78+(E_{ox}(Fc)-E^1_{ox}), E_{LUMO}=-4.78+(E_{ox}(Fc)-E^1_{red}). [d] HOMO-LUMO difference as obtained from CV.

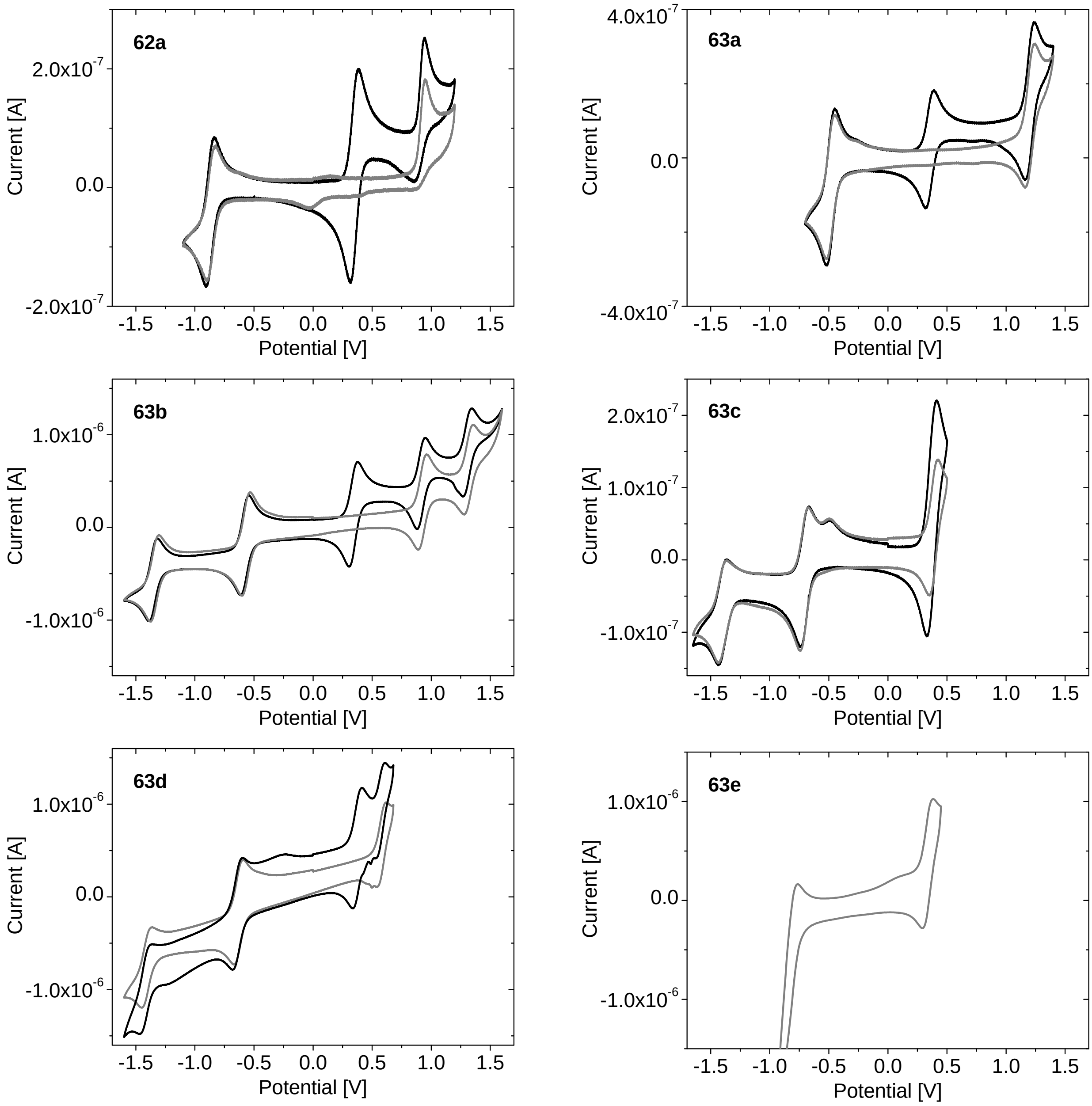

Figure 5.3: Cyclic voltammetry scans of aza-bodipys in dichloromethane against Ag/Ag$^+$. The gray curve indicates the CV scans of the neat material, the black one together with ferrocene (truncated in the last case for reasons of clarity).

The tetrakis(*p*-dimethylaminophenyl)-aza-bodipy **63e** exhibit the lowest potentials for both the reduction and the oxidation. The oxidation potential of the 3,5-bis-dimethylamino-substituted aza-bodipy **63c** is found at 0.2 V lower potential compared to the 1,7-bis-dimethylamino-substituted **63d**. A similar, but weaker trend is measured for the reduction potential of **63c-e**. The potential is found at 0.06 V lower potentials for the 3,5-bis-dimethylamino aza-bodipy. By using the measured oxidation and reduction potentials, the HOMO and LUMO energies were determined with the potential of Fc/Fc^+ as a reference energy and are listed in Table 5.2 and displayed in Figure 5.4. The energetic stabilization caused by the complexation with BF_3 is slightly more pronounced for the LUMO energy than for the HOMO energy (compare **62a** and **63a**). The HOMO-LUMO gap listed in Table 5.2 for **63a** is 0.1 eV smaller than for **62a**. This characteristic trend is in accordance with the one of the optical absorption measurements (see above). Comparing the HOMO energies of **63a** with **63b** and **63c** reveals that the HOMO energies increase significantly, whereas the LUMO energies increase only moderately. Consequently, the electric gap decreases strongly from 1.68 eV to 1.09 eV (see Figure 5.4) representing again the trend in the absorption spectra. The influence of the substitution position on the HOMO and LUMO energies can be recognized for the bis-dimethylaminophenyl-aza-bodipys **63c** and **63d**. The HOMO and LUMO energies for **63c** with the substitution at the 3,5-position are higher compared to **63d** with the substituents at the 1,7-position. The tetrakis(*p*-dimethylaminophenyl)-aza-bodipy **63e** demonstrated the highest HOMO and LUMO energies compared to all other investigated aza-bodipys but it possesses not the smallest electrical gap, as derived from CV measurements.

Quantum Chemical Calculations

DFT calculations for the aza-bodipys **62a** and **63a-63e** were performed in order to gain a deeper insight into the experimentally measured optical and electrochemical structure-property relationship.[101, 111] The electronic structures of the aza-bodipys provide some general characteristics for the understanding of substituent effects on the electrochemical and optical properties. To discuss this correlation, the HOMO and LUMO orbitals are displayed, exemplarily for **63a** in Figure 5.5. Unambiguously, it can be seen that both, the HOMO and LUMO exclusively have π-characteristics, as expected. The distributions of the MO coefficients for both frontier orbitals show essential differences. Thus, at the aza-bodipy core the LUMO exhibits the largest coefficients with a strong contribution on the nitrogen atoms and, particularly, at the azamethene-bridge (in

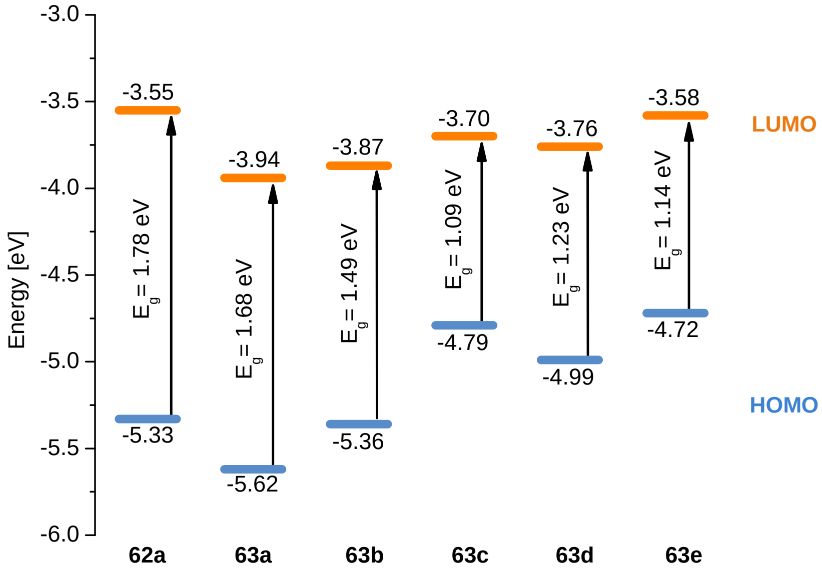

Figure 5.4: HOMO and LUMO energy values for the azadipyrromethene **62a** and the aza-bodipys **63a-63e**, derived from the CV measurements.

position 8, shown in Figure 5.5, right). Corresponding to the larger LUMO coefficient at the nitrogen atoms, the complexation with borontrifluoride has a stronger impact on the LUMO energy. Accordingly, the stabilization of the energy levels due to the electron withdrawing character of the borondifluoride moiety is more pronounced for the LUMO in **63a**. As a consequence, a reduced electrical gap for **63a** compared to **62a** can be confirmed by CV measurements (see above). In the HOMO (shown in Figure 5.5, left) the coefficients are small at the pyrrole nitrogen atoms, and zero at the azamethene bridge nitrogen atom due to a nodal plane. In contrast, the coefficients at the residual aza-bodipy core and on the aryl rings linked at the 3,5-position are relatively large. From these findings, it can be concluded that substituents at the phenyl ring in the 3,5-position at the aza-bodipy influence predominantly the HOMO of this molecule. Accordingly, the HOMO energies can be increased more effectively than the LUMO energies by attaching electron donating substituents at the aza-bodipy core, as it is the case for methoxy- and dimethylamino groups.[116] Moreover, this effect is larger at the 3,5-position than at the 1,7-position. This can be seen for the dimethylamino-substituted compounds. Compound **63c** shows a higher HOMO energy than **63d**. In **63e**, the overall electron donating character is enhanced due to the 1,3,5,7-tetrakis(*p*-dimethylaminophenyl) substitution and the HOMO energy is further increased.

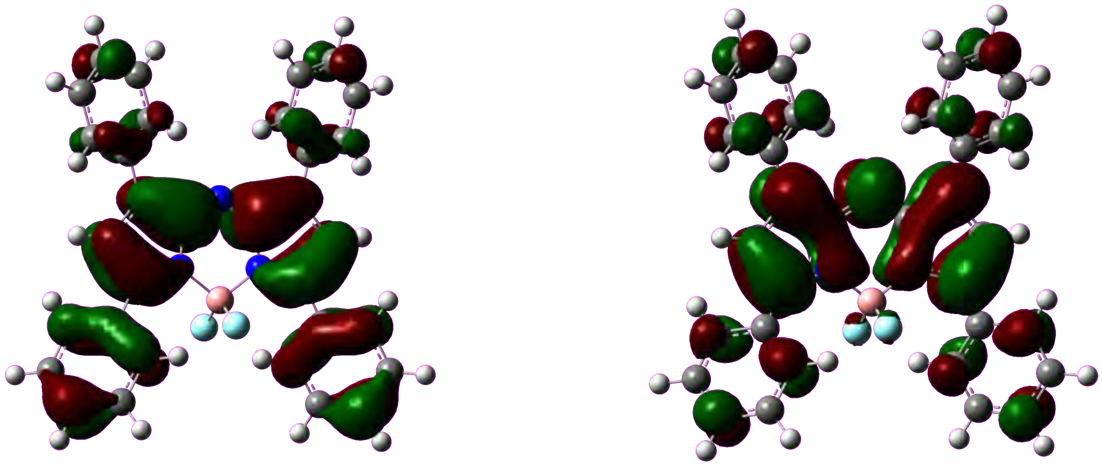

Figure 5.5: Representation of the highest occupied molecular orbital (HOMO) on the left and the lowest unoccupied molecular orbital (LUMO) on the right of the borondifluoride tetraphenyl-azadipyrromethene.

Additionally, the absorption spectra of the dipyrromethene **62a** and the aza-bodipys **63a-63e** were calculated with TDDFT. The results are listed in Table 5.3. The absolute value of the absorption wavelengths differ stronger with respect to the experimental values. However, the calculations revealed a lower excitation energy (a greater wavelength) together with a higher extinction in the borondifluoride complex as it is the case in the experimental spectra of both compounds **62a** and **63a**. It also can be seen that the electron donating groups lead to a redshift, as the wavelengths increase within the calculated series.

The calculated HOMO energies agree well with the energies derived from CV measurements with a maximum difference of only 0.01 eV to 0.05 eV (compare Table 5.3 and Table 5.2). Only the HOMO energy of **63e** and the differences in the LUMO energies with respect to the experiments are higher, in the order of 0.39 eV to 0.54 eV. The essential differences are found in the principal orbital contribution for the transition to the first excited state. In the dipyrromethene **62a**, the HOMO and the HOMO-1 together with the LUMO are involved in the lowest energy excitation. The complexation with borondifluoride has an influence on the principal orbital contribution in the excitation, as it can be seen in Table 5.2. In the calculated borondifluoride complexes **63a-63c**, the first excited states are characterized by a pure HOMO-LUMO transition. The compounds **63d** and **63e** with dimethylamino groups in the 1,3-position display mixed orbital contributions for the lowest energy excitation. The secondary absorption maxima and the intensities in the dimethylamino-substituted bodipys **63c-63e** are predicted fairly well. It is shown that the second maxima are related to transitions from the HOMO-1 to LUMO, and additionally in **63d** from the

Table 5.3: Calculated energy, wavelength, oscillator strength, and principal orbital contribution of the lowest energy transitions of the azadipyrromethene **62a** and the aza-bodipys **63a-63e**.

	Energy [eV]	Wavelength [nm]	Oscillator strength	Principal orbital contributions	HOMO [eV]	LUMO [eV]
62a	2.24	552.10	0.64	H-1→L, H→L	-5.38	-3.07
63a	2.19	565.89	0.72	H→L	-5.67	-3.47
63b	2.04	605.63	0.72	H→L	-5.34	-3.28
63c	1.83	675.65	0.73	H→L	-4.80	-2.95
	2.42	510.62	0.50	H-1→L (86%), H→L+3 (3%)		
63d	1.78	693.42	0.40	H-2→L (10%), H→L (68%)	-5.02	-3.04
	2.09	591.40	0.42	H-1→L (86%)		
	2.35	525.93	0.33	H-2→L (72%), H→L (4%)		
63e	1.79	690.58	0.73	H-2→L (4%), H→L (67%)	-4.44	-1.86
	2.15	576.09	0.64	H-1→L (87%)		

Calculation with B3LYP/6-31+g(d,p), H: HOMO, L: LUMO.

HOMO-2 to the LUMO in a third excitation as it can be identified indeed in the experimental spectra. The origin for this absorption behavior might be in the specific electron configuration in the dimethylamino-substituted aza-bodipys. Their occupied orbitals are energetically close together. In **63d** the HOMO-1 is 0.4 eV lower in energy than the HOMO, whereas in **63a** the HOMO-1 is 0.9 eV lower. An excitation from these low lying orbitals to the LUMO leads evidently to a hypsochromic shift. To obtain additional information of the absorption properties, the density differences of the ground and the lowest excited state was calculated and visualized in Figure 5.6. This electron density difference map is a representation of the changes in electron density that occur for the specific transition from the ground to the first excited state. The purple and gold colored areas in Figure 5.6 do have a physical meaning in terms of an observable. The gold colored areas indicate an electron depletion, the purple areas show an electron accumulation upon excitation. In this representation the characteristics of the frontier orbitals can be identified, as one would expect it for a HOMO-LUMO contribution. In general the charge redistribution from the periphery to the central core is visible here and the borondifluoride dipyrromethene core can be regarded as a central acceptor moiety.

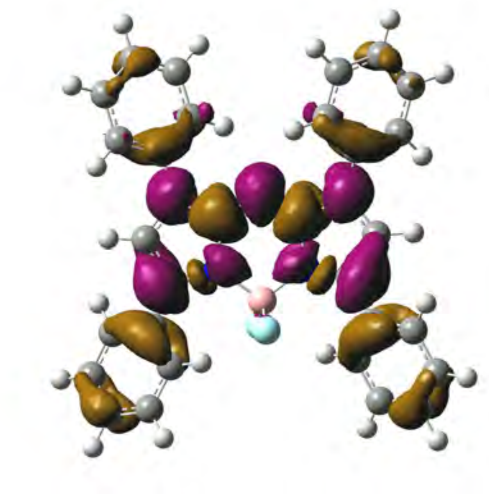

Figure 5.6: Difference density plot of the ground and the lowest excited state for **63a**, illustrating the charge transfer character. Purple regions display electron density accumulation, and gold regions electron density depletion upon excitation.

Hence, the lowest excitation has a strong charge transfer (CT) character which is experimentally confirmed in the positive solvatochromism leading to a redshift of the absorption maximum with increasing solvent polarity. Furthermore, the solvatochromism is stronger for the dimethylamino-substituted azadipyrromethenes, where the CT might be particularly strong due to the significant electron donor effect of the dimethylamino group. O'Shea et al. showed nicely that upon blocking the lone pair by protonation, the CT is omitted and a blue shift accompanied by a diminished absorbance is observed.[28] An increased CT character by the introduction of appropriate substituents on the other hand would lead to a bathochromic shift.

Thermal Properties

A high thermal stability up to about 300°C is necessary for the processability of the materials by thermal vacuum sublimation, in order to guarantee a robust sublimation process without any degradation losses. Hence, the thermal stability of the complexes **63a-63e** were investigated by thermogravimetric analysis (TGA). The measurements were done in an inert nitrogen gas atmosphere, and the results are summarized in Figure 5.7. It is assumed that the degradation of the materials is associated with a fragmentation of the molecules leading to an evaporation of smaller fragments. Accordingly, the observed mass loss of the materials is interpreted as degradation, although an evaporation of the whole molecule cannot be excluded despite of its unlikeliness at atmospheric pressure. The aza-dipyrromethene **62a** shows a continuous mass loss over the whole temperature range, without any pronounced features. Degradation of this material is assumed to occur beyond 300°C as the slope decreases slightly at these temperatures (Figure 5.7, top panel). In contrast, the aza-bodipy **63a** displays a small kink around 280°C. This is more than 50°C beyond the melting point of 230°C. The distinct mass loss is attended by a decreasing slope at 300°C and denotes the materials degradation.

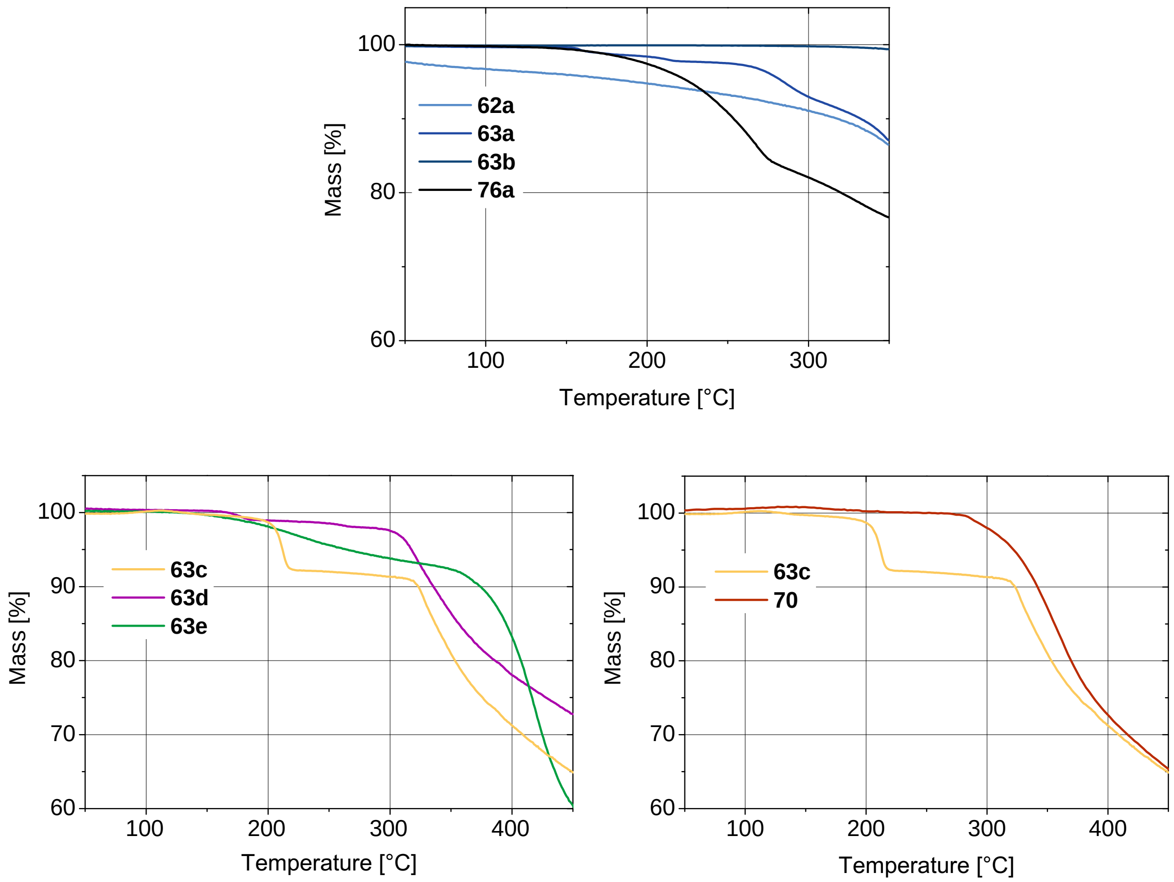

Figure 5.7: Termogravimetric analysis of different aza-bodipys. Top: Comparison of the azadipyrromethene **62a** with certain aza-bodipys. Left: Different thermal stabilities in the dimethylaminophenyl-substituted aza-bodipys **63c-63e**. Right: Increased thermal stability of the boroncatechol complex **70** compared to the borondifluoride complex **63c** of the 3,5-bis(*p*-dimethylaminophenyl)-aza-dipyrromethene **62c**.

From the comparison of **62a** and **63a**, the complexation with borondifluoride does not lead to a significant increase in thermal stability, since in both cases, a residual mass of 90 % is measured above 300°C and the slopes of the curve is very similar. The *p*-methoxyphenyl-aza-bodipy **63b** displays no mass loss up to a temperature of 350°C and is the most stable compound in the series. This is particular remarkable since the melting point is reached already at 200°C and the compound forms a melt which is stable over 150°C. The thienyl-aza-bodipy **76a** (Figure 5.7, top panel) shows a significant mass loss beginning at 210°C. This characterizes the compound as rather fragile and might be related to the free 5-position in the thiophene heterocycle, which is known to be very reactive. The thermogravigrams of the dimethylaminophenyl substituted aza-bodipys (Figure 5.7, lower left panel) revealed a pronounced dependence on the substitution position. A specific degradation can be observed for the 3,5-bis(*p*-dimethylaminophenyl)-aza-bodipy **63c**. A pronounced mass loss of about 8-9 % is observed at 200°C, which is present as a kink in the TGA curve as shown in Figure 5.7 in the lower left panel. At higher temperatures the mass stays constant up to 320°C until a further mass loss occurs. In contrast, the 1,7-bis(*p*-dimethylaminophenyl)-aza-bodipy **63d** is stable up to 310°C, without any mass loss. The thermogravigram of the 1,3,5,7-tetrakis(*p*-dimethylaminophenyl)-aza-bodipy **63e** is difficult to evaluate since the slope is steadily decreasing without a kink. However, the mass decreases about 8-9 % as it is the case for **63c** and, therefore, a degradation is assumed. With the help of TGA coupled to mass spectrometry, the lost fragments could be analyzed in the case of **63c** and related to different boron species. The masses 14 (BH_3), 50 (HBF_2) and 44 (H_2BBHF) were found amongst others.

This led to the idea to substitute the borondifluoride moiety with a boroncatechol moiety where the F atoms are replaced by the chelate complex of catechol as shown with **70** in Figure 5.4. Indeed, the thermal stability of **70** increases and a mass loss occurs at significantly higher temperatures (of around 100°C), as it can be seen in Figure 5.7 on the lower right panel.

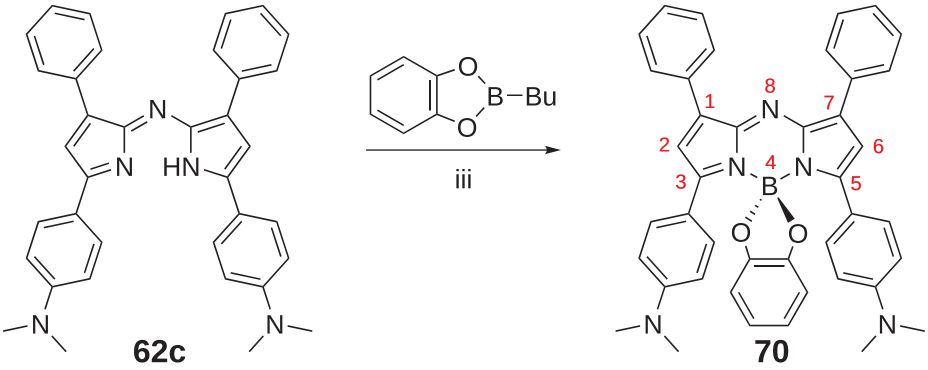

Scheme 5.4: Complexation of azadipyrromethene with 2-butylbenzo[d][1,3,2]dioxaborole. Reagents and conditions: (i) *i*-$PrNEt_2$, $CH_2Cl_2Et_2$, reflux.

Accordingly, the catechol complexes like **70** are one possible way to increase the thermal stability of aza-bodipys, without changing the electrochemical and optical properties drastically, as it can be derived from Table 5.1 and Table 5.2, respectively.

5.2 Borondifluoride thienyl-azadipyrromethenes

In particular, thienyl substituents in the bodipy series give rise to compounds with interesting properties, such as donor-acceptor systems, as well as redox-stable polymers.[121, 122, 123] Surprisingly, no thienyl-aza-bodipys have been prepared yet, although promising properties may be expected, since thiophene derivatives have been found to feature exciting optical and electrochemical qualities.[124, 125] Furthermore, thiophene containing molecules are frequently used in particular as active components in opto-electronic materials.[126, 127] As discussed in section 5.1.2, the absorption of the aza-bodipys should be redshifted with increasing CT character. Thiophene could be an ideal π-conjugated building block for this purpose due to its electron rich character. The aim of the present study is to prepare a series of novel thienyl-aza-bodipys and to systematically explore the optical and electrochemical characteristics with respect to the substitution pattern and in comparison to the parent aza-bodipy (**63a**). In addition to the experimental characterization, quantum chemical calculations with DFT were applied to obtain insights into the absorption behavior and the energy levels which are essential for understanding their (opto-)electronic properties.

5.2.1 Synthesis

The synthesis of the thiophene-substituted aza-bodipys follows the route described in Scheme 2.1 and is outlined in Scheme 5.5. In the crucial step of this synthesis, 4-nitro-1,3-di(het-)arylbutanones **74** are reacted with ammoinum acetate in butanol to the corresponding azadipyrromethenes **75** via an in situ formation of the related pyrroles (see Scheme 5.5). Heating in formamide instead of butanol indicates the dye formation by a change in color, but no product could be isolated. The necessary 4-nitro-1,3-di(het-)arylbutanones **74** are readily available by a base-mediated Michael-addition of nitromethane to a thiophene substituted chalcone **73**. After aqueous work-up, the reaction gave essentially quantitative yields of 4-nitro-1,3-di(het-)arylbutanones **74** which were directly used without further purification. The required substituted chalcones **73** were synthesized in the first step via an aldole condensation of (het)arylketones **71** with (het)arylaldehydes **72** in excellent yields.[113] However, by using this procedure, the azadipyrromethenes **75a-75c** were obtained with yields of 6 % to 12 %. Finally, the desired thiophene substituted aza-bodipyss **76a-76c** were prepared in yields between 71 % and 82 % by complexation of the azamethenes **75a-75c** with borontrifluoride etherate under standard conditions. For the synthesis of the star-shaped 2,5-dithienyl substituted aza-bodipys **76d** and **76e** an extended route was employed, where the dibromo aza-bodipy **76** was used as a key intermediate, (see Scheme 5.5).[28, 114] This dibromo species **77** is a versatile starting material for palladium-catalyzed cross-coupling reactions. Thus, the Stille-coupling of **77** with 2-tributylstannyl-thiophene gave the target compounds in a yield of 85 % .

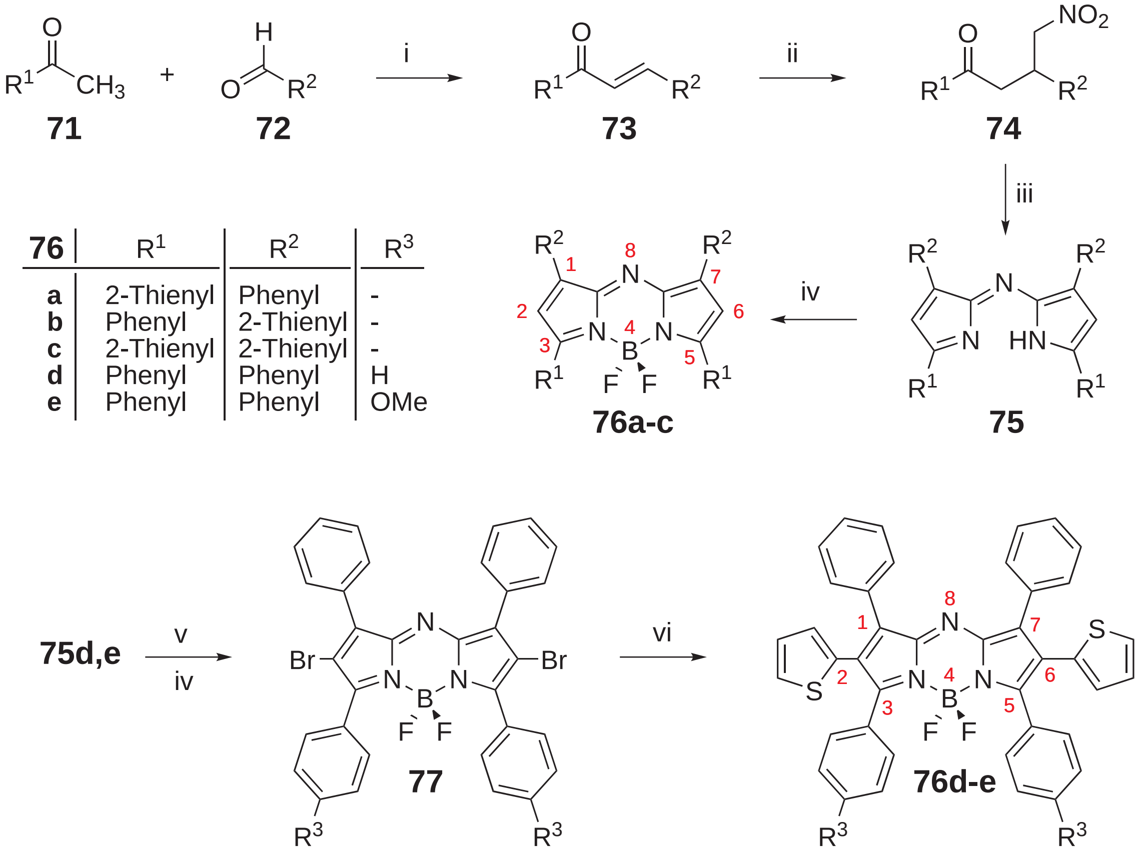

76	R1	R2	R3
a	2-Thienyl	Phenyl	-
b	Phenyl	2-Thienyl	-
c	2-Thienyl	2-Thienyl	-
d	Phenyl	Phenyl	H
e	Phenyl	Phenyl	OMe

Scheme 5.5: Synthetic route to thienyl-substituted aza-bodipys **76**. Reagents and conditions: (i) KOH in EtOH, rt; (ii) CH_3NO_2 in EtOH, K_2CO_3, reflux; (iii) BuOH, NH_4HOAc, reflux; (iv) $BF_3 \cdot OEt_2$, *i*-$PrNEt_2$, $CH_2Cl_2Et_2$, reflux; (v) Br_2, benzene, rt; (vi) 2-tributylstannyl-thiophene, $Pd^0(PPh_3)_4$, toluene, reflux.

5.2.2 Physical Properties

Absorption, fluorescence as well as the electrochemical properties are characterized in this section and are compared to the theoretic results of quantum chemical calculations.

Spectroscopic characteristics

The spectroscopic data of the aza-bodipys **76a-76e** and the thienyl-azadipyrromethenes **75a-75c** are summarized in Table 5.4 and the corresponding spectra are shown in Figure 5.8.

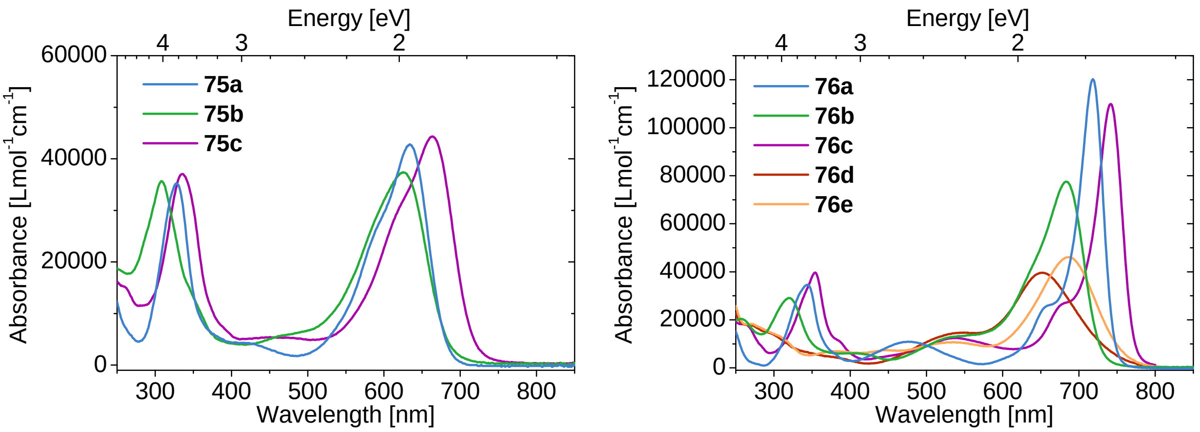

Figure 5.8: Spectroscopic characteristics of the thiophene azadipyrromethenes. Left: Absorption spectra of the thienyl-azadipyrromethenes **75a-75c**. Right: Absorption spectra of the thienyl-aza-bodipys **76a-76e**. For details on the wavelength and the extinction coefficients see Table 5.4.

The absorption spectra of all azadipyrromethenes **75** exhibit two intense peaks, one in the UV region (which is the maximum in case of **75d**) and one in the visible region (usually the maximum). The absorption maxima of the thienyl-azadipyrromethenes **75a-75c** are found at 625 nm, 633 nm and 663 nm, in the visible region. These maxima are significantly shifted into the red region compared to the 1,3,5,7-tetraphenyl-azadipyrromethene **62a** which absorbs at 589 nm.
The extinction of both absorption peaks in the UV and the visible are comparable for all azadipyrromethenes **75** and found to be between 35,000 and 37,000 $\mathrm{Lmol^{-1}cm^{-1}}$ for the first absorption bands and between 40,000 and 45,000 $\mathrm{Lmol^{-1}cm^{-1}}$ for the absorption maximum, as can be seen from Table 5.4. The complex formation with borontrifluoride has a tremendous influence

Table 5.4: Spectroscopic characteristics of the dipyrromethenes **75** and the aza-bodipys **76** in dichloromethane solution.

	λ_{UV} [nm]	$\epsilon^{[a]}$ [$\mathrm{Lmol^{-1}cm^{-1}}$]	λ_{max} [nm]	$\epsilon^{[b]}$ [$\mathrm{Lmol^{-1}cm^{-1}}$]	λ_{flu}[c], Φ[d]
75a	328	35,500	633	43,000	-
75b	308	36,000	625	37,500	-
75c	335	37,500	663	45,000	-
76a	344	35,000	718	120,500	740 (22), 0.44
76b	320	29,000	683	78,000	725 (42), 0.10
76c	354	40,000	742	110,000	764 (22), 0.11
76d	270	18,500	650	40,000	-
76e	270	18,500	657	47,000	-

[a] Extinction of the UV band; [b] Extinction of the absorption maximum; [c] Stokes-shift is specified in brackets; [d] Fluorescence quantum yield measured relative to the one of rhodamine 101.

on the absorption characteristics of the thiophene-substituted aza-bodipys **76a-76c**, giving rise to a strong bathochromic shift. This bathochromic shift is unusually strong for **76a** and **76c** with 85 nm and 79 nm, since for the 1,3,5,7-tetraphenyl-aza-bodipy **63a** it amounts only to 61 nm compared to the 1,3,5,7-tetraphenyl-azadipyrromethene **62a**. As a result, by replacing the phenyls with thiophenes in 1,3,5,7-positions at the aza-bodipy core, the absorption maximum can be shifted by 92 nm into the red. Surprisingly, the 2,6-dithienyl-aza-bodipys **76d** and **76e** show the most hypsochromic and most broadened absorbance in this series with the maximum at 650 nm. This value is the same as for compound **63a** and indicates that the thiophenes do not have any influence at the 2,6-positions. However, in the UV part of the spectrum of **76d** and **76e**, the absorption band is diminished, which is in contrast to the other thienyl-aza-bodipys. The extinctions of the thiophene-substituted aza-bodipys **76a-76e** differ significantly in dependence of the substitution pattern. The strongest extinction with 120,000 $\mathrm{Lmol^{-1}cm^{-1}}$ is found for the 3,5-dithienyl-aza-bodipy **76a**, followed by the 1,3,5,7-tetrathienyl-derivative **76c** with 110,000 $\mathrm{Lmol^{-1}cm^{-1}}$. The 1,7-dithienyl-substituted species **76b** shows a weaker absorbance with 78,000 $\mathrm{Lmol^{-1}cm^{-1}}$. The 2,6-dithienyl-aza-bodipys **76d** and **76e** exhibited with 40,000 $\mathrm{Lmol^{-1}cm^{-1}}$ the smallest extinction coefficient, one third of the wavelength of **76a**.

Besides of the star-shaped aza-bodipys **76d** and **76e**, all other thienyl-derivatives **76a-76c** emit in the red spectral region. The corresponding fluorescence spectra are shown in Figure 5.9. As can be seen, **76a-76c** exhibit the emission maxima between 725 nm for **76b** and 764 nm for **76c**. The Stokes shift is in the usual range, but it is significantly larger with 42 nm for the compound **76b** than for the other compounds **76a** and **76c** with a Stokes-shift of only 22 nm. This indicates, that the excited state geometries of the compounds **76a** and **76c**, in contrast to the one of compound **76b**, differ only slightly from the corresponding ground state geometries.[43]

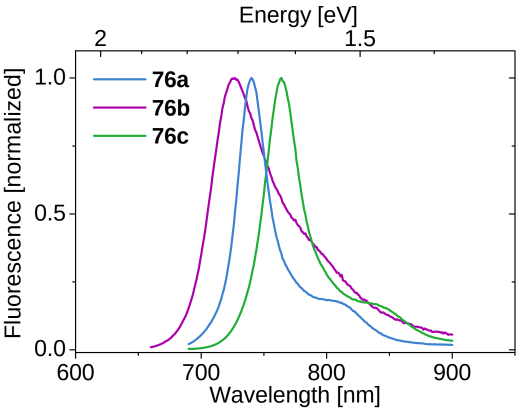

Figure 5.9: Fluorescence spectra of **76a-76c** in dichloromethane. Compounds **76d** and **76e** did not show any measurable fluorescence.

Electrochemical Characterization

Both series **75** and **76** and the dibromo compounds **77d,e** were analyzed by CV to obtain the corresponding oxidation and reduction potentials. The measurements were done in dichloromethane, using an Ag/AgCl reference electrode with Fc/Fc$^+$ as internal redox standard.[119, 120] All examined dyes exhibit a reversible one-electron reduction and an irreversible one-electron oxidation waves, which is shown for the aza-bodipys **76** and **77** in Figure 5.10.

This indicates the formation of stable radical anions under the applied conditions. The reason for the irreversible oxidation waves might be the unsubstituted 5-position at the thiophene ring, which is known to be reactive and can undergo electrochemical polymerization via the corresponding radical cations.[128] From the redox potentials, listed in Table 5.11, it can be seen that the borondifluoride-free azadipyrromethenes **75** show the lowest oxidation and reduction potentials. The redox potentials in the aza-bodipy series **56** are shifted to higher potentials compared to **75**. This effect is caused by the electron withdrawing character of the BF$_2$ moiety in the aza-bodipys **76** and leads to a facilitated reduction of these compounds, whereas the oxidation becomes less favored. This trend is intensified for the dibromo substituted aza-bodipys **77** which is easily reducible due to the electron negativity of the bromo substituent.

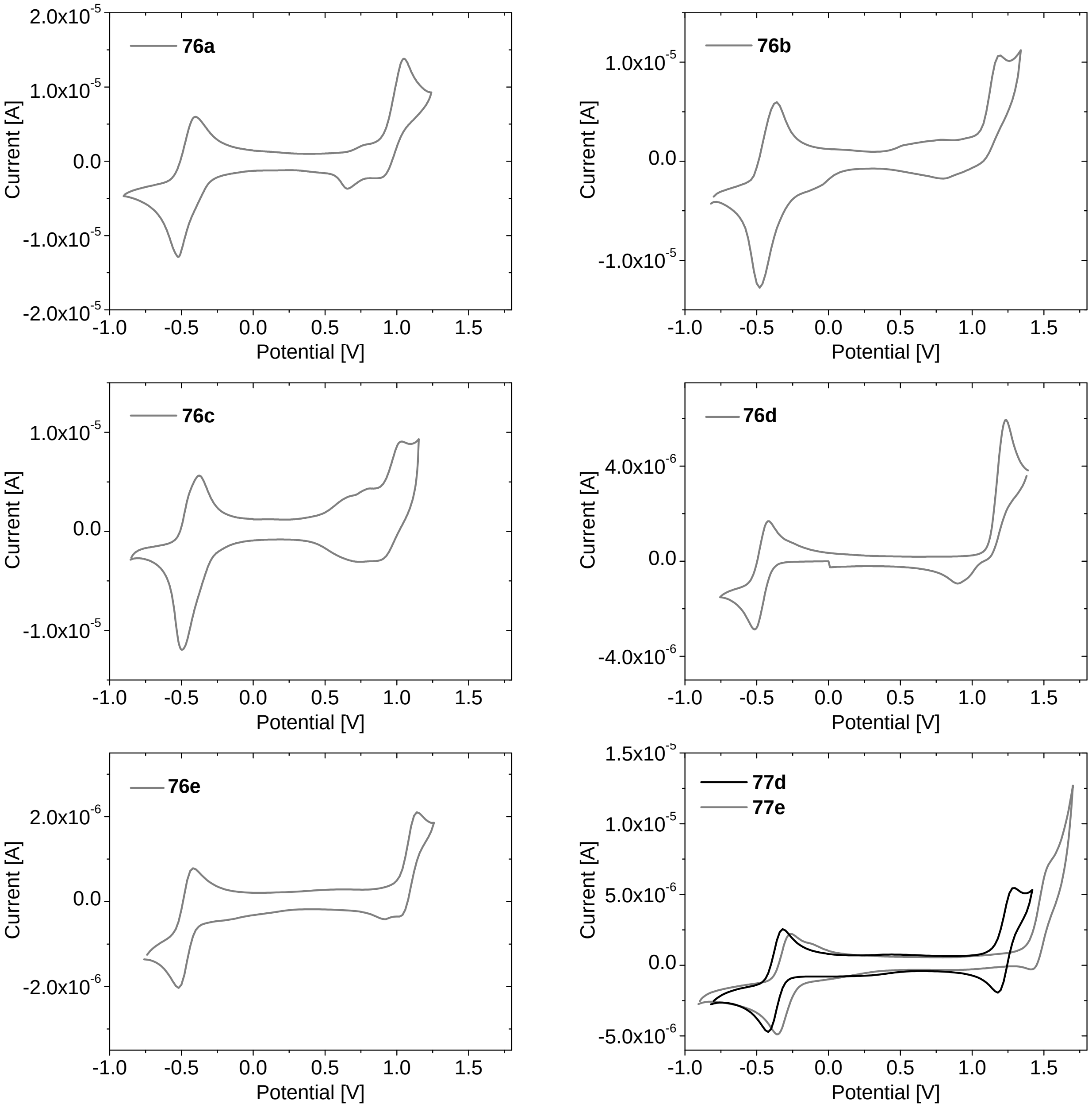

Figure 5.10: Cyclic voltammetry scans of the thienyl aza-bodipys **56** and dibromo species **57** in dichloromethane against Ag/Ag$^+$.

Table 5.5: Electrochemical characteristics of the dipyrromethines **55**, and the aza-bodipys **56** and **57**.

	E_{ox} [a] [V]	E_{red}[a] [V]	HOMO[b] [eV]	LUMO[b] [eV]	E_{gap}[c] [eV]
75a	0.41	-1.19	-5.19	-3.59	1.60
75b	0.44	-1.18	-5.22	-3.60	1.62
75c	0.35	-1.16	-5.13	-3.62	1.51
76a	0.62	-0.82	-5.40	-3.96	1.44
76b	0.72	-0.86	-5.50	-3.92	1.58
76c	0.57	-0.84	-5.35	-3.94	1.41
76d	0.84	-0.84	-5.62	-3.94	1.68
76e	0.69	-0.87	-5.47	-3.91	1.56
77d	1.09	-0.69	-5.87	-4.09	1.78
77e	0.84	-0.77	-5.62	-4.01	1.61

[a] Redox-potentials of the first oxidation E_{ox} and first reduction E_{red} vs. Fc/Fc$^+$, in CH_2Cl_2, Bu_4PF_6 (0.1 M), scan rate 100 mVs^{-1}. [b] E_{HOMO}(Fc) = -4.78 eV, E_{HOMO}=-4.78+(E_{ox}(Fc)-E_{ox}), E_{LUMO}=-4.78+(E_{ox}(Fc)-E_{red}). [c] HOMO-LUMO difference as obtained from CV.

By using the measured oxidation and reduction potentials, the HOMO and LUMO energies of **75** and **76** were determined with the potential of Fc/Fc$^+$ as a reference energy and are listed in Table 5.5. The obtained frontier orbital energies for **76** are displayed in Figure 5.11. The energetic stabilization caused by the complexation with BF_3 is slightly more pronounced for the LUMO energies than for the HOMO energies, as can be seen by calculating the corresponding **76**(HOMO)-**75**(HOMO) and **76**(LUMO)-**75**(LUMO) differences for **76** and **75**, respectively. Consequently, the HOMO-LUMO gap listed in Table 5.5 for the aza-bodipys **76** is smaller than for the azadipyrromethenes **75**. This characteristic is in accordance with the trend of the optical absorption measurements (see above). The comparison of the HOMO energies of the parent aza-bodipy **63a** to the thienyl-aza-bodipys **76a-76e**, reveals that the 2,6-dithienyl-substituted compound **76d** has the same HOMO and LUMO energy as **63a**, whereas the HOMO energies of **76a-76c** are significantly increased. The thiophene in the 3,5-position (**76a**) results in an increase of 0.20 eV, whereas in the 1,7-position (**76b**) it amounts to 0.16 eV. In **76d** the influence of the thiophenes in the 2,6-position on the HOMO energy is negligible, as no differences in the redox-potentials can be seen compared to **63a**. The largest effect was found for the 1,3,5,7-tetrathienyl-aza-bodipy **76c** with an increased HOMO energy of 0.43 eV compared to **63a**. In contrast to the HOMO energies, the LUMO energies of **76a-76e** are rather constant with minor

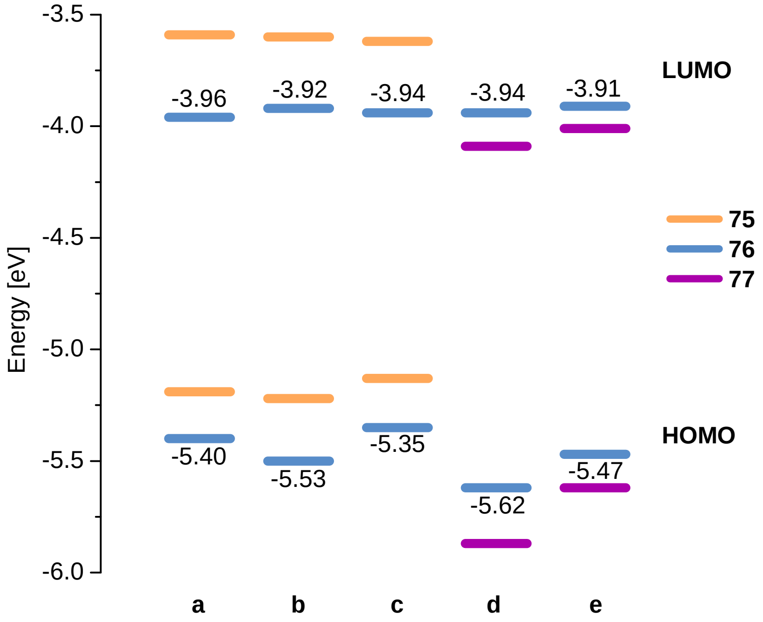

Figure 5.11: HOMO and LUMO energy values of the aza-bodipys **75**, **76** and **77** derived from the CV measurements, specified for **76**.

changes of maximum 0.05 eV in maximum. This allows a systematic HOMO energy level tuning by the choice of an appropriate substituent position at the aza-bodipy core.

Quantum Chemical Calculations

In order to obtain a better understanding of the thienyl-aza-bodipys, DFT calculations for **76a**-**76d** were performed.[101, 111] The HOMO and LUMO frontier orbitals in the thienyl-aza-bodipys have a very similar appearance compared to the phenyl substituted aza-bodipys. Therefore, the influence of the substituents is similar to those discussed in the previous section. The substituents in the 3,5-position at the aza-bodipy core influence predominantly the HOMO of this system. Accordingly, the HOMO energies can be increased more effectively than the LUMO energies by attaching thiophenes instead of phenyl rings at the aza-bodipy core.[116] This effect is slightly larger at the 3,5-positions than at the 1,7-positions. Therefore, compound **76a** shows a higher HOMO energy than compound **76b**. In compound **76c**, the overall electron donating character is enhanced due to the 1,3,5,7-tetrathienyl substitution and the HOMO energy is further increased compared to **76a** and **76b**. On the other hand, the influence of substituents on the frontier orbital energies depends on the dihedral angles between the aza-bodipy core and the substituents, as the conjugation decreases with an increasing angle.[32] The thiophene in **76d** and **76e** causes a marginal influence on the energy levels compared to **63a** and **63b**. In these cases, a sterical hindrance of the thiophenes can be assumed, due to the presence of adjacent phenyl rings at the aza-bodipy core. Geometry optimizations illustrate a propeller-like structure of the peripheral (het)aryl-rings with increased dihedral angles between 56° and 60° in **76d**. In contrast, the thiophene moieties in the compounds **76a-76c** exhibit smaller dihedral angles between 14° and 19° and the phenyl rings in **76a** and **76b** showed angles between 28° and 36°, respectively. Hence, this result confirms the diminished influence of the thiophene moiety in **76d** due to sterical hindrance. The calculated HOMO energies agree well with the energies derived from CV measurements with a maximum difference of only 0.02 eV to 0.15 eV, with the largest deviation for **76c** (see Table 5.5 and Table 5.6). The differences in the LUMO energies with respect to the experiments are higher, on the order of 0.39 eV to 0.54 eV. This originates to some extent from the idealized calculations in gas phase and might be improved slightly by applying an appropriate solvation model.[99, 98] The energies of the absorption maxima of the aza-bodipys **76a-76d** were calculated with the TDDFT approach which has proven to be superior compared to semi-empirical methods.[111, 129] The results were in good agreement with the experimental values with a tolerance in the range from 0.19 eV to 0.29 eV. These deviations can be attributed to overestimated LUMO energies.

Table 5.6: Calculated energy, wavelength, oscillator strength, and principal orbital contribution of the most intense transitions of the thienyl-aza-bodipyss **76a-76d**, and calculated energy levels.

	Energy [eV]	Wavelength [nm]	Oscillator strength	Principal orbital contributions	HOMO [eV]	LUMO [eV]
76a	3.73	331.84	0.70	H-3→L, H→L+1, H→L+2		
	2.01	615.11	0.73	H→L (91%)	-5.44	-3.48
76b	3.85	317.26	0.28	H→L+1, H→L+2		
	2.01	614.60	0.60	H→L (64%), H-1→L (4%)	-5.58	-3.53
76c	3.59	344.55	0.63	H-4→L, H→L+1, H→L+2		
	1.90	651.57	0.68	H→L (63%), H-1→L (2%)	-5.39	-3.53
76d	2.30	537.83	0.49	H-2→L (52%), H→L (22%)		
	2.05	604.28	0.32	H-2→L (36%), H→L (48%)	-5.71	-3.47

Calculation with B3LYP/6-31+g(d,p), H: HOMO, L: LUMO.

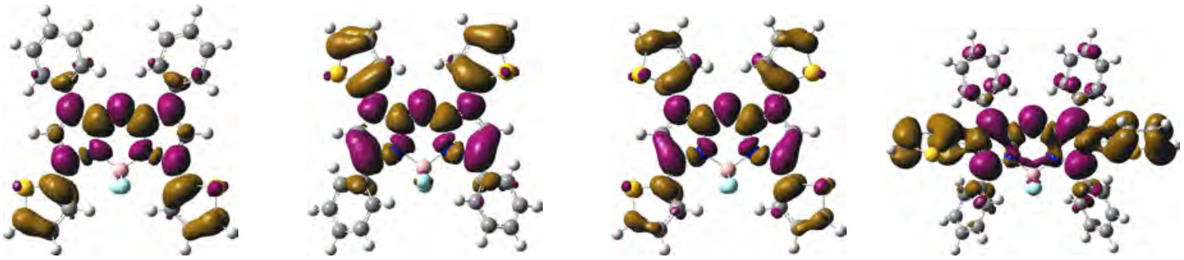

Figure 5.12: Difference density plots of the thienyl-aza-bodipys **76a**, **76b**, **76c**, and **76d** (from the left to the right) illustrate the charge transfer character from the thiophenes to the central core, of the first excited state. Purple regions display electron density accumulation, gold regions electron density depletion, upon excitation.

However, the predicted oscillator strengths for the absorption maxima reflect the measured trend of the extinction correctly. The DFT calculations revealed that the UV absorptions of the aza-bodipys **76a-76c** can be ascribed to transitions from the HOMO and some of the lower lying occupied levels (HOMO-1, HOMO-3, HOMO-4) to the LUMO and several higher lying unoccupied levels (LUMO+1, LUMO+2). In accordance with the experiment, no noteworthy oscillator strength in this spectral region was calculated for **76d**. The absorption maxima in the visible range of the compounds **76a-76c** are predominantly HOMO-LUMO transitions, although other excitations are involved to a minor extent, in case a thiophene unit is present in the 1,7-positions as it is the case for **76b** and **76c** (see Table 5.6). The experimentally observed bathochromic shifts in the series **76a-76c** are induced by the reduced HOMO-LUMO gap, as it was already suggested by the CV results. The star-shaped aza-bodipy **76d** offers a discrepancy compared to **76a-76c**. Here, two transitions with a HOMO-2→LUMO and HOMO→LUMO component, differing about 0.25 eV in energy, are responsible for the absorption maxima (see Table 5.6). Accordingly, the absorption band of **76d** follows from a superposition of these two excitations which leads to a broadening of the absorption band of the 2,6-dithienyl-aza-bodipy **76d**. In all calculated thiophene-functionalized aza-bodipys the excitation to the first excited state is accompanied by a charge transfer from the thiophene unit to the aza-bodipy core, as shown in Figure 5.12.

Attempts to prepare dimethylamino substituted thiophene aza-bodipys

Both thienyl-aza-bodipys and *p*-dimethylaminophenyl-aza-bodipys exhibit a bathochromic shift of the absorption maximum compared to the tetraphenyl-aza-bodipy, as discussed in the previous sections. In order to combine both effects and benefit from the electron donating character of both fragments, dimethylamino-thiophene-aza-bodipys **87** would be a promising material class.

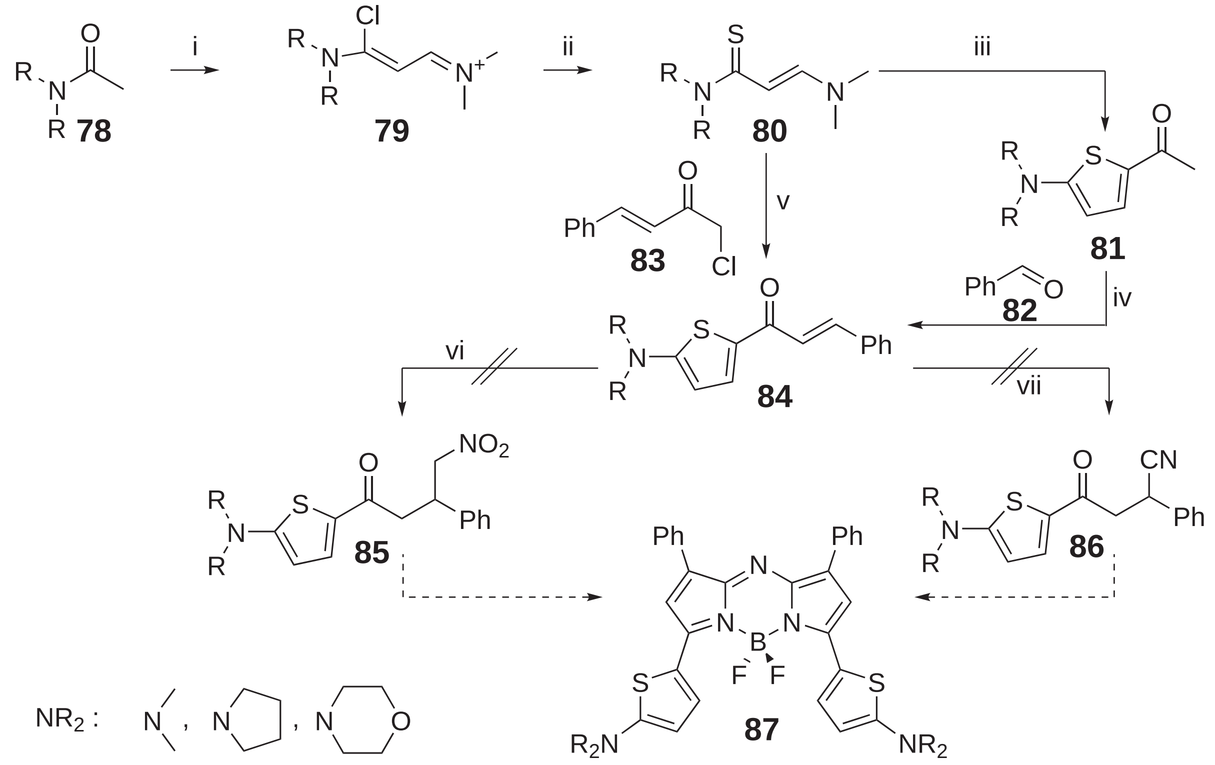

Scheme 5.6: Tested synthetic routes to aminothienyl-substituted azadipyrromethenes. Reagents and conditions: (i) DMF, $POCl_3$, $HClO_4$; (ii) Na_2S, H_2O, acetonitrile ; (iii) chloroaceton, NEt_3, acetonitrile; (iv) KOH, EtOH; (v) NEt_3, acetonitrile; (vi) NO_2CH_3, EtOH, K_2CO_3/pyrrolidin; (vii) NaCN/HOAc, Me_3SiCN/THF.

The synthesis strategy of these species follows the usual synthesis described in Figure 5.6, from the reaction of the γ-nitroketones with ammonium acetate. The corresponding Michael acceptor was synthesized via two different routes starting from 3-aminothioacrylamides **80**. The aminothiophene synthesis follows a route developed by Hartmann et al..[130, 131, 132, 133] The starting 3-aminothioacrylamides **70** can be easily obtained with sodiumsulfide from the 1-chlorovinamidinium salts **79**, which were synthesized from simple N-disubstituted acetamides **78**. In the first route, the Michael acceptor was obtained via an aldole condensation from benzaldehyde **82** and 5-dialkylamino-2-acetyl-thiophene, which was synthesized via a ring closing reaction from the 3-aminothioacrylamides with chloroacetone. The second route combines the reaction steps of the dialkylamino-thiophene synthesis and the aldole condensation. Chlorophenylbutenone (chloro-benzylideneacetone) **83** instead of chloroacetone was used. This turned out to be a improved route and accordingly, the yield to **84** could be increased. Unfortunately, all attempts to realize the Michael addition with nitromethane or cyanide failed under the applied conditions. Mass spectrometry did not show a mass corresponding to the desired product **75** and **76**. Consequently, the aminothiophene aza-bodipys **87** could not be synthesized via this strategy. One additional possibility might be in a previous synthesis of a bromo-thiophene aza-bodipy with a subsequent Buchwald-Hartwig amination, under the assumption of the stability of the azadipyrromethene under the strong basic butanolate conditions. Using the borondifluoride azadipyrromethenes, would lead to the fluoro substituted boronbutoxy compound.

6 Azadiisoindomethenes

The conformational restrictions in the aza-bodipy system, shown in the chemical introduction, strongly influenced the optical properties of these compounds.[32, 41, 42] Besides that, one may expect an impact of the rigidization as well as on the electrochemical and solid state packing properties. Especially, the benzannulated azadiisoindomethenes and the corresponding dibenzo-aza-bodipys seem to be promising in terms of applications for organic electronics due to the large planar and conjugated core. However, the synthetic pathways to the azadiisoindomethenes were not yet studied extensively. This chapter describes the synthesis of new azadiisoindomethenes, the respective dibenzo-aza-bodipys and metal complexes. The optical and electrochemical properties were studied experimentally as well as theoretically.

6.1 Borondifluoride azadiisoindomethenes

The more demanding synthesis to the benzannulated compounds **89** and **91** compared to **88** and **90** is one of the major disadvantages of these compounds and they are therefore little known.[34, 42] This is mainly due to the rather complicated preparation routes of isoindoles as precursors, their low stability under normal conditions, as well as their unusual reactivity towards usual dye-forming reagents.[134, 135, 136] Thus, by reaction of 1-phenyl-isoindole with nitrous acid an oxidative dimerization as well as a ring opening reaction of the starting material occurs, instead of the formation of the corresponding 3-nitroso derivative as intermediate for the azadiisoindomethene **91**.[135, 136] Nevertheless, a few azadiisoindomethenes **91** were prepared, but the applied preparation method suffers from very low yields.[34, 42] Hence, no larger series of azadiisoindomethenes **91** has been synthesized and investigated so far. The aim of the present study is to improve the synthetic route to these compounds and to explore their properties systematically. The reaction conditions were studied, and a series of azadiisoindomethenes with different substituents were prepared and the influence of the substitution pattern on the absorption properties investigated. Furthermore, the new compounds were studied in terms of their electrochemical characteristics. In addition to the experimental measurements, quantum chemical calculations with DFT were applied to gain deeper insights in the energetics and absorption spectra.

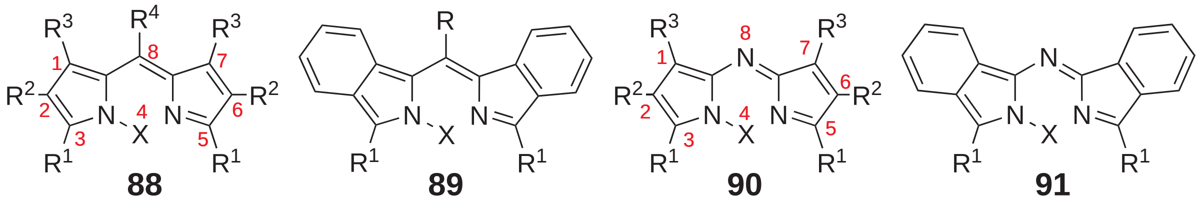

Scheme 6.1: Structures of bodipy **88**, aza-bodipy **90**, and the benzanullated diisoindomethene **99** and the here investigated dibenzo-aza-bodipy **101**. X can be H, BF_2 or other species.

6.1.1 Synthesis

The synthesis of azadiisoindomethenes reported in the literature either starts from phthalodinitrile **92** or from 2-cyanobenzophenone **98**.[34] In the first method, phthalodinitrile was reacted with aryl magnesium bromides. After steam distillation and recrystallization of the crude product **93** from pyridine the azadiisoindomethene **96** was isolated in low yields. In the second method, cyanobenzophenone **98**, available via a reaction developed by Knochel et al.,[137, 138] was refluxed with formamide, as it is known for other beta-keto-nitriles.[26, 33, 34] However, several unintended side reactions proceeded simultaneously during this reaction. As a result, the desired azadiisoindomethene **96** was isolated in poor yields, only.[34, 42] Since the addition of aryl Grignard reagents to phthalodinitrile **92** seems more variable with respect to the products, we studied the appropriate reaction conditions in more detail and prepared a series of new azadiisoindomethenes **96**. It was found that only one equivalent of an aryl magnesium bromide is required and that no water steam distillation is necessary to obtain **96**. The addition of an aryl Grignard to phthalodinitrile leads to intermediates **93** that can be transformed, via **94** and **95**, into the azadiisoindomethenes **96** by heating in formamide under reflux. In order to optimize the yield, the temperature, the solvent and the order of the Grignard addition were varied. The addition of the phenyl Grignard reagent (in diethyl ether) to phthalodinitrile in toluene at room temperature gave the product in 20 % yield, whereas the addition of phthalodinitrile, dissolved in THF, to the phenyl Grignard (in diethl ether) gave 17 % of the product.

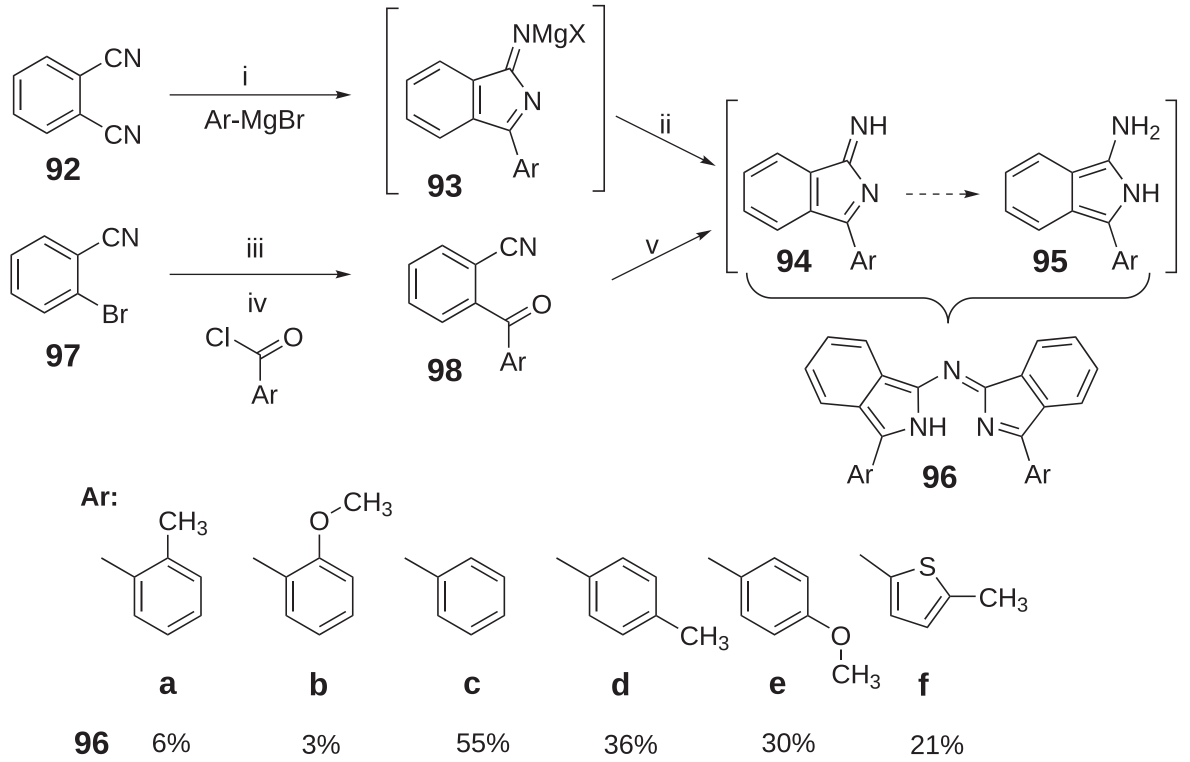

Scheme 6.2: Synthesis to the azadiisoindomethenes. Reagents and conditions: (i) Et_2O, -20 °C; (ii) formamide, reflux; (iii) *i*-PrMgCl·LiCl, THF; (iv) THF, -20 °C; (v) NH_4CO_2H, EtOH, reflux, or formamide, reflux.

Using THF as the only solvent for the Grignard and phthalodinitrile as well as increasing the temperature above room temperature or using two equivalents of phenyl Grignard reagents, as described in the literature [34, 42], drastically increased the amount of side products and rendered the workup of the reaction mixture difficult. The best results were received for the addition of phenyl Grignard to an ethereal suspension of phthalodinitrile at about -10 to -20 °C, although the stirring of the reaction mixture is difficult. For the methylthiophene derivative toluoene or a mixture with diethyl ether as solvent for phthalodinitrile gave better results due to less agglutination. Afterwards, the reaction mixture was quenched by addition of ammoniumchloride water solution or evaporated directly to dryness.

The obtained raw material, most likely the magnesium salt **93**, was reacted with formamide. It turned out that aqueous workup of the addition product has a positive effect on the reaction with formamide and the products appeared to be more pure. Due to the bad solubility of the addition product, even in DCM, this procedure was not used regularly. For the reaction of the intermediate product **93** with formamide, several temperatures were tested. The best results for this step were obtained by rapid heating of the precursor in formamide to reflux for a few minutes. Thereby, the color of the reaction mixture turned from a bright yellow over dark brown to deep blue and a dark solid began to precipitate. After cooling, the formed product was isolated from the reaction mixture by filtration. The yields and the side products varied strongly at this stage and the best yields were obtained for the phenyl Grignard reagent of about 55 %. The filtered product were washed extensively with a water/methanol mixture. In case of insoluble side products, the raw product was extracted with chloroform and subsequently purified by column chromatography. All azadiisoindomethenes **96a-96f** depicted in Scheme 6.2 were prepared according to this procedure and their structures were confirmed by the recorded analytical data.

Reaction Mechanism

Regarding the final product, the first step during the reaction is without doubt a nucleophilic addition of the Grignard reagent to the phthalodinitrile with a subsequent ring closing reaction yielding **93**. The 1-aryl-isoindolylimines **94** can be considered as the essential intermediates. In contrast, the subsequent steps responsible for the transformation of **94** to the azadiisoindomethenes **96** are rather ambiguous. Starting from this intermediate product **94**, a reduction step has to occur in order to obtain the final product **96**. Bredereck et al. already described a possible reaction mechanism, and postulated a reduction due to the second equivalent Grignard reagent used.[34] Since only one equivalent Grignard is used, this assumption cannot be proceeded here. Accordingly, only the formamide remains as a possible reducing agent, but no information about the detailed reaction mechanism to azadiisoindomethenes **96** via this route is known.

It can be postulated that the reaction of the 1-aryl-isoindoylimines **94** into the products **96** is initiated by a formamide mediated reduction, according to a Leuckart-Wallach type reaction, because no other reducing agent is present during this process.[139, 140] This leads either to 3-aryl-1H-isondol-1-ylamines **95a** or to 3-aryl-2,3-dihydro-isoindol-1-ylideneamines **95b** (see Scheme 6.3). Both of them can tautomerize to yield 3-aryl-2H-isoindol-1-ylamines **95**. The resulting 3-aryl-2H-isoindol-1-ylamine **95** can finally react with the starting 1-aryl-isoindoylimines **94** to the end product **96** via **99** and the loss of ammonia. In order to confirm the reaction mechanism displayed in Scheme 6.3, quantum chemical calculations on the B3LYP/6-31g(d) level of theory were performed, starting from **94** (Ar = Ph).[111]

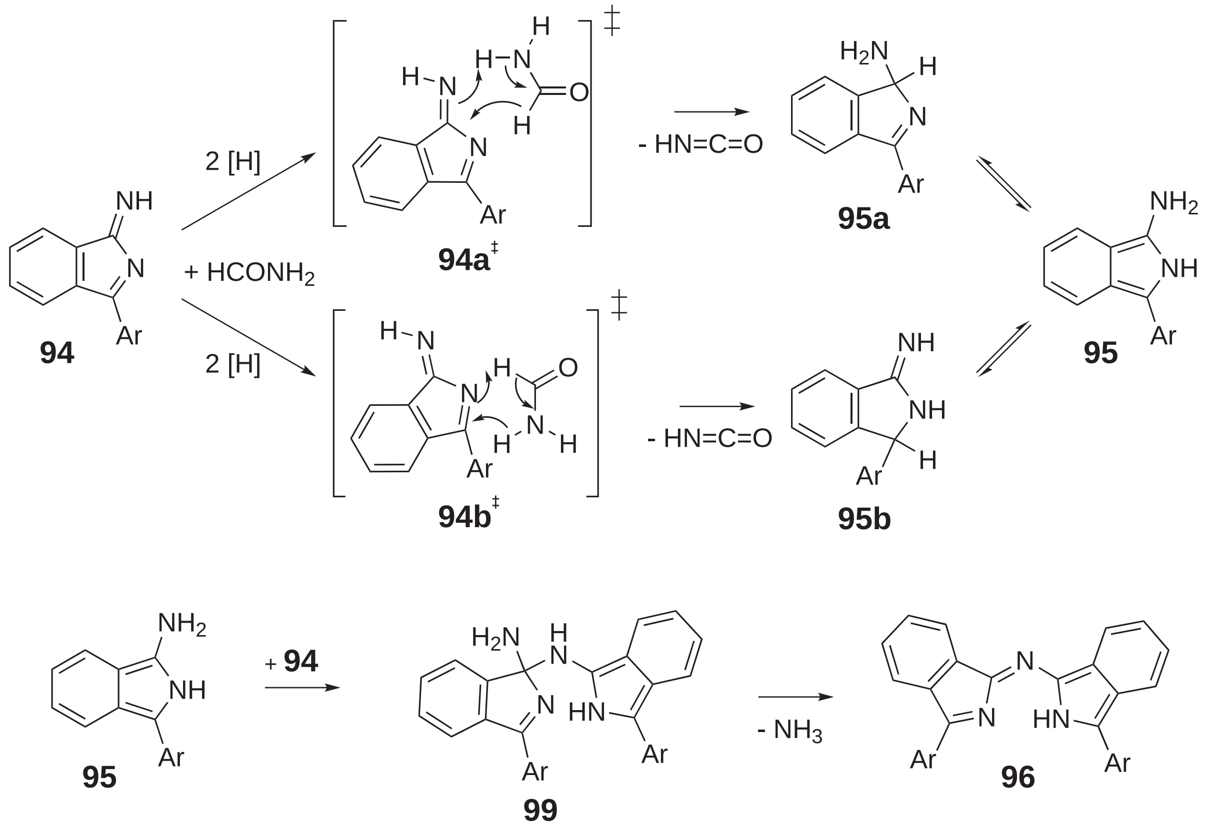

Scheme 6.3: Concerted reaction mechanism proposed: Formamide mediated Leuckart-Wallach-type reduction of **94** to the corresponding isoindoleamine **95** via two possible planar six-membered transition states, **94a** and **94b**, and the final condensation to **96**.

It was found, that the reduction of **94** by formamide can run alternatively via two planar six-membered transition states **94a** or **94b** and yields either the reduced species **95a** or **95a** besides isocyanic acid. Detailed information on the cartesian coordinates for the calculated transition states can be found in the literature.[141] The activation energies for this concerted mechanism is 211.5 $\mathrm{kJmol^{-1}}$ and 213.9 $\mathrm{kJmol^{-1}}$ for the 3,4- and the 1,2-addition, respectively, and are depicted in Scheme 6.3. The activation energy for a non-concerted mechanism is 784.18 $\mathrm{kJmol^{-1}}$ for the 3,4- and 936.07 $\mathrm{kJmol^{-1}}$ for the 1,2-addition and can therefore be considered as unfavored. The resulting amine **95** is stabilized compared to the starting imine **94**, but the complete reaction step is weakly endothermic (9.27 $\mathrm{kJmol^{-1}}$) due to the evolved isocyanic acid. As next step, we assume that the condensation of the amine **95** with the imine **94** yields the intermediate **99**.

This compound is finally transformed under the loss of ammonia into the product **96** in a highly exothermic reaction. The total Gibbs free energies for the stationary points of the proposed reaction mechanism, starting from the imine **94**, are plotted in Figure 6.1.

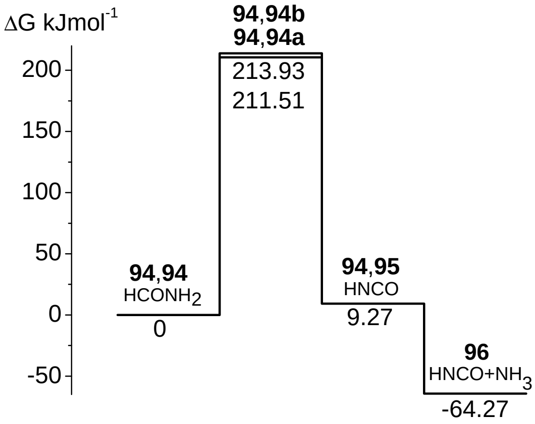

Figure 6.1: Quantum chemically calculated energetic pathway for the proposed reaction mechanism of two isoindoleimines **94** with formamide ($HCONH_2$) into the product **96** via the reduced isoindoleamine **95**. Structures are calculated for Ar = Ph (see Scheme 6.3) with B3LYP/6-31g(d).

Boron complexes of azadiisoindomethenes dyes

Subsequent reaction of the azadiisoindomethenes **106a-f** with boron trifluoride etherate in presence of diisopropylethylamine (DIPEA) gives rise to the formation of corresponding borondifluoride dibenzo-aza-bodipys **100a-f** in analogy to standard procedures reported in the literature (see Scheme 6.4).[28, 31]

The complexation of **100f** works best under ambient conditions and 50°C until no educt can be seen with TLC. The products **100a-f** were purified by column chromatography using dichloromethane or trichloromethane/hexane or trichlormethane as eluent and silica as absorbent. Besides the BF_2 compounds, a new straightforward synthetic pathway towards boroncatechol complexes was examined, which is shown in Scheme 6.4. In the literature described reaction to the boronalkoxy complexes, the BF_2 complex of the corresponding compound has to be synthesized in advance. In a next step, this BF_2 compound is reacted with a lewis acid ($AlCl_3$) and alcohols.[142] The reaction described here of butoxyphenyleneborate uses the azadiisoindomethenes directly, and avoids a second reaction step. Butoxyphenyleneborate is readily available from the reaction of brenzcatechol, boronacid, and n-butanol, heated in toluene in a Dean-Stark apparatus with subsequently distillation and can be stored in a refrigerator. The boroncatechol dibenzo-aza-bodipys **101c-e** was prepared by heating the azadiisoindomethenes **96c-e** with butoxyphenyleneborate in dichloroethane and DIPEA under reflux.

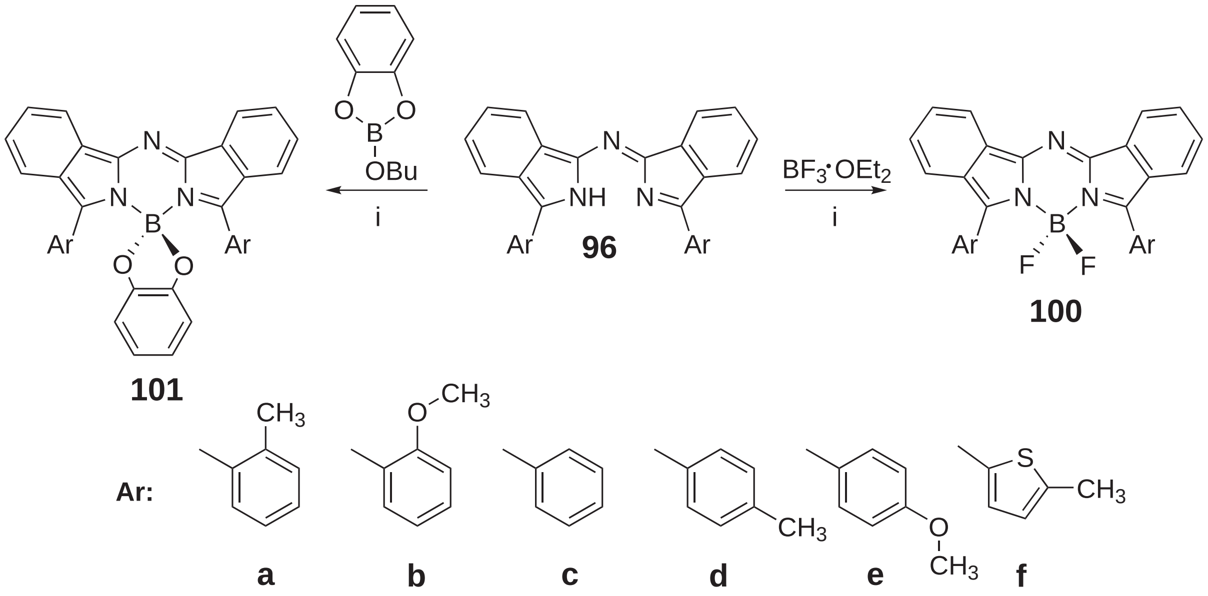

	a	b	c	d	e	f
100	56%	62%	78%	74%	65%	54%
101			25%	25%	26%	

Scheme 6.4: Complexation of the azadiisoindomethenes with boron pecies. Reagents and conditions: (i) $BF_3 \cdot OEt_2$, i-$PrNEt_2$, $CH_2Cl_2Et_2$, reflux.

From the purification of the complex with standard flash chromathography (DCM/hexane) the desired complex is obtained with a yield of 25%. Single crystals suitable for X-ray structural analysis were obtained from **100d** and **100f** and the determined molecular structure as well as the packing is shown in Figure 6.2. The crystal data and structure refinement details are summarized in the appendix. In both structures, the B atom exhibits a distorted tetrahedral environment. The bond angles are 105.7(1) for N-B-N and 111.6(4) for F-B-F in **100d** and 106.8(4), 110.8 (3) for **100f**, respectively. The average B-N bond lengths are 1.56(5) Å for **100d** and 1.55(5) Å for **100f**, and comparable to the bond lengths observed in other aza-bodipys.[114] In **100d**, the boron atom is displaced from the mean plane of the central six-membered bora-triazine moiety by 0.28(0) Å, while in **100f** the displacement is decreased to 0.09(9) Å. The central bora-triazine ring is not coplanar oriented with respect to the adjacent isoindole fragments. A large deviation is measured for **100d** with 7.1° and 10.3°, whereas in **100f** the deviation is only 0.7° for both isoindole fragments. The bis-isoindole plane in compound **100d** is strongly bent in contrast to **100f** which can be regarded as planar. The average dihedral angle between the isoindole moiety and the (het)aryl-ring is with 45.5° significantly larger for the tolyl-derivative **100d** compared to the 27.6° for the 5-methyl-thiophene compound **100f**.

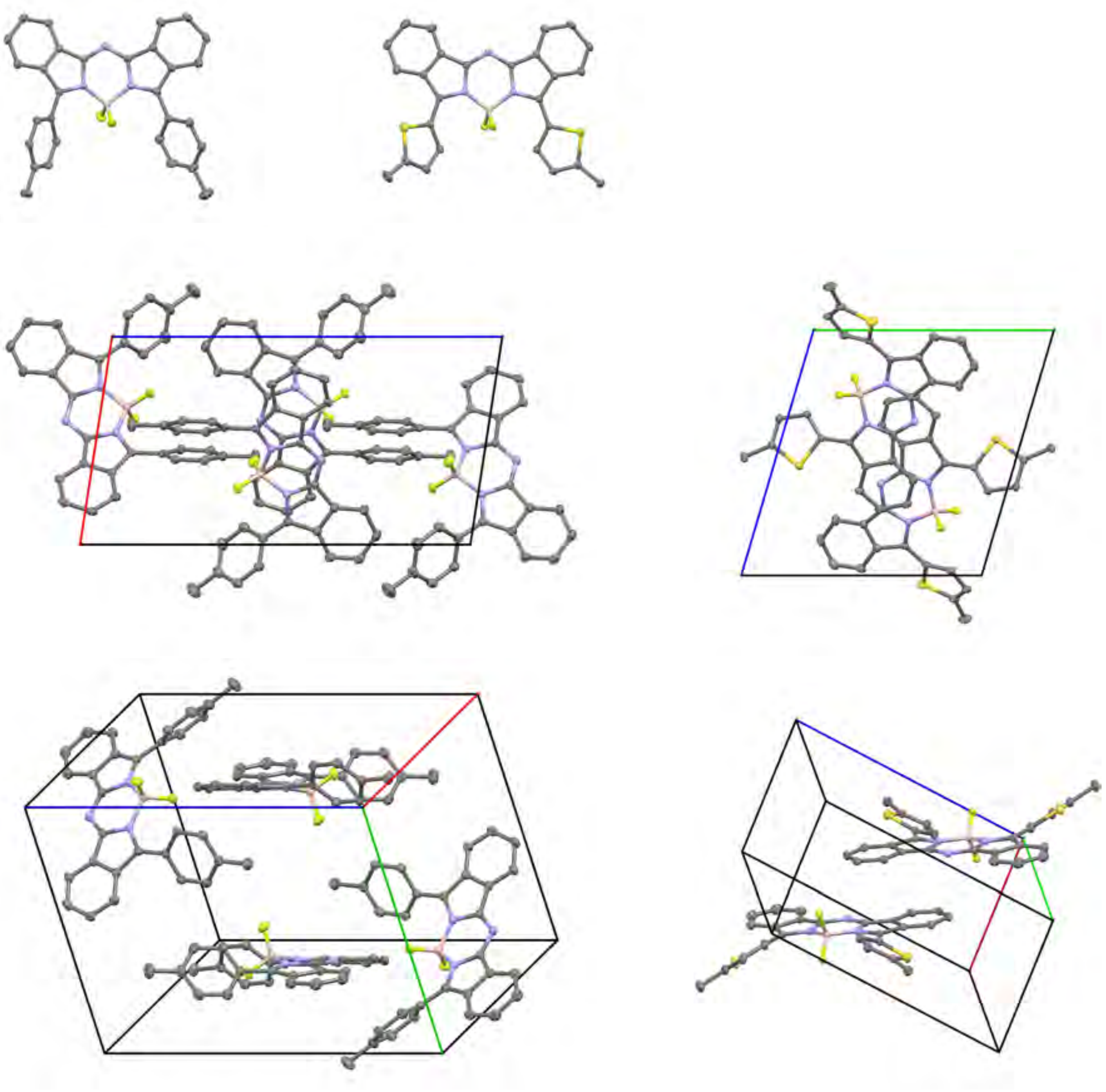

Figure 6.2: Crystal structures for **100d** (left) and **100f** (right). Top: Molecular structure; Middle and bottom: Solid state packing of the molecules and orientation in the unit cell.

6.1.2 Physical Properties

Spectroscopic characteristics

The spectroscopic characteristics of the azadiisoindomethenes **96a-f** and the boron complexes **100a-f** and **101c-e** were recorded in DCM and the spectra are displayed in Figure 6.3. The corresponding spectroscopic data are summarized in Table 6.1. The dibenzo-aza-bodipys **100a-f** demonstrate outstanding absorption characteristics with intense bands in the visible and NIR region.

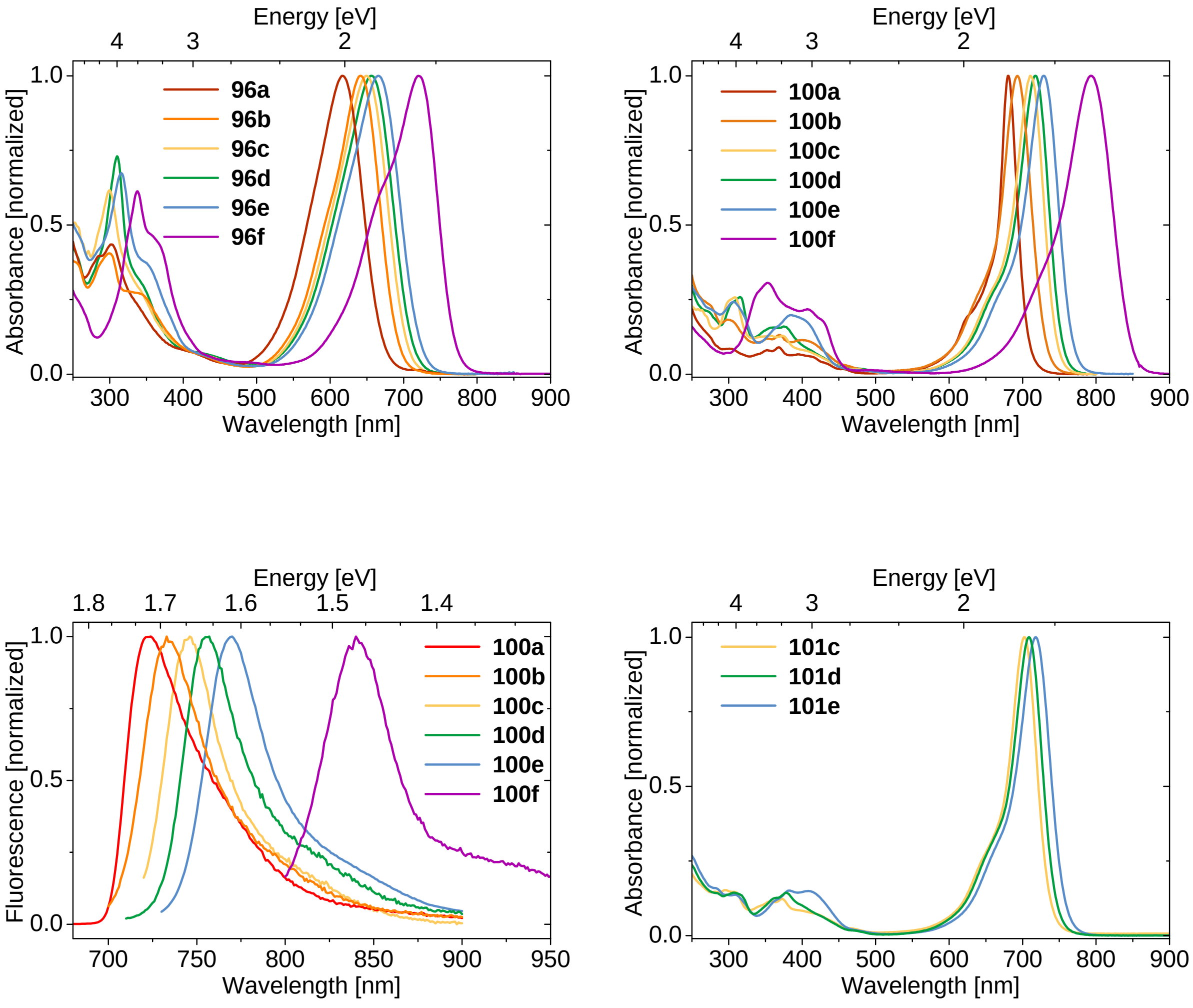

Figure 6.3: Spectroscopic characteristics. Upper left: Absorption spectra of the azadiisoindomethenes **96**. Upper right: Absorption spectra of the BF_2 dibenzo-aza-bodipys **100**. Lower Left: Fluorescence spectra of the BF_2 dibenzo-aza-bodipys **100**. Lower Right: Absorption spectra of the boroncatechol dibenzo-aza-bodipys **101**.

The shortest wavelength absorption was found at 681 nm for the *o*-tolyl compound **100a**, whereas the longest wavelength absorption was recorded for the bis(5-methyl-2-thienyl)dibenzo-aza-bodipy **100f** which absorbs at 793 nm. The fluorescence of the dibenzo-aza-bodipys **100a-f** is in the range between 723 nm for the *o*-tolyl compound **100a** and 841 nm for the 5-methyl-2-thienyl species **100f**, clearly showing an emission in the NIR. The Stokes-shift is between 33 nm for **100c** and 48 nm for **100a-f**. The extinction coefficients for the absorption maxima in the visible range are strongly increased in the dibenzo-aza-bodipys **100a-f** (79,000-106,000 $\mathrm{Lmol^{-1}cm^{-1}}$) compared to the azadiisoindomethenes **96a-96f** (41,000-60,000 $\mathrm{Lmol^{-1}cm^{-1}}$). In contrast, the extinction coefficients of the UV absorption for the dibenzo-aza-bodipys **100a-100f** (10,000-29,000 $\mathrm{Lmol^{-1}cm^{-1}}$) are decreased in comparison to the ones of the compounds **96a-96f** (21,000-43,000 $\mathrm{Lmol^{-1}cm^{-1}}$). Again, the bis-(*o*-phenyl) compounds **96a**, **96b**, **100a**, and **100b** showed the weakest absorbance, both for the absorptions in the UV and in the visible range. The bis-(*p*-aryl)-substituted compounds **96d-96f** and **100d-100f** exhibited higher extinction coefficients in total. The highest extinction coefficient was observed for the unsubstituted parent compound

Table 6.1: Absorption data of the azadiisoindomethenes **96a-f**, **100a-f** and **101c-d** in DCM.

	$\lambda_{\mathrm{UV}}^{[a]}$ [nm]	$\epsilon^{[a]}$ [$\mathrm{Lmol^{-1}cm^{-1}}$]	$\lambda_{\mathrm{max}}^{[b]}$ [nm]	$\epsilon^{[b]}$ [$\mathrm{Lmol^{-1}cm^{-1}}$]	$\lambda_{\mathrm{flu}}{}^{[c]}$ [nm]
96a	300	21000	615	41000	-
96b	298	20000	640	47000	-
96c	299	34000	653	56000	-
96d	311	43000	657	55000	-
96e	317	40000	668	60000	-
96f	336	24000	720	40000	-
100a	302	10000	681	79000	723 (42)
100b	300	15000	693	85000	734 (41)
100c	305	28000	715	106000	748 (33)
100d	314	27000	718	94000	758 (40)
100e	305	26000	729	91000	769 (40)
100f	336	29000	793	95000	841 (48)
101c	292	14000	703	90000	-
101d	307	13500	709	94000	-
101e	306	15000	718	90500	-

[a] Extinction of the UV band; [b] Extinction of the absorption maximum; [c] Stokes-shift is specified in brackets.

100c with a value of 106,000 Lmol^{-1}cm^{-1}. Comparing the absorption spectra of **96a-f** and **100a-f** altogether, the notable features in the spectra of **100a-f** are at first, the bathochromically shifted absorption maximum and secondly the weakened absorption in the UV region. The bathochromic shift is characteristic for the complexation with boron trifluoride and originates from the stabilization effect of the energy levels, especially of the LUMO levels (see below). The weakened absorbance in the UV results in a transparent window over the visible spectral range and qualifies the dibenzo-aza-bodipys **100a-f** as candidates for NIR absorption applications. In comparison to the (non-benzannulated) aza-bodipy dyes, the bathochromic shift as a result of the benzannulation is between 50 nm for the *p*-methoxy-phenyl species **100e** and 65 nm for the phenyl compound **100c**.[8] The bathochromic shift of the boroncatechol compounds **101c-e** compared to the dipyrromethenes **96c-e** is about 50 nm, slightly less than of the BF_2 complexes **100c-100e**. The shape of the absorption spectra of **101** is well comparable to the one of **100**, in combination with a similar high extinction coefficient. It can be concluded, that the F atoms have only a minor influence on the absorption characteristics. However, differences can be found in the 10 nm hypsochromically shifted absorption maximum and the surprisingly weak absorbance in the UV for the catechol complex, less than for the BF_2 complexes. The extinction coefficients range from 90000 to 95000 M^{-1}cm^{-2} and are much higher than those of the azadiisoindoemethenes **96**, but slightly smaller than the dibenzo-aza-bodipys **100**.

Electrochemical Characterization

Both series **96a-f** and **100a-f** were examined by CV, to obtain the corresponding oxidation and reduction potentials. The measurements were done in DCM, using an Ag/AgCl reference electrode with the Fc/Fc^{+} couple as internal redox standard. All dyes, except **96b**, exhibit complete reversible one electron redox potentials for oxidation and reduction, as displayed in Figure 6.4. The bis-(5-methyl-2-thienyl)-substituted compounds **96f** and **100f** exhibit two reversible oxidation waves which indicate the formation of stable dications. Two reversible oxidation waves and a second reduction wave were observed for the bis-(*p*-methoxyphenyl)dibenzo-aza-bodipy **100e** indicating the formation of stable dianions and stable dications. Second redox waves similar to **100e** have already been observed for another *p*-methoxyphenyl-bodipy.[143] Within each series, the *o*-methyl substituted compounds **96a** and **100a** displayed the highest and the thiophene-substituted compounds **96f** and **100f** the lowest oxidation potential. The higher potential for the bis-(*ortho*-phenyl)-substituted azamethenes **96a,b** and **100a,b** in comparison to the bis-(*para*-phenyl)-substituted compounds **96d,e** and **100d,e** can be explained by conformational differences in the dihedral angles between the corresponding aryl rings and the rigid bis-isoindole units. By using the half wave oxidation and reduction potentials of the compounds **96a-f** and **100a-f** the HOMO and LUMO energies have been calculated with the potential of Fc/Fc$^+$ as reference energy of E_{HOMO} = -4.78 eV.[119] All obtained potentials and calculated frontier orbital energies are listed in Table 6.2 and displayed in Figure 6.5.

Table 6.2: Electrochemical data of the azadiisoindomethenes **96a-f**, and the dibenzo-aza-bodipys **100a-f** and **101c-d** in DCM.

	$E_{ox}^{[a]}$ [V]	$E_{red}^{[a]}$ [V]	HOMO[b] [eV]	LUMO[b] [eV]	E_{gap}[c] [eV]
96a	0.21	-1.52	-4.99	-3.26	1.73
96b	0.06	-1.56	-4.84	-3.22	1.62
96c	0.19	-1.40	-4.97	-3.38	1.59
96d	0.11	-1.48	-4.89	-3.30	1.59
96e	0.08	-1.47	-4.86	-3.31	1.55
96f	0.00	-1.43	-4.78	-3.35	1.43
100a	0.50	-1.18	-5.28	-3.60	1.68
100b	0.42	-1.18	-5.20	-3.60	1.60
100c	0.44	-1.13	-5.22	-3.65	1.57
100d	0.38	-1.15	-5.16	-3.63	1.53
100e	0.31	-1.18	-5.09	-3.60	1.49
100f	0.18	-1.08	-4.96	-3.70	1.26
101c	0.41	-1.18	-5.19	-3.60	1.59
101d	0.36	-1.19	-5.14	-3.59	1.56
101e	0.30	-1.22	-5.08	-3.56	1.52

[a] First oxidation and reduction potentials vs. Fc/Fc$^+$, in CH_2Cl_2, Bu_4PF_6 (0.1 M), scan rate 100 mVs^{-1}. [b] $E_{HOMO}(Fc)$ = -4.78 eV, E_{HOMO}=-4.78+(E_{ox}(Fc)-E_{ox}), E_{LUMO}=-4.78+(E_{ox}(Fc)-E_{red}). [c] HOMO-LUMO difference as obtained from CV.

The energetic stabilization caused by the BF_2-complexation is slightly more pronounced for the LUMO energies than for the HOMO energies, as can be seen by calculation of the **96**(HOMO)-**100**(HOMO) and **96**(LUMO)-**100**(LUMO) differences for the **a-f** series, respectively, derived from the CV measurements. Consequently, the HOMO-LUMO gap for the boron complexes **100a-f** is smaller than for the azadiisoindomethenes **96a-f** which is in accordance with the trend of the optical absorption measurements. However, the small difference between the electrical gaps of **96a-f** and **100a-f** cannot completely explain the large bathochromic shift observed in

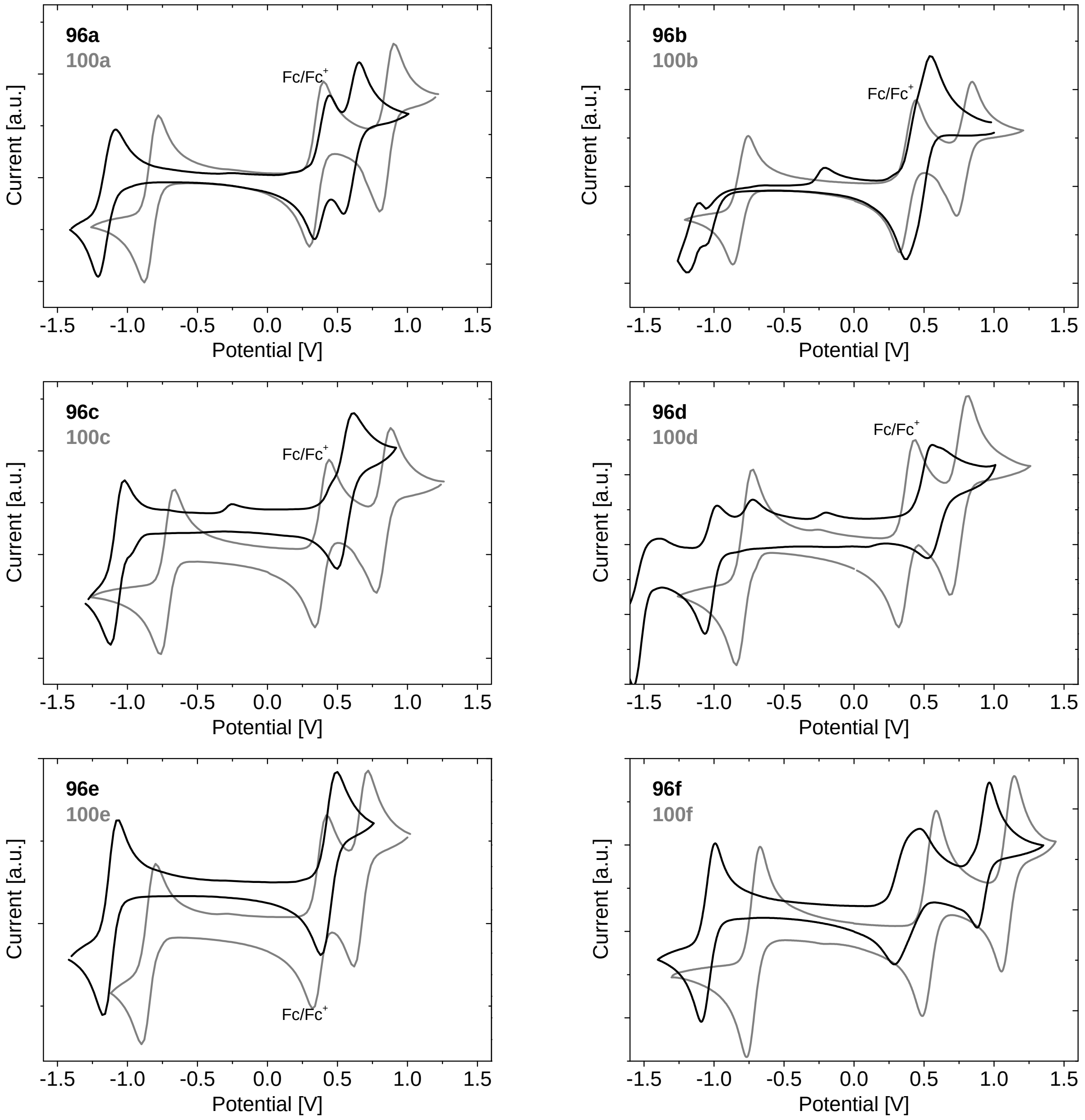

Figure 6.4: Cyclic voltammetry scans of the azadiisoindoemethenes **96a-f** (dark gray) and **100a-f** (light gray) in DCM against Ag/Ag$^+$. The ferrocene redox wave is indicated for **100a-e**. **100f** shows two oxidation waves.

the optical spectra. It is worth mentioning that the LUMO energies of the compounds **100a-f** show a narrow energetic spreading of only 0.1 eV whereas the HOMO energies are distributed within a range of approximately 0.3 eV. This leads to the conclusion that the substitution pattern in compounds **100** has a larger influence on the HOMO energies than on the LUMO energies and enables a specific HOMO tuning accompanied by the control of the electrical and optical band gap.

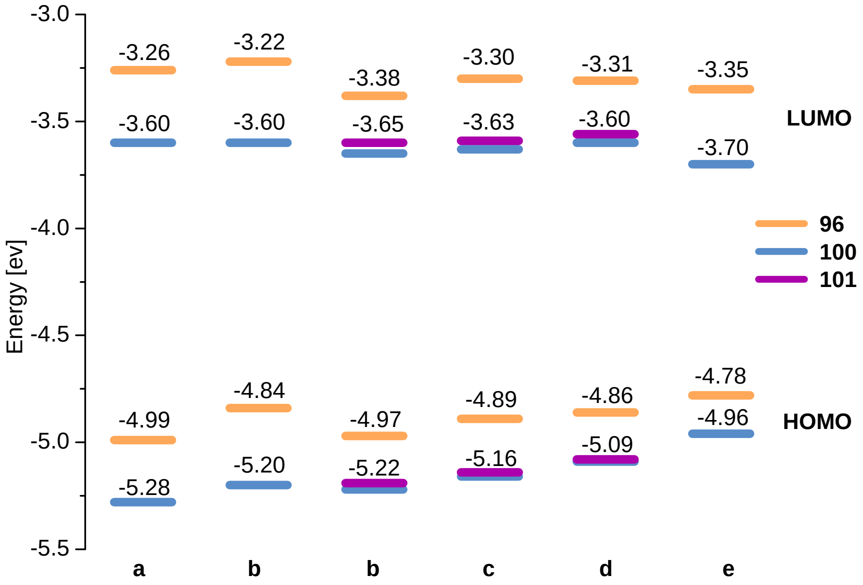

Figure 6.5: HOMO and LUMO energy values for the azadiisoindomethenes **96a-f**, **100a-f** and **101c-e**, derived from the CV measurements.

The boroncatechol complex **101** displayed a reversible wave for one-electron oxidation and for one-electron reduction. As expected, the oxidation is shifted about 260 mV to higher potentials with respect to the ligand, due to the stabilizing character of the boron complex. Accordingly, the reduction is more facile by 230 mV. Compared to the corresponding BF_2 complexes, the redox waves are slightly shifted to lower potentials by 60 mV for the reduction and 20 mV for the oxidation. Thus, the stabilizing effect is marginally larger for the borondifluorid compared to the boroncatechol compounds. The electrochemical behavior and the determined HOMO-LUMO gaps are in good accordance with the observed absorption spectra of these species. All data are summarized in Table 6.2.

Quantum Chemical Calculations

The frontier orbital energies, the energies of the absorption bands, as well as the orbitals involved in the absorption process were calculated by means of DFT and compared to the measured results of **96** and **100**.[111] The calculated HOMO energies agree well with the energies obtained from CV measurements with a maximum difference of only 0.01 eV to 0.15 eV. The largest deviation was found for the bis-(ortho-anisyl)-substituted compound **96b** and for the bis-(para-anisyl)-substituted compounds **96** with differences up to 0.15 eV and 0.13 eV, respectively. The LUMO energy differences with respect to the experiments are higher on the order of 0.45 to 0.68 eV. This can partly be explained by the fact that the calculations were performed in gas phase, which might be improved slightly by applying an appropriate solvation model. However, it is known to be a challenge for DFT in general to predict virtual orbital energies accurately.[99, 98]

Table 6.3: Calculated energy, oscillator strength, and principal orbital contribution of the azadiisoindomethenes **96a-f** and the dibenzo-aza-bodipys **100a-f**.

	Wave length[a,b]	Oscillator strength[b]	Principal orbital contributions[b]	Wave length[a,c]	Oscillator strength[c]	Principal orbital contributions[c]
96a	371.1	0.051	H-2→L, H-1→L	568.8	0.752	H→L
96b	383.5	0.044	H-4→L, H-3→L H-2→L, H→L+1	583.7	0.730	H→L
96c	382.0	0.084	H-1→L, H→L+1	582.9	0.775	H→L
96d	384.2	0.071	H-3→L, H-2→L H→L+1	588.0	0.798	H→L
96e	384.2	0.053	H-2→L, H-1→L H→L+1	593.5	0.839	H→L
96f	405.7	0.082	H-2→L, H-1→L H→L+1	643.7	0.774	H→L
100a	405.4	0.007	H-2→L, H-1→L	561.2	0.720	H→L
100b	446.3	0.028	H-1→L	585.4	0.733	H→L
100c	382.0	0.037	H-1→L, H→L+2	599.0	0.742	H→L
100d	381.4	0.031	H-3→L, H-2→L H→L+3	606.7	0.762	H→L
100e	404.2	0.001	H-1→L	619.0	0.790	H→L
100f	398.0	0.018	H-1→L, H→L+2	672.0	0.746	H→L

[a] Wavelength given in nm; [b] $S_0 \rightarrow S_2$ transition and [c] the $S_0 \rightarrow S_1$ transition respectively, calculated with TDDFT B3LYP/6-31+g(d,p); H = HOMO, L = LUMO.

Again, the bis-(*o*-anisyl)-azadiisoindomethenes **96b** and **100b** exhibit the largest deviations. All calculated energy values are summarized in Table 6.3. As the results of TDDFT calculations for absorption energies of organic dyes have shown to be clearly superior to those of semi-empirical INDO-CIS and PPP calculations,[129] this method was applied to calculate the transition energy for the compounds of the series **96a-f** and **100a-f**. It was found that throughout both series **106** and **100**, the absorption maxima are related to intense HOMO-LUMO transitions, whereas the absorptions in the UV can be attributed to transitions from the HOMO and some of the lower lying occupied levels (HOMO-1, HOMO-2, HOMO-3, HOMO-4) into the LUMO and higher lying unoccupied levels (LUMO+1, LUMO+2, LUMO+3). The calculated oscillator strengths for the $S_0 \rightarrow S_1$ transitions are in the same range for **96a-f** and **100a-f**. The oscillator strengths for the high energy absorption $S_0 \rightarrow S_2$ were significantly smaller for **100a-f** than for **96a-f**, reflecting the decrease in the measured extinction in this region. The energies of the absorption maxima were predicted more accurately with respect to the experimental value for **96a-f** with a tolerance in the range from 0.22 eV for **96e** to 0.16 eV for **96a**. The results for **100a-f** gave larger deviations with the best prediction in case of **100f**. The bathochromic shift originated by complexation was fairly underestimated within this approach and, surprisingly, this trend was turned around for the compounds **96a** and **100a**. From the analysis of the DFT optimized molecular geometries, it can be traced that the dihedral angle between the aryl moiety and the isoindole fragment correlates with the absorption wavelength. It is known from literature that a planarization of the aryl rings in the aza-bodipy system lead to a strong bathochromic shift.[32] The dihedral angle of the aryl ring in the series **100a-f** decreases continuously from 75° for the bis-(*o*-tolyl) compound **100a** to 31° for the bis-(5-methyl-thienyl)-substituted species **100f**, as this trend is also supported by the measured dihedral angles of the crystal structures of **100d** and **100f**. The corresponding absorption maxima are continuously red-shifted with decreasing dihedral angle. The large dihedral angle found for **100a** and **100b** might be the reason for the unusual hypsochromic shift of **100a** compared to the unsubstituted **100c**, even though **100a** and **100b** are substituted with electron donating groups.

The calculated difference densities for the first excited state of the dibenzo-aza-bodipys show significant differences compared to the aza-bodipys and is strongly dependent of the substitution pattern. In Figure 6.6 the difference density is exemplarily shown for the compounds **100c** and **100f**. It can be seen, that less charge density is shifted from the periphery to the central core, for **100c** compared to **63a**. This is also found for the other compounds **100a-e**. Only the thienyldibenzo-aza-bodipy shows a significant contribution of the thiophene moitey at the charge redistribution.

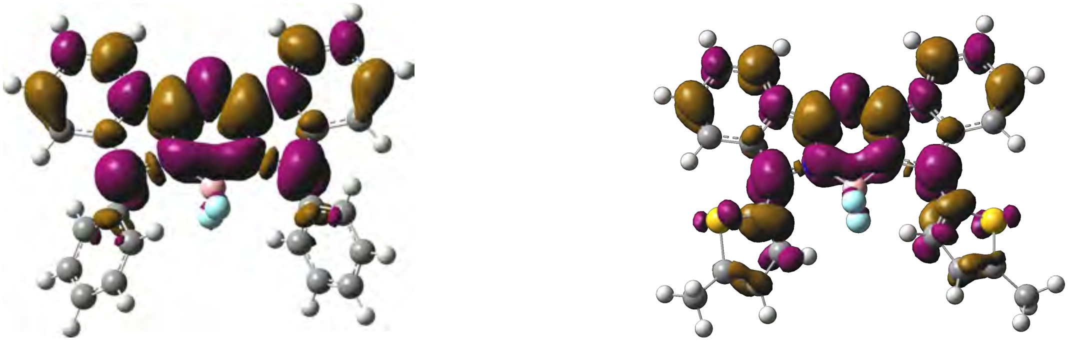

Figure 6.6: Difference density plot of the ground and the first (lowest) excited state. Left: bis(phenyl)dibenzo-aza-bodipy **100c**. Right: Bis(5-methylthiophen)dibenzo-aza-bodipy **100f**. Purple regions display electron density accumulation, gold regions electron density depletion, upon excitation.

This leads to the conclusion that the central acceptor in the dibenzo-aza-bodipy **100** is weakened compared to the aza-bodipy **63**, due to the benzannulation. Accordingly, the donor-acceptor character in the system is reduced. One effect of the reduced charge-transfer character is the less distinct bathochromic shift upon substitution with electron donating groups. The bathochromic shift from the phenyl **100c** to the *p*-methoxyphenyl dibenzo-aza-bodipy **100e** is only 14 nm. This is in contrast to the behavior of the corresponding aza-bodipys **63a** and **63b**, where the redshift is more than twice as large with 37 nm. The thienyl-dibenzo-aza-bodipy **100f** instead exhibits an extraordinary large bathochromic shift of 78 nm with respect to **100c**. In this case the CT character of the excitation is very strong as can be seen from Figure 6.6 on the right, which might be to some extent also due to the smaller dihedral angle in **100f** compared to **100c**.

Thermal properties

The TGA were carried out for the series **100a-f** and the unsubstituted **96c** as well as the boron-catechol complex **101c-e**. The measurement results are shown in Figure 6.7.

The TGA of some compounds showed a mass drift, with an increasing mass until 200°C. This can be considered as a systematic error due to the heating of the materials crucible. It was shown that the stability of the boron complexes is increased compared to the ligand as it is illustrated in Figure 6.7, right panel. However, the catechol complex does not lead to a further increase in thermal stability as it was the case for the bis(*p*-dimethylaminophenyl)aza-bodipy **70**, and accordingly the slope of the mass loss looks similar.

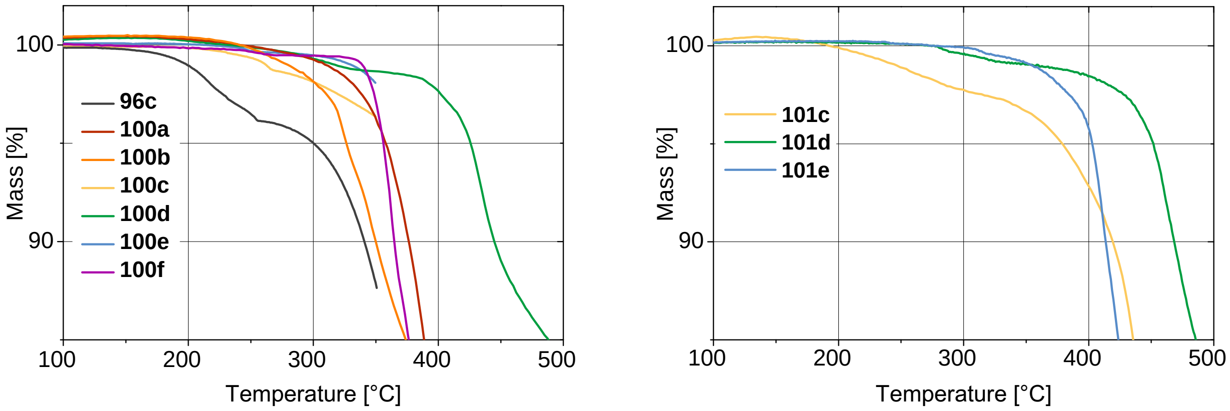

Figure 6.7: Thermogravimetric analysis. Right: Comparison of the thermal stability of the azadiisoindomethene ligand **96c** and all borondifluoride compounds **100a-f**. Left: Thermal stability of the boroncatechol complexes **101c-e**.

All dibenzo-aza-bodipys (shown in Figure 6.7, right panel) demonstrate a constant mass over 300°C and can be regarded as stable up to this temperature. The decomposition proceeds very abruptly and allows for an objective comparison of the thermal properties in this series. It can be concluded that substitution at the *para*-position of the phenyl ring (Me, MeO) **100d,e** leads to an increased thermal stability compared to the *ortho* substituted compounds **100a,b**. For the methyl substituted dibenzo-aza-bodipys, the decomposition takes place at around 400°C for the *p*-methyl **100d** and at around 320°C for the *o*-methyl species **100a**. The methoxy substituted compounds are less stable, but show the same trend for the thermal stability with the substitution pattern. Here, the *p*-methoxy compound **100e** decomposes beyond 350°C and the *o*-methoxy **100b** at around 300°C. The parent dibenzo-aza-bodipy **100c** is stable above 320°C but did not show a very rapid mass loss which hinders an clear interpretation. In the *p*-methyl-thiophene substituted dibenzo-aza-bodipy **100f**, the decomposition happens very abruptly at around 330°C. Overall, the dibenzo-aza-bodipys feature a good thermal stability and the compounds **100c-f** are evaporable in high vacuum (10^{-10} mbar) with moderate temperatures, in case the material is carefully cleaned.

6.2 Azadiisoindomethene metal-(II)-complexes

In case of the azadiisoindomethene ligand described in the previous section, only a Cu complex was synthesized, but no spectroscopic data were given.[34] In this section the synthesis and systematic characterization of five divalent transition metal derivatives of the bis(phenyl)azadiisoindomethene ligand with Co (cobalt), Ni (nickel), Cu (copper), Zn (zinc) and Hg (mercury) are studied. The spectroscopic and electrochemical properties of these metal complexes were investigated and compared to the ligand and the borondifluoride complex.

6.2.1 Synthesis

For the synthesis of the metal complexes **102**, corresponding metal-(II)-acetate salts were reacted with two equivalents of **96** in either *n*-butanol or THF as shown in Scheme 6.5.

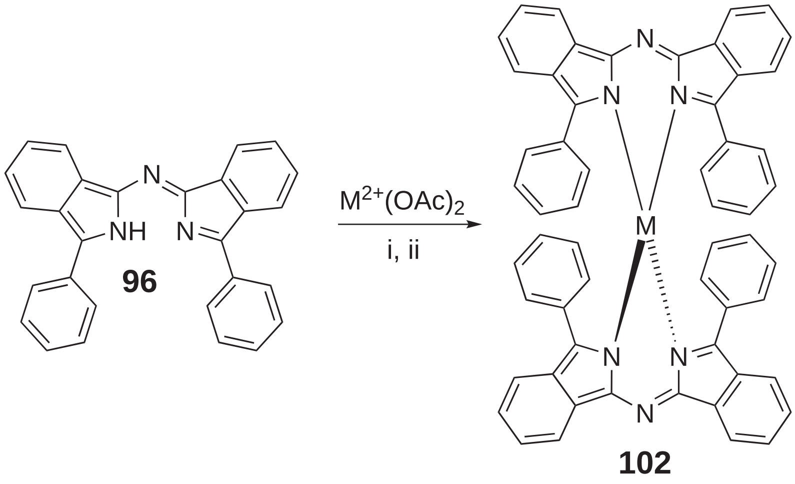

M=	Co	Ni	Cu	Zn	Hg
	38%	55%	66%	84%	53%
	a	**b**	**c**	**d**	**e**

Scheme 6.5: Synthesis of the metal complexes. Reagents and conditions: *i*-PrNEt$_2$, reflux in (i) BuOH (for a,b,d) or (ii) THF (for c,e) and the respective yields.

This preparation method leads to the appropriate bis-homoleptic complexes **102a-e** as crystalline solids in moderate to excellent yields, ranging from 38 % to 84 %. The Co, Ni, and Zn acetate salts were refluxed with **96c** in *n*-butanol, until no starting material could be assessed by thin layer chromathography (for **102a**, **102b**) or until the product precipitated (in case of the Zn complex **102d**). The Cu and Hg complexes **102c** and **102e** were synthesized by heating the acetate salts in THF solution with DIPEA for six hours up to four days. In all cases, the precipitated products were purified by recrystallization from dichloromethane/hexane solution, yielding pure crystalline complexes. The mass spectra of all prepared compounds **102a-e** evidently showed the formation of the bis-homoleptic metal complexes. As further characterization, ^{1}H-NMR spectra were recorded for all compounds except for the paramagnetic Co and Cu complex. The Zn and the Hg complexes gave spectra in the typical 0-10 ppm range. The ^{1}H-NMR spectrum of the Ni complex is of particular interest, as it displayed considerable positive and negative peak shifts between -2 to +40 ppm at room temperature (see experimental section). Similar ^{1}H-NMR characteristics were already described for a Ni bis-dipyrromethene and other Ni complexes.[36, 144, 145, 146] The distortion of the usually favored planar geometry to a pseudo-tetrahedral geometry due to the sterically demanding ligands in these complexes is presented in the literature as an explanation and can also be expected to be the reason for **102b**. Nickel complexes exhibiting a pseudo-tetrahedral geometry, have short electron-spin lifetimes and allow therefore to record well-resolved NMR spectra.[36]

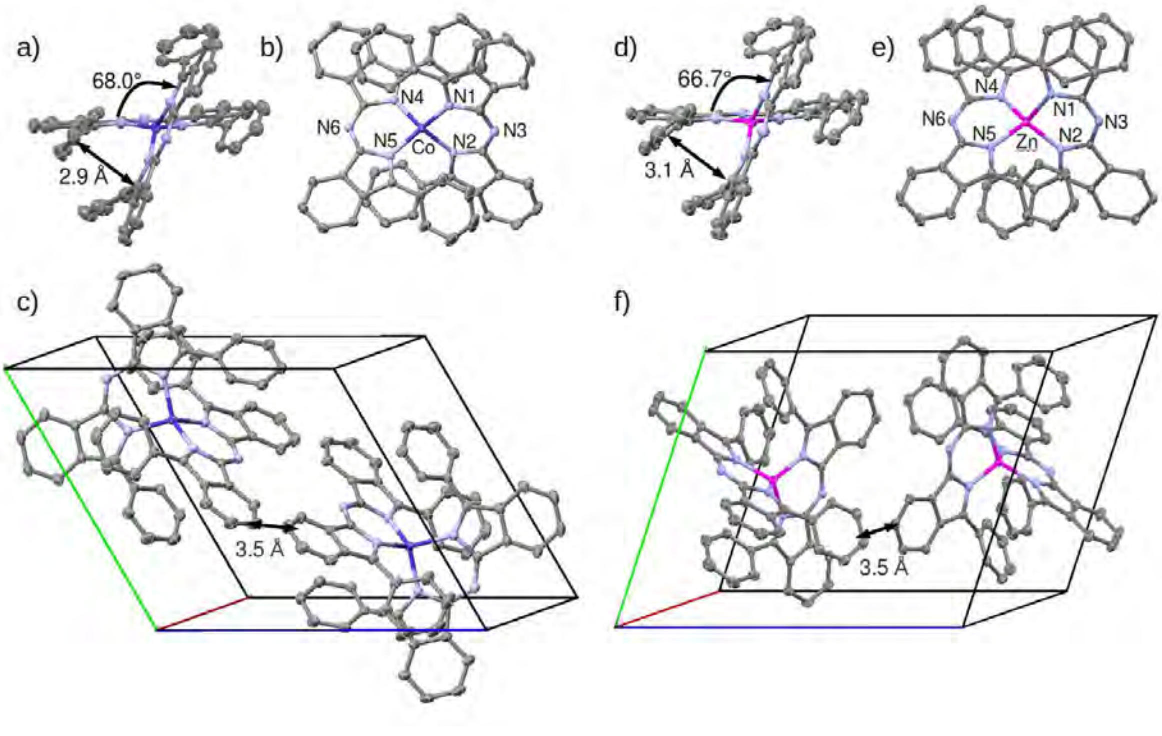

Figure 6.8: Single crystal structure of the Co complex a)-c) and the Zn complex d)-f). a) and d) pseudo tetrahedral conformation; b) and d) top view; c) and f) unit cell (solvent molecule truncated for reasons of clarity). H- atoms are truncated for reasons of clarity.

Single crystals of the Co and Zn complexes **102a** and **102d** were grown by slow evaporation of a chlorobenzene or toluene solution. Attempts to grow X-ray quality crystals for the other metal complexes, e.g. by slow vapor diffusion of pentane in a THF or chloroform solution, were not successful and resulted in too small crystals. Both, the Co complex **102a** and the Zn complex **102d** crystallize in the triclinic space group $P1$ with one solvent molecule in the unit cell (see Figure 6.8). The molecular structure of both bis-chelates **102a** and **102d** can be regarded as a pseudotetrahedral coordination geometry with the metal atom in the center. The corresponding angle between the isoindole planes are 68.0(6)° for the Co complex **102a** and 66.7(9)° for the Zn complex **102d**, which is significantly distorted from an ideal D_{2d} symmetry, as shown in Figure 6.8 a) and d). The metal-nitrogen bond lengths (M-N) range between 1.98(1) Å and 1.99(2) Å for the Co-complex **102a** and are 1.99(1) Å and 1.99(8) Å long for the Zn-complex **102d**. These bond lengths are similar to those found for comparable Zn(II) bis-dipyrromethene complexes, but significantly longer than for the corresponding borondifluoride complex, with the N-B-bond being 1.57(9) Å long.[42]

The nitrogen-metal-nitrogen (N-M-N) bite angle differs for each azadiisoindomethene ligand in both metal complexes. In the Co complex **102a**, the angle N1-Co-N2 is 95.15° and 93.94 for the N4-Co-N4 angle. In the Zn complex **102d**, the angle is 94.2(2)° for the N1-Zn-N2 and 95.3(4)° for the N4-Zn-N4. The bite angle in the metal complexes is significantly smaller compared to the corresponding borondifluoride complex with 105.7(3)°[42] and is consistent with the longer N-metal bond length. Additionally, the C-N3/N6-C angle is widened in the metal azadiisoindomethene bis-chelates in the range between 126.2(4)° and 128.0(4)° compared to 119.7(1)° in the borondifluoride complex.[42] The sterically induced ligand-ligand interactions between the phenyl ring of one ligand and the azadiisoindomethene plane of the opposite ligand is an interesting aspect, worth to discuss in more detail. In the Co complex **102a** the minimum distance of the phenyl ring to the opposite isoindole plane is 2.9(0) Å, with an angle of 23.2(2)° to the plane. In the Zn complex **102d** the distance is slightly increased to 3.09(4) Å but the angle is decreased to 20.8(8). This distance, of the phenyl ring to the isoindole plane in **102a** and **102d** is much shorter compared to non-benzannulated aza-bodipy Zn complexes, having a minimum distance of 3.6(2) Å.[37] By consequence, an intermolecular π-π-interaction can be considered to be present in these bis-chelate complexes. The interaction increases with an enlarging π-system. Accordingly, the distance of the phenyl ring plane to the opposite ligand is reduced in the dibenzo-aza-bodipys compared to the aza-bopdipys with their smaller, non-annulated π-system on the backbone.[37]

6.2.2 Physical Properties

In this section, the unique series of transition metal complexes of dibenzo-aza-bodipys is studied in terms of their optical and electrochemical as well as thermal properties, with respect to the central metal atom.

Spectroscopic characteristics

The UV-Vis absorption properties of all metal complexes **102a-e** were investigated and compared with respect to the free ligand **96c** and the borondifluoride complex **100c**. The spectroscopic data are shown in Figure 6.9 and are summarized in Table 6.4. All spectra of the ligand **106c** and the metal complexes **102a-e** exhibit an intense absorption band in the UV region, and the absorption maximum in the visible regime. In contrast to the spectrum of **100c**, the absorption maxima of the metal complexes **102a-e** display a broadening and the appearance of shoulders.

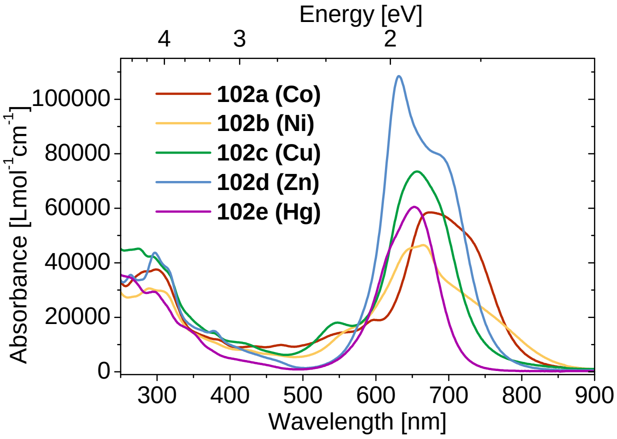

Figure 6.9: Absorption spectra of the azadiisoindomethene metal complexes in dichloromethane.

The absorption maxima of the metal complexes are in the range between 632 nm and 674 nm in DCM, depending on the metal (Table 6.4). The Co and Ni complexes **102a** and **102b** show a red-shifted absorption maximum by 24 nm compared to the ligand **96c**, and an absorption tail extending into the NIR region over 800 nm. The absorption maximum of the Cu complex **102c** is red-shifted by about 3 nm, with respect to the ligand, whereas the absorption maximum of the Hg complex **102e** is at the same wavelength. The Zn complex **102d** displays a hypsochromic shift of the maximum but exhibits an intense red-shifted shoulder at 685 nm, compared to **96c**.

All metal complexes **102a-e** feature in comparison to the maximum a strong absorbance in the UV part of the spectra around 300 nm as it is also the case for the free ligand. This is in contrast to the borondifluoride complex, where this absorbance in the UV is weakened compared to the maximum. The extinction coefficients of **102a-e** are in the range between 46,000-108,000 Lmol^{-1}cm^{-1} for the corresponding absorption maxima and therefore increased compared to the ligand **96c**, except of the Ni complex **102b** (see Table 6.4). While the absorbance of the Ni and Co complexes **102b** and **102a** is weak (with 46,500-58,500 Lmol^{-1}cm^{-1}) the extinction rises from the Hg over Cu to the Zn chelate **102b**, **102a** and **102d** from 60,000 over 73,000 up to 108,500 Lmol^{-1}cm^{-1}. This intense absorbance is comparable to the borondifluoride complex (as shown above) or even stronger in the case of the Zn complex **102d**. The Zn complex **102d** displays the strongest absorbance for this ligand system so far. All bisphenylazadiisoindomethene metal complexes **102a-e** are nonemissive and show no fluorescence, which is in contrast to the emissive borondifluoride compounds. Similar behavior was observed for comparable azadipyrromethene-zinc(II) and -mercury(II) complexes,[37] but these azadipyrromethenes offer four rotatable phenyl-rings. However, since the more rigidified compounds **102** do likewise not emit, the quenching is due to the heavy-atom effect, induced by the central transition metal ion.

Table 6.4: Absorption data of the azadiisoindomethene metal complexes, recorded in DCM.

	$\lambda_{\mathrm{UV}}^{[a]}$ [nm]	$\epsilon^{[a]}$ [Lmol^{-1}cm^{-1}]	$\lambda_{\mathrm{max}}^{[b]}$ [nm]	$\epsilon^{[b]}$ [Lmol^{-1}cm^{-1}]	$\lambda^{[c]}$ [nm]	$\epsilon^{[c]}$ [Lmol^{-1}cm^{-1}]
102a (Co)	298	37,500	674	58,500	725	50,500
102b (Ni)	288	27,000	674	46,500	645	35,500
102c (Cu)	290	38,000	656	73,500	-	-
102d (Zn)	297	43,000	632	108,500	685	80,500
102e (Hg)	260	24,000	653	60,500	626	49,500

[a] UV band, [b] absorption maximum and [c] the most pronounced shoulder of the absorption maxima.

Electrochemical Characterization

The electrochemical properties of all prepared metal complexes **102a-e** were examined with CV, to obtain the corresponding oxidation and reduction potentials. The results were compared to the potentials of the free ligand **96c** and the borondifluoride complex **100c**. The measurements were done in DCM, against the Ag/AgCl reference electrode with Fc/Fc^{+} as internal redox standard.[120]

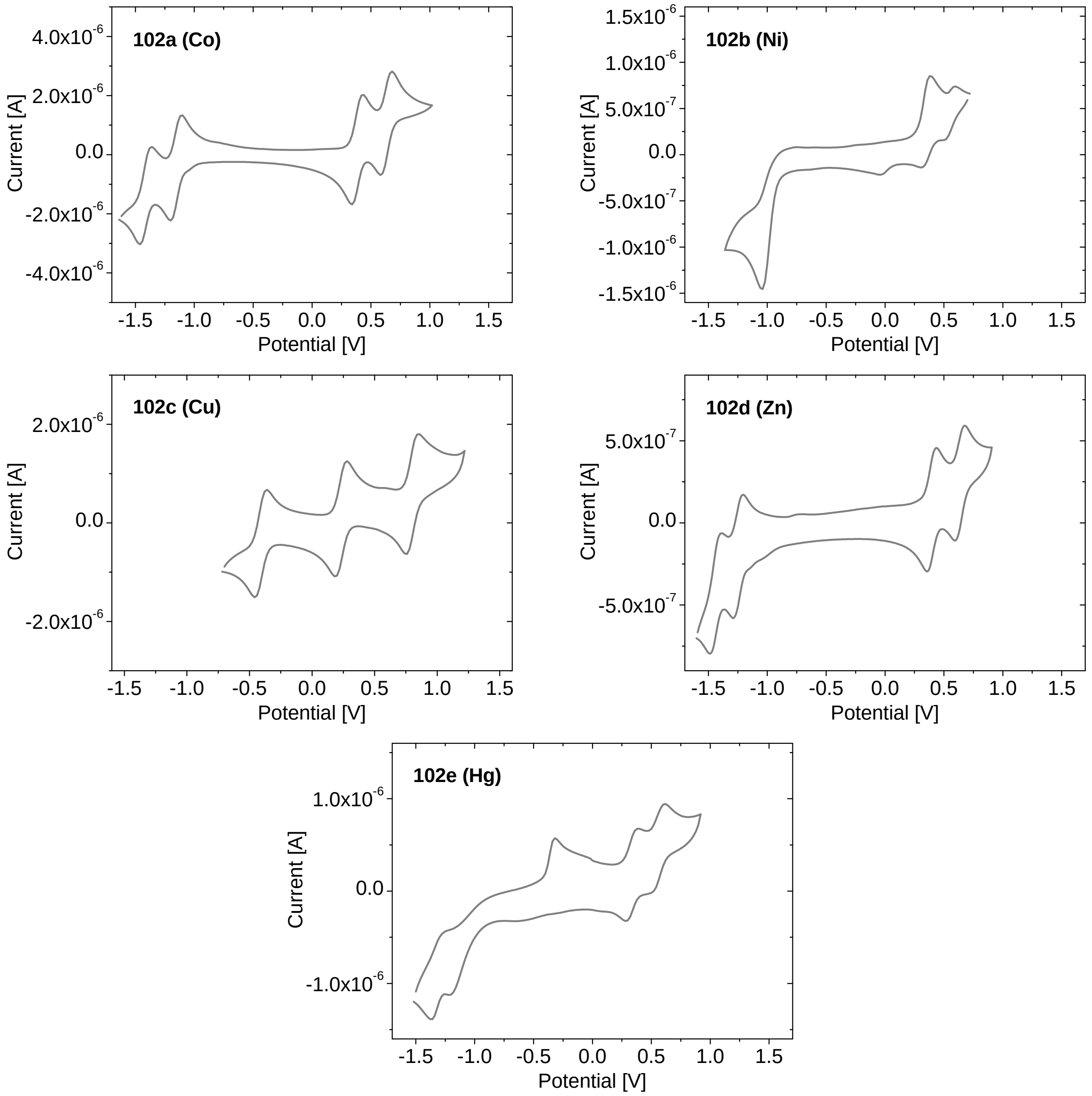

Figure 6.10: Cyclic voltammetry scans of the different bis(phenyl)azadiisoindomethene metal complexes.

The metal compounds exhibit a complex electrochemical behavior. All reversible redox states were only measured for the Co and Zn complexes **102a** and **102d**, with two reversible oxidation and reduction waves (see Figure 6.10) in each case. The Co complex displayed potentials at -1.52 V vs. Fc and at -1.78 V vs. Fc for the first and the second reduction, respectively. The oxidation waves were observed at 0.02 V and 0.26 V vs. Fc for the first and second oxidation wave respectively. The Zn complex **102d** showed the same redox potentials as the Co complex apart from the first reduction wave which was shifted by -100 mV to lower potentials. The complexes **102b** (Ni), **102c** (Cu) and **102e** (Hg) displayed only reversible one-electron oxidation waves, whereas the second oxidation and the one electron reduction (and two electron reduction for **102e** processes appeared to be irreversible. All measured cyclic voltammetry scans are shown in Figure 6.10 and the determined redox potentials are listed in Table 6.5. The one-electron reduction potentials of the Co, Ni, Cu, and Zn complexes **102a-102d** reflect the periodic trend of the electron affinity for the first row transition metal elements. According to this trend one would expect an increase of the electron affinity from Co to Ni to Cu, and a decrease for Zn. The experimental reduction in fact becomes more facile from the complexes **102a** (Co) to **102b** (Ni) by 0.16 V, to **102c** (Cu) by 0.74 V, and less favored for **102d** (Zn) by 0.10 V. This characteristic is also represented in the LUMO energies in the Figure 6.12.[147] The one-electron oxidation shows a trend in the CV measurement with a decreasing ionization potential from the complex **102a** (Co) to **102b** (Ni) by 0.03 V, to **102c** (Cu) by 0.16 V, and further increase in the potential for the complex **102d** (Zn) and **102e** (Hg) by 0.02 V. On one hand, this behavior is in contrast to the trend of the pure transition metals M(0), where a higher oxidation potential for Cu than

Table 6.5: Electrochemical data of the azadiisoindomethene metal complexes **102a-e**.

	E^2_{red} [a] [V]	E^1_{red} [a] [V]	E^1_{ox} [b] [V]	E^2_{ox} [b] [V]	HOMO[c] [eV]	LUMO[c] [eV]	E_{gap} [d] [eV]
102a (Co)	-1.78	-1.52	0.02	0.26	-4.80	-3.26	1.54
102b (Ni)	-	-0.81	-0.01	0.21	-4.77	-3.42	1.35
102c (Cu)	-	-0.76	-0.14	0.44	-4.64	-3.49	1.15
102d (Zn)	-1.78	-1.62	0.02	0.26	-4.80	-3.16	1.64
102e (Hg)	-1.59	-1.49	0.04	0.26	-4.82	-3.29	1.53

[a,b] First E^1 and second E^2 oxidation and reduction potentials vs. Fc/Fc$^+$, in CH_2Cl_2, Bu_4PF_6 (0.1 M), scan rate 100 mVs^{-1}. [c] E_{HOMO}(Fc) = -4.78 eV, E_{HOMO}=-4.78+(E_{ox}(Fc)-E^1_{ox}), E_{LUMO}=-4.78+(E_{ox}(Fc)-E^1_{red}). [d] HOMO-LUMO difference as obtained from CV.

for Co is expected, due to the higher ionization energy. One the other hand, this trend can be qualitatively understood with the simple Pearson concept of hard and soft Lewis acid and bases (HSAB).[148] In the HSAB concept, the hardness of transition metal ions M(II+) is decreasing (or the softness is increasing) in the periodic table by going from Co(II) via Ni(II) to Cu(II).[147]

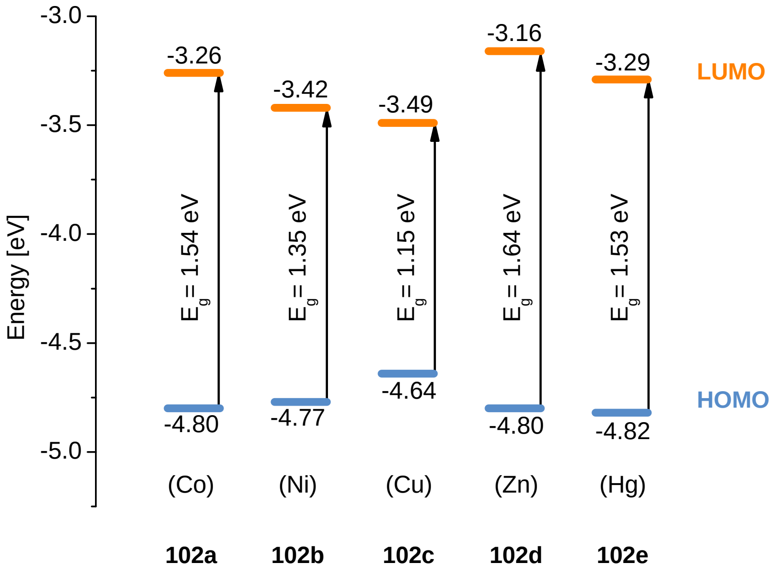

Figure 6.11: HOMO and LUMO energy values for the azadiisoindomethene metal complexes **102a-e**, derived from the CV measurements.

Consistently, the oxidation potentials of **102a-c** are continuously shifted towards lower potentials. The higher oxidation potential of the Zn and the Hg compound **102d** and **102e** can be considered to be due to the additional stability of the electronic configuration for a closed s-atomic orbital shell.[147] The electrical gaps of the metal complexes obtained from the CV measurements (see Figure 6.12) do not correlate with the observed absorption properties (see Figure 6.9). According to the electrochemical data, the Cu complex **102c** should have the most red-shifted absorption, assuming a pure HOMO-LUMO transition. However, this is neither the case for the absorption maximum nor for the red-shifted shoulder occurring in the spectrum. For this reason, the electrochemical measurements confirm that no pure HOMO-LUMO transitions takes place in the absorption process, as it was evaluated by quantum chemical calculations for the Zn complex **102d**.

Quantum chemical calculations

In order to study the absorption properties in more detail, the absorption spectrum of the Zn complex **102d**, regarded as a model system, was calculated with TDDFT.[111, 149] For this purpose, the crystal structure and the optimized geometry were taken into account to calculate the optical transitions up to the first ten excited states. Although the prediction of the absorption maximum deviated about 0.28 eV, the agreement with the observed spectra is good since both absorption features were predicted correctly. All absorption features in the azadiisoindomethene ligand system **96c** result from π-$\pi*$ transition, as it is shown in Table 6.3. The calculation of the absorption maximum in the visible regime for **96c** clearly showed the principal orbital contribution for this absorption to be a HOMO→LUMO transition. In the ligand, the next occupied levels lower in energy (HOMO-1, -6.35 eV) and the next unoccupied levels higher in energy (LUMO+1, -0.89 eV) differ significantly in energy compared to the HOMO (-4.67 eV) and LUMO (-2.54 eV) energy values. Consequently, optical transitions from these lower lying occupied orbitals to the LUMO or LUMO+1 are involved for the high energy absorption in the UV, in case of the ligand **96c** which is already depicted in Table 6.3. The calculations on the optimized structure of the Zn complex **102d** showed degenerated HOMO energies (-4.56 eV) and nearly similar LUMO and LUMO+1 energies (-2.47 eV and -2.36 eV). This energetic situation, which is different to **96c**, leads to several allowed optical transitions with absorption energies very close to each other, observed in the optical spectra as shoulders. The TDDFT calculations revealed, that the absorption maximum including the shoulder in the visible regime arises from two contributions. First, transitions from the HOMO→LUMO and HOMO-1→LUMO+1 lead to the most intense absorption. Second, the intense red-shifted shoulder arises due to transitions

Table 6.6: Energy, wavelength, oscillator strength, and principal orbital contribution of the azadiidoindomethenes zinc complex **102d**.

	Energy [eV]	Wavelength [nm]	Oscillator strength	Principal orbital contributions
102d*	2.14	577.16	0.552	H-1→L, H→L+1
	2.24	553.26	0.878	H→L, H-1→L+1
102d$^{\#}$	2.10	588.63	0.382	H-1→L, H→L+1
	2.29	540.12	0.878	H→L, H-1→L+1

Calculation with B3LYP/6-31g(d); (*)with the optimized Zn-complex structure **102d***; ($^{\#}$) and with the single crystal structure **102d**$^{\#}$. H = HOMO, L = LUMO.

from the HOMO-1 to LUMO and the HOMO to LUMO+1. The relative intensities of these transitions were predicted in agreement with the experiment, with a lower extinction for the red-shifted shoulder, in case of the Zn complex **102d**. For the high energy absorption in **102d**, detected in the UV, deeper lying orbitals are involved as for **96c** which are listed in detail in Table 6.6.

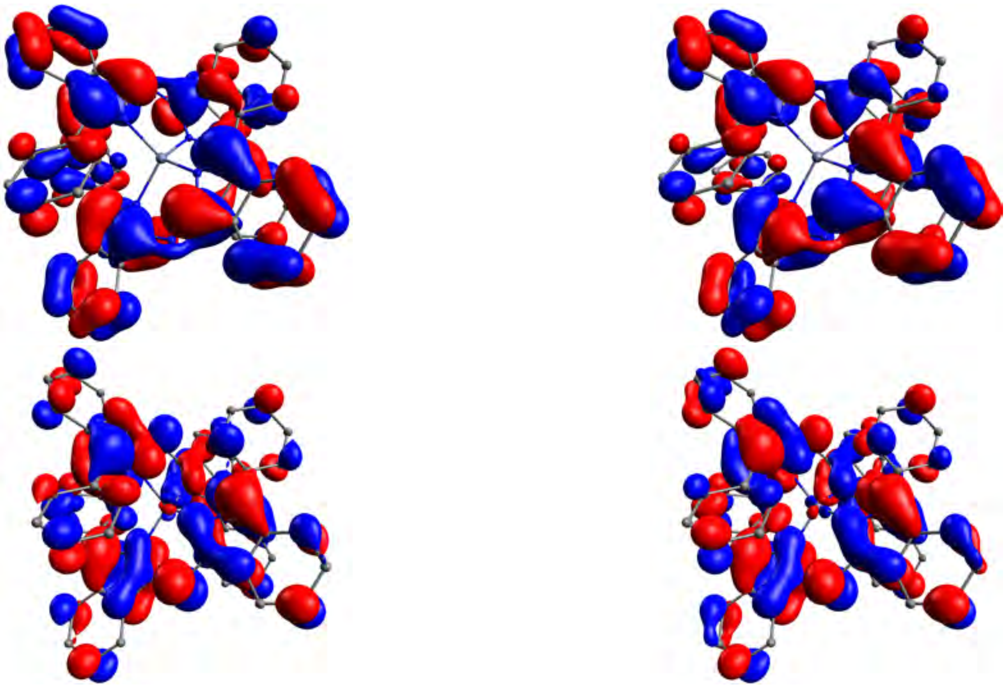

Figure 6.12: Frontier orbitals of the optimized Zn complex **102d** involved in the lowest energy absorption. Note the ligand-only character of the HOMO-1 (top left) and HOMO (top right) and the partially metal located LUMO (bottom left) and LUMO+1 (bottom right).

Calculations based on the single crystal structure of **102d** support the findings of the optimized geometry. The results showed a quasi-degeneration of the HOMO and HOMO-1 energy levels with a deviation of only 0.0232 eV. This breakup of degeneracy compared to the optimized structure is most likely due to variations from an ideal D_{2d} symmetry, induced by solid state packing effects. However, the absorption features were predicted similar to those of the optimized structure without any significant changes (see Table 6.6). A detailed analysis of the frontier orbitals of the Zn complex **102d** (see Figure 6.12) displayed the HOMO and HOMO-1 orbital to be only ligand located. The LUMO and LUMO+1 instead are partially metal located with a clearly visible alternation of the orientation of the metal d-orbital in the center. This indicates that the optical transitions in **102d** leading to the absorption maximum including the shoulder have a partially ligand to metal L(π)→M(d*) charge transfer character (LMCT).

Thermal properties

To evaluate a possible processability of these materials by thermal vacuum sublimation, the thermal stability of the complexes **102a-e** was investigated by TGA, additionally. The mass loss of the metal complexes was measured in an inert nitrogen gas atmosphere and is shown in Figure 6.13.

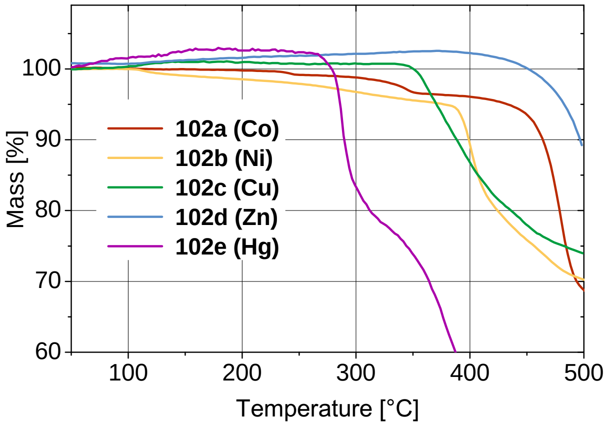

Figure 6.13: Thermogravimetric analysis of the metal complexes **102a-e** in the temperature regime from 50°C to 500°C.

Since the ligand in these systems remained the same, the measured stability is related to the stability of the metal-nitrogen bond and the thermal activation of the metal-(II)-ions and associated decomposition reactions. Although there is a mass drift present in a few samples, the decomposition proceeds very abruptly and hence allows for an objective analysis of the data. All of the investigated compounds, except of the Hg-complex **102e** exhibit a good thermal stability and a significantly increased stability compared to the free ligand which was already shown in Figure 6.7. For the compounds **102a-e** incorporating first-row transition elements (Co, Ni, Cu and Zn), the thermal stability correlates with the oxidation potential of these complexes **102a-d**. The most stable compounds were those with the Zn and Co as central metal atoms. These materials showed a negligible mass loss (< 5 %) until 420°C but with a rapid mass loss in higher temperature regimes. In terms of thermal stability, the next stable compound is the Ni complex **102b** with a decomposition temperature around 385°C, followed by the Cu complex **102c** with decomposition at 345°C. The Hg-complex **102e** is the thermally most fragile compound with degradation at 286°C combined with a very rapid mass loss. This material behavior may be related to the larger Hg(II)-ion and hence a longer, and therefore weaker Hg-N bond, as it was shown for a related Hg complex.[36] It is worth mentioning, that the Co and the Zn complex are both evaporable in high vacuum (10^{-6} mbar) at moderate temperatures (200°C), providing the chance of an easy processability.

7 Thin film characterization

In this chapter, the semiconducting properties of selected aza-bodipys are characterized in thin films and devices. Since the charge carrier mobility of organic materials is considered to be of particular importance, the charge transport behavior of aza-bodipys is evaluated in more detail in the first part. In this process, the differences in the experimental charge carrier mobilities are analyzed with respect to the molecular properties, on basis of single crystal structures. In the second part, the photovoltaic performance of these materials is investigated in organic solar cells, which were processed either from solution or by vacuum thermal evaporation.

7.1 Evaluation of the charge carrier mobility

The evaluation of charge carrier mobilities is a very challenging task, if the underlying structural conditions are considered for the interpretation of the experimental results. This is due to the fact that the solid state structures of a material on the molecular scale are in general not sufficiently known. For a theoretical prediction of the charge carrier mobility, simplifications have to be made in order to receive at least an approximate result.

One widely used method for the prediction of charge carrier mobilities transport trends in different materials was introduced by Brédas.[54] In this method the reorganization energy and the transfer integral are analyzed, which are the parameters limiting the charge transport according to Marcus theory (see eq. 3.1.3). Usually a model system is chosen to determine them, and the results are interpreted.[150, 151, 152, 153] On one hand, this static approach is very limited and far from reality. On the other hand, more sophisticated calculations are highly time consuming. Methods beyond the static approach use molecular dynamics simulation, in order to incorporate thermal fluctuations of the molecular structure and hence the transport parameters. The charge carrier mobilities are calculated with kinetic Monte Carlo simulations based on the hopping rates.[154, 155] Here, different theoretical approaches are used to understand the differences in the experimentally determined charge carrier mobilities of selected aza-bodipys and dibenzo-aza-bodipys. The charge carrier mobilities were measured with an organic field effect transistor setup, comprising a silicon gate and gold source and drain contacts and a silicondioxde dielectric layer. For any details of the setup and the device fabrication, the reader is referred to the Diploma thesis of Moritz Hein.[156, 58] The results for electron and hole mobilities are summarized in Table 7.1.

Table 7.1: Experimental charge carrier mobilities.

[$cm^2V^{-1}s^{-1}$]	**63a**	**63b**	**100c**	**100e**	**100f**
Hole	1.2^{-6}	1.3^{-5}	6.9^{-5}	2.6^{-5}	2.3^{-4}
Electron	1.2^{-5}	3.5^{-6}	3.7^{-5}	-	3.5^{-5}

From the data it can be seen that the hole and electron mobility is in general low, on the orders of 10^{-4} to 10^{-6} $cm^2V^{-1}s^{-1}$. Compared to the aza-bodipy **63a**, every compound exhibits a greater hole mobility in this series. The difference of the charge carrier mobilities in **63a** and **63b** is pronounced by one order of magnitude. The bis(thienyl)dibenzo-aza-bodipy compound shows the highest hole mobility on the order of 10^{-4} $cm^2V^{-1}s^{-1}$. The corresponding electron mobility in **100f** is ten times smaller as it is also the case in **63b**. In contrast to these distinct differences, compound **100c** does not show any favored carrier transport. To gain insights in the favored type of charge carrier transport (electrons or holes) and the mobility differences, the approach of Brédas for the evaluation of transport parameters in an ideal case (single crystal) is followed. The calculated reorganization energies are shown Table 7.2.

Table 7.2: Calculated reorganization energies λ for hole and electron transfer, calculated with B3LYP/6-31+g(d,p).

[meV]	**63a**	**63b**	**100c**	**100e**	**100f**
λ_{hole}	227	290	141	210	186
$\lambda_{\text{electron}}$	203	232	212	191	149

In case of the aza-bodipy compounds **63a** and **63b**, the reorganization energies are in both cases smaller for electron than for hole transfer and increase with the introduction of the

OMe substituent. Within the dibenzo-aza-bodipys, a smaller reorganization energy for holes is calculated for **100c**, whereas the methoxy-substituted **100e** as well as the thienyl species **100f** display smaller ones for electron transfer.All calculated values are within the usual range of reorganization energies, with surprisingly low values for **100c** and **100f**. These energies are comparable to that of the rigid pentacene, which has a reorganization energy of 130 meV for hole transfer.[157] A low reorganization energy is desired in order to achieve a high charge transfer rate. The determined energies point only for **63a** in the experimental direction of favored charge transport, since mainly the transfer integrals, as limiting transport parameters have to be considered.

The transfer integrals were calculated for the tetra(phenyl)-aza-bodipy **63a**, the bis(phenyl)dibenzo-aza-bodipy **100c** and the bis(5-methylthienyl)dibenzo-aza-bodipy **100f**, because crystal structures are only available for these molecules.[42] The respective molecular orientations from the crystal structure which were taken into account are shown in Figure 7.1. For **63a** the two different orientation of the molecule in the unit cell were considered as it is indicated by the orange and green box. The bis(phenyl)dibenzo-aza-bodipy **100c** forms columns in the crystalline phase and there is only a small overlap of neighboring columns.[42] For this reason, only one molecular configuration was taken into account, but with horizontal and vertical displacement. The unit cell of the bis(5-thienyl)dibenzo-aza-bodipy **100f** also comprises two relevant configurations, which are highlighted by the red and purple rectangles in Figure 7.1.

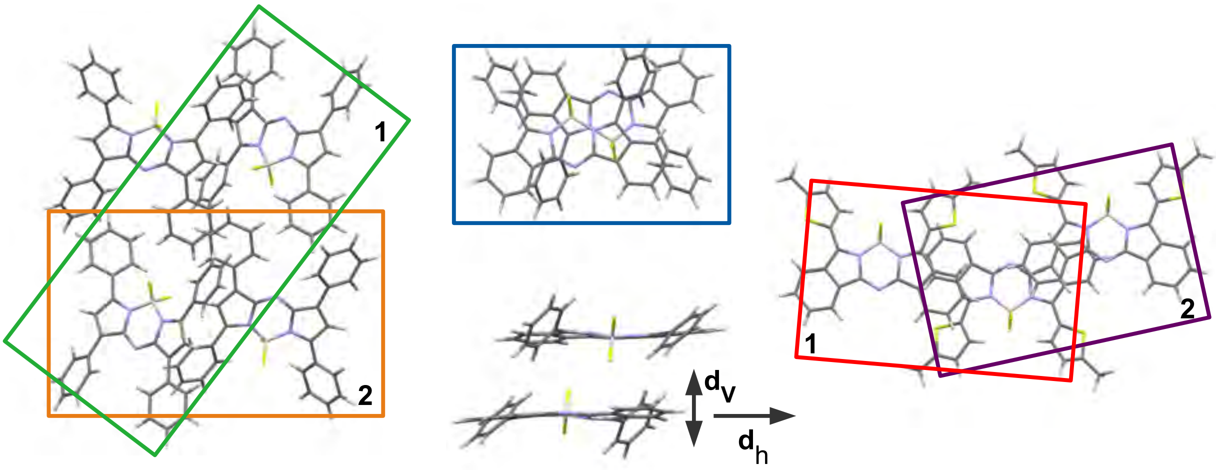

Figure 7.1: Molecular orientation derived from the crystal structure taken into account for the calculation of the transfer integrals. Left: **63a**. Middle: **100c**. Right: **100f**. For **100c** transfer integrals were calculated for a vertical and horizontal displacement.

Table 7.3: Transfer integrals t, calculated according to equation 3.13 with B3LYP/6-31+g(d,p).

[meV]	**63a** 1	**63a** 2	**100c**	**100f** 1	**100f** 2
t_{hole}	1.6	5.8	18.4 (20.1)[a]	68.5	42.2
t_{electron}	4.4	4.8	10.4 (7.4)[a]	35.1	21.5

[a] Transfer integrals in parentheses are calculated according to the energy splitting in dimer approach equation 3.16.

The results of the calculations (shown in Table 7.3) revealed higher transfer integrals for the dibenzo-aza-bodipys, both for electrons and holes, compared to the aza-bodipy. It is obvious that the overlap for **100c** and **100f** is larger than for **63a** in the respective configurations displayed in Figure 7.1. The transfer integrals of **63a** are small but t_{electron} is of similar size for the two calculated orientations 1 (green) and 2 (orange) whereas t_{hole} is even smaller for the orientation 1 (green). In the dimer of **100c** t_{hole} is higher than t_{electron}. Compound **100f** exhibits the largest transfer integrals for electron and holes within these dimers. As reasons, the large overlap of two adjacent molecules and the distance between two molecules of **100f** which is 3.5 Å and therefore smaller than in case of **100c** with a distance of 4.6 Å can be considered.[42, 141] To account for structural variations in the structure of **100c**, the transfer integrals were calculated for several horizontal and vertical displacements (see Figure 7.1, bottom in the middle) and are shown in Figure 7.2.

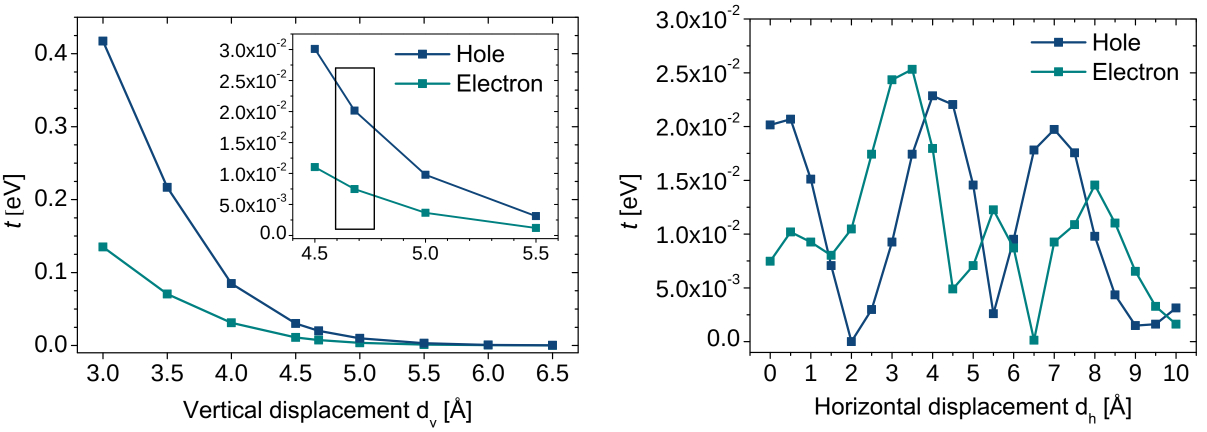

Figure 7.2: Transfer integrals (calculated according to equation 3.16) for a dimer of **100c** as a function of the vertical (d_v) and horizontal (d_h) displacement (see Figure 7.1). The inset highlights the vertical displacement around the initial distance (4.6 Å), indicated by the black rectangle.

The transfer integrals t_{hole} and t_{electron} increase exponentially with decreasing vertical distance $\mathrm{d_v}$, as expected. The variations for t_{hole} and t_{electron} due to the horizontal displacement $\mathrm{d_h}$ are related to the nodal structure of the frontier orbitals in the molecules. The particular shape of the electronic structure of the HOMO and the LUMO in **100c** results in a larger t_{hole} over a wider displacement range, compared to t_{electron}.

These considerations offer a first insight into the atomistic transport characteristics. However, the major drawback of this investigation can be attributed to the fact that only a static small part of the crystal structure was analyzed with respect to the transfer integrals. In a collaboration with the group of Prof. Cuniberti from TU Dresden, the systems were investigated in more detail with respect to a larger collection of molecules also including thermally induced structural distortions.[158]

The basic approach is shortly summarized here. In a first consideration, the transfer integrals of a supercell of the materials **63a**, **100c** and **100f** were calculated from a central molecule to every other molecule within the cell to gain deeper insight as well as to visualize the anisotropy of the electronic coupling. Subsequently, molecular dynamics (MD) simulations at 300 K of these super cell structures with 3D periodic boundary conditions were performed, to account for the thermal structural distortions and fluctuations of the transport parameters. The latter ones, namely the transfer integrals from one molecule to every other molecule in the supercell and the molecular orbital energies were determined by *ab initio* methods with a femtosecond resolution of the MD trajectory. The obtained distribution of transport parameters are used to calculate the charge transfer (hopping) rates within Marcus theory (equation 3.1.3). Based on kinetic Monte Carlo simulations of the hopping rates, the charge carrier mobilities are determined.

In Figure 7.3, the transfer integrals are visualized in the supercells, as seen from the central molecule, displayed by the ball-and-stick structure to the nearest neighboring molecules. The color code of the molecules represent the respective coupling strengths. High transfer integrals are illustrated in green, moderate to low in yellow and red, very low transfer integrals are displayed in black. This analysis clearly demonstrates the anisotropy and dimensionality of the transfer integral. In the structure of **63a** mainly low transfer integrals (marked in red) to the adjacent molecules are found. Though, the couplings are present in every direction likewise, without any noteworthy anisotropy. In contrast, the structure of **100c** exhibits a wide range of coupling strengths. In the crystal structure, the columns are formed of close pairs of molecules with a larger distance to the next pair inside the column. Therefore, a very large transfer integral (green) to the lower molecule in the column exists, but it is weaker (yellow) to the upper molecule in the column. The interactions with the surrounding molecules are significantly lower (black), and a strong anisotropy is present in this molecular structure.

The arrangement of the compound **100f** provides a balanced quantity of transfer integrals into every direction. The coupling strength is moderate and smaller than the maximum in the **100c**, but the central molecule interacts with the whole vicinity. The calculated charge carrier mobilities are highly anisotropic as determined by the molecular structure. The total mobilities for **63c** are 0.031 $cm^2V^{-1}s^{-1}$ for holes and 0.216 $cm^2V^{-1}s^{-1}$ for electrons and in case of **100c**, 0.979 $cm^2V^{-1}s^{-1}$ for holes and 0.027 $cm^2V^{-1}s^{-1}$ for electrons, respectively. The values clearly reflect the trend of a significant higher hole mobility for **100c** and a higher electron mobility for **63a**. Nevertheless, the theoretically determined charge carrier mobility values differ by orders of magnitudes from the experimental results. This is to a major extent due to the highly ordered crystal structures, which were taken as basis for the calculations. X-ray diffraction exhibited completely amorphous thin films, without any crystalline order. Additionally, the ambipolar measurement within the same field effect setup might offer injection barriers for one charge type. Accordingly, the experimentally obtained mobilities can as well be defective, and might not necessarily represent the intrinsic materials charge carrier mobilities. Nonetheless, the calculations of the charge carrier transport parameters and mobilities strongly supports the identifications of the differences in the intrinsic properties and contribute to the understanding of the structure-property relationship.

7.2 Application in organic solar cells

The most promising materials synthesized and presented in this thesis in terms of absorption, thermal and electrochemical properties were characterized in solar cells. The selected aza-bodipy derivatives were tested in solution processed as well as in vacuum processed devices. The solution processed devices were prepared during a research visit in the group of Prof. T. Marks at the Northwestern University (IL), USA. The vacuum processed solar cells were prepared by Toni Müller and David Wynands at the IAPP. For the fabrication of the solution processed cells a standard configuration was used, with ITO coated glass substrate and PEDOT:PSS for smoothening the ITO surface. As active layer, a mixture with varying ratio of the compound $PC_{61}BM$ and $PC_{71}BM$ in a certain solvent was used, as shown in Table 7.4. The layer thickness varied, depending on the spin-coating speed from approximately 30 to 60 nm. Aluminum was used as top electrode, with a 1 nm thick interfacial layer which was found to improve the contact

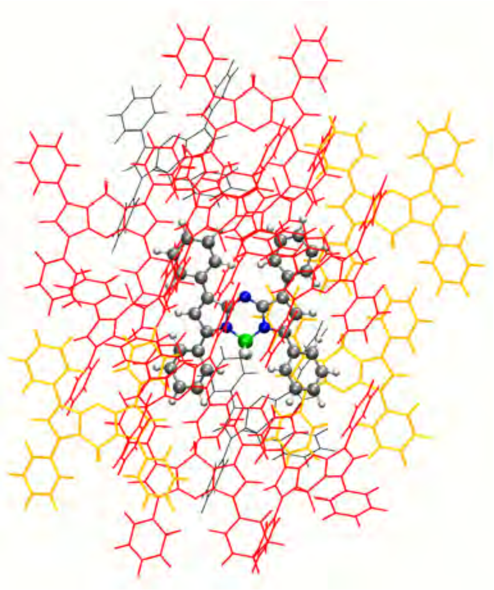

tetra(phenyl)-aza-bodipy **63a**

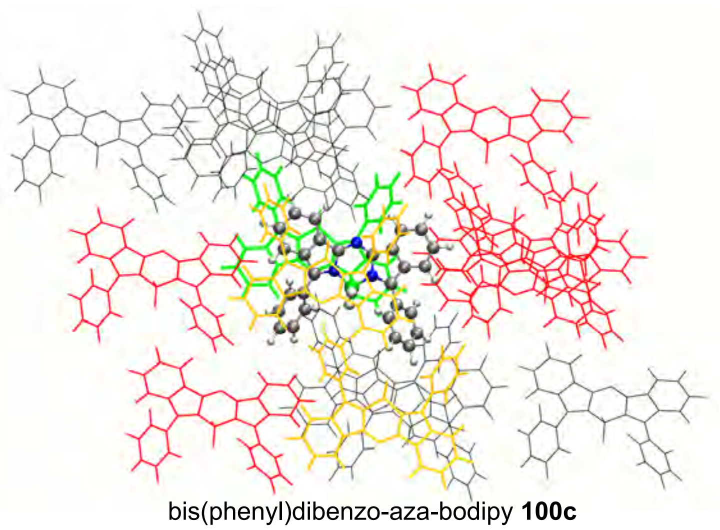

bis(phenyl)dibenzo-aza-bodipy **100c**

🟩 high |t(ij)| > 0.1
🟨 0.1 > |t(ij)| > 0.01
🟥 0.001 > |t(ij)| > 0.01
⬛ 0.001 > |t(ij)| low

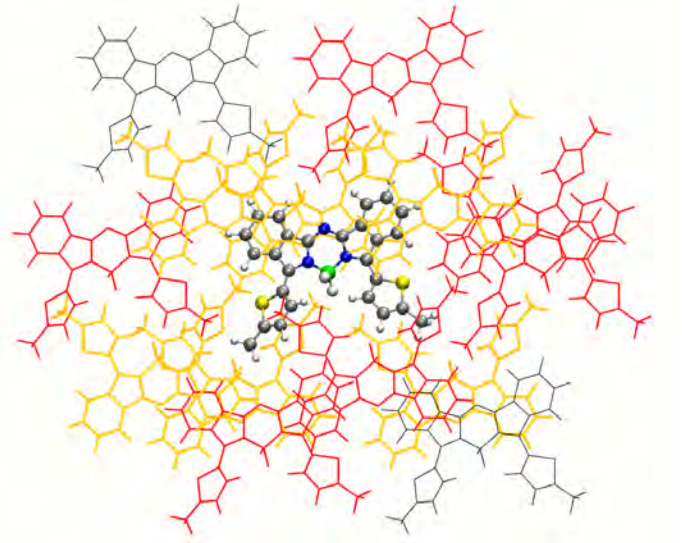

bis(5-methylthienyl)dibenzo-aza-bodipy **100f**

Figure 7.3: Representation of the electronic coupling (t(ij)) strengths as seen from the central ball-and-stick structure to the neighboring molecules. The color indicates the quantity of t(ij), with green the largest and black the smallest transfer integral.

efficiency.[159] The full fabrication procedure is described in detail in the experimental section.

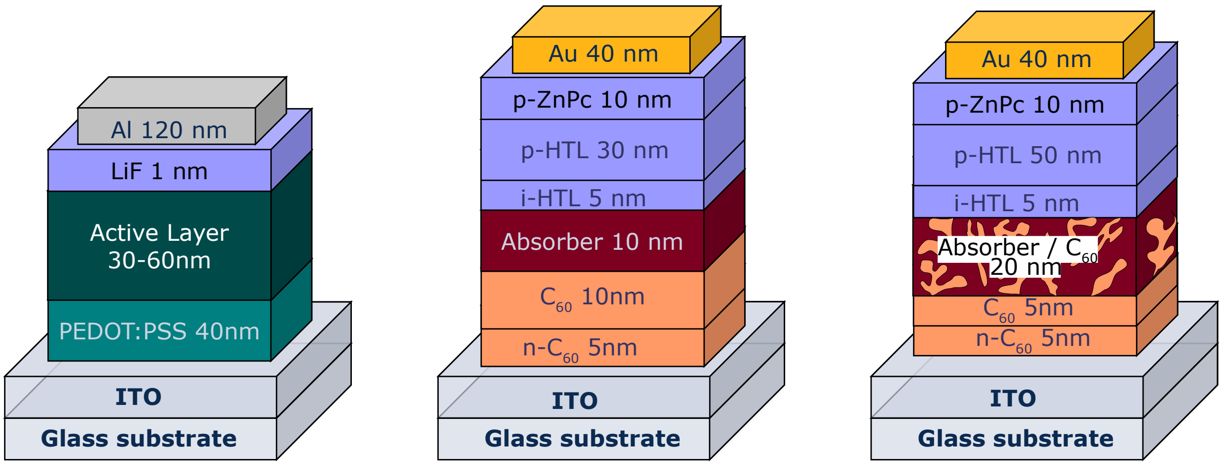

Figure 7.4: Solar cell architectures used for the materials characterization. Left: Solution processed bulk heterojunction device; Middle: Vacuum processed flat heterojunction; Right: Vacuum processed bulk heterojunction device.

The best results for the solution processed devices were achieved with a high spin coating speed (5000 rpm) and a resulting thin active layer of approximately 30 nm. It turned out, that an excess ratio of fullerene is beneficial for the solar cell efficiency, as the photocurrent increases. The results for the solution processed devices are listed in Table 7.4. The aza-bodipys **63c** and **76a** did not work at all in this setup. This might be due to the low LUMO level, which prevents an efficient charge separation process. In contrast to that, the dibenzo-aza-bodipys **100c** and **100d** reached reasonable efficiency values. The IV-characteristics are shown in Figure 7.5.

The open circuit voltage in both materials **100c** and **100d** was about 0.7 V. Thus, it does not correlate strictly with the difference of the materials' HOMO level. The short circuit current density ranges between 4.95 mAcm^{-2} for **100c** and 7.65 mAcm^{-2} for **100d**, when mixed with PC$_{61}$BM. Using the PC$_{71}$BM derivative, the short circuit current density can further be increased to 10.23 mAcm^{-2}. As can be seen for **100d** in Table 7.4, the photocurrent increases with the fullerene content in the active layer mixture. This increasing short circuit current density is also reflected by the increasing external quantum efficiencies (EQE) of the different devices, shown in Figure 7.5 in the right. With increasing PC$_{61}$BM content, the absorbance of the device is enhanced, as the maximum peak at 750 nm in the EQE increases, and a shoulder arises at

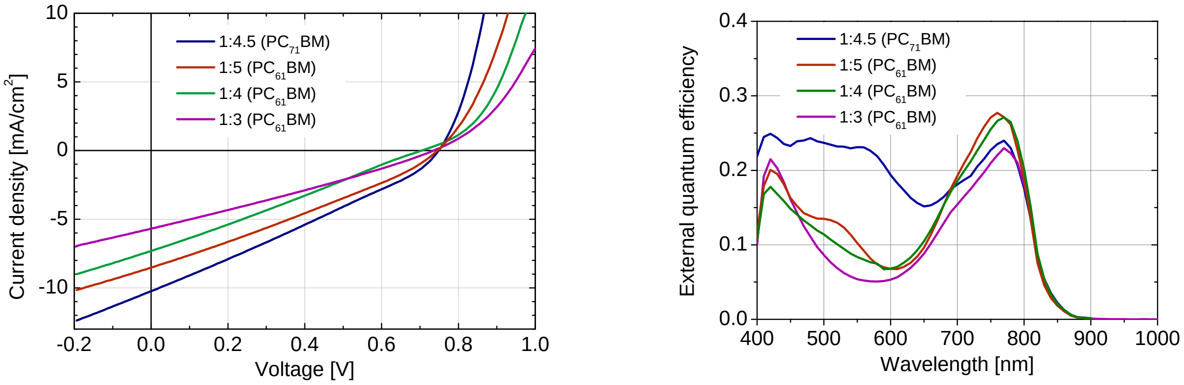

Figure 7.5: IV-characteristics and EQE of the best solution processed organic solar cell devices of the bis(tolyl)dibenzo-aza-bodipy **100d** with varying acceptor ratio.

550 nm. The shoulder might point to a more crystalline phase of either PC$_{61}$BM or **100d**. A dramatic enhancement in the EQE is obtained with PC$_{71}$BM as acceptor compound, especially in the lower wavelength regime (400-600 nm). This can be attributed to the higher absorbance of PC$_{71}$BM compared to PC$_{61}$BM and the resultant increased contribution to the photocurrent. The device efficiencies were between 1 % and 2 % for the best cells and are shown in Table 7.4. The efficiency limiting parameter in all devices is the low fill factor of 27 % to 30 %. The reasons for a low FF are manifold. One aspect might be a low or unbalanced charge carrier mobility of the active materials. Another one is a high series resistance due to overall low conductivity or a low parallel resistance due to short cuts or charge recombination, see Figure 3.7.[62] Systematic attempts to improve the fill factor by annealing or by the utilization of other solvents or solvent mixtures and additives were not succesful.

The architecture of the vacuum processed solar cells is shown in Figure 7.4, right. The materials **63a**, **100c**, and **100f** were characterized in flat heterojunction, and one of them also in a bulk heterojunction device. The flat heterojunction devices were prepared by Toni Müller, the bulk heterojunction device by David Wynands at the IAPP. The solar cells had the following layer sequence. On an ITO coated glass substrate, n-doped C$_{60}$ was evaporated, followed by a 10 nm neat C$_{60}$ layer and 10 nm absorber layer, forming the active heterojunction. For hole extraction, a neat 5 nm (hole transport layer) HTL, followed by a p-doped HTL was evaporated. Additional doped ZnPc was used to improve hole injection into gold, which was used as top electrode. Since the tested materials exhibit different HOMO energy levels, the choice of the appropriate HTL materials was necessary. Accordingly, for the flat heterojunction solar cells shown in Figure 7.4, MeO-TPD, PV-TPD and BPAPF was used (see Scheme 3.1), to avoid interfacial barriers.[78]

Table 7.4: Characteristics of solution processed solar cells.

Compound	Weight Ratio	Solvent	V_{OC} [V]	J_{SC}[e] [$mAcm^{-2}$]	FF [%]	η [%]
63c	1:3[a]	ODCB[c]	0.16	2.06	44	0.03
76a	1:3[a]	$CHCl_3$	0.28	0.12	32	0.01
100c	1:3[a]	$CHCl_3$	0.71	4.95	29	1.01
100d	1:3[a]	$CHCl_3$	0.71	5.03	28	1.02
100d	1:4[a]	$CHCl_3$	0.68	6.56	27	1.20
100d	1:5[a]	$CHCl_3$	0.71	7.65	30	1.64
100d	1:4.5[b]	$CHCl_3$[d]	0.71	10.23	30	2.16

[a] $PC_{61}BM$; [b] $PC_{71}BM$; [c] ODCB = ortho-dichlorobenzene; [d] 1,8-Diiodooctane (1 %) was added; [e] Not corrected with respect to the spectral mismatch.

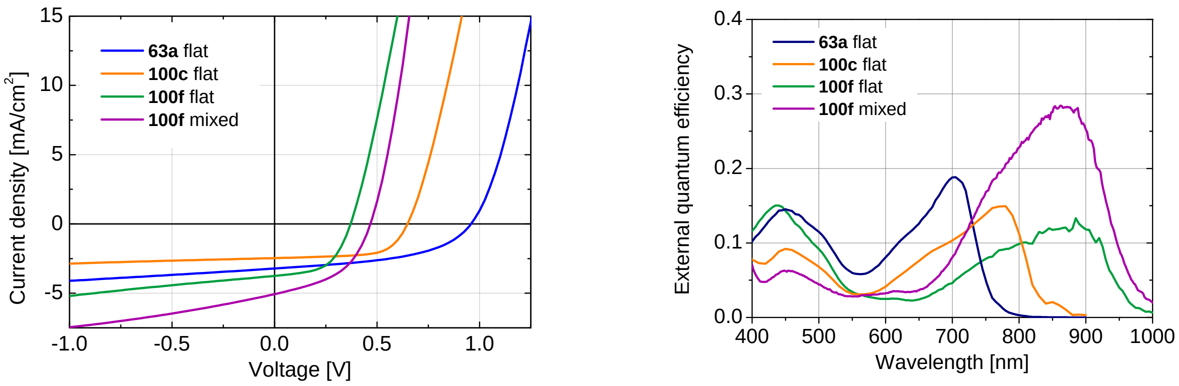

Figure 7.6: IV-characteristics and EQE of the vacuum processed organic solar cell devices.

In Figure 7.6, the IV characteristics (left) and the EQE (right) are shown, and Table 7.5 summarizes the solar cell characteristics. The device with the aza-bodipy **63a** shows a V_{OC} of 0.96 V, with the dibenzo-aza-bodipy **100c** a V_{OC} of 0.65 V and with **100f** a V_{OC} of 0.37 V. This is in accordance to the energy difference in the HOMO levels. It can be seen, that the V_{OC} in the devices is decreasing with increasing HOMO energy of the material. The fill factors of 65 % and 54 % are higher in the dibenzo-aza-bodipys compared to the aza-bodipy with 48 %. This might explain the difference in the charge carrier mobilities. On the other hand, the about 0.3 eV lower lying LUMO of the aza-bodipy compared to the dibenzo-aza-bodipys might hinder an effective charge separation to the LUMO of C_{60}. The short circuit current density is lowest for **100d** with

2.47 $mAcm^{-2}$ and highest for **100f** with 3.67 $mAcm^{-2}$. The overall low J_{SC} can be referred to the very thin active layers of only 10 nm. Consistently, the EQE reaches a comparable low value of 18 % for the device incorporating **63a** and 15 % and 12 % for the devices with **100c** and **100f**, respectively. The spectral response follows the thin film absorption and has its maxima at 700 nm, 775 nm and 868 nm in the near infrared region.

Table 7.5: Characteristics of vacuum processed solar cells.

Compound	HTL	V_{OC} [V]	J_{SC}[a] [$mAcm^{-2}$]	FF [%]	η [%]
63a	BPAPF	0.96	3.22	48	1.43
100c	PV-TPD	0.65	2.47	65	1.24
100f	MeO-TPD	0.37	3.67	54	0.65
100f	MeO-TPD	0.47	5.10	47	0.90

[a] Not corrected with respect to the spectral mismatch.

Compound **100f** was additionally tested in a bulk heterojunction device with a comparable solar cell architecture as for the flat heterojunction device, as shown in Figure 7.4 on the right. Basically, instead of the 10 nm flat absorber layer on 10 nm C_{60}, a 20 nm mixed layer (ratio 1:1) was used. A thin neat C_{60} layer is introduced between the active layer and the n-doped C_{60} layer, to avoid exciton quenching at the dopant molecules. As hole transport layer, also p-doped and neat MeO-TPD was used with a thickness of 50 nm. As top contact p-ZnPc and gold were evaporated in the same way as in the flat heterojunction devices. The characteristics are shown in Figure 7.6 and listed in Tabel 7.5. Surprisingly, the V_{OC} is 0.1 V larger in the mixed solar cell, which is currently under investigation but not fully understood yet. The J_{SC} increases to 5.10 $mAcm^{-2}$ as expected for mixed layers. However, the strong increase suggests a small exciton diffusion length of the material, which is overcome in the mixed layer. The slope of the IV-curve suggests charge recombination in the device. This leads to a lower fill factor of 47 % in the bulk heterojunction device, but it might be improved by heating the underlying layers upon evaporation. The EQE of the bulk heterojunction device with **100f** has a significant contribution in the NIR region from 700 nm to 950 nm, with a peak EQE of 28 %. The efficiency of the device reaches 0.90 %. Overall it can be conducted that the performance of these NIR absorbers are promising as second active material in organic tandem devices.

8 Conclusions and Outlook

In the first section, a brief summary of the main results of this thesis for the synthesis of aza-bodipy materials and characterization for organic solar cell applications is given and conclusions are drawn. In the outlook part, the potential of future molecules of the aza-bodipy materials class is estimated from calculations of optical and electronic properties of conceivable molecular structures.

8.1 Conclusions

Organic photovoltaics based on conjugated polymers or small molecular dyes has the potential of a low-cost and large area photovoltaic technology due to the processing by printing or evaporation in combination with a low material consumption. The successful launch of products, however, still requires higher efficiencies than the 8% reached today. One approach improving the device eficiency is to increase the photoactive spectral range of organic solar cells by appropriate low band gap absorbers, which are still rare. In this thesis, the material class of aza-bodipys and dibenzo-aza-bodipys were studied for the application as active donor absorber materials for the near infrared region in organic photovoltaics.

A series of aza-bodipys has been synthesized and systematically characterized in terms of the substitution pattern by both, experimental and theoretical methods. Novel star-shaped thienyl-substituted aza-bodipys have been synthesized via an extended route, employing Stille-coupling of a 2,6-dibromo-aza-bodipy with stannylated thiophene. Besides that, azadiisoindomethenes were prepared by the addition of aryl Grignard reagents to phthalodinitrile and a subsequent formamide mediated Leuckart-Wallach type reduction. A reaction mechanism for this synthesis is proposed and the corresponding transition states and intermediate structures were calculated with quantum chemical methods. Since the synthetic procedure abandoned the water steam distillation reported in literature and offered higher yields, it represents an improvement of the synthesis reported so far. Based on the azadiisoindomethene ligand, the borondifluoride, boroncatechol as well as transition metal (Co, Ni, Cu, Zn, Hg) complexes were prepared and studied.

It was found that the absorption maxima in aza-bodipys can be shifted into the red and NIR spectral region by electron donating groups, e.g. thiophene **76a-e** (742 nm) or dimethylaminophenyl moieties **63c-e** (805 nm). The dibenzo-aza-bodipys **100a-f** demonstrate also an intense absorption in the visible and near infrared region, up to 793 nm (in solution).

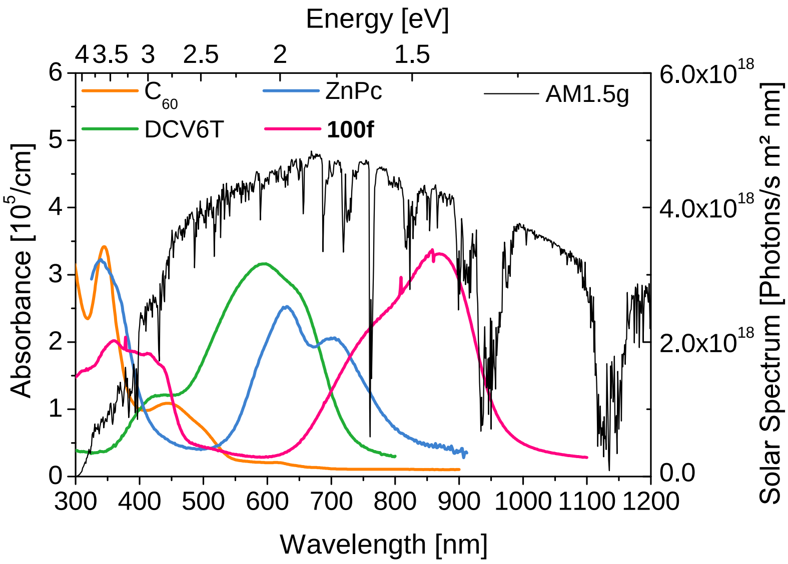

Figure 8.1: Thin film absorption spectra (20 nm on glass) of commonly used active materials (C_{60}, DCV6T, ZnPc) for small molecule organic tandem solar cells and improved absorption spectra of the bis(thienyl)dibenzo-aza-bodipy **100f**.

This effect can be attributed to an increase of the HOMO energies, while the LUMO energies remain nearly constant, resulting in an overall reduced gap as determined by cyclic voltammetry. DFT calculations confirmed the experimental results and displayed predominantly a HOMO-LUMO transition for the absorption. It was found that the absorption is characterized by a charge transfer from the periphery to the core, with a stronger electron accepting character in the aza-bodipy system compared to the dibenzo-aza-bodipys. This gives rise to very low energy levels in the aza-bodipys, with LUMO energies from -3.96 eV to -3.91 eV for the thienyl derivatives **76a-e**. This might lead to an insufficient charge transfer to C_{60} (LUMO: -4.0 eV). Higher LUMO energies in the range of -3.95 eV to -3.58 eV were observed for the *p*-dimethylaminophenyl-substituted aza-bodipys **63c-e**. These compounds seem to be more suitable, but in these compounds the thermal stability is not always given, although it can be enhanced by boroncatechol compared to borondifluoride complexes. Thus, only few aza-bodipys (e.g. **63d**) comprise every desired property, a near infrared absorption, appropriate energy levels and a high thermal stability. The dibenzo-aza-bodipys **100a-f** exhibit optimized energy levels, with a LUMO energy between -3.6 eV and -3.7 eV and HOMO energies from -5.28 eV to -4.96 eV combined with a near infrared absorption (as seen in Figure 8.1) and a high intrinsic thermal stability.

Promising materials in terms of absorption and energy levels were characterized in thin films and devices. The measurements in an organic field effect transistor revealed charge carrier mobilities in the range of 10^{-6} to 10^{-4} $cm^2V^{-1}s^{-1}$ for the (dibenzo)aza-bodipy derivatives. Theoretical simulations of the charge carrier transport parameters, as well as the mobility were achieved in a collaboration with the group of Prof. Cuniberti, on the basis of obtained single crystal structures for the tetraphenyl-aza-bodipy **63a**, the bis(phenyl)dibenzo-aza-bodipy **100c** and the bis(5-methylthienyl)dibenzo-aza-bodipy **100f**. The electronic coupling (transfer integrals) to adjacent molecules differs strongly in the materials and can be one or three dimensional, in the considered ideal cases. The highest charge carrier mobility measured for **100f** compared to the others can be attributed to first, a favored 3D overlap with the neighboring molecules and second, a high coupling strengths due to a very close packing and short distances.

The solar cell performances were evaluated in solution and vacuum processed devices. In solution processed solar cells the investigated aza-bodipys did not work, probably due to poor charge separation efficiency which can be related to the low LUMO energies. The dibenzo-aza-bodipys in contrast showed a solar cell behavior, with an excess of fullerene in the bulk heterojunction. Optimized solar cells with **100d** reached an efficiency of 1.6 with $PC_{61}BM$ and 2.1 % with $PC_{71}BM$. The main limiting factor in these devices is the low fillfactor of around 30 %. Vacuum processed devices were prepared with the parent aza-bodipy **63a** and the dibenzo-aza-bodipys **100c** and **100f**. All materials demonstrate a contribution to the photocurrent in the range from 700 nm to 950 nm, as seen in the EQE. According to the very low HOMO energy, **63a** showed a V_{OC} of 0.96 V and reached an efficiency of 1.4 %, whereas the V_{OC} decreases with increasing HOMO energy in the other materials **100c** and **100f**.

The most promising absorber material for near infrared absorption turned out to be the bis(thienyl)dibenzo-aza-bodipy **100f**. The material exhibited a comparatively high V_{OC} of 0.47 V, together with an EQE from 750 nm to 950 nm, with a peak EQE at 870 nm. An unoptimized bulk heterojunction device with a 20 nm mixed (1:1 C_{60}) active layer reached an efficiency of 0.9 %. This qualifies the bis(thienyl)-azadiisoindomethene **100f** for an suitable co-absorber material in vacuum processed organic tandem solar cells.

8.2 Outlook

From the synthetic point of view it is necessary to study the nitrosation-condensation reaction of 2-aryl-isoindoles to the correpsonding azadiisoindomethenes (as shown for pyrrole derivatives in Scheme 2.1). This reaction was already published in [160], but no azadiisoindomethenes were obtained. The reasons, however, might be found in the specific reaction conditions applied. An established reaction via 2-aryl-isoindoles and nitroso-2-aryl-isoindoles would lead to a facilitated and more tolerant route to the azadiisoindomethenes and hence the dibenzo-aza-bodipys.

An increased number of structures would get accessible and an improved tunability of the properties within this material class would be reached. The dinaphto-aza-bodipy **106** (Figure 8.2) was already synthesized and gives a prospect of future aza-bodipy materials. However, no spectroscopic data were reported.[161] As presented and discussed in this thesis, quantum chemical calculations are a capable tool for the prediction of optical and electronic properties. This method shall be also applied here, to give an outlook of the properties of conceivable donor and acceptor core substituted dibenzo-aza-bodipys **103-108**, as shown in Figure 8.2.

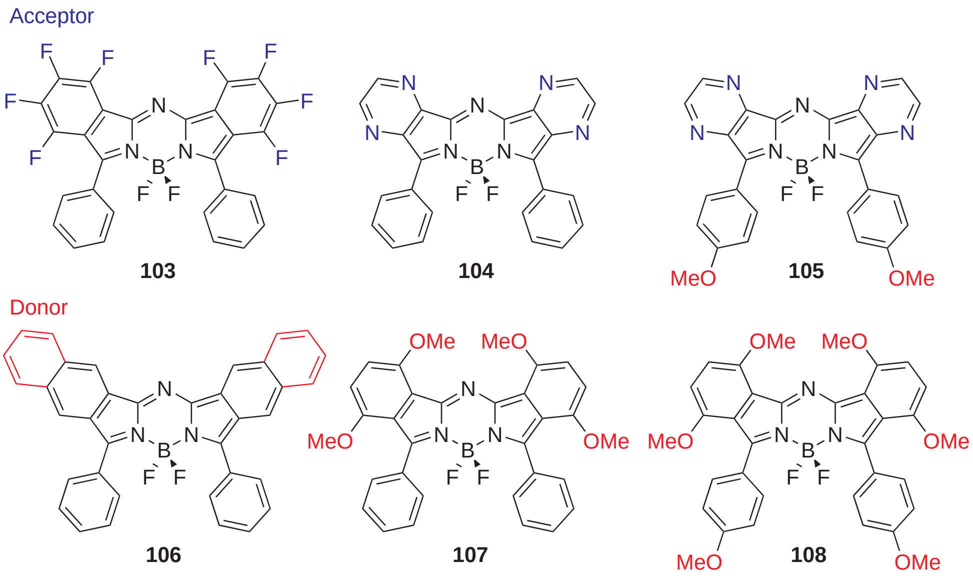

Figure 8.2: Electron-acceptor and electron-donor type substitution at the diisoindole core, taken into account for the quantum chemical calculation.

The acceptor substituted compounds contain the tetrafluoroisoindole **103** and pyrrolopyrazin unit **104** and **105**. As donor substitution, the benzisoindole unit **106** was considered as well as di-methoxyisoindole in **107** and **108**. The respective donor and acceptor features of the molecular structure are highlighted in Figure 8.2 in red and blue. Additionally, *p*-methoxyphenyl substituted compounds were calculated with each, a donor (**108**) and an acceptor (**105**) substituted dibenzo-aza-bodipy core.

Besides the calculation of the HOMO and LUMO energy values, the molecular excitation energies and oscillator strengths were determined. Since the molecular structure can have an impact on the electronic properties, the dihedral angles between phenyl rings at the cores are specified as well. All calculated data are shown in Table 8.1. In order to allow an easy comparison to the experimentally studied dibenzo-aza-bodipys **100a-f**, the calculated absorption wavelengths are given also relatively to the calculated one of the unsubstituted dibenzo-aza-bodipy **100c** and the electronic properties will be discussed with respect to **100c**.

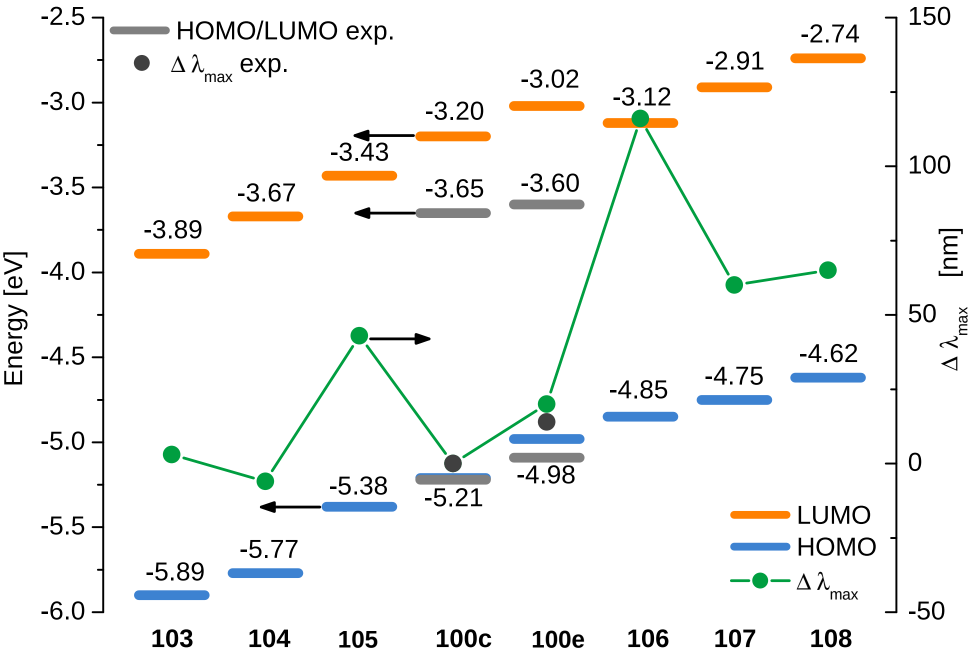

Figure 8.3: Absolute HOMO and LUMO energies (left scale) and the relative shift of the absorption wavelengths (right scale) against **100c** for the dibenzo-aza-bodipys **103-108**. The orange and blue levels show the calculated orbital energy values, the green dots represent the calculated difference of the absorption wavelength. The gray signs show the respective experimental values for reasons of comparison.

The calculations revealed a major impact of the core substitution on the electronic properties of the dibenzo-aza-bodipys. The energy levels of the acceptor dibenzo-aza-bodipys are stabilized (compared to **100c**), by -0.17 eV for the HOMO energy of **105** down to -0.68 eV in case of the HOMO energy of **103**. In contrast, the energy levels of the donor dibenzo-aza-bodipys are destabilized (compared to **100c**), from 0.36 eV for the HOMO energy of **106** up to 0.59 eV for the HOMO energy of **108**. As can be seen by the energy level diagram in Figure 8.3, the energy levels can be tuned over a wide range. Furthermore, it is possible to turn the donor character of **100c,d** (against C_{60}) into a strong electron acceptor character. The calculated absorption wavelengths of this series demonstrate that a strong bathochromic shift of over 100 nm (compared to **100c**) can be reached.

From the prediction of the absorption wavelenghts it turned out, that the donor groups in **106** and **107** lead to a strong bathochromic shift (up to 115 nm for **106**), whereas the acceptor moieties in **103** and **104** have a weak impact on the absorption. The relative shift of the absorption maximum is shown by the green dots in Figure 8.3 and in Table 8.1.

Especially the donor-substituted species **106** and **107** show both a strong shift of 60 and 115 nm into the infrared region. In contrast to that, pure acceptor species **103** and **104** have a weak impact on the absorption. Thus, the relative shift of the absorption wavelength is small with 3 nm and -6 nm. Upon substitution of the aryl ring with a methoxy group in para position, the absorption is also bathochromically shifted.

The electron donating *p*-methoxy group in **105** and **108** also leads to a redshift of the absorption, but it depends on the electron donor/acceptor character of the dibenzo-aza-bodipy core. Accordingly, the absorption maximum is shifted only by 5 nm for the donor-donor species **108**, whereas the shift in the donor-acceptor compound **105** is much larger with 49 nm. Consistently, the calculated shift for **100e** lies in between with 20 nm, with its unmodified dibenzo-aza-bodipy core. This points again to the CT character of the absorption, which is weakened in the donor but enhanced in the acceptor species. All calculated oscillator strengths are in the same range as for the **100a-f** and indicate a high absorbance. From the optimized molecular geometries of these species, the dihedral angles between the plane of the aryl ring and the adjacent diisoindole plane were derived and are briefly compared to the one of **100c** (46.7°). It was found that the fluorine atom in **103** and especially the methoxy groups in **107** and **108** lead to an increased dihedral angle of 5° and 12°. The pyrazine moiety **104** and **105** lead to a decreased dihredral angle, due to the missing hydrogen atom at the nitrogen. Accordingly, the steric influence of the core substituent has to be considered as relevant, in case a particular planar molecular structure is desired. This is often necessary for good crystallization behavior, required for improved charge transport properties or phase separation. Finally, the deviations of the calculated results com-

Table 8.1: Optical and electronic properties of donor-acceptor core substituted dibenzo-aza-bodipys **103-108**.

	Wave length[a,b]	Oscillator strength[b]	principal orbital contributions[b]	HOMO [eV]	LUMO [eV]	$\Delta\lambda_{abs}$[c] [nm]	α [°][d]
103	601.9	0.756	H→L	-5.89	-3.89	3	5.5
104	593.2	0.627	H→L, H→L+2	-5.77	-3.67	-6	-10.1
105	641.6	0.665	H→L, H→L+2	-5.38	-3.43	43	-13.2
106	714.7	0.735	H→L	-4.85	-3.12	116	0.4
107	659.0	0.706	H→L	-4.75	-2.91	60	11.8
108	664.2	0.751	H→L	-4.62	-2.74	65	11.0

Calculated with TDDFT B3LYP/6-31+g(d,p). [a] Given in nm; [b] $S_0 \rightarrow S_1$ transition; [c] Wavelength relative to the bis(phenyl)dibenzo-aza-bodipy **100c**; [d] Dihedral angle between the planes of the aryl ring and the isoindole plane, relative to **100c** (46.7°).

pared to experimental values are estimated. In Figure 8.3 it can be seen for **100c** and **100e**, that the calculated HOMO energy (in blue) fits well to the measured one (in gray), whereas the calculated LUMO energy is overestimated by 0.4-0.5 eV. As seen in the previous sections, the calculated absolute absorption wavelengths deviate from the experimental values. However, the relative change (in green) fits nicely to the experimental values. Accordingly, the above calculated optical and electronic properties of **103-108**, demonstrating a possible shift of the HOMO energy by 1.2 eV and a reachable bathochromic shift of >100 nm, are indeed realistic. The huge potential of dibenzo-aza-bodipys as absorber materials for organic photovoltaics is revealed due to the flexibility of the physical properties. The quantum chemical calculations state several possibilities for promising structural modifications and provide a basis towards a rational design of a pair of infrared absorbing donor- and acceptor-type (dibenzo)aza-bodipys, in order to optimally cover the sun spectrum and increase the device efficiency of organic tandem solar cells.

9 Experimental section

9.1 General remarks

All starting materials were obtained from commercial sources and were used without further purification. Diethylether, THF and toluene were dried over sodium/benzophenone and distilled right before use or stored over mole sieve $4\mathring{A}$, DCM was dried over P_4O_{10}, dichloroethane and butanol were dried over mole sieve $4\mathring{A}$.

NMR spectra for ^1H, ^{13}C and ^{19}F NMR spectra were recorded at 25 °C with a Bruker DRX 500 P instrument at 500.13, 125.76 and 282.24 MHz respectively. Chemical shift values (δ) are expressed in parts per million using residual solvent protons (^1H NMR, $^1H = 7.26$ for $CDCl_3$; ^{13}C NMR, $^{13}C = 77.0$ for $CDCl_3$) as internal standard. The splitting patterns are designated as follows: s (singulet), d (doublet), t (triplet) and m (multiplet).

Elemental analysis was performed with an Eurovektor Hekatech EA-3000 elemental analyzer. Melting points were determined with a Netzsch STA 449C instrument or with a hot stage microscope according to Boetius and are uncorrected. The thermogravimetric analysis were measured with a Netzsch STA 449C under nitrogen atmosphere. The thermogravimetric analysis coupled with mass spectrometry were measured with the system Netzsch STA 409 Luxx and QMS 403 Aeolos. In both cases, the heating rate was 10 K/min. The UV-VIS spectra were measured with a Perkin Elmer λ 25 spectrometer or SHIMADZU UV-VIS-NIR Recording spectrometer. Mass spectra were recorded with a Bruker Esquire-LC 00084 instrument with an ion trap detector and ESI source.

Thin layer chromatography was carried out on aluminum plates, pre-coated with silica gel, Merck Si60 F254. Preparative column chromatography was performed on glass columns packed with silica gel, Merck Silica 60, particle size 63-200 μm.

Cyclic voltammetry experiments were performed with a computer controlled Metrohm μ-Autolab potentiostat in a single-compartment cell. A typical three electrode configuration with an in laid platinum disk as working electrode, platinum wire as counter electrode and a silver rod coated electrochemically with AgCl was applied with a scan rate of 100 mVs^{-1}. The measurements were done under a nitrogen atmosphere in a degassed DCM (HPLC quality) solution with tetra-n-butylammonium hexafluorophosphate (TBAPF, 0.1 mol L^{-1}) as supporting electrolyte. All potentials were referenced to the ferrocene/ferrocenium redox couple as an internal standard and $\mathrm{E}°(\mathrm{Fc}/\mathrm{Fc}^{+})$ = -4.78 eV was used to calculate HOMO/LUMO energies with respect to the vacuum.

Single crystal data were collected on a Bruker Nonius Kappa CCD diffractometer using graphite-monochromated Mo-Kα ($\lambda = 0.71073$ $\mathring{A}$) radiation at 150 K. SADABS was used to perform area-detector scaling and absorption corrections.[162] The structures were solved by direct methods using Sir97[163] and were refined by full-matrix least-squares techniques against Fo2 by using SHELXL-97.[164] All non-hydrogen atoms were refined anisotropically. Hydrogen atom positions were generated by their idealized geometry and refined within a riding model.

For all quantum chemical calculations, the GAUSSIAN03 package was used at the Center for Information Services and High performance Computing (ZIH), Dresden Technical University. All *ab initio* calculations of the orbital energies and the absorption energies were performed with density functional theory (DFT) with the b3lyp functional and the basis set 6-31+g(d,p) except for the mechanistic studies where the basis set 6-31g(d) was used. No symmetry constrains were used for the optimization. All optimized structures were confirmed with subsequent frequency calculations to make sure that a true minimum was reached. The calculation of the absorption energies and the principal orbital contributions were done with time dependent DFT as implemented in the Gaussian package.

The vacuum processed solar cells shown in Figure 7.4 were prepared by Toni Müller and David Wynands as described in the thesis of Toni Müller, TU Dresden. Solution processed organic devices with the layer architecture shown in Figure 7.4 were prepared at the Department of Chemistry at the Northwestern University, Evanston (IL) USA, as follows. Commercial ITO film on glass substrates (1.1 mm, with a resistivity of $<20\Omega/\mathrm{sq}$) were patterned with aqueous HCl solution, and then cleaned by ultrasonic treatment in aqueous detergent, deionized water, methanol, isopropanol, and acetone for 30 min. After the final sonication step, the substrates were blown dry with a stream of N_2 gas. ITO substrates were then treated for 30 min in a UV/O_3 oven (Jelight Co.). PEDOT:PSS (Clevios P VP Al 4083) was then spun-cast at 5000 rpm for 30 sec and subsequently annealed at 150 °C for 15 min. Active layers containing donor (aza-bodiyp derivatice) and acceptor $\mathrm{PC}_{61}\mathrm{BM}$ or $\mathrm{PC}_{71}\mathrm{BM}$ (each >99.5% pure, American Dye Source) were formulated in various weight ratios (w:w) at a total concentration of 20 mgmL^{-1} in distilled solvents (see Table 7.4). Diiodooctane was added as high boiling point processing additive in order tocontrol the BHJ morphology by selective solubility of the fullerene components.[165] Active layer solutions were then allowed to stir for 1.5 h at 40 °C. The active layer solutions were spun-cast at 2000 rpm to 5000 rpm for 30 sec to afford an active layer thickness of 60 nm to 30 nm, respectively. The thicknesses of the active layer varied with the rotation speed of the spin coater, and were measured by profilometry (Tencor, P10). Samples were then either thermally annealed at various temperatures (90 °C to 150 °C) for 10 min on a temperature-controlled hot plate or left as cast. To complete device fabrication, LiF(1.0 nm)/Al(120 nm) were thermal evaporated, sequentially, at a base pressure of ca. $4.0x10^{-6}$ torr. The top Al electrodes were then encapsulated with epoxy and a glass slide before testing. IV characteristics were measured at 298K using a Class A Spectra-Nova Technologies solar cell analyzer having a xenon lamp that simulating AM1.5G light from 400 nm to 1100 nm. The instrument was calibrated with a monocrystalline Si diode fitted with a KG3 filter to bring spectral mismatch to unity. The calibration standard was calibrated by the National Renewable Energy Laboratory (NREL). Each pixel of the device was carefully masked with black rubber to prevent parasitic charge leakage and inaccurate electrode overlap. Each substrate had 4 pixels with a defined area of 0.06 cm^2.[166]

9.2 Synthesis of azadipyrromethene precursors

9.2.1 Synthesis of chalcones (59a-e and 73a-c)

General Procedure for the aldole condensation to **59** and **73** according to [113]: A ketone **57** or **71** (50 mmol) and an aldehyde **58** or **72** (50 mmol) were dissolved in 25 ml ethanol. Potassium hydroxide (0.2 g, 3.56 mmol), dissolved in 5 ml water was added at r.t. and the mixture was stirred for 24 h over night or in case of **59e** for two days, until the product began to precipitate. The mixture was neutralized with acetic acid and the precipitated products were filtered and washed with ethanol and water. Recrystallization from ethanol gave **59** or **73** as white or yellow solids in good yields. The spectroscopic data and the melting points for all compounds **59a-e** and **73a-c** were in accordance to those reported in the literature.[28, 31, 167, 168, 169]
(E)-Chalcone (59a) was available at the institute.

(E)-1-(4-Methoxyphenyl)-3-phenylprop-2-en-1-one (59b)
Yield: 83%, **M.p.**: 105-106 °C;
^{1}**H NMR** (500 MHz, $CDCl_3$): δ (ppm) = 8.03 (d, J = 8.8 Hz, 2H), 7.49 (m, 7H), 6.97 (d,

J = 8.8, 2H), 3.07 (s, 6H).

(E)-1-(4-(Dimethylamino)phenyl)-3-phenylprop-2-en-1-one (59c)

Yield: 83%, **M.p.**: 153-155 °C;

^{1}**H NMR** (500 MHz, $CDCl_3$): δ (ppm) = 8.01 (d, J = 8.9 Hz, 2H), 7.78 (d, J = 15.6 Hz, 1H), 7.62-7.65 (m, 2H), 7.57 (d, J = 15.6 Hz, 1H), 7.37-7.41 (m, 3H), 6.67 (d, J = 8.8 Hz, 2H), 3.07 (s, 6H).

(E)-3-[4-(Dimethylamino)phenyl]-1-phenylprop-2-en-1-one (59d)

Yield: 76%, **M.p.**: 93-96 °C;

^{1}**H NMR** (500 MHz, $CDCl_3$): δ (ppm) = 7.9 (d, J = 8.9 Hz, 2H), 7.89 (d, J = 15.4 Hz, 2H), 7.52-7.55 (m, 3H), 7.47 (t, J = 7.2 Hz, 2H), 7.33 (d, J = 15.4 Hz, 1H), 6.68 (d, J = 8.8 Hz, 2H), 3.02 (s, 6H).

(E)-1,3-bis(4-(Dimethylamino)phenyl)prop-2-en-1-one (59e)

Yield: 59%, **M.p.**: 151-152 °C;

^{1}**H NMR** (500 MHz, $CDCl_3$): δ (ppm) = 8.0 (d, J = 8.9 Hz, 2H), 7.75 (d, J = 15.4 Hz, 1H), 7.53 (d, J = 8.8 Hz, 2H), 7.40 (d, J = 15.4 Hz, 1H), 6.68 (d, J = 8.9 Hz, 4H), 3.05 (s, 6H), 3.01 (s, 6H).

(E)-3-Phenyl-1-(thiophen-2-yl)prop-2-en-1-one (73a)

Yield: 95%, **M.p.**: 68-69 °C;

^{1}**H NMR** (500 MHz, $CDCl_3$): δ (ppm) = 7.86 (m, 2H), 7.67 (dd, J = 1.0 Hz, J = 4.8 Hz, 1H), 7.64 (m, 2H), 7.42 (m, 4H), 7.18 (dd, J = 1.0 Hz, J = 4.9 Hz, 1H).

(E)-1-Phenyl-3-(thiophen-2-yl)prop-2-en-1-one (73b)

Yield: 89%, **M.p.**: 94-96 °C;

^{1}**H NMR** (500 MHz, $CDCl_3$): δ (ppm) = 7.99 (m, 2H), 7.94 (d, J = 15.1 Hz, 1H), 7.58 (m, 1H), 7.49 (m, 2H), 7.42 (d, J = 5.5 Hz, 1H), 7.35 (m, 2 H), 7.10 (m, 1H).

(E)-1,3-Di(thiophen-2-yl)prop-2-en-1-one (73c)

Yield: 70%, **M.p.**: 65-67 °C;

^{1}**H NMR** (500 MHz, $CDCl_3$): δ (ppm) = 7.95 (d, J = 15.2 Hz, 1H), 7.83 (dd, J = 1.0 Hz, J = 3.8 Hz, 1H), 7.66 (dd, J = 1.0 Hz, J = 4.9 Hz, 1H), 7.41 (d, J = 5.0 Hz, 1H), 7.35 (d, J = 3.6 Hz, 1H), 7.19 (d, J = 15.2 Hz, 1H), 7.16 (dd, J = 1.0 Hz, J = 3.8 Hz, 1H), 7.08 (dd, J = 1.2 Hz, J = 3.6 Hz, 1H) .

Synthesis of 1-(5-aminothien-2-yl)-3-phenylpropen-2-en-1-ones (84a-c)

Method A: The 5-amino-2-acetyl-thiophen **81** (10 mmol) (prepared according to [133]) and benzaldehyde **82** (12 mmol) in ethanol (25 ml) were dissolved in 25 ml ethanol. Potassium hydroxide (0.1 g, 2.3 mmol), dissolved in 5 ml water was added at r.t. and the mixture is stirred for 24 h over night and neutralized with acetic acid. In order to facilitate crystallization, either half of the solvent is removed in vacuum or water is added. The precipitate is filtered and recristallized from ethanol/water or ethanol/toluol, to obtain **84**.

Method B: An 3-aminothioacrylamide (7.5 mmol) (prepared according to [133] is suspended in ethanol (50 ml) and water (10 ml) and (E)-1-chloro-4-phenylbut-3-en-2-one (chlorobenzalacetone) is added dropwise at RT. The mixture is stired for 15 min and triethylamine (1 ml, 7.5 mmol) is added. The mixture is stirred for 1 h and the precipitate is filtered several times from the mother liquor. Recrystallization from ethanol/water or ethanol/toluol gave the desired product **84**.

(E)-1-[5-(Dimethylamino)thiophen-2-yl]-3-phenylprop-2-en-1-one (84a)

Yield: 28% (method A), 40% (method B); **M.p.**: 154-155 °C from ethanol/water.

^{1}**H NMR** (500 MHz, $CDCl_3$): δ (ppm) = 7.76 (d, J = 15.5 Hz, 1H), 7.72 (d, J = 4.3 Hz, 1H), 7.61 (m, 2H), 7.36 (m, 3H), 7.33 (d, J = 15.5 Hz, 1H) 5.94 (d, J = 4.3 Hz, 1H), 3.10 (s, 6H).

Elemental analysis: Calc. for $C_{15}H_{15}NOS$: C 70.01, H 5.87, N 5.44, S 12.46, found: C 69.91, H 5.82, N 5.44, S 12.58.

(E)-3-Phenyl-1-[5-(pyrrolidin-1-yl)thiophen-2-yl]prop-2-en-1-one (84b)

Yield: 42% (method B), **M.p.**: 207-208 °C from ethanol/toluol.

^{1}**H NMR** (500 MHz, $CDCl_3$): δ (ppm) = 7.72 (d, J = 15.5 Hz, 1H), 7.68 (d, J = 4.5 Hz, 1H), 7.60 (m, 2H), 7.36 (m, 4H), 5.85 (d, J = 4.5 Hz, 1H).

Elemental analysis: Calc. for $C_{17}H_{17}NOS$: C 72.05, H 6.05, N 4.94, S 11.31, found: C 71.61, H 5.96, N 4.92, S 11.33.

(E)-1-(5-Morpholinothiophen-2-yl)-3-phenylprop-2-en-1-one (84c)

Yield: 19% (method A), 33% (method B) **M.p.**: 193-194 °C from ethanol/toluol.

^{1}**H NMR** (500 MHz, $CDCl_3$): δ (ppm) = 7.77 (d, J = 15.5 Hz, 1H), 7.70 (d, J = 4.4 Hz, 1H), 7.60 (m, 2H), 7.39 (m, 3H), 7.34 (d, J = 15.5 Hz, 1H) 6.13 (d, J = 4.4 Hz, 1H), 3.84 (t, J = 5.0 Hz, 4H), 3.33 (t, J = 5.0 Hz, 4H).

Elemental analysis: Calc. for $C_{17}H_{17}NO_2S$: C 68.20, H 5.72, N 4.68, S 10.71, found: C 67.94, H 5.84, N 4.68, S 10.87.

9.2.2 4-nitro-1,3-diarylbutan-1-ones (60a-d, 65)

General Procedure for the preparation of 4-nitro-1,3-diarylbutan-1-ones according to [170]: A solution of a chalcone **59** (100 mmol), nitro methane (500 mmol), and K_2CO_3 (0.2 mmol) in ethanol (100 mL) is heated to reflux for 3-12 h. After cooling to room temperature, the mixture is concentrated in vacuum and a few drops of water added to force the precipitation and further cooled in a refrigerator. The precipitate is filtered and recrystallized from ethanol, the NMR-spectra are in accordance with the literature [28, 31].

4-Nitro-1,3-diphenylbutan-1-one (60a)
Yield: 90%, **M.p.**: 84-86 °C;
^{1}**H NMR** (500 MHz, $CDCl_3$): δ (ppm) = 7.91 (d, J = 8.5 Hz, 2H), 7.56 (t, J = 7.4 Hz, 1H), 7.45 (t, J = 7.5 Hz, 2H), 7.32 (t, J = 7.4 Hz, 2H), 7.26 (m, 3H), 4.75 (m, 2H), 4.23 (m, 1H), 3.45 (m, 2H).

1-(4-Methoxyphenyl)-4-nitro-3-phenylbutan-1-one (60b)
Yield: 79%, **M.p.**: 89-91 °C;
^{1}**H NMR** (500 MHz, $CDCl_3$): δ (ppm) = 7.91 (d, J = 9.0 Hz, 2H), 7.28 (m, 5H), 6.91 (d, J = 9.0 Hz, 2H), 4.75 (m, 2H), 4.18 (m, 1H), 3.85 (s, 3H), 3.39 (m, 2H).
1-[4-(Dimethylamino)phenyl]-4-nitro-3-phenylbutan-1-one (60c)
Yield: 60%, **M.p.**: 73-75 °C;
^{1}**H NMR** (500 MHz, $CDCl_3$): δ (ppm) = 7.81 (d, J = 7.0 Hz, 2H), 7.30 (m, 5 H), 6.62 (d, J = 7.1 Hz, 2H), 4.85 (m, 1H), 4.65 (m, 1H), 4.20 (m, 1H), 3.29 (m, 2H), 3.04 (s, 6H).

3-[4-(Dimethylamino)phenyl]-4-nitro-1-phenylbutan-1-one (60d)
Yield: 35%, **M.p.**: 99-101 °C;
^{1}**H NMR** (500 MHz, $CDCl_3$): δ (ppm) = 7.91 (d, J = 8.4 Hz, 2H), 7.55 (t, J = 7.4 Hz, 1 H), 7.44 (t, J = 7.7 Hz, 2 H), 7.12 (d, J = 8.7 Hz, 2 H), 6.66 (d, J = 8.6 Hz, 2H), 4.77 (m, 1H), 4.63 (m, 1H), 4.11 (m, 1H), 3.41 (m, 2H), 2.90 (s, 6H).

5-Nitro-4-phenylpentan-2-one (65)
Yield: 77%, **M.p.**: 95-97 °C;
^{1}**H NMR** (500 MHz, $CDCl_3$): δ (ppm) = 7.31 (m, 2H), 7.25 (m, 1H), 7.21 (m, 2H), 4,68 (m, 1H), 4.58 (m, 1H), 3.99 (m, 1H), 2.90 (d, J = 7.0 Hz, 2H), 2.10 (s, 3H).

9.2.3 Synthesis of 4-Keto-2,4-diphenylbutanenitrile (61)

The cyanide addition was carried out according to [171]. To a solution of E-chalcone **59a** (20.80 g, 100 mmol), acetic acid (6 g, 100 mmol) in ethanol (250 mL) at 35 °C, sodium cyanide (7.35 , 150 mmol) in 25 ml water is added dropwise. The solution is stirred for 4 h and cooled to room temperatur and stand overnight in the refrigerator. The precipitate is sucked of and washed with ethanol. Recrystallization from ethanol gave 4-keto-2,4-diphenylbutanenitrile (16 g, 68 mmol, 68 %).

4-Keto-2,4-diphenylbutanenitrile (61)
Yield: 68%, **M.p.**:122-124 °C;
^{1}**H NMR** (500 MHz, $CDCl_3$): δ (ppm) = 7.91 (d, J = 7.2 Hz, 2H), 7.58 (t, J = 7.5 Hz, 1H), 7.40 (m, 7H), 4.55 (m, 2H), 3.71 (m, 1H), 3.50 (m, 1H).

9.3 Synthesis of azadipyrromethenes (62a-d)

Method A: A mixture of a 1,3-bis-(het)aryl)-4-nitrobutanone **60** (1 mmol) and ammonium acetate (20 mmol) is refluxed in n-butanol (100 mL) for 24 h. After cooling to RT, the reaction mixture is diluted with water and extracted three times with dichloromethane. The combined organic layers were washed with water and brine, dried with sodium sulfate, and concentrated to give the crude product as a dark blue-black solid. Purification by column chromatography yields the desired products as coppery shiny crystals.

Method B: A mixture of a 1,3-bis-(het)aryl)-4-nitrobutanone **60** (1 mmol) and ammonium acetate (20 mmol) is refluxed in formamide (100 ml) for 2-10 min until the reaction miture turnes blue and a coppery shiny precipitate is formed. The reaction mixture is cooled to RT and the solid is filtered, and washed with cold methanol. Purification by column chromatography yields the desired products as coppery shiny crystals.

Method C: A mixture of a 4-keto-2,4-diphenylbutanenitrile **61** (4 g, 17 mmol) and ammonium acetate (200 mmol) is refluxed in butanol (100 ml) for 6 h. The reaction mixture is cooled to RT and the solid is filtered, and washed with cold methanol. Purification by column chromatography yields the desired products as coppery shiny crystals.

(3,5-Diphenyl-1*H*-pyrrol-2-yl)-(3,5-diphenyl-pyrrol-2-ylidene)-amine (62a)

Yield: 31% (method A), 24% (method B), 13% (method C) **M.p.**: 287-289 °C;

^{1}**H NMR** (500 MHz, $CDCl_3$): δ (ppm) = 8.05 (d, J = 7.2 Hz, 4H), 7.95 (d,J = 7.2 Hz, 4H), 7.52 (d, J = 7.2 Hz, 4H),7.40-7.48 (m, 4H), 7.52 (d, J = 7.2 Hz, 4H), 7.19 (s, 2H).

^{13}**C NMR** (126 MHz, $CDCl_3$): 155.1, 149.6, 142.7, 133.7, 132.2, 130.1, 129.2, 129.1, 128.3, 128.0, 126.6, 114.9.

MS (EI) m/z: 450.2 [M+H]

(3-(4-Methoxyphenyl)-5-phenyl-1*H*-pyrrol-2-yl)-(3-(4-methoxyphenyl)-5-phenylpyrrol-2-ylidene)-amine (62b)

Yield: 27% (method A), 12% (method B) **M.p.**: 238-240 °C;

^{1}**H NMR** (500 MHz, $CDCl_3$): δ (ppm) = 8.06 (d, J = 8.2 Hz, 4H), 7.90 (d, J = 8.8 Hz, 4H), 7.39 (m, 6H), 7.13 (s, 2H), 7.04 (d, J = 8.8 Hz, 4H), 3.91 (s, 6H).

^{13}**C NMR** (126 MHz, $CDCl_3$): 61.8, 154.2, 149.4, 142.4, 134.2, 129.2, 128.4, 128.3, 127.8, 125.5, 114.9, 114.7, 55.9.

MS (EI) m/z:510.2 [M+H];

(5-(4-Dimethylamino-phenyl)-3-phenyl-1*H*-pyrrole-2-yl)-(5-(4-dimethylamino-phenyl)-3-phenylpyrrol-2-ylidene)amine (62c)

Yield: 22% (method A), 16% (method B) **M.p.**: 228-230 °C (from dichloromethan/hexane).

^{1}**H NMR** (500 MHz, $CDCl_3$): δ (ppm) = 8.04 (d, J= 9.0 Hz, 4H), 7.94 (d, J = 7.0 Hz, 4H), 7.5 (m, 6H), 7.05 (s, 2H), 6.78 (d, J = 9.0 Hz, 4H), 3.04 (s, 12H).

^{13}**C NMR** (126 MHz, $CDCl_3$): 153.8, 151.3, 149.3, 141.0, 134.4, 129.0, 128.1, 127.9, 127.4, 120.3, 113.7, 112.3, 40.3.

MS (EI) m/z: 536.3 [M+H];

(3-(4-Dimethylamino-phenyl)-5-phenyl-1*H*-pyrrole-2-yl)-(3-(4-dimethylamino-phenyl)-5-phenylpyrrol-2-ylidene)amine (62d)

Yield: 41% (method B), **M.p.**: 249 °C (from hexan/dichloromethan).

^{1}**H NMR** (500 MHz, $CDCl_3$): δ (ppm) = 8.04 (d, J = 6.9 Hz, 4H), 7.94 (d, J = 7.22 Hz, 4H), 7.50 (t, J = 7.3 Hz, 4H), 7.42 (t, J = 7.3 Hz, 2H), 7.05 (s, 2H), 6.77 (d, J = 7.1 Hz, 4H), 3.03 (s, 12H).

^{13}**C NMR** (126 MHz, $CDCl_3$): 154.8, 150.4, 149.8, 143.1, 132.9, 130.5, 129.7, 129.2, 126.6, 122.9, 112.2, 111.9, 40.6.

MS (EI) m/z: 536.3 [M+H];

9.3.1 Synthesis of borondifluoride-azadipyrromethenes (63a-e)

General Procedure for the preparation of the borondifluoride-azadipyrromethenes **63**: An azamethene **62** (12.6 mmol) is dissolved in dichloroethane (150 mL) and diisopropylethylamine (10.5 mL, 60.8 mmol) is added and the mixture stirred for 1h. Then $BF_3{\cdot}OEt_2$ (7.5 mL, 60.5 mmol) is added at room temperature and the resulting mixture refluxed until the starting material was completely converted (ca. 1-3h) to the corresponding product (checked with TLC). The cold reaction mixture is diluted with water and extracted twice with dichloromethane (100 mL). The combined organic layers were dried with sodium sulfate and concentrated in vacuum. The crude product is purified by flash chromatography or recrystallization, to obtain the products as coppery shiny crystals. By this procedure, the following compounds were prepared:

1,3,5,7-Tetraphenyl-borondifluoride-azadipyrromethene (63a)
Yield: 82%, **M.p.**: 231-232 °C;
^{1}H NMR (500 MHz, $CDCl_3$): δ (ppm) = 8.05 (m, 8H), 7.46 (m, 12H), 7.03 (s, 2H).
^{13}C NMR (126 MHz, $CDCl_3$): 159.6, 145.7, 144.2, 132.4, 131.6, 130.9, 129.7, 129.6, 129.4, 128.7, 128.6, 119.2.
MS (EI) *m/z*: 498.1 [M+H];

1,7-Diphenyl-3,5-bis(4-methoxy-phenyl)-borondifluoride-azadipyrromethene (63b)
Yield: 71%, **M.p.**: 200-202 °C;
^{1}H NMR (500 MHz, $CDCl_3$): δ (ppm) = 8.07 (m, 8H), 7.45 (m, 6H), 7.03 (s, 2H), 7.01 (d, J = 7.2 Hz, 4H), 3.87 (s, 6H).
^{13}C NMR (126 MHz, $CDCl_3$): 162.0, 158.1, 145.4, 143.1, 132.5, 131.8, 129.5, 129.4, 128.6, 124.2, 118.7, 114.3, 55.5.
MS (EI) *m/z*: 558.2 [M+H];

1,7-Diphenyl-3,5-bis(4-dimethylamino-phenyl)-borondifluoride-azadipyrromethene (63c)
Yield: 62%, **M.p.**: 256 °C (from dichloromethan/cyclohexane).
^{1}H NMR (500 MHz, $CDCl_3$): δ (ppm) = 8.12 (d, J = 9.0 Hz, 4H), 8.08 (d, J = 7.2 Hz, 4H), 7.43 (t, J = 7.2 Hz, 4H), 7.37 (t, J = 9.0 Hz, 2H), 7.09 (s, 2H), 6.76 (d, J = 9.0 Hz, 4H), 3.07

(s, 12H).
^{13}**C NMR** (126 MHz, $CDCl_3$): 156.4, 151.8, 145.2, 140.9, 133.1, 131.6, 129.1, 128.5, 128.4, 119.3, 118.0, 111.9, 40.1.
MS (EI) m/z: 584.2 [M+H];

1,7-Bis(4-dimethylamino-phenyl)-3,5-diphenyl-borondifluoride-azadipyrromethene (63d)
Yield: 50%, **M.p.**: 260 °C (from dichloromethan/cyclohexane).
^{1}**H NMR** (500 MHz, $CDCl_3$): δ (ppm) = 8.07 (d, J = 8.9 Hz, 4H), 8.00 (d, J = 7.9 Hz, 4H), 7.45 (m, 6H), 6.92 (m, 4H), 6.82 (s, 2H), 3.09 (s, 12H).
^{13}**C NMR** (126 MHz, $CDCl_3$): 158.1, 151.3, 145.8, 144.0, 132.7, 131.1, 130.2, 129.5, 128.5, 121.5, 115.4, 112.2, 40.4.
MS (EI) m/z: 584.2 [M+H];

1,3,5,7-Tetra(4-dimethylamino-phenyl)-borondifluoride-azadipyrromethene (63e)
Yield: 0%, **M.p.**: 260 °C;
^{1}**H NMR** (500 MHz, $CDCl_3$): δ (ppm) = 8.00 (d, J = 8.7 Hz, 8H), 6.82 (s, 2H), 6.71 (d, J = 8.8 Hz, 8H), 3.09 (s, 24H).
^{13}**C NMR** (126 MHz, $CDCl_3$): not possible.
^{19}**F NMR** (282 MHz, $CDCl_3$): δ (ppm) = -131.0 (m)
MS (EI) m/z: 670.4 [M+H];

Synthesis of boroncatechole-azadipyrromethene (70)

The azamethene **62c** (1 mmol, 0.54 g) is dissolved in dichloroethane (50 mL) and diisopropylethylamine (1.2 mL, 10 mmol) is added and the mixture stirred for 1h. Then 2-butylbenzo-dioxaborole (1.76g, 10 mmol) is added at room temperature and the resulting mixture refluxed for 24 h. The cold reaction mixture is diluted with water and extracted twice with dichloromethane (100 mL). The combined organic layers were dried with sodium sulfate and concentrated in vacuum. The crude product is purified by flash chromatography with dichloromethane yielding 1,7-diphenyl-3,5-bis(4-dimethylamino-phenyl)-boroncatechol-azadipyrromethene (190 mg, 29%) as dark solid.

1,7-diphenyl-3,5-bis(4-dimethylamino-phenyl)-boroncatechol-azadipyrromethene (70)

Yield: 29%, **M.p.**: 245 °C; (DCM).

^{1}**H NMR** (500 MHz, $CDCl_3$): δ (ppm) = 8.09 (d, J = 8.1 Hz, 4H), 7.43 (t, J = 7.2 Hz, 4H), 7.38 (t, J = 7.3 Hz, 2H), 7.30 (m, 4H), 6.68 (s, 2H), 6.35 (m, 2H), 6.25 (d, J = 8.5 Hz, 2H), 6.17 (m, 2H), 2.86 (s, 12H).

^{13}**C NMR** (126 MHz, $CDCl_3$): 161.0, 151.2, 145.4, 141.9, 133.0, 130.4, 129.2, 128.7, 128.4, 119.9, 119.6, 118.4, 110.9, 109.2, 40.1.

MS (EI) m/z: 654.4 [M+H];

Elemental analysis: Calc. for $C_{42}H_{36}N_5O_2B$: C 77.18 H 5.55, N 10.72, found: C 76.15, H 5.26, N 10.50.

9.3.2 Synthesis of thienyl-substituted azadipyrromethenes (75a-c)

General Procedure for the preparation of the thienyl-substituted aza-dipyrromethenes **75a-75c**: A solution of a chalcone **73** (100 mmol), nitro methane (500 mmol), and K_2CO_3 (0.2 mmol) in ethanol (100 mL) was heated to reflux for 6-12 h.[170] After cooling to room temperature, the solvent was removed in vacuum and the oily residue obtained was dissolved in ethyl acetate and washed with water (3 x 50 mL). The combined organic layers were washed with brine, dried over sodium sulfate, and concentrated to give the nitro compounds **74** as a yellowish oily residue in nearly quantitative yields which were used in the next step without further purification. A mixture of the 1,3-bis-(het)aryl)-4-nitrobutanone **74** (1 mmol) obtained and ammonium acetate (20 mmol) was refluxed in n-butanol (100 mL) for 24 h. After cooling to r.t., the reaction was diluted with water and extracted three times with dichloromethane. The combined organic layers were washed with water and brine, dried with sodium sulfate, and concentrated to give the crude product as a dark blue-black solid. Purification by column chromatography yields the desired products as coppery shiny crystals. By this procedure, the following compounds were synthesized:

(3-Phenyl-5-thienyl-1*H*-pyrrol-2-yl)-(3-phenyl-5-thienyl-pyrrol-2-ylidene)-amine (75a)

Yield: 8%, **M.p.**: 262-263 °C; (chloroform/hexane 4:1).

^{1}**H NMR** (500 MHz, $CDCl_3$): δ (ppm) = 8.03 (d, J = 7.2, 4H), 7.60 (d, J = 3.7, 2H), 7.50 (d, J = 4.9, 2H), 7.41 (t, J = 7.2 Hz, 4H), 7.34 t, J = 7.3 Hz, 2H), 7.19 (t, J = 3.5 Hz, 2H), 7.06 (s, 2H).

^{13}**C NMR** (126 MHz, $CDCl_3$): 149.3, 149.0, 142.2, 137.0, 133.5, 129.0, 128.8, 128.7, 128.2, 128.0, 127.3, 114.7.

MS (EI) *m/z*: 462.1 [M+H];

Elemental analysis: Calc. for $C_{28}H_{19}N_3S_2$: C 72.86 H 4.15, N 9.10, S 13.89 , found: C 72.37, H 4.04, N 8.27, S 13.92.

(5-Phenyl-3-thienyl-1*H*-pyrrol-2-yl)-(5-phenyl-3-thienyl-pyrrol-2-ylidene)-amine (75b)

Yield: 6%, **M.p.**: 257-260 °C; (chloroform/hexane 2:1).

^{1}**H NMR** (500 MHz, $CDCl_3$): δ (ppm) = 7.91 (d, J = 7.2, 4H), 7.86 (d, J = 2.4, 2H), 7.52 (t, J = 7.1, 4H), 7.46 (d, J = 7.2, 3H), 7. (d, J = 4.1 Hz, 2H), 7.15 (t, J = 4.3, 2H), 7.09 (s, 2H).

^{13}**C NMR** (126 MHz, $CDCl_3$): 155.3, 149.1, 136.9, 135.9. 131.9, 130.1, 129.1, 127.9, 127.77, 127.2, 126.5.

MS (EI) *m/z*: 462.1 [M+H];

Elemental analysis: Calc. for $C_{28}H_{19}N_3S_2$: C 72.86 H 4.15, N 9.10, S 13.89, found: C 72.68, H 3.69, N 9.29, S 12.35.

(3,5-Dithienyl-1*H*-pyrrol-2-yl)-(3,5-dithienyl-pyrrol-2-ylidene)-amine (75c)

Yield: 12%, **M.p.**: 312-315 °C; (chloroform/hexane 4:1).

^{1}**H NMR** (500 MHz, $CDCl_3$): δ (ppm) = 7.84 (d, J = 3.6, 2H), 7.58 (d, J = 3.6, 2H), 7.50 (d, J = 4.9, 2H), 7.41 (d, J = 5.0 Hz, 2H), 7.19 (d, J = 4.9 Hz, 2H), 7.14 (d, J = 5.0 Hz, 2H), 6.93 (s, 2H).

^{13}**C NMR** (126 MHz, $CDCl_3$): δ (ppm) = 149.2, 148.9, 136.9, 136.6, 135.7, 128.8, 128.7, 127.9, 127.7, 127.4, 127.3, 113.0.

MS (EI) *m/z*: 474.0 [M+H];

Elemental analysis: Calc. for $C_{24}H_{15}N_3S_4$: C 60.86 H 3.19, N 8.87, S 27.08, found: C 61.23, H 2.77, N 8.21, S 27.10.

9.3.3 Synthesis of borondifluoride-thienyl-azadipyrromethenes (76a-c)

General Procedure for the preparation of the borondifluoride-azadipyrromethenes **76a-76c**: An azamethene **75a-c** (12.6 mmol) was dissolved in dichloroethane (150 mL) and diisopropylethylamine (10.5 mL, 60.8 mmol) was added and the mixture stirred for 1h. Then $BF_3{\cdot}OEt_2$ (7.5 mL, 60.5 mmol) was added at room temperature and the resulting mixture refluxed until the starting material was completely converted (ca. 2h) to the corresponding product (checked with TLC). The cold reaction mixture was diluted with water and extracted twice with dichloromethane (100 mL). The combined organic layers were dried with sodium sulfate and concentrated in vacuum. The crude products was purified by flash chromatography using chloroform/hexane as eluent, to obtain the products as coppery shiny crystals. By this procedure, the following compounds were prepared:

1,7-Diphenyl-3,5-dithienyl-borondifluoride-azadipyrromethene (76a)
Yield: 78%, **M.p.**: 297-298 °C; (chloroform/hexane 4:1).
^{1}**H NMR** (500 MHz, $CDCl_3$): δ (ppm) = 8.37 (d, J = 3.8, 2H), 8.05 (d, J = 8.3, 4H), 7.63 (d, J = 4.3, 2H), 7.42 (m, 3H), 7.27 (t, J = 4.0 Hz, 2H), 7.17 (s, 2H).
^{13}**C NMR** (126 MHz, $CDCl_3$): 159.5, 144.9, 138.3, 134.7, 131.5, 130.8, 130.3, 129.7, 129.4, 128.5, 128.3.
MS (EI) m/z: 474.0 [M+H];
Elemental analysis: Calc. for $C_{28}H_{18}BF_2N_3S_2$: C 66.02, H 3.56, N 8.25, S 12.59; found: C 66.22, H 3.25, N 7.74, S 11.61.

1,7-Dithienyl-3,5-diphenyl-borondifluoride-azadipyrromethene (76b)
Yield: 68%, **M.p.**: 272-274 °C; (chloroform/hexane 2:1).
^{1}**H NMR** (500 MHz, $CDCl_3$): δ (ppm) = 7.94 (m, 4H), 7.86 (dd, J = 3.6, J = 0.9, 2H), 7.51 (dd, J = 5.0, J = 0.9, 4H), 7.40 (t, J = 3.3, 6H), 7.14 (dd, J = 5.0 Hz, J = 1.2 Hz, 2H), 6.84 (s, 2H).
^{13}**C NMR** (126 MHz, $CDCl_3$): 159.5, 144.9, 138.3, 134.7, 131.5, 130.8, 130.3, 129.7, 129.4, 128.5, 128.3,
MS (EI) m/z: 510.1 [M+H];
Elemental analysis: Calc. for $C_{28}H_{18}BF_2N_3S_2$: C 66.02, H 3.56, N 8.25, S 12.59; found: C 66.12, H 3.67, N 7.51, S 12.25.

1,3,5,7-Tetrathienyl-borondifluoride-azadipyrromethene (76c)
Yield: 82%, **M.p.**: 318-320 °C; (chloroform/hexane 4:1).
^{1}**H NMR** (500 MHz, $CDCl_3$): δ (ppm) = 7.06 (s,2H), 7.19 (t, J = 5.0, 2H), 7.25 (t, 2H), 7.55 (d, J = 5.0 Hz, 2H), 7.62 (d, J = 5.0 Hz, 2H), 7.92 (d, J = 3.7 Hz, 2H), 8.34 (d, J = 3.8 Hz, 2H).
^{13}**C NMR** (126 MHz, $CDCl_3$): δ (ppm) = 151.8, 149.7, 148.2, 134.4, 133.9, 133.0, 131.5, 129.9, 129.7, 129.4, 129.1, 116.2.
MS (EI) m/z: 522.4 [M+H];

Elemental analysis: Calc. for $C_{24}H_{14}N_3BF_2S_4$: C 55.28, H 2.71, N 8.06, S 24.60, found: C 54.86, H 2.70, N 7.81, S 25.23.

Synthesis of 2,6-dithienyl-borondifluoride-azadipyrromethene dyes (76d,e)

To tetraaryl-azadipyrromethene **75d** (0.52 g, 1.16 mmol) dissolved in benzene (50 ml), bromine was added (0.55 g, 3.47 mmol) at RT and the mixture was stirred. After complete conversion (2 h) the reaction was quenched with saturated sodium thiosulfate and extracted with THF. The combined organic layers were washed with water and brine and evaporated in vacuum. This product (0.5 g, 60 % yield), was used directly in the next step. The received product was dissolved in dichloroethane (150 ml) and diisopropylethylamine (10.5 ml, 60.8 mmol) was added. The mixture was stirred for 1 h, and $BF_3 \cdot OEt_2$ (7.5 ml, 60.5 mmol) was added at room temperature. Then the mixture was refluxed until a complete conversion of the starting material was observed (checked with TLC, ca. 4 h). The cold reaction mixture was quenched with water and extracted twice with dichloromethane (100 mL). The combined organic layers were dried with sodium sulfate and concentrated in vacuum. The crude product was purified by flash chromatography (dichloromethane/hexane), yielding the desired product **57d** as coppery shiny crystals. The spectroscopic data were identical to those reported in the literature.[28] The dibromo compound **77** (0.2 g, 0.3 mmol) and 2-(tributylstannyl)thiophene (0.24 g, 0.61 g) were dissolved in dry toluene under nitrogen. Tetrakis(triphenylphosphine)palladium(0) (0.14 g, 0.1 mmol) was added and the mixture was refluxed over night, until no starting material could be detected by TLC. The reaction mixture was cooled to r.t. and evaporated to dryness. Purification by column chromatography with chloroform yielded the product 1d in a yield of 85 % (169 mg).

1,3,5,7-Tetraphenyl-2,6-dibromo-borondifluoride-azadipyrromethene (77d)

Yield: 86%, **M.p.**: 277-279 °C; (dichloromethane/hexane 4:1).

^{1}**H NMR** (500 MHz, $CDCl_3$): δ (ppm) = 7.87 (m, 4H), 7.71 (m, 4H), 7.46 (m, 12H).

^{13}**C NMR** (126 MHz, $CDCl_3$): δ (ppm) = 158.4, 144.2, 142.9, 130.8, 130.7, 130.5, 130.2, 129.6, 129.3, 128.0, 127.9, 110.2.

MS (EI) *m/z*: 656.1 [M+H].

1,3-Diphenyl-2,6-dibromo-5,7-di(4-methoxy-phenyl)-borondifluoride-azadipyrromethene (77e)

Yield: 78%, **M.p.**: 268-270 °C; (dichloromethane/hexane 4:1).

^{1}**H NMR** (500 MHz, $CDCl_3$): δ (ppm) = 7.85 (m, 4H), 7.76 (d, J = 8.8 Hz, 4H), 7.43 (m, 6H), 6.97 d, J = 8.8 Hz, 4H), 3.85 (s, 6H).

^{13}**C NMR** (126 MHz, $CDCl_3$): δ (ppm) = 161.7, 157.4, 154.7, 144.1, 142.4, 132.4, 130.7, 130.6, 129.4, 127.9, 121.7, 113.5, 110.1, 55.0.

MS (EI) *m/z* 717.2 [M+H].

1,3,5,7-Tetraphenyl-2,6-dithienyl-borondifluoride-azadipyrromethene (76d)

Yield: 85%, **M.p.**: 192 °C; (chloroform).

^{1}**H NMR** (500 MHz, $CDCl_3$): δ (ppm) = 6.62 (dd, J = 3.6 Hz, J = 1.1 Hz, 2H), 6.85 (dd, J = 5.1 Hz, J = 3.6 Hz, 2H), 7.20 (dd, J = 5.1 Hz, J = 1.1 Hz, 2H), 7.31 (m, 8H), 7.34 (t, J = 7.4 Hz, 4H) , 7.53 (d, J = 7.2 Hz, 4H), 7.54 (d, J = 6.8 Hz, 4H).

^{13}**C NMR** (126 MHz, $CDCl_3$): δ (ppm) =159.6, 145.1, 142.0, 133.5, 131.2, 130.9, 130.1, 130.0, 128.8, 128.7, 127.8, 127.7, 127.0, 126.8, 126.4, 125.8.

MS (EI) *m/z*: 662.3 [M+H];

Elemental analysis: Calc. for $C_{40}H_{26}BF_2N_3S_2$: C 72.62, H 3.96, N 6.35, S 9.69, found: C 72.86, H 3.70, N 6.13, S 9.23.

1,3-Diphenyl-2,6-dithienyl-5,7-di(4-methoxy-phenyl)-borondifluoride-azadipyrromethene (76e)

Yield: 90%, **M.p.**: 192 °C; (dichloromethan/hexane 4:1).

^{1}**H NMR** (500 MHz, $CDCl_3$): δ (ppm) = 7.51 (m, 4H), 7.49 (d, J = 8.8 Hz, 4H), 7.29 (m, 3H), 7.22 (dd, J = 5.1 Hz, J = 1.1 Hz, 2H), 6.88 (dd, J = 5.1 Hz, J = 1.5 Hz, 2H), 6.82 (d, J = 8.8 Hz, 4H), 6.66 (dd, J = 3.5 Hz, J = 1.1 Hz, 2H), 3.80 (s, 6H).

^{13}**C NMR** (126 MHz, $CDCl_3$): δ (ppm) = 161.1, 158.8, 145.03, 141.6, 134.0, 132.1, 131.3, 128.8, 128.5, 127.7, 126.7, 122.5, 113.3, 96.7, 55.1.

MS (EI) *m/z*: 722.2 [M+H];

Elemental analysis: Calc. for $C_{42}H_{30}BF_2N_3O_2S_2$: C 69.90, H 4.19, N 5.82, S 8.89, found: C 68.87, H 3.85, N 5.73, S 8.59.

9.4 Synthesis of azadiisoindomethene dyes

9.4.1 Synthesis of bis-(aryl)-aza-diisoindomethene dyes (96a-f)

General procedure for the preparation of bis-(aryl)-azadiisoindomethenes **96**: 1.1 eq phenyl Grignard in diethylether were added at -20 °C to a suspension of phthalonitrile (6.4 g, 50 mmol) in absolute diethylether (50 ml) under nitrogen. After complete addition, the reaction mixture was allowed to warm up to room temperature and was stirred for additional 3 h. The dark reaction mixture was evaporated to dryness and was heated in 3 portions with formamide (100ml each) rapidly until a coppery shiny precipitate was formed and a gas evolution occurs. The reaction mixture was refluxed for 2 minutes and then cooled to room temperature. The precipitate was filtrated and washed 5 times with methanol/water (2:1). Flash chromatography (dichloromethane/hexane) yielded aza-bis-(phenyl)-diisoindomethene (5.46g, 55%) as a coppery solid.

Bis-(*o*-methyl-phenyl)-azadiisoindomethene (96a)
Yield: 6%, **M.p.**: 192 °C; (chloroform/hexane 4:1).
^{1}**H NMR** (500 MHz, $CDCl_3$): δ (ppm) = 8.12 (d, J = 7.9 Hz, 2H), 7.62 (d, J = 6.6, 2H), 7.55 (d, J = 7.9 Hz, 2H), 7.40 (t, J = 7.7 Hz, 2H), 7.35 (m, 6H), 7.25 (d, J = 7.0 Hz, 2H), 2.50 (s, 6H).
^{13}**C NMR** (126 MHz, $CDCl_3$): δ (ppm) = 150.0, 142.8, 136.6, 134.3, 132.0, 131.3, 131.1, 130.0, 129.1, 127.5, 125.9, 125.8, 122.2, 12.9, 20.9.
MS (EI) m/z: 426.3 [M+H];
Elemental analysis: Calc. for $C_{30}H_{23}N_3$: C 84.68, H 5.45, N 9.87, found: C 84.63, H 5.50, N 9.62.

Bis-(*o*-methoxy-phenyl)-azadiisoindomethene (96b)
Yield: 3%, **M.p.**: 260 °C; (hexane/ethylacetat 5:1).
^{1}**H NMR**(500 MHz, $CDCl_3$): δ (ppm) = 8.12 (d, J = 8.0 Hz, 2H), 7.96 (dd, J = 7.5/1.6 Hz 2H), 7.78 (d, J = 8.0 Hz, 2H), 7.38 (m, 4H), 7.26 (t, J = 8.0 Hz, 4H), 7.10 (t, J = 7.5 Hz, 2H), 7.04 (d, J = 8.0 Hz, 2H), 3.79 (s, 6H).
^{13}**C NMR** (126 MHz, $CDCl_3$): δ (ppm) = 157.0, 147.2, 145.9, 134.6, 131.1, 130.2, 130.1, 126.9, 125.7, 122.9, 122.4, 120.9, 111.3, 55.6.
MS (EI)m/z: 458.2 [M+H].
Elemental analysis: Calc. for $C_{30}H_{23}N_3O_2$: C 78.75; H 5.07; N 9.18; found: C 77.90; H 4.96; N 8.35.

Bis-(phenyl)-azadiisoindomethene (96c)

Yield: 55%, **M.p.** 260 °C; (dichloromethane/hexane 1:1).

^{1}H NMR (500 MHz, $CDCl_3$): δ (ppm) = 8.13 (d, J = 7.9 Hz, 2H), 803 (d, J = 7.9, 4H), 7.96 (d, J = 8.0 Hz, 2H), 7.57 (t, J = 7.4 Hz, 4H), 7.48 (t, J = 7.4 Hz, 2H), 7.41 (t, J = 7.8 Hz, 2H), 7.32 (t, J = 7.9 Hz, 2H).

^{13}C NMR (126 MHz, $CDCl_3$): δ (ppm) = 148.6, 143.9, 135.5, 133.2, 129.9, 129.4, 129.2, 127.7, 127.6, 126.3, 122.1, 121.3.

MS (EI) (m/z): 398.2 [M+H].

Elemental analysis: Calc. for $C_{28}H_{19}N_3$ C: 84.61; H: 4.82; N 10.57; found: C 82.86, H 4.74, N 11.26.

Bis-(*p*-methyl-phenyl)-azadiisoindomethene (96d)

Yield: 36%, **M.p.**: 261 °C; (dichloromethane/hexane 2:1).

^{1}H NMR (500 MHz, $CDCl_3$): δ (ppm) = 8.11 (d, J = 7.9 Hz, 2H), 7.94 (d, J = 7.9, 2H), 7.93 (d, J = 8.1 Hz, 4H), 7.40 (t, J = 7.7 Hz, 2H), 7.38 (t, J = 7.0 Hz, 4H), 7.30 (d, J = 7.0 Hz, 2H), 2.47 (s, 6H).

^{13}C NMR(126 MHz, $CDCl_3$): δ (ppm) = 148.3, 143.6, 139.7, 135.3, 130.4, 129.9, 129.8, 127.6, 127.3, 126.4, 122.1, 121.2, 21.5.

MS (EI) m/z: 426.3 [M+H];

Elemental analysis: Calc. for $C_{30}H_{23}N_3$: C 84.68, H 5.45, N 9.87, found: C 84.93, H 5.77, N 9.87.

Bis-(*p*-methoxy-phenyl)-azadiisoindomethene (96e)

Yield: 30%, **M.p.**: 260 °C; (dichloromethane/hexane 2:1).

^{1}H NMR(500 MHz, $CDCl_3$): δ (ppm) = 8.10 (d, J = 7.9 Hz, 2H), 7.97 (d, J = 8.8, 4H), 7.91 (d, J = 8.0 Hz, 2H), 7.37 (t, J = 7.0 Hz, 4H), 7.29 (t, J = 7.0 Hz, 2H), 7.08 (d, J = 8.8 Hz, 2H), 3.91 (s, 6H) ppm.

^{13}C NMR (126 MHz, $CDCl_3$): δ (ppm) = 160.6, 147.6, 143.4, 135.3, 129.6, 129.2, 127.2, 126.1, 125.9, 122.1, 121.2, 114.7, 55.5 ppm.

MS (EI) m/z: 458.2 [M+H];

Elemental analysis: Calc. for $C_{30}H_{23}N_3O_2$: C 78.75 H 5.07, N 9.18, found: C 78.43, H 4.99, N 9.02.

Bis-(5-methyl-thienyl)-azadiisoindomethene (96f)

Yield: 21%, **M.p.**: 260 °C; (chloroform).

^{1}**H NMR** (500 MHz, $CDCl_3$): δ (ppm) = 8.06 (d, J = 7.9 Hz, 2H), 7.93 (d, J = 7.9 Hz 2H), 7.63 (s, 2H), 7.39 (d, J = 7.3 Hz, 2H), 7.31 (t, J = 7.3 Hz, 2H), 6.90 (d, J = 3.7 Hz, 2H), 2.61 (s, 6H) ppm.
^{13}**C NMR** (126 MHz, $CDCl_3$): δ (ppm) = 143.9, 143.6, 141.7, 135.0, 134.5, 129.4, 127.4, 127.3, 127.2, 126.2, 121.7, 121.2, 15.8 ppm.
MS (EI) m/z: 438.1 [M+H];
Elemental analysis: Calc. for $C_{26}H_{19}N_3S_2$: C 71.36, H 4.38, N 9.60, S 14.66 found: C 71.59, H 4.21, N 9.62, S 14.68.

9.4.2 Synthesis of borondifluoride bis-(aryl)-azadiisoindomethenes (100a-f)

General procedure for the preparation of borondifluoride aza-bis-(aryl)-diisoindomethenes: An aza-bis-(phenyl)-diisoindomethene **96** (5.01 g, 12.6 mmol) was dissolved in dichloroethane (150 ml) and diisopropylamine (10.5 ml, 60.8 mmol) was added. The mixture was stirred for 1 h and $BF_3{\cdot}OEt_2$ (7.5 ml, 60.5 mmol) was added at room temperature and then heated to reflux until complete conversion was observed (checked with DC chromatography, ca. 2 h) and was cooled down. The cold reaction mixture was then quenched with water and extracted with dichloromethane. The combined organic phases were dried and concentrated in vacuo. The crude product was purified by flash chromathography (dichloromethane/hexane 2:1) yielding boron difluoride aza-bis-(aryl)-diisoindomethenes (4.37 g, 78%).

Bis-(*o*-methyl-phenyl)-borondifluoride-azadiisoindomethene (100a)
Yield: 56%, **M.p.**: 260 °C; (hexane/ethylacetat 5:1).
^{1}**H NMR** (500 MHz, $CDCl_3$): δ (ppm) = 8.07 (d, J = 8.0 Hz, 1H), 8.06 (d, J = 8.0 Hz, 1H), 7.67 (d, J = 7.5 Hz 1H), 7.55(d, J = 7.5 Hz, 1H), 7.41 (m, 4H), 7.31 (d, J = 7.5 Hz, 1H), 7.21 (m, 2H), 7.06 (t, J = 7.5 Hz, 1H), 7.00 (t, J = 8.3 Hz, 1H), 6.98 (t, J = 8.3 Hz, 2H), 3.77 (s, 3H), 3.69 (s, 3H).
^{13}**C NMR** (126 MHz, $CDCl_3$): δ (ppm) = 157.7, 151.4, 151.1, 139.0, 131.7, 130.0, 126.2, 124.2, 120.8, 120.4, 119.6, 111.2, 111.0, 55.6.
^{19}**F NMR** (282 MHz, $CDCl_3$): δ (ppm) = 118.0 (o, J = 31.0), 133.1 (q, J = 31.0), 149.0 (q, J = 31.0).
MS (EI) m/z: 506.2 [M+H].
Elemental analysis: Calc. for $C_{30}H_{22}N_3O_2BF_2$: C 71.16, H 4.57, N 8.29, found: C 70.09, H 4.25, N 7.92.

Bis-(*o*-methoxy-phenyl)-borondifluoride-azadiisoindomethene (100b)

Yield: 62%, **M.p.**: 260 °C; (chloroform/hexane 4:1).

^{1}**H NMR** (500 MHz, $CDCl_3$): δ (ppm) = 8.10 (d, J = 8.0 Hz, 2H), 7.50 (t, J = 7.9 Hz 2H), 7.44 (d, J = 7.9 Hz,1H), 7.38 (d, J = 7.5 Hz, 1H), 7.34 (t, J = 7.5 Hz, 2H), 7.21 (m, 8H), 2.18 (s, 3H), 2.15 (s, 3H).

^{13}**C NMR** (126 MHz, $CDCl_3$): δ (ppm) = 154.2, 138.6, 137.2, 133.1, 131.5, 130.6, 130.0, 129.9, 129.8, 129.7, 126.7, 125.2, 123.7, 121.0, 20.0.

^{19}**F NMR** (282 MHz, $CDCl_3$): δ (ppm) = 127.2 (o, J = 31.0), 136.4 (q, J = 31.0), 145.6 (q, J = 31.0).

MS (EI) m/z: 474.2 [M+H].

Elemental analysis: Calc. for $C_{30}H_{22}N_3BF_3$: C 76.13, H 4.68, N 8.88, found: C 75.72, H 4.55, N 8.70.

Bis-(phenyl)-borondifluoride-azadiisoindomethene (100c)

Yield: 78%, **M.p.**: 268 °C; (dichloromethane/hexane 2:1).

^{1}**H NMR** (500 MHz, $CDCl_3$): δ (ppm) = 8.11 (d, J = Hz, 2H), 7.87 (dd, J = 2.3; 7.9 Hz, 4 H), 7.62 (d, J = 8.1 Hz, 1H), 7.51(m, 8H), 7.31(t, J = 7.6 Hz, 2H).

^{13}**C NMR** (126 MHz, $CDCl_3$): δ (ppm) = 153.2, 139.3, 133.6, 131.1, 130.5, 130.3, 130.2, 130.3, 128.5, 127.0, 124.1, 121.2.

^{19}**F NMR** (282 MHz, $CDCl_3$): δ (ppm) = 129.5 (q, J = 31.0).

MS (EI) m/z: 446.2 [M+H].

Elemental analysis: Calc. for $C_{28}H_{18}N_3BF_2$: C 75.53 H 4.07, N 9.44, found: C 75.33, H 3.94, N 9.27.

Bis-(*p*-methyl-phenyl)-borondifluoride-azadiisoindomethene (100d)

Yield: 74%, **M.p.** 268 °C; (dichloromethane/hexane 1:1).

^{1}**H NMR** (500 MHz, $CDCl_3$): δ (ppm) = 8.10 (d, J = 8.1 Hz, 2H), 7.79 (d, J = 8.1, 4H), 7.63 (d, J = 8.1 Hz, 2H), 7.49 (t, J = 7.1 Hz, 2H), 7.31 (t, J = 8.1 Hz, 4H), 7.29 (d, J = 7.1 Hz, 2H), 2.43 (s, 6H).

^{13}**C NMR** (126 MHz, $CDCl_3$): δ (ppm) = 153.2, 140.7, 139.2, 133.5, 131.1, 130.2, 130.1, 129.2, 127.5, 126.8, 124.2, 121.1, 21.6.

^{19}**F NMR** (282 MHz, $CDCl_3$): δ (ppm) = 129.5 (q, J = 31.0).

MS (EI) m/z: 474.2 [M+H].

Elemental analysis: Calc. for $C_{30}H_{22}N_3BF_2$: C 76.13, H 4.68, N 8.88, found: C 76.37, H 5.22, N 8.89.

Bis-(*p*-methoxy-phenyl)-borondifluoride-azadiisoindomethene (100e)

Yield: 65%, **M.p.**: 254 °C; (dichloromethane/hexane 2:1).

^{1}**H NMR** (500 MHz, $CDCl_3$): δ (ppm) = 8.10 (d, J = 8.0 Hz, 2H), 7.90 (d, J = 8.8, 4H), 7.65 (d, J = 8.0 Hz, 2H), 7.48 (t, J = 7.1 Hz, 4H), 7.29 (t, J = 7.1 Hz, 2H), 7.04 (d, J = 8.8 Hz, 2H), 3.88 (s, 6H).

^{13}**C NMR** (126 MHz, $CDCl_3$): δ (ppm) = 161.3, 152.4, 139.1, 133.5, 132.0, 131.0, 130.1, 126.8, 124.1, 122.9, 121.1, 114.1, 55.3.

^{19}**F NMR** (282 MHz, $CDCl_3$): δ (ppm) = 129.7 (q, J = 31.0).

MS (EI) *m/z*: 506.2 [M+H].

Elemental analysis: Calc. for $C_{30}H_{22}N_3O_2BF_2$: C 71.16, H 4.57, N 8.29, found: C 71.14, H 4.58, N 8.22.

Bis-(5-methyl-thienyl)-borondifluoride-azadiisoindomethene (100f)

Yield: 54%, **M.p.**: 260 °C; (chloroform).

^{1}**H NMR** (500 MHz, $CDCl_3$): δ (ppm) = 8.08 (m, 6H), 7.47 (d, J = 6.5 Hz, 2H), 7.36 (t, J = 6.5 Hz, 2H), 6.97 (d, J = 3.5 Hz, 2H), 2.62 (s, 6H).

^{13}**C NMR** (126 MHz, $CDCl_3$): δ (ppm) = 147.2, 143.7, 140.2, 134.0, 133.2, 131.0, 130.0, 129.7, 127.7, 127.3, 124.4, 121.3, 15.7.

^{19}**F NMR** (282 MHz, $CDCl_3$): δ (ppm) = 133.9 (q, J = 31.0).

MS (EI) *m/z*: 486.1 [M+H].

Elemental analysis: Calc. for $C_{26}H_{18}N_3S_2BF_2$: C 64.34, H 3.74, N 8.66, S 13.21 found: C 63.72, H 3.45, N 8.20, S 13.38.

9.4.3 Synthesis of boron catecholat bis-(aryl)-azadiisoindomethenes (101c-e)

General procedure for the preparation of boron catecholat bis-(aryl)-azadiisoindomethenes: An aza-bis-(phenyl)-diisoindomethene **96** (0.43g, 1.09 mmol) was dissolved in dichloroethane (400 ml) and diisopropylethylamine (7.59 mmol) and butoxy-boron-catechol (0.6ml, 3.35 mmol) was added. The reaction was heated to reflux for 24h. Subsequently, the cold reaction mixture was quenched with NaCl-solution. The organic layer was washed three times with NaCl solution, dried and evaporated to dryness. The crude product was purified by flash chromathography (dichloromethane/hexane 1:1) yielding boron catecholat bis-(aryl)-azadiisoindomethenes (140 mg, 26 %).

Bis-(phenyl)-boroncatechol-azadiisoindomethene (101c)

Yield: 26%, **M.p.**: 260 °C.

^{1}**H NMR** (500 MHz, $CDCl_3$): δ (ppm) = 8.11 (d, J = 8,19 Hz, 2H), 7.49 (t, 2H), 7.34 (d, $J_{6/5}$ = 7.88 Hz, 2H), 7.24 (m, 4H), 6.27 (s, 2H), 5.97 (s, 2H)

^{13}**C NMR** (126 MHz, $CDCl_3$): δ (ppm) = 155,71, 149, 85, 139,11, 133,56, 131,94, 130,66, 129,12, 128.98, 127.28, 126.82, 125.85, 123.87, 121.13, 118.66, 109.16

MS (EI) m/z: 516.2 [M+H].

Elemental analysis: Calc. for $C_{34}H_{22}BN_3O_2$: C 79.24, H 4.30, N 8.15 found: C 78.38, H 4.75, N 7.87.

Bis-(*p*-methyl-phenyl)-boroncatechol-azadiisoindomethene (101d)

Yield: 25%, **M.p.**: 260 °C.

^{1}**H NMR** (500 MHz, $CDCl_3$): δ (ppm) = 8.09 (d, J = 8.04 Hz, 2H), 7.48 (t, 2H), 7.36 (d, J = 8.04, 2H), 7.22 (t, 2H), 7.14 (d, J = 8.02 Hz, 4H), 6.75 (d, J = 7.80 Hz, 4H), 6.26 (m, 4H), 5.96 (m, 4H), 2.13 (s, 6H).

^{13}**C NMR** (126 MHz, $CDCl_3$): δ (ppm) = 155.95, 1479.94, 139.28, 139.02, 133.49, 131.91, 130.47, 128.89, 128.01, 126.65, 126.24, 123.86, 121.07, 118.38, 109.15, 21.13.

MS (EI) m/z: 544.2 [M+H].

Elemental analysis: Calc. for $C_{36}H_{26}BN_3O_2$: C 79.57, H 4.82, N 7.73 found: C 79.71, H 4.51, N 7.88.

Bis-(*p*-methoxy-phenyl)-boroncatechol-azadiisoindomethene (101e)

Yield: 26%, **M.p.**: 260 °C.

^{1}**H NMR** (500 MHz, $CDCl_3$): δ (ppm) = 8.10 (d, J = 8,10Hz, 2H), 7.48 (t, 2H), 7.39 (d, J = 8.05 Hz, 2H), 7.23 (m, 6H), 6.48 (d, J = 9.56 Hz, 2H), 6.33 (m, 2H), 6.04 (m, 2H), 3.64 (s, 6H) .

^{13}**C NMR** (126 MHz, $CDCl_3$): δ (ppm) = 155.71, 149.85, 139.11, 133.56, 131.94, 130.65, 126.67, 123.81, 121.61, 121.09, 118.65, 112.96, 109.24, 55.23.

MS (EI) m/z: 576.2 [M+H].

Elemental analysis: Calc. for $C_{36}H_{26}BN_3O_4$: C 75.14, H 4.55, N 7.30 found: C 75.07, H 4.50, N 7.34.

9.4.4 Synthesis of bis-(aryl)-azadiisoindomethene metal complexes (102a-e)

Synthesis of bis-(aryl)-azadiisoindomethene Co, Ni and Zn complexes

General procedure for the preparation of Co, Ni and Zn complexes bis-(aryl)-azadiisoindomethene: The bis-(aryl)-azadiisoindomethene **100c** (1.00 g, 2.52 mmol) and 1.3 eq. zinc acetate (0.60 g, 3.28 mmol) are refluxed n-butanol with 2 eq. triethylamine (0.7 ml,4.95 mmol)) until the product starts to precipitate from solution. The cold reaction mixture is filtered and the so obtained product is recrystallized fronm dichloromethane/hexane 4:1 to yield the zinc-di-bis-(aryl)-azadiisoindomethene as yellow needles (0.91 g, 84 %).

Cobalt-di-bis-(phenyl)-azadiisoindomethene (102a)
Yield: 37%, **M.p.**: 260 °C;
^{1}**H NMR**: not possible.
^{13}**C NMR**: not possible.
MS (EI) m/z: 852.3 [M+H].
Elemental analysis: Calc. for $C_{56}H_{36}N_6Co$: C 78.96, H 4.26, N 9.87; found: C 78.84, H 4.17, N 9.75.

Nickel-di-bis-(phenyl)-azadiisoindomethene (102b)
Yield: 57%, **M.p.**: 260 °C;
^{1}**H NMR** (500 MHz, $CDCl_3$): δ (ppm) = 40.55 (s, 4H), 13.75 (s, 2H), 6.71 (s, 2H), 6.42,(s, 4H), 5.49 (s, 2H), 3.93 (s, 1H), - 1.96,(s, 2H).
^{13}**C NMR**: not possible.
MS (EI) m/z: 851.2 [M+H].
Elemental analysis: Calc. for $C_{56}H_{36}N_6Ni$: C 78.98, H 4.26, N 9.87; found: C 77.94, H 4.29, N 9.49.

Zinc-di-bis-(phenyl)-azadiisoindomethene (102d)
Yield: 84%, **M.p.**: 260 °C;
^{1}**H NMR** (500 MHz, $CDCl_3$): δ (ppm) = 8 .07,(d, J = 7.88 Hz, 2H), 7.58,(d, J = 7.88 Hz, 2H),

7.40,(t, $J = 7.88$ Hz, 6H), 7.20,(t, 2H), 6.93,(t, 2H), 6.83,(t, $J = 7.56$ Hz, 2H).
^{13}C NMR (126 MHz, $CDCl_3$): δ (ppm) = 153.23, 141.53, 137.23, 132.8, 130.34, 128.60, 128.05, 127.47, 127.31, 124.90, 121.58, 120.62.
MS (EI) m/z: 857.3 [M+H].
Elemental analysis: Calc. for $C_{56}H_{36}N_6Zn$: C 78.36, H 4.23, N 9.79; found: C 77.53, H 4.95, N 9.53.

Synthesis of bis-(phenyl)-azadiisoindomethene Cu and Hg complexes

General procedure for the preparation of Cu and Hg complexes of bis-(aryl)-azadiisoindomethene: The aza-bis-(aryl)-diisoindomethene (1.00 g, 2.52 mmol) and 1.3 eq. Cu acetate (1.08 g, 3.18 mmol) are refluxed 10 ml THF with 3 eq. triethylamine for 30 min. Subsequently, 1.3 eq. of the metal acetate together with 10 ml THF is added. The solution is refluxed until no starting material is detectable with TLC. The reaction mixture is cooled to RT and the solid filtered. recrystallization from dichloromethane/hexane 4:1 gave the cu complex as violet plates (0.72 g, 66%).

Copper-di-bis-(phenyl)-azadiisoindomethene (102c)
Yield: 66%, **M.p.**: 260 °C;
^{1}H NMR: not possible.
^{13}C NMR: not possible.
MS (EI) m/z: 856.3 [M+H].
Elemental analysis: Calc. for $C_{56}H_{36}N_6Cu$: C 78.53, H 4.24, N 9.81; found: C 78.41, H 4.41, N 9.79.

Mercury-di-bis-(phenyl)-azadiisoindomethene (102e)
Yield: 53%, **M.p.**: 260 °C;
^{1}H NMR (500 MHz, $CDCl_3$): δ (ppm) = 8.10 (d, $J = 7.92$ Hz, 2H), 7.59 (d, $J = 7.90$ Hz,), 7.45 (t, $J = 7.98$ Hz, $J = 7.04$ Hz, 2H), 7.42 (d, $J = 7.92$ Hz, 4H), 7.26 (t, H, $J = 6.99$ Hz, 2H), 6.98 (m, 6H)
^{13}C NMR (126 MHz, $CDCl_3$): δ (ppm) = 153.88, 140.98, 137.82, 133.63, 130.25, 129.02, 128.43, 127.35, 124.85, 121.57, 120.55.
MS (EI) m/z: 993.3 [M+H].
Elemental analysis: Calc. for $C_{56}H_{36}N_6Hg$: C 67.70, H 3.65, N 8.46; found: C 67.24, H 3.36, N 8.92.

10 Appendix

Table 10.1: List of abbreviations.

AM1.5g	Air mass 1.5 global
BODIPY	4,4'–Difluoro–4–boro–3a,4a–diaza–s–indacen
BPAPF	9,9-Bis[4-(N,N-bis-biphenyl-4-yl-amino)phenyl]-9H-fluorene
$CDCl_3$	Deuterated chloroform
CT	Charge transfer
CV	Cyclic voltammetry
DCM	Dichlormethane
DCV6T	α,ω-bis(dicyanovinylene)-sexithiophene
DFT	Density functional Theory
DIPEA	Di-isopropylethyleneamine
DMF	Dimethylformamide
DMSO	Dimethylsulfoxid
eq.	Equivalents
ETL	Electron transport layer
Fc	Ferrocene
FF	Fill factor
GGA	Generalized gradient approximation
HF	HARTREE-FOCK
HTL	Hole transport layer
HOMO	Highest occupied molecular orbital
ITO	Indium tin oxide
LDA	Local density approximation
LUMO	Lowest unoccupied molecular orbital
M	Molar (mol/l)
Me	Methyl

MeCN	Acetonitrile
MeO-TPD	N,N,N',N'-tetrakis(4-methoxyphenyl)benzidine
M.p.	Melting point
MO	Molecular orbital
MPP	Maximum power point
MS	Mass spectrometry
NIR	Near infrared
nm	Nanometer
NMR	Nuclear magnetic resonanz
o	ortho
OAc	Acetate
OMe	Methoxy
Ox	Oxidation
p	para
^{i}Pr	Isopropyl
$PC_{61}BM$	[6,6]-phenyl-C_{61}-butyric acid methyl ester
$PC_{71}BM$	[6,6]-phenyl-C_{71}-butyric acid methyl ester
PCPDTBT	Poly[2,1,3-benzothiadiazole-4,7-diyl[4,4-bis(2-ethylhexyl)-4H-cyclopenta[2,1-b:3,4-b']dithiophene-2,6-diyl]]
PEDOT:PSS	Poly(3,4-ethylenedioxythiophene) poly(styrenesulfonate)
PES	Potential energy surface
ppm	Parts per million
PV-TPD	N,N'-Di(4-(2,2-diphenyl-ethen-1-yl)-phenyl)-N,N'-di(4-methylphenylphenyl)benzidine
Red	Reduction
STO	Slater type orbital
TBAPF	Tetra-n-butylammonium hexafluorophosphate
TDDFT	Time-dependent DFT
TEA	Triethylamine
TGA	Thermogravimetric analysis
THF	Tetrahydrofuran
TLC	Thin layer chromatography
UV	Ultraviolet
ZnPc	Zinc phthalocyanine

Table 10.2: Crystal data and structure refinement for **63a**.

Empirical formula	$C_{32}H_{22}BF_2N_3$	
Formula weight	497.34 g/mol	
Temperature	198(2) K	
Wavelength	0.71073 Å	
Crystal system	Monoclinic	
Space group	P2(1)/c	
Unit cell dimensions	a = 11.885(2) Å	$\alpha = 90\,^\circ$
	b = 10.464(2) Å	$\beta = 103.82(3)\,^\circ$
	c = 20.223(4) Å	$\gamma = 90\,^\circ$
Volume	2442.2(8) $Å^3$	
Z	4	
Density (calculated)	1.353 g cm^{-3}	
Absorption coefficient	0.090 mm^{-1}	
F(000)	1032	
Crystal size	0.25 x 0.22 x 0.15 mm^3	
Theta range for data collection	3.03 to 30.00°	
Index ranges	$-16 \leq h \leq 16$	
	$-14 \leq k \leq 14$	
	$-28 \leq l \leq 24$	
Reflections collected	51724	
Independent reflections	7091 [R(int)=0.0519]	
Completeness to theta [%]	99.5	
Max. and min. transmission	0.9866 and 0.9778	
Data / restraints / parameters	7091 / 0/ 343	
Goodness-of-fit on F	1.095	
Final R indices [I 2σ(I)]	R_1 = 0.0568, wR_2 = 0.0976	
R indices (all data)	R_1 = 0.1186, wR_2 = 0.1202	
Largest diff. peak / hole	0.241 / -0.307 e$\cdot$ $Å^3$	

Table 10.3: Crystal data and structure refinement for **100d**.

Empirical formula	$C_{30}H_{22}BF_2N_3$	
Formula weight	473.32 g/mol	
Temperature	198(2) K	
Wavelength	0.71073 Å	
Crystal system	Monoclinic	
Space group	$P2(1)/c$	
Unit cell dimensions	a = 9.773(2) Å	$\alpha = 90\,^\circ$
	b = 13.618(3) Å	$\beta = 98.73(3)\,^\circ$
	c = 18.112(4) Å	$\gamma = 90\,^\circ$
Volume	2382.6(9) $Å^3$	
Z	4	
Density (calculated)	1.320 g cm^{-3}	
Absorption coefficient	0.088 mm^{-1}	
F(000)	984	
Crystal size	0.36 x 0.32 x 0.24 mm^3	
Theta range for data collection	3.20 to 25.40°	
Index ranges	$-11 \leq h \leq 11$	
	$-16 \leq k \leq 16$	
	$-21 \leq l \leq 21$	
Reflections collected	52963	
Independent reflections	4372 [R(int) = 0.0375]	
Completeness to theta [%]	99.6	
Max. and min. transmission	0.9791 and 0.9688	
Data / restraints / parameters	3459 / 0 / 327	
Goodness-of-fit on F	1.087	
Final R indices [I 2σ(I)]	R_1 = 0.0413, wR_2 = 0.0900	
R indices (all data)	R_1 = 0.0596, wR_2 = 0.1015	
Largest diff. peak / hole	0.291 / -0.257 e· $Å^3$	

Table 10.4: Crystal data and structure refinement for **100f**.

Empirical formula	$C_{26}H_{18}BF_2N_3S_2$	
Formula weight	485.36 g/mol	
Temperature	193(2) K	
Wavelength	0.71073 Å	
Crystal system	Triclinic	
Space group	P–1	
Unit cell dimensions	a = 7.699(2) Å	$\alpha = 105.47(3)\,^\circ$
	b = 11.941(2) Å	$\beta = 94.88(3)\,^\circ$
	c = 12.608(3) Å	$\gamma = 98.29(3)\,^\circ$
Volume	1096.1(4) $Å^3$	
Z	2	
Density (calculated)	1.471 g cm^{-3}	
Absorption coefficient	0.281 mm^{-1}	
F(000)	500	
Crystal size	0.27 x 0.23 x 0.10 mm^3	
Theta range for data collection	3.34 to 30.0°	
Index ranges	$-10 \leq h \leq 10$	
	$-16 \leq k \leq 16$	
	$-17 \leq l \leq 17$	
Reflections collected	45723	
Independent reflections	6361 [R(int) = 0.0329]	
Completeness to theta [%]	99.4	
Max. and min. transmission	0.9724 and 0.9279	
Data / restraints / parameters	6361 / 0 / 309	
Goodness-of-fit on F	1.074	
Final R indices [I 2σ(I)]	R_1 = 0.0389, wR_2 = 0.0864	
R indices (all data)	R_1 = 0.0639, wR_2 = 0.0965	
Largest diff. peak / hole	0.367 / -0.303 e· $Å^3$	

Table 10.5: Crystal data and structure refinement for **102a**.

Empirical formula	$C_{59.5}H_{40}N_6Co$	
Formula weight	897.91 g/mol [$C_{56}H_{H36}N_6Co\cdot$ 1/2C_7H_8]	
Temperature	198(2 K	
Wavelength	0.71073 Å	
Crystal system	Triclinic	
Space group	*P*–1	
Unit cell dimensions	a = 12.229(5) Å	$\alpha = 113.080(5)\,^\circ$
	b = 13.097(5) Å	$\beta = 99.950(5)\,^\circ$
	c = 16.199(5) Å	$\gamma = 98.860(5)\,^\circ$
Volume	2279.4(15) $Å^3$	
Z	2	
Density (calculated)	1.308 g cm^{-3}	
Absorption coefficient	0.424 mm^{-1}	
F(000)	932	
Crystal size	0.14 x 0.12 x 0.08 mm^3	
Theta range for data collection	3.15 to 25.40°	
Index ranges	$-14 \leq h \leq 14$	
	$-15 \leq k \leq 15$	
	$-19 \leq l \leq 19$	
Reflections collected	59570	
Independent reflections	8340 [R(int) = 0.0583]	
Completeness to theta [%]	99.3	
Max. and min. transmission	0.9656 and 0.94498	
Data / restraints / parameters	8340 / 0 / 620	
Goodness-of-fit on F	1.202	
Final R indices [I 2σ(I)]	$R_1 = 0.0482$, $wR_2 = 0.0938$	
R indices (all data)	$R_1 = 0.0773$, $wR_2 = 0.1119$	
Largest diff. peak / hole	0.261 / -0.332 e$\cdot$ $Å^3$	

Table 10.6: Crystal data and structure refinement for **102d**.

Empirical formula	$C_{62.5}H_{42}Cl_2N_6Zn$	
Formula weight	1013.29 g/mol [$C_{56}H_{H36}N_6Zn \cdot C_6H_5Cl \cdot 1/2CH_2Cl_2$]	
Temperature	153(2) K	
Wavelength	0.71069 Å	
Crystal system	Triclinic	
Space group	*P*–1	
Unit cell dimensions	a = 13.239(5) Å	α = 72.130(5) °
	b = 13.699(5) Å	β = 68.380(5) °
	c = 16.251(5) Å	γ = 68.570(5) °
Volume	2499.49 $Å^3$	
Z	2	
Density (calculated)	1.346 g cm^{-3}	
Absorption coefficient	0.646 mm^{-1}	
F(000)	1046	
Crystal size	0.25 x 0.22 x 0.15 mm^3	
Theta range for data collection	3.02 to 27.99°	
Index ranges	$-17 \leq h \leq 16$	
	$-18 \leq k \leq 18$	
	$-21 \leq l \leq 21$	
Reflections collected	90345	
Independent reflections	11995 [R(int) = 0.0799]	
Completeness to theta [%]	99.4	
Max. and min. transmission	0.9647 and 0.8567	
Data / restraints / parameters	11995/ 0/ 631	
Goodness-of-fit on F	1.075	
Final R indices [I 2σ(I)]	R_1 = 0.0606, wR_2 = 0.1484	
R indices (all data)	R_1 = 0.0807, wR_2 = 0.1598	
Largest diff. peak / hole	1.023 / -0.935 e· $Å^3$	

Bibliography

[1] IEA, *Key World Energy Statistics*, www.iea.org, **2008**.

[2] S. Solomon, D. Qin, M. Manning, Z. Chen, M. Marquis, K. Averyt, M. Tignor, H. Miller, (Eds.), *Climate Change 2007: The Physical Science Basis*, Cambridge University Press, Cambridge, United Kingdom and New York, NY, USA, **2007**.

[3] A. Goetzberger, C. Hebling, H.-W. Schock, *Materials Science and Engineering* **2003**, *R40*, 1.

[4] C. Tang, *Appl. Phys. Lett.* **1986**, *48*, 183.

[5] C. Brabec, V. Dyakonov, U. Scherf, (Eds.), *Organic Photovoltaics*, Wiley-VCH, Weinheim, **2008**.

[6] R. F. Service, *Science* **2011**, *332*, 293.

[7] G. Qian, Z. Y. Wang, *Chem. Asian J.* **2010**, *5*, 1006.

[8] A. Loudet, K. Burgess, *Chem. Rev.* **2007**, *107*, 4891.

[9] T. Eicher, S. Hauptmann, *Heterocyclic Chemistry, 2nd Edition*, Wiley-VCH, Weinheim, **2003**.

[10] I. Fleming, *Nature* **1967**, *216*, 151.

[11] J. M. Berg, J. L. Tymoczko, L. Stryer, *Biochemie, 6th Edition*, Spektrum Akademischer Verlag, Elsevier, München, **2007**.

[12] G. Löbbert, *Phthalocyanines in Ullmann's Encyclopedia of Industrial Chemistry*, Wiley-VCH, Weinheim, **2002**.

[13] T. E. Wood, A. Thompson, *Chem. Rev.* **2007**, *107*, 1831.

[14] A. Jasat, D. Dolphin, *Chem. Rev.* **1997**, *97*, 2267.

[15] T. Torres, *Angew. Chem.* **2006**, *118*, 2900.

[16] R. Ziessel, G. Ulrich, A. Harriman, *New J. Chem..* **2007**, *31*, 496.

[17] G. Ulrich, R. Ziessel, A. Harriman, *Angew. Chem. Int. Ed.* **2008**, *47*, 1184.

[18] H. Fischer, H. Orth, *Die Chemie des Pyrrols*, Akademische Verlagsgesellschaft: Leipzig, **1937**.

[19] A. Johnson, I. Kay, E. Markham, K. S. R. Price, *J. Chem. Soc* **1959**, 3416.

[20] D. Eley, D. Spivey, *Trans. Farad. Soc.* **1962**, *58*, 405.

[21] A. Treibs, F.-H. Kreuzer, *Justus Liebigs Ann. Chem.* **1968**, *718*, 208.

[22] G. Scheibea, E. Daltrozzo, *Adv. Heterocyclic Chem.* **1967**, *7*, 153.

[23] S. S. Malhotra, M. C. Whiting, *J. Chem. Soc.* **1960**, 3812.

[24] A. Schmitt, B. Hinkeldey, M. Wild, G. Jung, *J. Fluoresc.* **2009**, *19*, 755.

[25] M. A. T. Rogers, *J. Chem. Soc.* **1943**, 590.

[26] M. A. T. Rogers, *J. Chem. Soc.* **1944**, 126.

[27] G. Sathyamoorthi, M.-L. Soong, T. W. Ross, J. H. Boyer, *Heteroatom Chemistry* **1993**, *4*, 603.

[28] A. Gorman, J. Killoran, C. O'Shea, T. Kenna, W. M. Gallagher, D. F. O'Shea, *J. Am. Chem. Soc.* **2004**, *126*, 10619.

[29] J. Nef, *Liebigs Ann. Chem.* **1894**, *280*, 264.

[30] R. Ballini, M. Petrini, *Tetrahedron* **2004**, *60*, 1017.

[31] M. J. Hall, S. O. McDonnel, J. Killoran, D. F. O'Shea, *J. Org. Chem.* **2005**, *70*, 5571.

[32] W. Zhao, E. M. Carreira, *Chem. Eur. J.* **2006**, *12*, 7254.

[33] E. B. Knott, *J.Chem. Soc.* **1947**, 1190.

[34] H. Bredereck, H. W. Vollmann, *Chem. Ber.* **1972**, *105*, 2271.

[35] C. W. Bird, L. Jiang, *Tetrahedron Lett.* **1992**, *33*, 7253.

[36] A. Palma, J. F. Gallagher, H. Müller-Bunz, J. Wolowska, E. J. McInnesc, D. F. O'Shea, *Dalton Trans.* **2009**, 273.

[37] T. S. Teets, D. V. Partyka, J. B. Updegraff, T. G. Gray, *Inorg. Chem.* **2008**, *47*, 2338.

[38] S. O. McDonnell, D. F. O'Shea, *Org. Lett.* **2006**, *8*, 3493.

[39] A. Coskun, M. D. Yilmaz, E. U. Akkaya, *Org. Lett.* **2007**, *9*, 607.

[40] A. Loudet, R. Bandichhor, L. Wu, K. Burgess, *Tetrahedron* **2008**, *64*, 3642.

[41] A. Loudet, R. Bandichhor, K. Burgess, A. Palma, S. O. McDonnell, M. J. Hall, D. F. O'Shea, *Org. Lett.* **2008**, *10*, 4771.

[42] V. F. Donyagina, S. Shimizu, N. Kobayashi, E. A. Lukyanets, *Tetrahedron Lett.* **2008**, *49*, 6152.

[43] P. Atkins, *Lehrbuch der Physikalischen Chemie, 2. Ed.*, Wiley-VCH, Weinheim, **1996**.

[44] P. Würfel, *Physik der Solarzellen*, Spektrum Akademischer Verlag GmbH, Heidelberg, **2000**.

[45] J.-M. Nunzi, *C. R. Physique* **2002**, *3*, 523.

[46] D. Wöhrle, O. Hild, *Chem. Unserer Zeit* **2010**, *44*, 174 – 189.

[47] M. Pope, C. Swenberg, *Electronic processes in organic molecular crystals, 2nd Ed.*, Oxford University Press, New York, **1999**.

[48] B. A. Gregg, S.-G. Chen, R. A. Cormier, *Chem. Mater.* **2004**, *16*, 4586.

[49] C. Kittel, *Einführung in die Festkörperphysik*, Oldenburg-Verlag, München, Wien, **1991**.

[50] W. Demtröder, *Experimetalphysik*, Springer-Verlag, Berlin-Heidelberg, **2000**.

[51] R. Kersting, U. Lemmer, M. Deussen, H. J. Bakker, R. F. Mahrt, H. Kurz, V. I. Arkhipov, H. Bassler, E. O. Gobel, *Phys. Rev. Lett.* **1994**, *73*, 1440.

[52] P. Peumans, S. R. Forrest, *Chem. Phys. Lett.* **2004**, *398*, 27.

[53] A. W. Hains, Z. Liang, M. A. Woodhouse, B. A. Gregg, *Chem. Rev.* **2010**, *110*, 6689.

[54] J. Cornil, D. Beljonne, J.-P. Calbert, J.-L. Brédas, *Adv. Mater.* **2001**, *13*, 1053.

[55] J.-L. Brédas, D. Beljonne, V. Coropceanu, J. Cornil, *Chem. Rev.* **2004**, *104*, 4971.

[56] J. Cornil, V. Coropceanu, D. A. da Silva Filho, Y. Olivier, R. Silbey, J.-L. Brédas, *Chem. Rev.* **2007**, *107*, 926.

[57] H. Spanggaard, F. Krebs, *Sol. Energy Mater. Sol. Cells* **2004**, *83*, 125.

[58] D. Hertel, H. Bässler, *Chem. Phys. Chem.* **2008**, *9*, 666.

[59] A. Miller, E. Abrahams, *Phys. Rev.* **1960**, *120*, 745.

[60] R. Marcus, *Rev. Mod. Phys.* **1993**, *65*, 599.

[61] P. F. Barbara, T. J. Meyer, M. A. Ratner, *J. Phys. Chem.* **1996**, *100*, 13148.

[62] H. Hoppe, N. S. Sariciftci, *J. Mater. Res.* **2004**, *19*, 1924.

[63] P. Würfel, *Chimia* **2007**, *61*, 770.

[64] P. Peumans, A. Yakimov, S. Forrest, *J. Appl. Phys.* **2003**, *93*, 3693.

[65] R. Loutfy, J. Sharp, *J. Chem. Phys.* **1979**, *71*, 1211.

[66] N. S. Sariciftci, L. Smilowitz, A. J. Heeger, F. Wudl, *Science* **1992**, *528*, 1474.

[67] C. Braun, *J. Chem. Phys.* **1984**, *80*, 4157.

[68] C. J. Brabec, C. Winder, N. S. Sariciftci, J. C. Hummelen, A. Dhanabalan, P. A. van Hal, R. Janssen, *Adv. Funct. Mater.* **2002**, *12*, 709.

[69] C. Winder, G. Matt, J. C. Hummelen, R. A. J. Janssen, N. S. Sariciftci, C. J. Brabec, *Thin Solid Films* **2002**, *403*, 3734.

[70] C. Deibel, V. Dyakonov, *Physik Journal* **2008**, *7*, 51–54.

[71] B. Maennig, J. Drechsel, D. Gebeyehu, P. Simon, F. Kozlowski, A. Werner, F. Li, S. Grundmann, S. Sonntag, M. Koch, K. Leo, M. Pfeiffer, H. Hoppe, D. Meissner, N. Saricifci, V. Dyakonov, J. Parisi, *J. Appl. Phys. A* **2004**, *79*, 1.

[72] W. Ma, C. Yang, X. Gong, K. Lee, A. Heeger, *Adv. Funct. Mater.* **2005**, *15*, 1617.

[73] S. Gunes, H. Neugebauer, N. S. Sariciftci, *Chem. Rev.* **2007**, *107*, 1324–1338.

[74] Y. Kim, S. Cook, S. M. Tuladhar, S. A. Choulis, J. Nelson, J. R. Durrant, D. D. C. Bradley, M. Giles, I. McCulloch, M. R. C.-S. Ha, *Nat. Mater.* **2006**, *5*, 197.

[75] P. Peumans, S. Forrest, *Appl. Phys. Lett.* **2001**, *79*, 126.

[76] R. Fitzner, E. Reinold, A. Mishra, E. Mena-Osteritz, H. Ziehlke, C. Körner, K. Leo, M. Riede, M. Weil, O. Tsaryova, A. Weiß, C. Uhrich, M. Pfeiffer, P. Bäuerle, *Adv. Funct. Mater.* **2011**, *21*, 897.

[77] C. Soci, I.-W. Hwang, D. Moses, Z. Zhu, D. Waller, R. Gaudiana, C. J. Brabec, A. J. Heeger, *Adv. Funct. Mater.* **2007**, *17*, 632.

[78] Y. Shirota, H. Kageyama, *Chem. Rev.* **2007**, *107*, 953.

[79] M. Hiramoto, H. Fukusumi, M. Yokoyama, *Appl. Phys. Lett.* **1991**, *58*, 1062.

[80] J. Halls, C. Walsh, N. Greenham, E. Marseglia, R. F. andS.C. Moretti, A. Holmes, *Nature* **1995**, *376*, 498.

[81] G. Yu, J. Gao, J. Hummelen, F. Wudl, A. Heeger., *Science* **1995**, *270*, 1789.

[82] C. Brabec, N. Sariciftci, J. Hummelen, *Adv. Funct. Mater.* **2001**, *11*, 15.

[83] F. Padinger, R. Rittberger, N. Sariciftci, *Adv. Funct. Mater.* **2003**, *13*, 85.

[84] M. Hiramoto, M. Suezaki, M. Yokoyama, *Chem. Lett.* **1990**, *19*, 327.

[85] J. Xue, B. Rand, S. Uchida, S. Forrest, *Adv. Mater.* **2005**, *17*, 66.

[86] M. Riede, C. Uhrich, J. Widmer, R. Timmreck, D. Wynands, G. Schwartz, W.-M. Gnehr, D. Hildebrandt, A. Weiss, J. Hwang, S. Sundarraj, P. Erk, M. Pfeiffer, K. Leo, *Adv. Funct. Mater.* **2011**, *21*, 3019.

[87] M. Pfeiffer, A. Beyer, B. Plönnigs, A. Nollau, T. Fritz, K. Leo, D. Schlettwein, S. Hiller, D. Wöhrle, *Sol. Energy Mater. Sol. Cells* **2000**, *63*, 83.

[88] K. Walzer, B. Maennig, M. Pfeiffer, K. Leo, *Chem. Rev.* **2007**, *4*, 1233.

[89] *http://www.heliatek.com/news-19* .

[90] *http://www.konarka.com/index.php/newsroom/press-release-list/* .

[91] *http://www.solarmer.com* .

[92] G. Dennler, M. C. Scharber, T. Ameri, P. Denk, K. Forberich, C. Waldauf, C. Brabec, *Adv. Mater.* **2008**, *20*, 579.

[93] V. I. Arkhipov, H. Bässler, *Phys. Status Solidi A* **2004**, *201*, 1152.

[94] B. C. Thompson, J. M. J. Fréchet, *Angew. Chem. Int. Ed.* **2008**, *47*, 58.

[95] J. Peet, M. L. Senatore, A. J. Heeger, G. C. Bazan, *Adv. Mater.* **2009**, *21*, n/a.

[96] T. L. Benanti, D. Venkataraman, *Photosynthesis Research* **2006**, *87*, 73.

[97] H. Haken, C. Wolf, *Molekülphysik und Quantenchemie, 2nd Edition*, Springer Verlag, Berlin, Heidelberg, **1994**.

[98] C. Cramer, *Essentials of Computational Chemistry: Theories and Models, 2nd Edition*, Wiley-VCH, Weinheim, **2004**.

[99] A. Szabo, N. Ostlund, *Modern Quantum Chemistry*, Dover Publ. Inc., Mineola, New York, **1996**.

[100] I. Levin, *Quantum Chemistry, 5th Edition*, Prentice Hall, Upper Saddle River, **1999**.

[101] J. Foresmann, A. Frisch, *Exploring Chemistry with Electronic Structure Methods, 2nd Edition*, Gaussian Inc., Pittsburg, **1996**.

[102] P. Hohenberg, W. Kohn, *Phys. Rev.* **1964**, *136*, 864.

[103] W. Kohn, L. J. Sham, *Phys. Rev.* **1965**, *140*, 1133.

[104] A. D. Becke, *J. Chem. Phys.* **1993**, *98*, 5648.

[105] C. Lee, W. Yang, R. G. Parr, *Phys. Rev. B* **1988**, *37*, 785.

[106] G. Rauhut, *Nachrichten aus der Chemie* **2004**, *52*, 315.

[107] R. van Leeuwen, *Phys. Rev. Lett.* **1998**, *80*, 1280.

[108] E. Runge, E. Gross, *Phys. Rev. Lett.* **1984**, *52*, 997.

[109] J. Gauss, *Nachrichten aus der Chemie* **2002**, *50*, 330.

[110] D. Feller, E. R. Davidson, K. L. (Ed.), D. B. (Ed.), *Reviews in Computational Chemistry*, Wiley-VCH, Weinheim, New York, **1990**.

[111] M. J. Frisch, G. W. Trucks, H. B. Schlegel, G. E. Scuseria, M. A. Robb, J. R. Cheeseman, J. A. Montgomery, Jr., T. Vreven, K. N. Kudin, J. C. Burant, J. M. Millam, S. S. Iyengar, J. Tomasi, V. Barone, B. Mennucci, M. Cossi, G. Scalmani, N. Rega, G. A. Petersson, H. Nakatsuji, M. Hada, M. Ehara, K. Toyota, R. Fukuda, J. Hasegawa, M. Ishida, T. Nakajima, Y. Honda, O. Kitao, H. Nakai, M. Klene, X. Li, J. E. Knox, H. P. Hratchian, J. B. Cross, V. Bakken, C. Adamo, J. Jaramillo, R. Gomperts, R. E. Stratmann, O. Yazyev, A. J. Austin, R. Cammi, C. Pomelli, J. W. Ochterski, P. Y. Ayala, K. Morokuma, G. A. Voth, P. Salvador, J. J. Dannenberg, V. G. Zakrzewski, S. Dapprich, A. D. Daniels, M. C. Strain, O. Farkas, D. K. Malick, A. D. Rabuck, K. Raghavachari, J. B. Foresmanv, J. V. Ortiz, Q. Cui, A. G. Baboul, S. Clifford, J. Cioslowski, B. B. Stefanov, G. Liu, A. Liashenko, P. Piskorz, I. Komaromi, R. L. Martin, D. J. Fox, T. Keith, M. A. Al-Laham, C. Y. Peng, A. Nanayakkara, M. Challacombe, P. M. W. Gill, B. Johnson, W. Chen, M. W. Wong,

C. Gonzalez, J. A. Pople, *Gaussian 03, Revision E.01; Gaussian Inc.*, Wallingford CT, **2004**.

[112] J. Killoran, S. O. McDonnell, J. F. Gallaghe, D. F. O'Shea, *New J. Chem.* **2008**, *32*, 483.

[113] K. Schwetlick, (Ed.), *Organikum 23. Ed.*, Wiley-VCH, Weinheim, **2009**.

[114] J. Killoran, L. Allen, J. Gallagher, W. Gallagher, D. O'Shea, *Chem. Commun.* **2002**, *17*, 1862.

[115] Y. Li, D. Dolphin, B. O. Patrick, *Tetrahedron Lett.* **2010**, *51*, 811.

[116] H. Hartmann, J. Fabian, *Light Absorption of Organic Colorants*, Springer-Verlag Heidelberg New York, **1980**.

[117] M. Liras, J. B. Prieto, M. Pintado-Sierra, F. L. Arbeloa, I. Garcya-Moreno, A. Costela, L. Infantes, R. Sastre, F. Amat-Guerri, *Org. Lett.* **2007**, *9*, 4183.

[118] N. Engel, W. Steglich, *Angew. Chem. Int. Ed.* **1978**, *17*, 676.

[119] N. Connelly, W. E. Geigerm, *Chem. Rev.* **1996**, *96*, 877.

[120] J. Heinze, *Angew. Chem.* **1984**, *96*, 823.

[121] S. Rihn, P. Retailleau, N. Bugsaliewicz, A. D. Nicola, R. Ziessel, *Tetrahedron Lett.* **2009**, *50*, 7008.

[122] D. Collado, J. Casado, S. R. G. J. L. Navarrete, R. Suau, E. Perez-Inestrosa, T. Pappenfus, M. Manuela, M. Raposo, *Chem. Eur. J.* **2011**, *17*, 498–507.

[123] J. Forgie, P. Skabara, J. Stibor, F. Vilela, Z. Vobecka, *Chem. Mater.* **2009**, *21*, 1784.

[124] I. Perepichka, D. Perepichka, *Handbook of Thiophene-Based Materials; Applications in Organic Electronics and Photonics. Vol. 2*, John Wiley & Sons: New York,, **2009**.

[125] A. Mishra, C.-Q. Ma, P. Baeuerle, *Chem. Rev.* **2009**, *109*, 1141.

[126] A. Facchetti, M.-H. Yoon, C. Stern, H. Katz, T. Marks, *Angew. Chem. Int. Ed.* **2003**, *42*, 3900.

[127] D. Wynands, M. Levichkova, M. Riede, M. Pfeiffer, P. Baeuerle, R. Rentenberger, P. Denner, K. Leo, *J. Appl. Phys.* **2010**, *107*, 0145171.

[128] J. Roncali, *Chem. Rev.* **1992**, *92*, 711.

[129] J. Fabian, *Dyes and Pigments* **2010**, *84*, 36.

[130] H. Hartmann, C. Heyde, I. Zug, *Synthesis* **2000**, 805.

[131] H. Hartmann, C. Heyde, I. Zug, *Eur. J. Org. Chem.* **2000**, 3273.

[132] H. Hartmann, P. Gerstner, D.Rohde, *Org. Lett.* **2001**, *3*, 1673.

[133] A. Noack, H. Hartmann, *Tetrahedron* **2002**, *58*, 2137.

[134] D. F. Veber, W. Lwowski, *J. Am. Chem. Soc.* **1964**, *86*, 4152.

[135] R. Bonnett, S. A. North, R. F. Newton, D. I. C. Scopes, *Tetrahedron* **1983**, *39*, 1401.

[136] G. E. M. Moussa, M. N. Basyouni, M. E. Shaban, A. F. El-Kafrawy, N. K. Al-Aasar, *Rev. Roum. Chim.* **1982**, *27*, 549.

[137] A. Krasovskiy, P. Knochel, *Angew. Chem.* **2004**, *116*, 3396.

[138] R. J. Kloetzing, A. Krasovskiy, P. Knochel, *Chem. Eur. J.* **2007**, *13*, 215.

[139] R. Leuckart, *Ber. Dtsch. Chem. Ges.* **1885**, *18*, 2341.

[140] R. Leuckart, *Ber. Dtsch. Chem. Ges.* **1891**, *24*, 3992.

[141] R. Gresser, M. Hummert, H. Hartmann, K. Leo, M. Riede, *Chem. Eur. J* **2011**, *17*, 2939.

[142] C. Tahtaoui, C. Thomas, F. Rohmer, P. Klotz, G. Duportail, Y. Mély, D. Bonnet, M. Hibert, *J. Org. Chem.* **2001**, *72*, 269.

[143] J. Chen, A. Burghart, A. Derecskei-Kovacs, K. Burgess, *J. Org. Chem.* **2000**, *652*, 2900.

[144] E. Szajna, P. Dobrowolski, A. L. Fuller, A. M. Arif, L. M. Berreau, *Inorg. Chem.* **2004**, *43*, 3988.

[145] L. Do, S. R. Halper, S. M. Cohen, *Chem. Commun.* **2004**, 2662.

[146] L. Yu, K. Muthukumaran, I. V. Sazanovich, C. Kirmaier, E. Hindin, J. R. Diers, P. D. Boyle, D. F. Bocian, D. Holten, J. S. Lindsey, *Inorg. Chem.* **2003**, *42*, 6629.

[147] A. Holleman, N. Wiberg, *Lehrbuch der Anorganischen Chemie, 101. Ed.*, de Gruyter, Berlin, **1995**.

[148] R. Pearson, *J. Am. Chem. Soc.* **1968**, *45*, 3533.

[149] M. Bühl, H. Kabrede, *J. Chem. Theory Comput.* **2006**, *2*, 12820.

[150] G. R. Hutchison, M. A. Ratner, T. J. Marks, *J.Am.Chem.Soc.* **2005**, *127*, 2339.

[151] S. E. Koh, C. Risko, D. A. da Silva-Filho, O. Kwon, A. Facchetti, J.-L. Brédas, T. J. Marks, M. A. Ratner, *Adv. Funct. Mater.* **2008**, *18*, 332.

[152] B. Lin, C. Cheng, Z. M. C.P. Lao, *J. Phys. Chem. (C)* **2008**, *112*, 16561.

[153] S. Arulmozhiraja, T. Ohno, *J. Phys. Chem. (A)* **2003**, *107*, 5241.

[154] D. Andrienko, J. Kirkpatrick, V. Marcon, J. Nelson, K. Kremer, *Phys. Stat. Sol. (B)* **2008**, *5*, 830.

[155] V. Marcon, W. Pisula, J. Dahl, D. W. Breiby, J. Kirkpatrick, S. Patwardhan, F. Grozema, D. Andrienko, *J. Am. Chem. Soc.* **2009**, *131*, 11426.

[156] M. P. Hein, *Bestimmung der Ladungsträgerbeweglichkeit in organischen Materialien für organische Solarzellen*, TU Dresden, **2010**.

[157] O. Kwon, V. Coropceanu, N. E. Gruhn, J. C. Durivage, J. G. Laquindanum, H. E. Katz, J. Cornil, J. L. Brédas, *J. Chem. Phys.* **2004**, *120*, 8186.

[158] S. Radke, *Charge transport in organic semiconductors*, TU Dresden, **2011**.

[159] C. Brabec, S. Shaheen, C. Winder, N. Sariciftci, P. Denk, *Appl. Phys. Lett.* **2002**, *80*, 1288.

[160] G. E. M. Moussa, M. N. Basyouni, M. E. Shaban, A. F. El-Kafrawy, N. K. Al-Aasar, *Rev. Roum. Chim.* **1982**, *27*, 549.

[161] H. Lu, S. Shimizu, J. Mack, Z. Shen, N. Kobayashi, *Chem. Asian J.* **2011**, *6*, 1026.

[162] Bruker, Delft, Netherlands, *Bruker SADABS - Area Detector Absorption and Other Corrections, 2.03*, **2002**.

[163] A. Altomare, M. C. Burla, M. Camalli, G. L. Cascarano, C. Giacovazzo, A. Guagliardi, A. G. Moliterni, G. Polidori, R. Spagna, *J. Appl. Cryst.* **1999**, *32*, 115.

[164] G. M. Sheldrick, *SHELXL-97 Program for the Refinement of Crystal Structures*, Universität Göttingen, Göttingen (Germany), **19972**.

[165] J. K. Lee, W. L. Ma, C. J. Brabec, J. Yuen, J. S. Moon, J. Y. Kim, K. Lee, G. C. Bazan, , A. J. Heeger, *J. Am. Chem. Soc.* **2008**, *130*, 3619.

[166] M. Irwin, B. Buchholz, A. Hains, R. Chang, T. Marks, *PNAS* **2008**, *105*, 2783.

[167] H.-H. Koa, L.-T. Tsao, K.-L. Yuc, C.-T. Liuc, J.-P. Wang, C.-N. Lin, *Bioorganic & Medicinal Chemistry* **2003**, *11*, 105.

[168] B. Ramesh, B. S. Rao, *E-Journal of Chemistry* **2010**, *7*, 433.

[169] G. Dannhardta, W. Kiefera, G. Krämera, S. Maehrleina, U. Nowea, B. Fiebich, *European Journal of Medicinal Chemistry* **2000**, *35*, 499.

[170] K. Peseke, L. Götze, H. Reinke, Q. Cedeño, J. Q. Suarez, M. G. Andreu, H. V. Castro, *J. Prakt. Chem.* **1997**, *339*, 656.

[171] R. Davis, *J. Org. Chem.* **1959**, *24*, 879.

Acknowledgements

First I would like to thank my supervisor Prof. Dr. K. Leo for giving me the opportunity to work on this topic at his institute and to support me also beyond this thesis. I also would like to thank Prof. Dr. T. Wolf for the second review of this thesis. I am indebted to Prof Dr. H. Hartmann, for his scientific support and guidance and his endless ideas. His encouraged examination of the papers and the manuscript helped to improve them essentially.

The group leaders Dr. Moritz Riede and Dr. Markus Hummert for creating an excellent working atmosphere and a very well equipped chemistry lab.

I would like to thank a lot of people of the OSOL group. First of all Toni Müller for the good team work. From the discussions I gained a deeper understanding about organic solar cell and beyond physics. Furthermore, I thank Moritz Hein for the preparation of the OFET devices and the charge carrier mobility measurements. Thanks goes also to Dr. David Wynands for the preparation of vacuum processed solar cells. Further I would like to thank Alexander Hoyer for his work on the metal complexes and Sylke Furkert for the absorption measurements, together with Marion Wrackmeyer helping in determining the fluorescent quantum yields.

I would like to express many thanks to Prof. G. Cuniberti and his group, in particular Dr. Caroline Gollub and Sebastian Radke for the fruitful collaboration about the simulation of charge carrier mobilities in the aza-bodipy materials. Further I want to thank Prof. Dr. T. Marks and Prof. Dr. A. Facchetti at the Northwestern University, Evanston for giving me the opportunity to prepare and characterize the solution processed devices in their group. I particular thank Steven Loser for introducing me to spin coating and Jangdae Youn for the discussions.

I thank my colleague in the lab Jörg Alex and all other colleagues at the IAPP (TU Dresden) for the open minded and motivating working atmosphere. It is a pleasure to work in such an environment and I personally enjoyed the many discussions and bringing in my chemical point of view.

I would like to thank Kai Schmidt for the IT and Eva Schmidt, Jutta Hunger, and Angelika Wolf for helping me in all administrative affairs.

Last but not least, I want to thank my friends and my family. Without the constant support from my parents, this work would not have been possible. Especially, I thank my partner Caroline for her tremendous support, her patience and her improvements to the language of the manuscript. I also thank Caroline's family for their enormous support during the last month.

Versicherung

Hiermit versichere ich, dass ich die vorliegende Arbeit ohne unzulässige Hilfe Dritter und ohne Benutzung anderer als der angegebenen Hilfsmittel angefertigt habe; die aus fremden Quellen direkt oder indirekt übernommenen Gedanken sind als solche kenntlich gemacht. Die Arbeit wurde bisher weder im Inland noch im Ausland in gleicher oder ähnlicher Form einer anderen Prüfungsbehörde vorgelegt. Diese Arbeit wurde am Institut für Angewandte Photophysik der Technischen Universität Dresden unter der wissenschaftlichen Betreuung von Prof. Dr. Karl Leo angefertigt. Ich erkenne die Promotionsordnung der Fakultät Mathematik und Naturwissenschaften der Technischen Universität Dresden vom 23.02.2011 an.

Roland Gresser
Dresden, den 27.09.2011